



UNIVERSITÀ DEGLI STUDI DI PADOVA
DIPARTIMENTO DI INGEGNERIA INDUSTRIALE

SCUOLA DI DOTTORATO DI RICERCA IN INGEGNERIA INDUSTRIALE
INDIRIZZO IN INGEGNERIA CHIMICA, DEI MATERIALI E DELLA
PRODUZIONE

CICLO XXVII

**Fatigue Performance Evaluation of
Gears used in Off-Highway Drivelines**

Direttore della Scuola:
Ch.mo prof. Paolo Colombo

Supervisore Universitario:
Ch.mo prof. Giovanni Meneghetti

Supervisore in Carraro Group S.p.a.:
Ing. Fulvio Lo Conte

Dottorando: Carlo Dengo

Summary

Gears are the core of power transmission systems. The study of their fatigue performances is essential for the companies dealing with the design and manufacturing of transmissions. The work here presented faces the study of pitting and bending fatigue performances of gears mounted on Off-Highway drivelines.

This work was carried out under the formulation of "High Apprenticeship PhD" and was financed by Carraro Drive Tech. The research activity was executed partly inside the Company and partly at the University. The work started from the study of standards on gear design, especially ISO 6336 for cylindrical gears. Then the commercial software packages oriented to gear design were studied. Using this background, the gear durability tests for axles' validation performed by Carraro Drive Tech in the last years were modeled. The bending and pitting allowable fatigue curves were then estimated using the calculated stress and the life exhibited during the analyzed tests. Results obtained showed that the statistical scatter on bending and pitting fatigue performances may be remarkable. The allowable limits obtained by statistical inference at high survival probabilities resulted lower than the corresponding values declared by the standards, at least for the analyzed applications.

The work was then focused on the study of tooth-root bending fatigue of gears, planning a test campaign involving different case-hardening steels coming from the areas where the Company is localizing the production of its components. Both static and fatigue comparative tests were performed on plain case-hardened specimens realized in order to resemble as more as possible the teeth surface state of a specific gear used by the Company. The steels exhibited high mechanical strength and similar characteristics, in line with the best case-hardened steels presented in the literature, independently from the origin area. Additional attention was paid to 20MnCr5 steel, carrying

out bending fatigue tests also on notched specimens and gears. Experimental data were then used as starting point in the application of the different gear design methods reported in ISO 6336, with the purpose of investigating their reliability. The correlation between the fatigue curves obtained on specimens and gears is of particular interest for companies dealing with the design of power transmission systems, since the fatigue tests on specimen are potentially faster, more inexpensive and easier than using gears. Furthermore, the use of specimens allows to compare the manufacturing process of different suppliers directly in terms of experimental endurance limits. This approach is more detailed than using the standardized curves of ISO 6336, where the fatigue behavior is given only on the base of the steel quality, that is defined by a number of quality controls that do not consider explicitly the fatigue limit. The experimental behavior of the gear was resembled only partially by the methods, especially for notch sensitivity. For this reason, the experimental data collected in this work were used to develop and improve the design methods of the standard, leading to more satisfactory results. The endurance limit of specimens and gears resulted located in the range of 50,000 ÷ 300,000 cycles, that are values much shorter than the 3,000,000 of cycles reported in ISO 6336 standard. The gear testing procedure presented in the work resulted more complete and effective than current testing procedures of the Company, being able to characterize the whole fatigue curve in much shorter time.

The study of the bending fatigue performances was accompanied with the SEM observations of specimens' fracture surfaces, the analysis of residual stress induced by case-hardening treatment, the influence of grinding on case-hardened surfaces and the presence of a mean stress. Results were discussed and compared to recommendations of ISO 6336, finding in some cases only a partial agreement.

Sommario

Le ruote dentate costituiscono il cuore dei sistemi di trasmissione di potenza. Lo studio della loro resistenza a fatica è indispensabile per le aziende che progettano e producono trasmissioni. Il lavoro qui presentato affronta lo studio della resistenza a fatica flessionale e da contatto di ingranaggi montati su assali e trasmissioni di veicoli fuoristrada.

Questo lavoro è stato svolto nell'ambito di un Dottorato in Alto Apprendistato finanziato da Carraro Drive Tech, e ha previsto lo svolgimento dell'attività parte in Azienda e parte presso l'Università. Il lavoro è stato strutturato dapprima affrontando lo studio delle normative che trattano la progettazione di ruote dentate, in particolar modo la normativa ISO 6336 per le ruote cilindriche. Si sono poi appresi gli strumenti di calcolo commerciali per la loro applicazione in modo automatico su modelli virtuali. Con tali conoscenze si sono modellati i test mirati alla validazione di nuovi assali eseguiti negli ultimi anni da Carraro Drive Tech. Incrociando i risultati dei calcoli con le durate riscontrate durante i test si sono costruite le curve a fatica flessionale e da contatto per le applicazioni dell'Azienda. I risultati sperimentali hanno dimostrato che la dispersione statistica relativa alla resistenza a fatica flessionale e da contatto può essere notevole, e l'estrapolazione di curve ad elevate probabilità di sopravvivenza ha mostrato come i limiti dichiarati nella normativa ISO 6336 risultino troppo ottimistici per le applicazioni considerate. Il lavoro si è poi concentrato sullo studio della fatica a base dente di ruote dentate, pianificando un programma di prova che ha coinvolto acciai cementati provenienti da diverse aree dove l'Azienda sta localizzando la produzione di componentistica. I test comparativi, sia statici che a fatica, sono stati realizzati su provini lisci e cementati in modo da ricreare il più possibile la condizione superficiale dei denti di una particolare ruota dentata usata in Azienda. I vari acciai hanno dimostrato resistenza meccanica in linea con quella dei migliori acciai cementati presenti in letteratura, e caratteristiche

comparabili tra le diverse aree di provenienza. Maggiore attenzione è stata riservata al 20MnCr5, eseguendo prove di fatica a flessione anche su provini intagliati e su ruote dentate. I dati sperimentali ottenuti sono stati usati come base per applicare i diversi metodi di progettazione della normativa ISO 6336 e verificarne l'attendibilità. La correlazione tra le curve di fatica ricavate su provini e ruote dentate è di forte interesse per le aziende che operano nel settore delle trasmissioni di potenza, perchè eseguire prove di fatica su provini è potenzialmente più rapido, economico e semplice di eseguire prove su ruote dentate. L'uso di provini inoltre permette di confrontare le capacità produttive di fornitori diversi, confrontando direttamente i limiti di fatica sperimentali. Tale approccio è più dettagliato di utilizzare le curve standardizzate della ISO 6336, dove il comportamento a fatica è fornito solo in funzione della qualità dell'acciaio considerato, che però non viene valutata con controlli che considerano in modo esplicito il limite di fatica. I metodi della normativa hanno saputo rappresentare il comportamento della ruota dentata osservato sperimentalmente solo in modo parziale, specialmente per quanto riguarda la stima della sensibilità all'intaglio. Per questa ragione, i dati sperimentali raccolti sono stati usati per sviluppare e migliorare i metodi di progettazione riportati in normativa, portando a risultati più soddisfacenti. Il limite di durata ottenuto su provini ed ingranaggi è risultato essere collocato tra i 50,000 e 300,000 cicli, valori molto più bassi dei 3,000,000 di cicli proposti dalla ISO 6336. La metodologia di prova su ingranaggi usata nello studio è risultata più completa ed efficace delle attuali procedure di prova aziendali, riuscendo a caratterizzare l'intera curva di fatica in tempi molto più ridotti.

Lo studio delle proprietà a fatica flessionale è stato corredato anche dalla osservazione al microscopio a scansione elettronica delle superfici di rottura ottenute sui provini, all'analisi delle tensioni residue indotte dalla cementazione, all'influenza che la rettifica può apportare sulle superfici cementate e alla presenza di una tensione media. I risultati sono stati discussi e confrontati con le prescrizioni riportate nella ISO 6336, trovando in alcuni casi solo parziale accordo.

Acknowledgments

I would like to express sincere gratitude to my supervisor, Professor Giovanni Meneghetti, for showing me how to face new challenges, combining technical competences and human relationships. It was a pleasure for me working with you.

I would like to thank Carraro S.p.a. for believing in me and for giving me the possibility to attend this PhD project. Special thanks to all the colleagues of the Engineering and Innovation Department who supported me during the project. Thanks also to the research team of Machine Design of the University of Padova, for the support given to me during the experimental tests in the Laboratory.

Most important thanks go to my loved ones, for the encouragement and affection they gave to me in these last three years. Thank you for being beside me!

Contents

Introduction	1
1 Carraro Drive Tech	3
1.1 Carraro Group	3
1.2 Carraro Drive Tech	4
1.3 CDT's products	5
1.4 Axle schematic	10
2 Analysis of Test Archive	13
2.1 Introduction	13
2.2 Gear tests	14
2.2.1 Four Square Test	15
2.2.2 Chicken Test	18
2.2.3 Endurance Structural Test	19
2.2.4 Power Test	21
2.3 Failure mode analysis of axles	21
2.3.1 FST failure modes	21
2.3.2 CT failure modes	23
2.3.3 EST failure modes	24
2.3.4 Failure mode summary	29
2.4 Pitting curves extrapolated from FSTs	32
2.4.1 KISSsys models	33
2.4.2 Statistical analysis	38
2.4.3 Statistical results	42
2.4.4 Evolution of pitting	47
2.5 Bending performances of bevel gear sets	53
2.5.1 Bevel gear set models	54
2.5.2 Reliability of Gleason calculation method	57

2.5.3	Bending fatigue curves extrapolated from CTs	63
2.6	Conclusions	71
3	Experimental Tests on Specimens	75
3.1	Introduction	75
3.2	Literature survey	79
3.3	Test plan	86
3.4	Specimens	86
3.4.1	Design of specimens	86
3.4.2	Manufacturing process of specimens	92
3.4.3	Microstructure of steels	93
3.4.4	Micro-hardness profiles	95
3.5	Static tests	99
3.6	Fatigue tests	102
3.6.1	Four point plane bending test, R=0.1	102
3.6.2	Cantilever plane bending test, R=-1	112
3.6.3	Axial fatigue test, R=0.1	120
3.7	Observation of fracture surfaces	121
3.7.1	Failures starting from surface	122
3.7.2	Non-defect internal matrix failures	127
3.8	Residual stresses	130
3.9	Discussion of experimental results	131
3.10	Conclusions	139
4	ISO 6336-3 Analysis	141
4.1	Introduction	141
4.2	Derivation of methods B , B_p and B_k	142
4.2.1	Theoretical basis	142
4.2.2	Method B_p	148
4.2.3	Method B_k	151
4.2.4	Method B	153
4.3	Application of methods to literature data	154
4.3.1	Results of pulsator tests on gears	154
4.3.2	Fatigue data of plain specimens	162
4.3.3	Fatigue data of notched specimens	168
4.3.4	Application of methods B , B_p and B_k to literature data	171
4.3.5	Summary of the exploratory analyses	173
4.4	Fatigue tests on gears	174
4.4.1	Pulsator tests on 20MnCr5 gears	175
4.4.2	Calculation of tooth root bending stress	179
4.4.3	SN curve of 20MnCr5 gears	186

4.4.4 Pulsator tests on EN 353 gears	187
4.5 Application of methods to experimental data	189
4.6 Improvement of specimen-based methods	198
4.7 Conclusions	204
Conclusions	207
Appendix A Statistical Analysis of Fatigue Data	211
A.1 Introduction	211
A.2 Finite life region	212
A.3 Endurance limit	217
A.4 Estimation of a full S-N curve	222
Appendix B Technical Drawings	225
References	245

Introduction

The research project here presented was carried out under the formulation of "High Apprenticeship" with Carraro Drive Tech, a Company belonging to Carraro Group. Carraro Group is a multinational corporation that design and manufacture power transmission systems. The core business of the Company is focused on the development of drivelines for Off-Highway vehicles (mainly agricultural tractors and earth moving machines). The release of a new driveline follows several steps, including design, calculations and bench testing. It is important to minimize costs and times of these activities, in order to reduce the final cost of the product and increase the proficiency. The use of gear steels coming from new emerging markets complicates the scenario, since new experience on them must be acquired in order to have reliable calculation models. For the Company it is important to investigate new methodologies to measure in shorter time the fatigue performances of gears realized by different suppliers. The definition of the fatigue performances is dependent on the calculation approach used in the fatigue analyses. The Company estimates fatigue lives using approaches described in the international standards on gear design. However, the allowable limits reported in the standards are generalized to families of materials, while the Company is interested in the definition of the specific properties of the steels.

The work here presented was oriented to obtain useful results under three different areas of interest for the Company: (i) the collection and analysis of gear fatigue performances collected in the past years by means of experimental tests, (ii) the investigation of fatigue performances of case-hardened gear steels coming from different world areas, and (iii) the study, applicability and calibration of the design methods proposed by ISO 6336 Standard.

Concerning point (i), the Company's test archive was analyzed, starting from the identification of the gear failure modes exhibited during experimental tests. The aim was to obtain the allowable fatigue limits of the case-hardened

steels commonly adopted to manufacture gears inside the Company. A couple of test typologies were found to be valuable for the definition of pitting and bending performances of gears. Virtual models of tested axles were built, and calculations were performed in order to obtain the corresponding pitting and bending stresses. Calculations were made using the international standards concerning gear design, in particular ISO 6336. Using the fatigue lives recorded during the tests, the allowable fatigue curves according to ISO 6336-5 were drawn for different survival probabilities, by means of statistical models adopted in reliability analyses.

Concerning point (ii), a test plan involving six different case-hardened steels coming from Italy, India and China was defined. Static and fatigue tests on plain specimens were carried out in order to compare static and fatigue performance of the steels under the same loading conditions. The specimens were designed in order to resemble a real gear tooth, in terms of dimensions, manufacturing process, working conditions and heat treatment. For a particular case-hardening steel, additional fatigue tests were carried out on specimens with different surface finishing and with a notch similar to the real tooth-root fillet of a gear used in Off-Highway axles. The results were compared to the literature and discussed involving considerations on microstructure and residual stress field induced by case-hardening treatment, along with the analysis of the fracture surfaces. Experimental fatigue design factors were estimated and compared to ISO 6336 recommendations.

Concerning point (iii), the bending design approach presented in ISO 6336-3 was analyzed from the theoretical point of view, in order to show the origin of the design factors involved in the calculation algorithms. According to the standard, the bending life prediction of a gear can be made using fatigue data obtained from reference gears (with fixed geometry), from plain specimens or from notched specimens. The three methods were used to predict the fatigue life of a gear used in Off-Highway applications, using the fatigue curves previously obtained on specimens at point (ii), being the gears and specimens made of the same case-hardened steel. The results of the methods were then compared to the experimental curve obtained on the gear under study by means of fatigue pulsator tests. Since the application of specimen-based methods resulted inaccurate, the experimental data of gears and specimens were used to calibrate the calculation factors of the methods. In particular, new values of the notch sensitivity factors were proposed to obtain results closer to the experimental evidence.

Chapter 1

Carraro Drive Tech

This chapter shows the organizational structure of Carraro Group, defining the role of Carraro Drive Tech. Main products and applications of Drive Tech are reported, giving some examples of Off-Highway drivelines for agricultural and construction markets.

1.1 Carraro Group

Carraro Group is an international group that designs, manufactures and commercializes power transmissions all over the world.

The group is made of three companies, working in a specific business area:

- *Carraro Drive Tech* for the business area of *Drivelines*
- *Agritalia* for the business area of *Vehicles*
- *Santerno* for the business area of *Power Controls*

Markets and products of the three Companies are different. Drive Tech produces transmissions, axles and drives for earth-moving and agricultural vehicles, Agritalia develops and produces agricultural tractors, while Santerno produces inverters for industrial applications, solar and wind energy. The first two companies operate mainly in the mechanical field, while the third in the electrical one.

Carraro Group was founded in 1932, starting from the production of sowing machines and equipment for agricultural works. The Company grew constantly, moving the business to the production of tractors. It became one of the most important Italian tractor manufacturers. From the 1970s the

Company focused its business to axles and transmissions, but the production of tractors was kept alive and moved to a new plant. To increase the manufacturing capabilities, Carraro acquired some other mechanical Companies, such as OMG (that became PNH later) and SIAP. During the 1990s the Company began to settle in foreign markets, starting from United States (Carraro North America) and Germany (CarraroVertiebs). From 1997 to 2005 new plants were opened in India, Poland, Argentina, Germany and China. In 2006 the Company acquired Santerno, in 2007 Gear World and in 2008 Carraro Drive Tech was established.

1.2 Carraro Drive Tech

Carraro Drive Tech (CDT) is the most important business area of the Group. it deals with the design and manufacturing of drivelines. Applications vary from agricultural tractors to earth-moving machines, from automotive commercial light vehicles to military vehicles. However, core business is made of drivelines for Off-Highway (agricultural and industrial) vehicles. CDT counts 4 Research and Development Centers, located in:

- Italy: CDT's Headquarter
- Germany: O&K ¹
- India: Carraro Technologies India Pvt. ltd.
- Argentina: Carraro Argentina

R&D Centers support the corresponding manufacturing plants.

There are also sales, spare parts and logistic offices in the United States and Brazil. In sum, CDT's organic is made of more than 1600 people, more than 100 of them in R&D centers.

The choice of locating R&D departments in different areas of the world is not only due to economic reasons. It ensures a better fulfillment of philosophy *Local to Local*, that consists in designing products that are suitable for the market where the product will be sold, in terms of functionality, features, quality, materials. This approach requires the modification of the manufacturing and design methods used in Western Europe, in order to match with foreign cultures and capabilities. In this way, emerging markets can perceive the products as satisfactory.

¹O&K is specialized in design of drives

1.3 CDT's products

First of all it is important to explain what a driveline is. A driveline is the summation of all the devices which deliver the motion from the source of power of a vehicle to the wheels. Generally the vehicle's source of power is an internal combustion engine, but there are some applications where hydraulic or electric motors can be used as well. CDT produces drivelines for wheeled vehicles, but it must be remembered that in the field of big industrial machines also crawler vehicles are widely used.

Just for example, the drivelines for a tractor and a backhoe loader are reported in Figure 1.1 and 1.2 respectively. It can be seen that driveline conformation can change significantly from application to application. However, for a wheeled vehicle, there are always a transmission (with the capability of gear shifting) and the axles.

The markets where CDT operates are:

- Agricultural
- Construction equipment
- Material Handling
- Automotive

Since these markets are very different one from the other, it is here impossible to make a thorough description of all the products offered by the Company. The technical solutions are different from vehicles to vehicles, not only in terms of load/torque carrying capacity, but also in terms of functional principle. However, it is possible to divide the products in three main categories: *axles*, *transmissions* and *drives*.

Axles are to be intended as the supports of a vehicles where the wheels are mounted on. They can be different for a lot of features: the axle housing (monolithic or modular), steering capacity (rigid or steering), presence of suspensions, presence of brakes, driving capacity, and others. Some examples of different axles are reported in Figures 1.3.

The main function of transmissions is to reduce the rotational speed coming from the power source and multiply the torque, in order to suit the requirements of the working operation carried out by the vehicle. Since vehicles work under several working conditions, the transmission must ensure gear shifting too. The number of speeds varies from vehicle to vehicle, changing from 2 for the simplest industrial vehicle to 32 forward speeds and 32 reverse speeds for agricultural tractors. Some example of transmissions are reported in Figure 1.1, 1.2, 1.4 and 1.5. Drives are produced by O&K di-

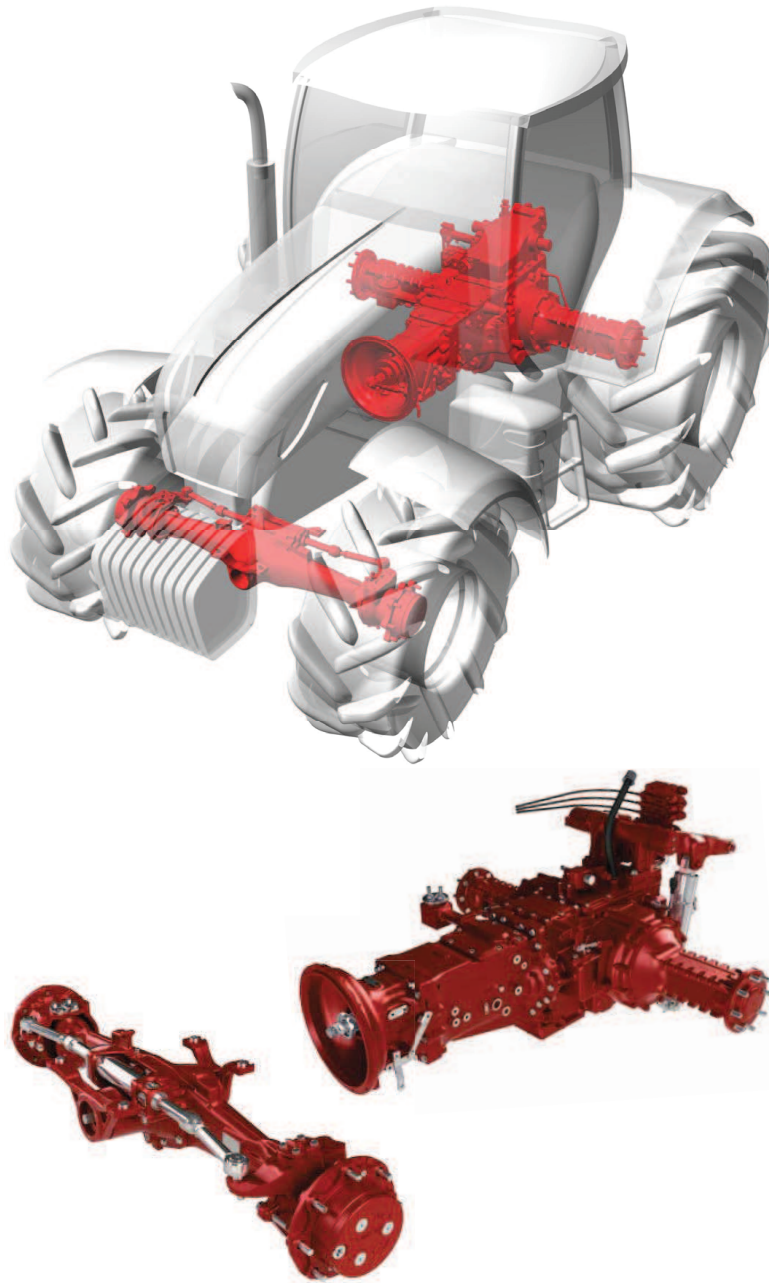


Figure 1.1: Example of driveline for a tractor.

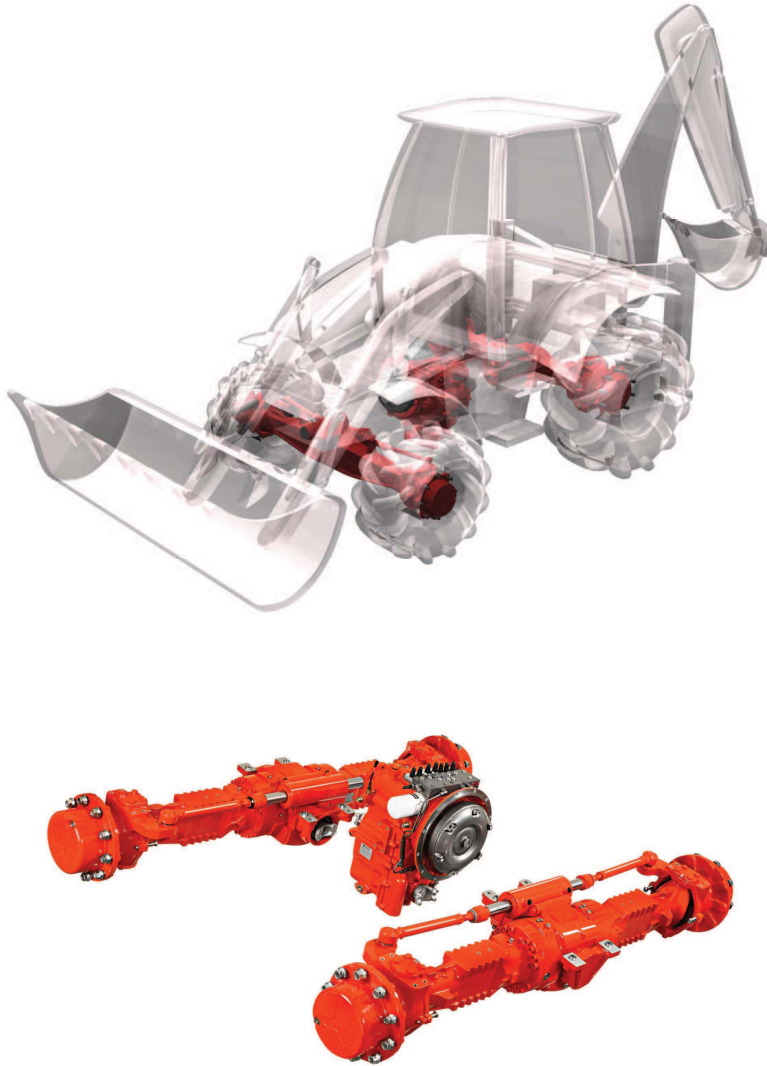


Figure 1.2: Example of driveline for a backhoe loader.

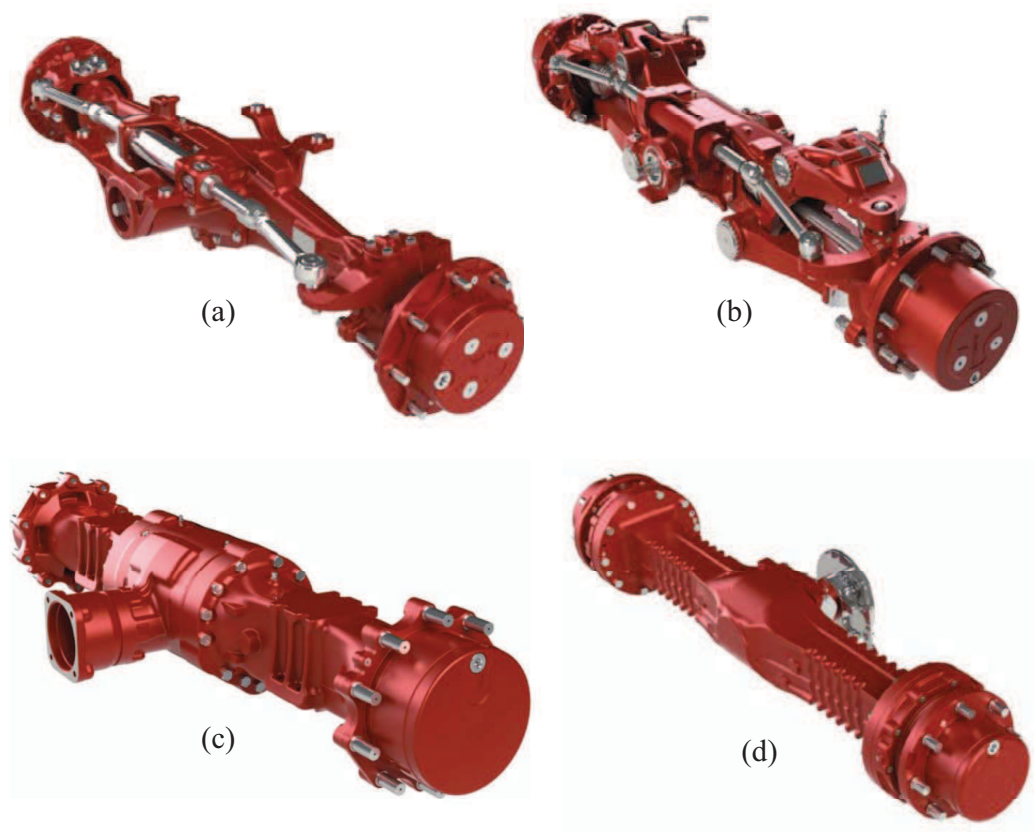


Figure 1.3: Various axles: (a) monolithic steering axle, (b) suspended axle, (c) modular rigid axle, (d) monolithic rigid axle.

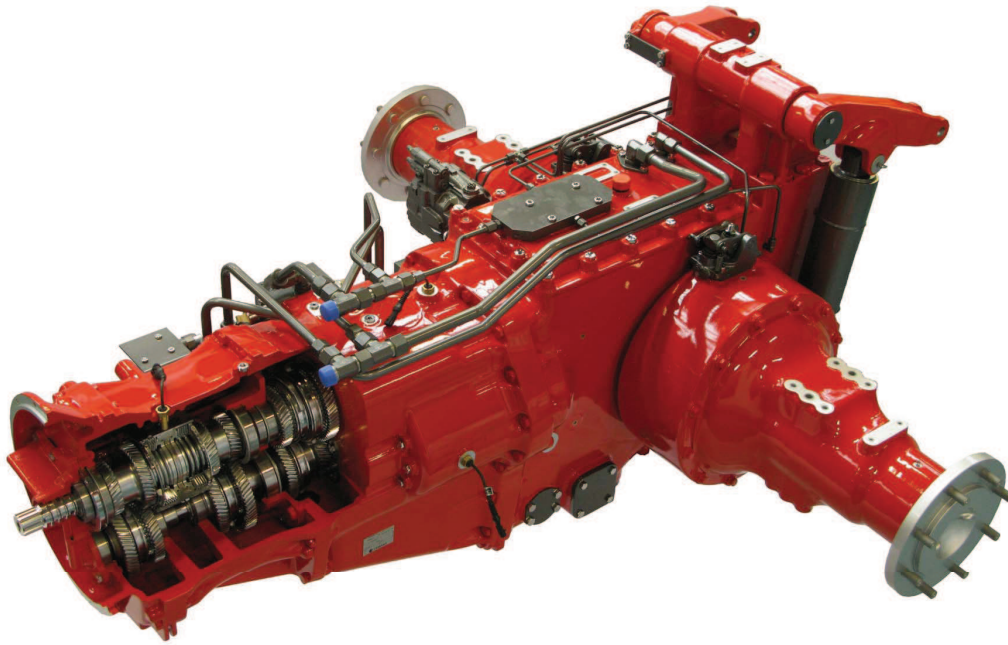


Figure 1.4: Agricultural transmission with cut on clutch housing (T15).

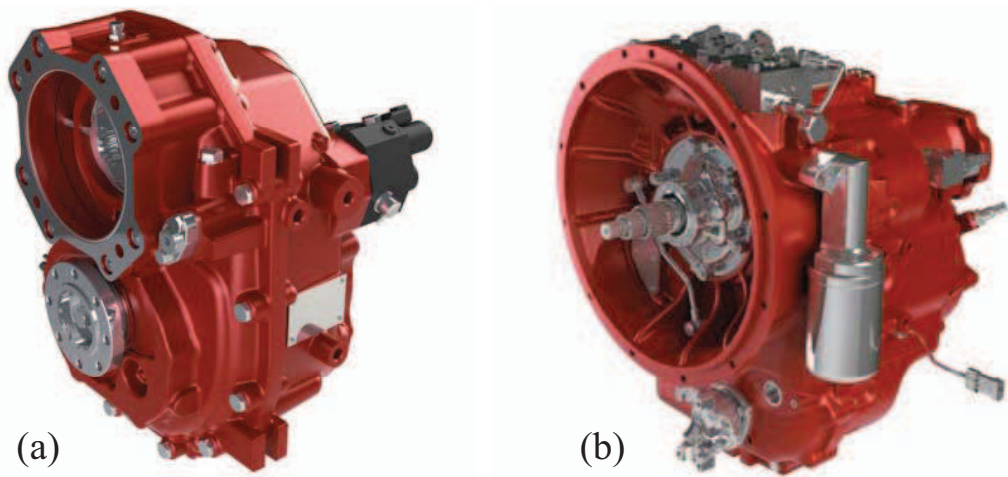


Figure 1.5: Construction Equipment transmission: (a) hydrostatic transmission (TB172) and (b) hydrodynamic transmission (TLB1).

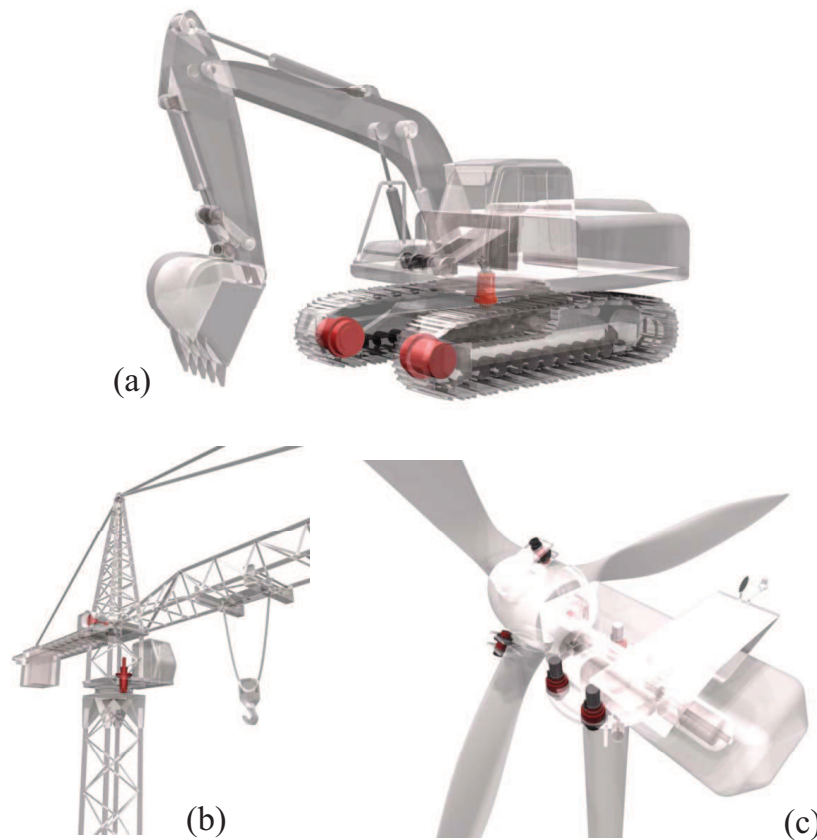


Figure 1.6: Drive applications: (a) crawler, (b) crane and (c) wind turbine.

vision of CDT. Drives are used into a lot of different applications, where an high torque is required. For instance, Figure 1.6 shows some applications. In crawler vehicles, drives are used to move the crawler tracks, but also to rotate the turret of the cabin. In cranes drives are used to move the turntable and the boom, while in wind turbines the drives are used to orient the wind blades and permit yaw corrections.

1.4 Axle schematic

A brief description of the functions of an axle is important to understand next chapters. Only the explanation of an axle will be made, since transmissions can be different from case to case, while axle architecture is more standard and can be recognized in different size and models.

In a driving axle for off-highway vehicles, the power comes from the vehicle's source of power, enters the axle by the input bevel pinion, is transmitted to

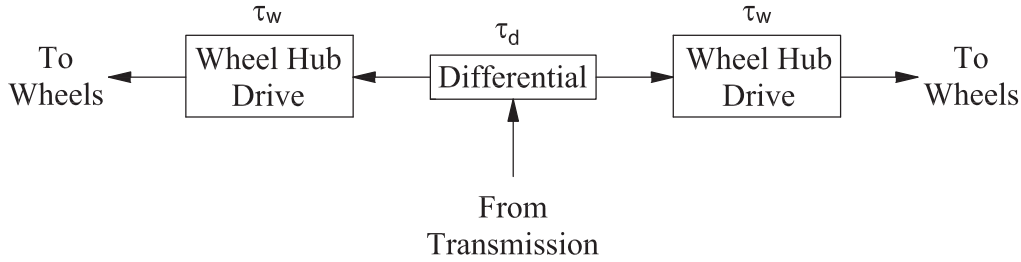


Figure 1.7: Scheme of power flow in an axle.

the differential and then pass through the left and right axle shafts to arrive to wheel hub drives (or *final drives*) and exit to the wheel hubs (see Figure 1.7). Two speed reductions are made through the power line: one by the bevel gear set in the differential group (τ_d) and one by the wheel hub drives (τ_w). Speed ratio of total axle (τ_{axle}) is then the product of the two reduction stage:

$$\tau_{axle} = \tau_d \cdot \tau_w \quad (1.1)$$

Wheel hub drive is generally a planetary drive, since this technical solution permits to obtain high speed ratio in small space and ensures coaxiality between input and output shafts. Moreover, the radial loads generated by the transmission of power are self-balanced.

A cut-away view of a driving modular steering axle is shown in Figure 1.8. The axle is modular since it can be divided in three main parts: the left trumpet, the central body and the right trumpet. The three pieces are fixed together by means of bolts. Modularity permits the mounting of different trumpets on the same central body, making possible an easier modification of the design. The axle is mounted on the transmission by means of an input yoke, which can be of several shapes depending on the kind of vehicle. The axle is fixed to the vehicle's chassis by means of a trunnion anchoring. It contains a pivot that makes possible oscillations of the axle respect to the vehicle. Some external features on the trumpets (pads) permit the proper mounting of the axle on the vehicle's chassis.

For the axle in the picture, the central body contains the bevel gear set, the differential and wet brakes. However, brakes can be located on the wheel hub drives as well. Two axle shafts (left and right) connect the power exits of the differential to the wheel hub drives. Since it is a steering axle, a king pin connects the end part of the trumpet (knuckle) to the swivel housing. Power transmission is ensured by means of double U joints which maintain the toothed end of the axle shaft (sun gear) properly aligned to planetary gears. On the wheel hubs there are some bolts to make the mounting of the

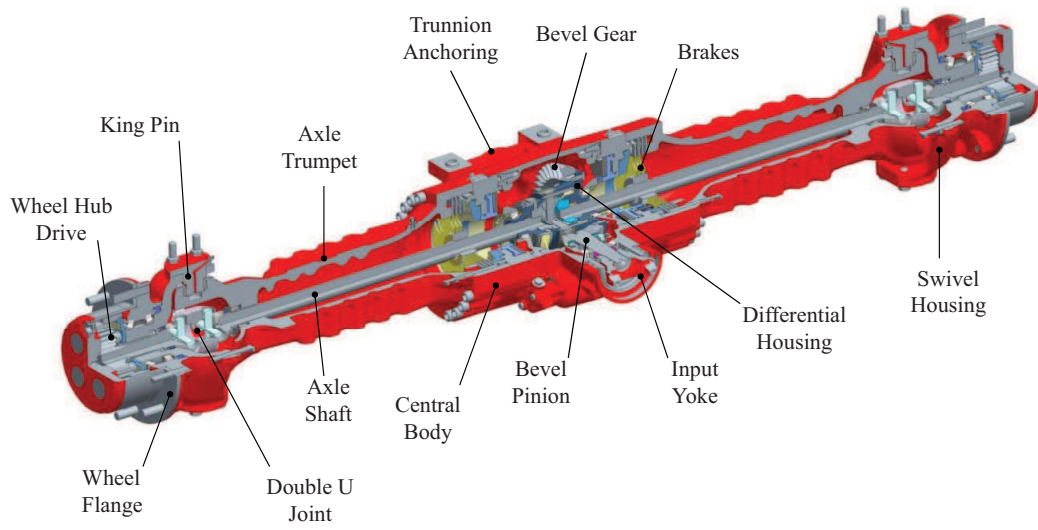


Figure 1.8: Description of main features and components of a steering modular axle (26.27 Axle).

tire possible.

Analysis of Test Archive

This chapter analyzes the test made inside the Company to investigate the durability of gears. The failure modes recorded for each test type were reported and compared. Then the attention was focused on pitting failures of the sun gears of axles' planetary final drives, and on bending failures of the bevel gear sets of axles' differential housings recorded in the last years. The experimental data were analyzed according ISO 6336 in order to derive fatigue curves under the nominal conditions reported in the Standard. The allowable limits of case-hardened steels were therefore derived for different survival probabilities by means of a statistical model. The results were finally used to show the pros and cons of the actual testing procedures used inside the Company to investigate the fatigue behavior of gears.

2.1 Introduction

First of all, a rapid overview of the gear tests carried out within the Company is presented. Since a driveline is a very complex device, many tests are necessary to validate it at all. Mainly, the following functional components of a driveline must be tested to ensure that the vehicle will not go through a field failure:

- gears and gear shifting devices
- brakes
- cast housings
- steering devices

- lube
- seals

Many other tests are carried out to investigate the proper operation of specific components, but these tests are designed ad hoc for each case, therefore they are not reported here.

Each component is tested with different procedures since different failure modes must be investigated. Since the focus of this work is on gears, only the tests involving gear fatigue are here presented. The purpose is to show the limitations of the gear testing activity and the strength data that can be extrapolated from the test approach followed by the Company.

2.2 Gear tests

The main part of the validation of a new transmission or axle concerns gears. Testing of gears is very expensive because requires long times to simulate fatigue failures and requires complex test rigs. Skilled personnel able to recognize the failure modes and to assemble the system properly is necessary too. Therefore, Ph.D. activity started from the analysis of gear tests and fatigue failures, in order to understand the fatigue behavior and the strategies used to investigate them. This may help to develop easier tests able to save money and reduce the time to market of a new product, or at least to be able to design a new product being sure of passing tests at the first time.

The tests used to investigate the fatigue performance of gears are:

- Four Square Test
- Chicken Test
- Power Test
- Endurance Structural Test

Each one of these tests is designed to investigate different failure modes and to test different components of the driveline, since they simulate different working conditions of a vehicle during its service on the field. A short description and analysis of the aforementioned tests is reported in the next paragraphs.

2.2.1 Four Square Test

The Four Square Test (FST) [1] is carried out to investigate the fatigue strength of both gears mounted on axles and transmissions. A picture of the test scheme is shown in Figure 2.1, where both tests on a transmission (a) and an axle (b) are represented. Two transmissions (axles) are placed one in front of the other and are joined together with a joint, which connects the two input shafts of the transmissions (axles). The system is then statically preloaded using a wrench that impose a rotation of a prefixed angle on one input shaft, while the other one remains fixed. The imposed torque (T) is proportional to the rotational angle (ϕ) by the torsional stiffness constant (K_T), according to the following expression:

$$T = K_T \phi \quad (2.1)$$

To close the system, avoiding the relaxation of the torque, two chains are used to connect the wheel hubs of the two transmissions (axles). Once the preload is applied, rotation is provided by the electric motor by means of belts and pulleys. This kind of configuration is generally called *power recirculating configuration*. The advantage of this principle is that the power required to lead the system to rotate at the desired speed is the only power dissipated by friction. The motor is only used to give rotational speed to the system, not to load it. With this method, high power can be simulated inside the system with low input power. Test rig is thus cheaper, since low-power motor can be used.

However, this system has some disadvantages, related to:

- need for two transmissions (axles);
- chains cannot provide smooth working conditions;
- the two tested transmissions (axles) withstand to different powers due to power losses in the power line.

Even if two transmissions are involved in the FST, only one is considered validated after the completion of the test. The reason is that only the first transmission actually works like the in-field operations, since the power follows the correct direction, entering from input shaft and exiting from the wheel hubs (see Figure 2.1). In the auxiliary transmission the power follows the wrong direction, therefore the auxiliary transmission is considered only a device to close the power-flow line. Actually, it could be substituted by a drive (or a series of drives) with the same speed ratio of the tested transmission. Although the use of a drive would be cheaper, there is the problem

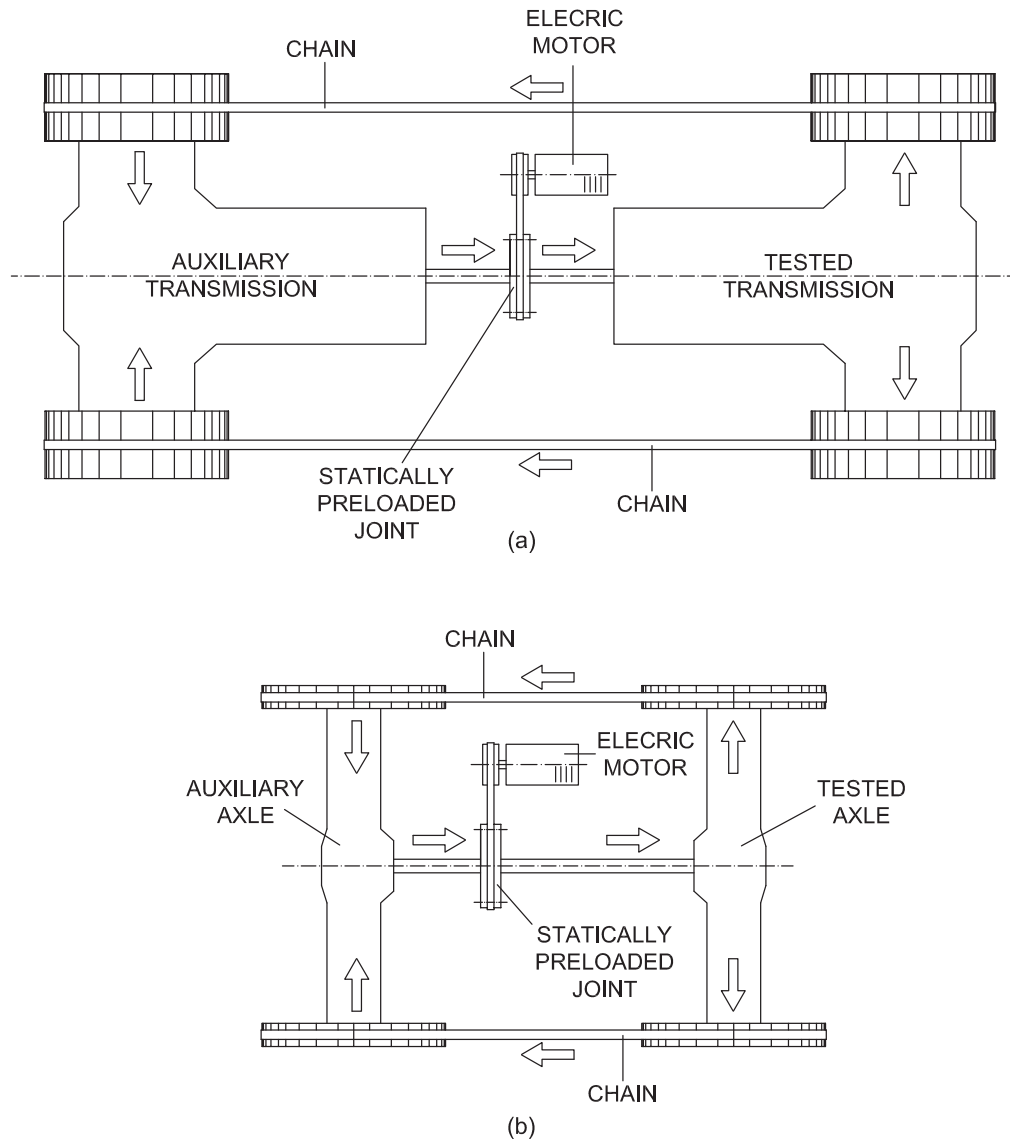


Figure 2.1: Scheme of the FST on a tractor transmission (a) and an axle (b).

Table 2.1: Duty cycle of FST for *axles*.

Load Case	Wheel Torque	Wheel Speed [rpm]	Duration [h]	Running Direction
1	Continuous	30	320	FWD
2	Continuous	30	80	REV
1	Continuous	30	80	FWD
4	Peak	10	2	FWD

that the speed ratio of the tested transmission varies depending on the engaged gear, making necessary the use of several drives to complete a FST. Conversely, the use of an identical transmission ensures a perfect match on the speed ratios. It is only necessary that the auxiliary transmission has the same engaged gear of the tested one. However, the use of two transmissions can raise the statistical significance of the test on some components.

It is important highlighting that the duty cycle imposed to axles can be very different from that imposed to transmissions. The former is standardized for each kind of axles, while the latter can significantly vary from application to application, being thus not standardized.

The duty cycle imposed to axles is reported in Table 2.1. It was found that the *Continuous torque* T_c corresponds to the torque that produces a nominal hertzian contact stress around $1600 \div 1650$ MPa on the tooth flanks of the sun gear inside the wheel hub. The *peak torque* T_p is defined as:

$$T_p = \frac{T_c}{0.48} \quad (2.2)$$

The continuous torque is representative of heavy working conditions of the vehicle (such as plowing for a tractor), while the peak torque represents the peaks of torque that can take place for improper use of the vehicle. FST is carried out mainly in forward direction, but reverse direction is investigated as well. The sense of directions affects the direction of the bearing loads, since helical gears are commonly used.

The duty cycle for transmissions is more complex than for the axles. It contains load cases for each speed ratio, for forward and reverse direction. The duty cycle is calculated imposing the equivalence of the damage obtained by the test and the damage obtained during predicted (or required) in-field operations, by means of some damage factors defined by experience.

Axles are declared to have passed positively a FST if they are still functioning after the completion of all the load cases reported in Table 2.1, and if any eventual pitting on the flanks of the gears is not exceeding level 4 of Table

Table 2.2: Pitting levels declared by [1].

Pitting Level	Percentage of pitted flank area
1	5%
2	10%
3	25%
4	50%
5	100%

2.2, or level 3 if also spalling occurred. The tolerated pitting level is high because FST duty cycle is actually heavier than typical duty cycles on field and because pitting phenomenon is not critical for the functionality of the vehicle (in the sense that pitting is not a catastrophic failure and does not result in the stop of the vehicle). Periodical inspections every 100 hours are carried out to check the evolution of the damage on the axle components. For *transmissions* the same acceptability criteria are used, but generally the inspections are carried out when each load case is finished.

From the point of view of fatigue and design characterization, FST has some important lacks, that can be mainly summarized in:

- the test does not necessarily lead to pitting or bending breakage;
- for axles, pitting stress investigated on sun gears of final drives is always the same, since the applied torque is related to the axle size;
- for transmission, no data to extrapolate pitting damage obtained under constant torque are available, since duty cycle is very complex.

This means that always the same portion of the pitting curve is investigated, and that no data on the fatigue limit of the material can actually be obtained.

2.2.2 Chicken Test

FST architecture is used to carry out also the so-called "Chicken Test" (CT). The test rig and the principle is the same as the FST, but in this case the *peak torque* is applied and kept constant during the whole test. A lower rotational speed is imposed (internal standard [2] suggests to use 10 rpm at wheels) and the test is carried out only in forward direction. CT is applied only to axles, and was introduced to have a faster validation procedure, since the typical duration of a FST can be of several months (including assembly operation and periodical inspections), while CT can be carried out in few

days. According to [2] the CT must last at least 10 hours without failure to be considered successfully passed. Generally, because of short duration, the test continues until a rupture occurs on a gear in the axle. CT can therefore be used to define the real fatigue strength of the broken component.

Since the peak torque is dependent on the axle size, different CTs lead to the same stress on gear teeth of the wheel hub drive, even if different models and size of axles are tested. However, the stress on the bevel gears can be different depending on the total axle ratio. Since peak torque is significantly higher than continuous torque, failure modes of CTs differ from those of FSTs, as described later.

2.2.3 Endurance Structural Test

The Endurance Structural Test (EST) is a test where both gears and structural components are tested. The test is carried out only on axles by applying both torque and vertical load impulses. The torque impulses are applied at the input pinion of the axle, while the load impulses are applied on the beam of the axle. Two big wheels are mounted on the wheel hubs and are fixed to the ground by means of a connecting rods, which prevent wheel rotation (see Figure 2.2). When a torque is applied to the input pinion of the axles, the wheel hubs cannot rotate, thus the gear teeth of the power line are loaded. A vertical load is applied by means of an hydraulic linear actuator on the middle of the axle beam simultaneously with the torque impulses. A complete test cycle is made of 5 torque impulses in forward direction and 1 torque impulse in reverse direction. The torque applied is the *peak torque*, while the vertical load is the *dynamic load* of the axle. The dynamic load is defined as the load that the axle withstands under the heaviest working operation of the vehicle. The dynamic load is a key design parameter of the axle and is therefore related to axle size. The test has a target of 20,000 complete cycles for agricultural axles, and of 50,000 complete cycles for industrial axles.

EST is passed if, at the end of the test, the axle does not show ruptures and if specific required wear limits are not exceeded. Generally, the axles that passed the EST are then subject to the Bump Test (BP), which is another kind of test where an axle withstands to 500,000 falls from a certain height (wheel hubs are equipped with tires).

Like the FST, the fatigue limit is not investigated, since the EST is interrupted after the completion of the prefixed number of cycles, even if the rupture is not occurred.

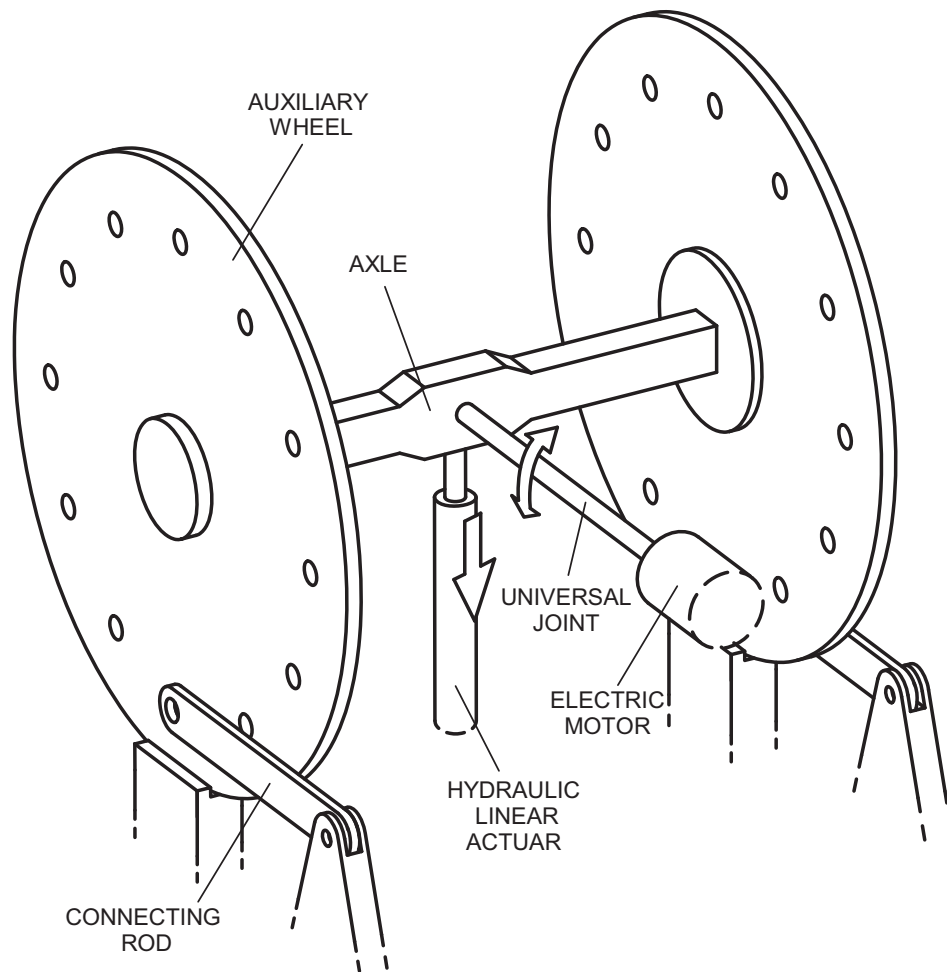


Figure 2.2: Scheme of the EST.

2.2.4 Power Test

The Power Test (PT) is a test where the endurance of the power transmitting components is investigated. This test can be carried out on both transmissions and axles, since it consists in the run of a duty cycle using electric motors. However, PTs are generally performed on transmissions, where complex duty cycles are required. The motors can provide the motion, or act as brakes. This approach is indispensable in the cases where a single product must be tested (an auxiliary product is unavailable), or the cases where the components to test are not connected to the wheels, such as the Power Take-Off (PTO) or the 4-Wheel Drive (4WD) power output of an agricultural transmission. This typology of test permits to hold a constant and regular torque, since no chains are used and the effect of internal deformations or deflections of the components are automatically compensated. On the other hand, at least two motors has to be used; for agricultural transmissions, up to 5 motors can be necessary (depending on the number of power inputs and outputs). The motors must be able to provide the maximum power imposed by the duty cycle, while in the FST architecture the size of the motor is significantly lower. For this reason, PTs are generally used on transmissions of small power.

2.3 Failure mode analysis of axles

A qualitative analysis of the failures occurred on axles during FSTs, CTs, and ESTs is here presented¹. The aim is to identify the critical gears and the related failure modes for each test. The tests carried out from 2008 to 2012 were investigated.

2.3.1 FST failure modes

The failures occurred during the analyzed FSTs carried out on axles are shown in Table 2.3. It is important noting that the failures are mainly related to the wheel hub drives. Main failure mode is pitting, which is located mainly on sun gears (see Figure 2.3) and on planet pins (see Figure 2.4). There is only one case where the failure is located on the differential group but it is probably related to a design problem, or to some quality casting defects of the differential housing.

The application of a relatively low torque - like the *continuous torque* -

¹PTs are not here reported, since they are seldom applied to axles. However, typical failures occurred during PTs are the same of those occurred during CTs and FSTs.

Table 2.3: Failures occurred during some FSTs carried out on axles.

Test number	Axle	Failed group	Failed component	Failure mode
3436	28.32M	Wheel Hub Drive	Sun gear Planet gear	Pitting on tooth flanks Pitting on tooth flanks
3353	26.27M	Wheel Hub Drive	Planet pins Sun gear	Pitting on roller raceways Pitting on tooth flanks
3334	20.10	Wheel Hub Drive	Sun gear Planet pins	Pitting on tooth flanks Pitting on roller raceways
3319	28.38M	Wheel Hub Drive	Sun gear Planet pins / Planet gears / Rollers	Pitting on tooth flanks Pitting on roller raceways
3268	28.32E	Wheel Hub Drive	Sun gear Planet gear Planet pins / Rollers	Pitting on tooth flanks Pitting on tooth flanks* Pitting on roller raceways*
3218	28.38M	Hub Wheel Drive	Planet gear Planet pins Sun gear	Bending** Pitting on roller raceways Pitting on tooth flanks
3098	20.29	Hub Wheel Drive	Sun gear	Pitting on roller raceways
3060	20.43	Hub Wheel Drive Differential	Sun gear Planet gear Fracture of differential house Pinion tapered roller bearing	Pitting on tooth flanks Pitting on tooth flanks Fatigue Pitting on raceways and rollers

* Pitting was reached after an over test

** Quality problems of gear steel were recognized

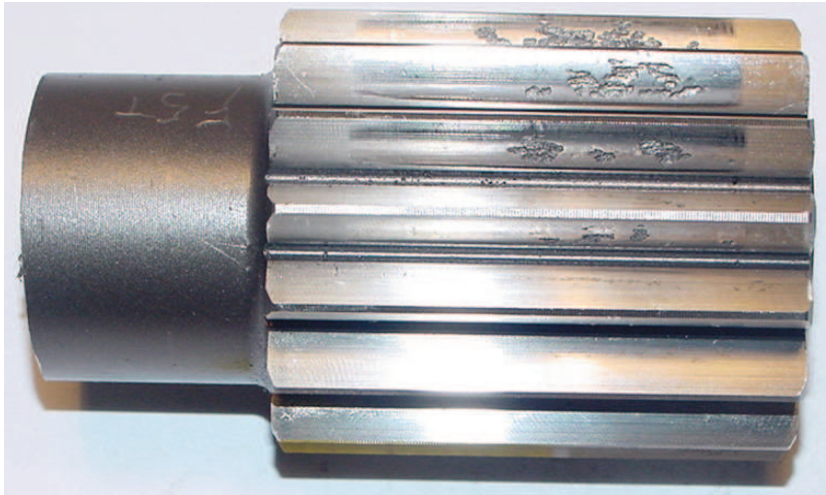


Figure 2.3: Pitting on sun gear (FST 3268).

leads to relatively low stresses on the gear teeth. Since the tooth root stress is small, the gears generally fail by pitting instead of bending. Failures are concentrated on sun gears because they withstand to a lot of cycles if compared to the other gears in the wheel hub drive. Sun gears rotate faster and during a single revolution there can be three or four contacts with the planet gears depending on their number. It is important noting that also planet pins shows fatigue problems with an high frequency. However, the fatigue problem of pins will not be analyzed in this work.

2.3.2 CT failure modes

CTs are carried out by applying *peak torque*, therefore the failures take place in a shorter time than the FSTs. These tests can lead to failure in few hours. For this reason, sometimes the customers require them as a fast way to validate the axle.

However, the failure modes obtained in CTs are completely different from the ones obtained in FSTs. Since the load is high, pitting on gears is very uncommon in CTs, where almost all the gear failures are due to bending fatigue. Pitting can take place marginally on the tapered roller bearing mounted on the bevel pinion. The type of failure mode registered during the analyzed CTs is reported in Table 2.4. As it can be seen, most critical groups in this test are the differential and the wheel hub drives. Failures on differential are focused mainly on the teeth of the bevel pinion (Figure 2.5), but sometimes they can involve also the bevel gear teeth (Figure 2.6). In some cases the breakage of the roller cage of the tapered roller bearing of



Figure 2.4: Pitting on planet pins (FST 3353).

the bevel pinion take place (Figure 2.7). The failures on the wheel hub drive are concentrated on the external ring or planet gears which generally fail by bending fatigue (Figure 2.8).

CTs are commonly used to validate bevel gear sets. The same bevel gear set can be mounted on different axle models and sizes, depending on the dimensions of the axle housing. For this reason, sometimes the bevel gear set results oversized if compared with the power-transmitting capability of the wheel hub drives. In such cases, in order to get the right input torque on the bevel gear pinion, the wheel hub drives result severely loaded and fail several times during the test for tooth root bending fatigue.

2.3.3 EST failure modes

ESTs are performed by applying pulsating high loads and torques. Therefore these tests simulate the ability of axles/transmissions to resist to overloads and impulsive working conditions. In such tests, power-transmitting components actually do not rotate completely, but they oscillate at each impulse. In this way, mainly bending fatigue resistance is investigated. Pitting fatigue is never observed on gear teeth, but sometimes fretting and wear phenomena take place in contact faces between components.

The failures recorded during the analyzed ESTs are reported in Table 2.5. As it can be seen, EST shows fatigue failures on lot of components. However, most critical groups are the axle-shafts, the differential and the wheel hub drive. Axle shafts fail for combined torsion and bending fatigue on

Table 2.4: Failures occurred during some CTs.

Test number	Axle	Failed Group	Failed Component	Failure Mode
3368	28.50MR2	Wheel Hub Drive	Planet Gear	Bending at tooth root
		Differential	Pinion Tapered Bearing	Pitting on rollers and raceways
		Differential	Bevel Pinion	Bending at tooth root
3348	28.50MR2	Wheel Hub Drive	Planet Needle Bearing	Slippage of roller out of raceways*
		Differential	Bevel Gear Set	Bending at tooth root
3420	28.40FR	Differential	Bevel Gear Set	Bending at tooth root
3412	26.32M	Differential	Bevel Pinion	Bending at tooth root
3384	28.32M	Differential	Bevel Gear Set	Bending at tooth root (mainly on pinion)
		Differential	Pinion Tapered Bearing	Cage breakage + pitting on raceways
		Wheel Hub Drive	Ring	Bending at tooth root
		Wheel Hub Drive	Planet Needle Bearing	Slippage of roller out of raceways*

* The slippage of the rollers out of their raceways led to tooth chipping of wheel hub gears



Figure 2.5: Failure of teeth of a bevel pinion (CT 3884).



Figure 2.6: Failure of teeth of a bevel gear (CT 3884).



Figure 2.7: Failure of tapered roller bearing of bevel pinion (CT 3884).



Figure 2.8: Failure by bending tooth root fatigue of the ring of a wheel hub drive (CT 3884).

Table 2.5: Failure occurred during some ESTs.

Test number	Axle	Failed Group	Failed Component	Failure type
3443	28.32M	Axle shaft Differential Wheel Hub Drive	Axle shaft Bevel gear pinion Wheel carrier hub	Fatigue on spline Fatigue on the shaft Fatigue on relief holes
3396	26.24(J)	Differential Axle shaft	Spider Gears Double-U Joint	Bending on gear teeth Joint Spider
3345	28.32E	Wheel Hub Drive	Planetary carrier	Loosening of wheel drive screws
3304	28.28	none	none	none
3288	28.38	none	none	none
3278	26.24	none	none	none
3191	28.28	Differential	Differential Housing	Fatigue on fillet zone
3214	28.38M	none	none	none
3116	26.24(J)	Differential Axle shaft	Spider Gears Double-U Joint	Bending on gear teeth Joint Spider
3044	28.32M	Wheel Hub Drive Wheel Hub Drive	Wheel carrier hub Wheel carrier hub screw	Fatigue on screw holes Fatigue failure



Figure 2.9: Failure of the axle shaft on spline (EST 3443).

splines (Figure 2.9) and for bending fatigue on the spider inside the double U joint (Figure 2.10). Failures on differential can be very different: tooth root bending fatigue failures (on bevel gear sets and on the spider gears inside differential housing, see Figure 2.11), fatigue failure of differential housing in fillet zones (Figure 2.12), and combined torsion and bending fatigue on bevel pinion shaft (on key slot, see Figure 2.13). Failures of the wheel hub drive generally involve the wheel carrier hub, which fails in the zone of relief holes (Figure 2.14).

2.3.4 Failure mode summary

The investigation of the failure modes occurred during tests showed the different behavior of gears under different loading conditions. Most probable failures in an axle are located in differential and wheel hub drive. For low applied torque, the failures are principally located on the sun gear of the axle shaft. In such a case, pitting is the most frequent failure mechanism. The sun gear withstands to three or four contacts during each complete rotation, thus becoming the most critical component. When the input torque raises, the failures tend to move to the bevel gear set mounted on the differential, which fail by bending. Bending on tooth root is more common on bevel pinion than gear, even if failures of both these components were recognized. It must be noted that the failure of bevel pinion or bevel gear is a consequence of the

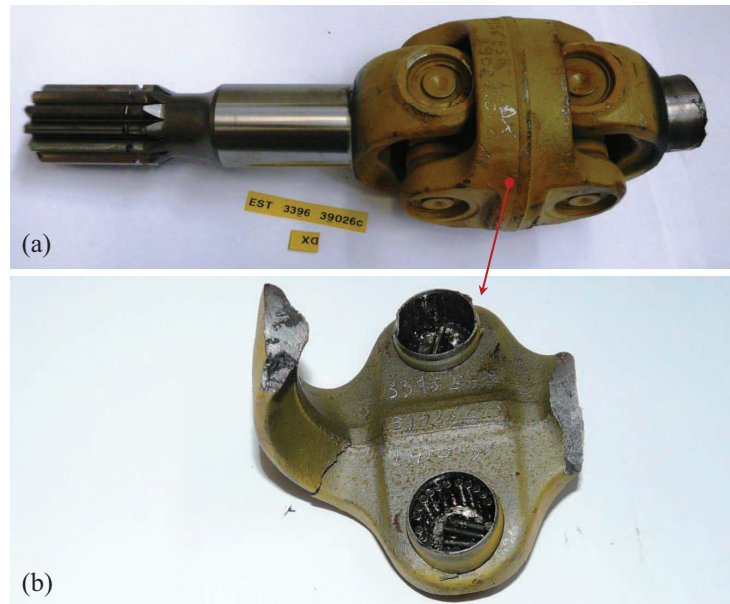


Figure 2.10: Failure of joint spider on axle shaft: double U joint before failure (a) and after (b) (EST 3396).



Figure 2.11: Failure of spider gear of differential (EST 3396).



Figure 2.12: Failure of differential housing on fillet (EST 3191).



Figure 2.13: Failure of bevel pinion shaft on key slot (EST 3443).

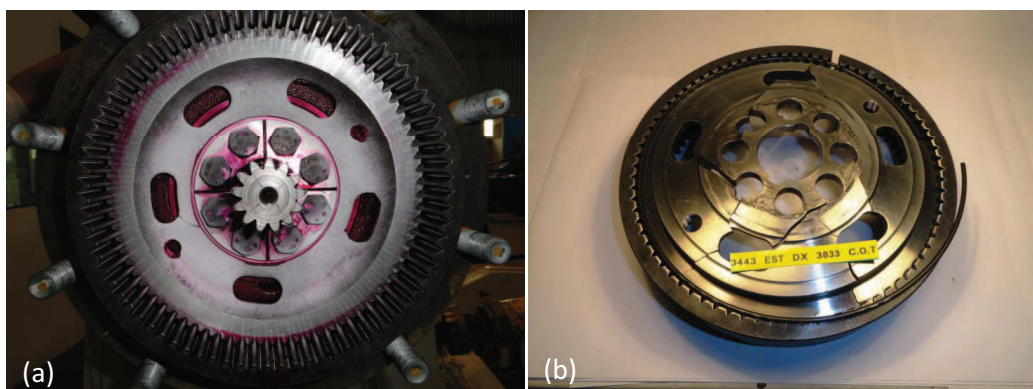


Figure 2.14: Failures of the wheel carrier hub starting from relief holes: figure (a) shows crack origin, (b) shows catastrophic failure (EST 3443).

strategy chosen during the design phase of the bevel gear set. Sometimes the failures of the bevel gear set can be located also on the pinion shaft, due to torsion fatigue at notches, such as the key slots or threads.

A recurring failure cause was recognized as the slippage of the planetary rollers out of their raceways in the final drive. This leads to a catastrophic destruction of the drive, since the rollers go between the engaging gears. The slippage may be caused by an high deflection of the planetary pins, or by the improper assembly or breakage of the retaining components for the rollers. This failure mode is thus very dangerous, and comparable to the bending failure of the bevel gear set, since it can lead to the stop of the vehicle during the in-field operations. From this point of view, the failures by pitting on the sun gears are less dangerous, since pitting can get worse for long time before causing the stop of the vehicle.

2.4 Pitting curves extrapolated from FSTs

Since the FSTs lead to the pitting failure of sun gears, a deeper investigation was made on these components in order to try to define the pitting performance of the case-hardened steels used by the Company. The analysis was carried out using the pitting design approach of ISO6336-2 [3].

Each FST reported in Table 2.3 was modeled using KISSsys software [4]. The models permitted the calculation of the pitting stress, while the pitting life was taken from the test report of the analyzed FSTs. Since each FST was carried out with different working conditions in terms of lubrication, speeds and stiffness of the shafts, the only way to overlap results obtained from different tests was considering the nominal conditions according to ISO6336-2. Fundamental equation for pitting stress verification of ISO6336 is:

$$\sigma_H \leq \sigma_{HP} \quad (2.3)$$

When the pitting stress is equal to the permissible stress, i.e. at the fatigue limit:

$$\sigma_H = \sigma_{HP} \quad (2.4)$$

This expression can be made explicit obtaining:

$$\sigma_{H0} Z_B \sqrt{K_A K_V K_{H\beta} K_{H\alpha}} = \frac{\sigma_{Hlim} Z_{NT}}{S_{Hmin}} Z_L Z_V Z_R Z_W Z_X \quad (2.5)$$

The term $\sigma_{Hlim} Z_{NT}$ corresponds to the pitting stress of the tested steel for a nominal working condition and is independent from the type of oil used during the test, the design of the shafts and the input speed of the hub drive.

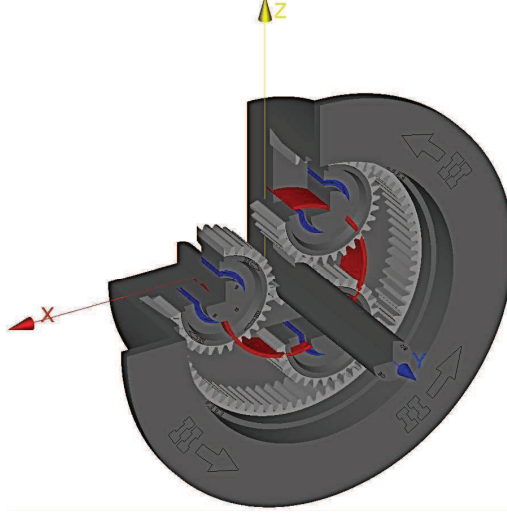


Figure 2.15: 3D model of a planetary hub drive (FST 3436).

This stress can be associated to the pitting level observed during the test inspections defining a point on a fatigue chart. The expression of $\sigma_{Hlim}Z_{NT}$ is therefore:

$$\sigma_{Hlim}Z_{NT} = \frac{\sigma_{H0}Z_B\sqrt{K_AK_VK_{H\beta}K_{H\alpha}}}{Z_LZ_VZ_RZ_WZ_X} \quad (2.6)$$

To consider the true pitting limit, S_{Hmin} must be set equal to 1. It is important to note that the correction factors Z_L , Z_V , Z_R , Z_W and Z_X depend on the number of contacts of the considered gear. This is due to the procedure used in [3] to define these factors: they are evaluated for the low-cycle and for the high-cycle knees of the pitting fatigue curve and then a linear interpolation in a $\log \sigma_H$ - $\log N$ chart is made to obtain the right value for the considered number of cycles.

2.4.1 KISSsys models

A model was created for each wheel hub drive that was tested. Figure 2.15 shows the model created for FST 3436. The design of the hub drives was lightly different from case to case, varying the number of planet gears, the support configuration of planet pins, planetary carrier design and the type of planet bearings. However, the kinematic scheme of the hub drives was always the same: the power entered from the sun gear and was transmitted to the planet gears. Since the outer ring was fixed, the power exited from the planet carrier.

Table 2.6: Correction factors for analyzed FST.

FST	σ_{H0}	Z_B	K_V	$K_{H\beta}$	Z_L	Z_V	Z_R	$\sigma_{Hlim}Z_{NT}$	Pitting Level	N	Elapsed Time	Shot Peening
[-]	[MPa]	[-]	[-]	[-]	[-]	[-]	[-]	[MPa]	[Level]	[cycles]	[h]	[-]
3879A	1462	1.10	1.00	1.27	0.96	0.96	0.95	2070	4	6.48E+06	300	-
3879B	1462	1.10	1.00	1.27	0.96	0.96	0.95	2051	2	4.32E+06	200	-
3879B	1462	1.10	1.00	1.27	0.96	0.96	0.95	2074	5S	6.37E+06	295	-
3879C	1462	1.10	1.00	1.27	0.96	0.96	0.95	2099	1	8.64E+06	400	-
3879D	1462	1.10	1.00	1.27	0.96	0.96	0.95	2048	2	4.32E+06	200	-
3879D	1462	1.10	1.00	1.27	0.96	0.96	0.95	2070	3	6.48E+06	300	-
3879D	1462	1.10	1.00	1.27	0.96	0.96	0.95	2088	5S	8.64E+06	400	-
3879E	1462	1.10	1.00	1.27	0.99	0.97	0.96	1954	2	2.16E+06	100	-
3879E	1462	1.10	1.00	1.27	0.99	0.96	0.95	1986	3	4.32E+06	200	-
3879E	1462	1.10	1.00	1.27	0.99	0.96	0.95	2006	4	6.48E+06	300	-
3436	1506	1.13	1.00	1.22	0.96	0.96	0.96	2106	1	6.40E+06	200	TYPE 1
3436	1506	1.13	1.00	1.22	0.96	0.96	0.96	2106	1	6.40E+06	200	TYPE 1
3436	1506	1.13	1.00	1.22	0.96	0.96	0.96	2130	3	9.60E+06	300	TYPE 1
3436	1506	1.13	1.00	1.22	0.96	0.96	0.95	2147	4S	1.28E+07	400	TYPE 1
3353	1456	1.14	1.00	1.22	0.96	0.96	0.95	2084	0	7.20E+06	200	TYPE 2
3353	1456	1.14	1.00	1.22	0.96	0.96	0.95	2106	1	1.03E+07	285.4	TYPE 2
3353	1456	1.14	1.00	1.22	0.96	0.95	0.94	2128	4S	1.44E+07	400	TYPE 2
3353	1456	1.14	1.00	1.22	0.96	0.95	0.94	2128	0	1.44E+07	400	TYPE 2

Continues on next page

Table 2.6 – *Continues from previous page*

FST	σ_{H0}	Z_B	K_V	$K_{H\beta}$	Z_L	Z_V	Z_R	$\sigma_{Hlim}Z_{NT}$	Pitting Level	N	Elapsed Time	Shot Peening
[-]	[MPa]	[-]	[-]	[-]	[-]	[-]	[-]	[MPa]	[Level]	[cycles]	[h]	[-]
3334	1670	1.12	1.00	1.29	0.97	0.97	0.93	2417	0	2.08E+06	100	-
3334	1670	1.12	1.00	1.29	0.97	0.96	0.92	2492	2	4.15E+06	200	-
3334	1670	1.12	1.00	1.29	0.97	0.96	0.92	2492	0	4.15E+06	200	-
3334	1670	1.12	1.00	1.29	0.96	0.96	0.91	2533	4	6.23E+06	300	-
3334	1670	1.12	1.00	1.29	0.96	0.96	0.91	2533	4	6.23E+06	300	-
3319	1589	1.06	1.00	1.13	0.98	0.96	0.95	2022	1	8.75E+06	300	-
3319	1589	1.06	1.00	1.13	0.97	0.96	0.94	2038	5	1.17E+07	400	-
3319	1589	1.06	1.00	1.13	0.97	0.96	0.94	2038	0	1.17E+07	400	-
3319	1589	1.06	1.00	1.13	0.97	0.96	0.94	2038	0	2.33E+06	80	-
3319	1589	1.06	1.00	1.13	0.97	0.96	0.94	2038	0	2.33E+06	80	-
3319	1589	1.06	1.00	1.13	0.98	0.97	0.96	1964	0	2.92E+06	100	-
3319	1589	1.06	1.00	1.13	0.98	0.96	0.95	2000	0	5.83E+06	200	-
3319	1589	1.06	1.00	1.13	0.98	0.96	0.95	2019	0	8.16E+06	280	-
3268	1402	1.06	1.00	1.18	0.96	0.97	0.96	1808	1	3.65E+06	100	-
3268	1402	1.06	1.00	1.18	0.95	0.96	0.95	1855	0	8.33E+06	227.9	-
3268	1402	1.06	1.00	1.18	0.95	0.96	0.94	1871	3	1.10E+07	300	-
3268	1402	1.06	1.00	1.18	0.96	0.96	0.95	1848	0	7.31E+06	200	-
3268	1402	1.06	1.00	1.18	0.95	0.96	0.95	1866	0	9.94E+06	272.1	-
3268	1402	1.06	1.00	1.18	0.95	0.96	0.94	1885	4	1.39E+07	380	-
3268	1402	1.06	1.00	1.18	0.95	0.96	0.94	1896	1	1.65E+07	452.1	-

Continues on next page

Table 2.6 – *Continues from previous page*

FST	σ_{H0}	Z_B	K_V	$K_{H\beta}$	Z_L	Z_V	Z_R	$\sigma_{Hlim}Z_{NT}$	Pitting Level	N	Elapsed Time	Shot Peening
[-]	[MPa]	[-]	[-]	[-]	[-]	[-]	[-]	[MPa]	[Level]	[cycles]	[h]	[-]
3268	1402	1.06	1.00	1.18	0.96	0.96	0.95	1853	0	8.04E+06	220	-
3268	1402	1.06	1.00	1.18	0.94	0.95	0.94	1919	4	2.46E+07	672.1	-
3268	1402	1.06	1.00	1.18	0.95	0.96	0.94	1871	2	1.10E+07	300	-
3268	1402	1.06	1.00	1.18	0.95	0.96	0.94	1871	0	1.10E+07	300	-
3268	1402	1.00	1.00	1.18	0.96	0.96	0.95	1742	0	7.07E+06	1200*	-
3218	1589	1.06	1.00	1.13	0.98	0.96	0.95	2000	1	5.83E+06	200	-
3218	1589	1.06	1.00	1.13	0.98	0.96	0.95	2000	2	5.83E+06	200	-
3218	1589	1.06	1.00	1.13	0.98	0.96	0.95	2020	5S	8.40E+06	288.1	-
3218	1589	1.06	1.00	1.13	0.98	0.96	0.95	2020	4	8.40E+06	288.1	-
3218	1589	1.06	1.00	1.13	0.98	0.97	0.96	1964	1	2.92E+06	100	-
3218	1589	1.06	1.00	1.13	0.98	0.96	0.95	1995	3	5.32E+06	182.3	-
3218	1589	1.06	1.00	1.13	0.98	0.97	0.96	1964	0	2.92E+06	100	-
3218	1589	1.06	1.00	1.13	0.98	0.96	0.95	2000	0	5.83E+06	200	-
3218	1589	1.06	1.00	1.13	0.98	0.96	0.95	2000	2	5.83E+06	200	-
3218	1589	1.06	1.00	1.13	0.98	0.96	0.95	2022	4	8.75E+06	300	-
3218	1589	1.06	1.00	1.13	0.98	0.97	0.96	1964	0	2.92E+06	100	-
3218	1589	1.06	1.00	1.13	0.97	0.96	0.94	2038	3	1.17E+07	400	-
3098	1639	1.13	1.00	1.25	0.96	0.96	0.96	2318	0	5.39E+06	168.5	TYPE 1
3098	1639	1.13	1.00	1.25	0.96	0.96	0.96	2321	3	5.64E+06	176.2	TYPE 1

Continues on next page

Table 2.6 – *Continues from previous page*

FST	σ_{H0}	Z_B	K_V	$K_{H\beta}$	Z_L	Z_V	Z_R	$\sigma_{Hlim}Z_{NT}$	Pitting Level	N	Elapsed Time	Shot Peening
[-]	[MPa]	[-]	[-]	[-]	[-]	[-]	[-]	[MPa]	[Level]	[cycles]	[h]	[-]
3098	1639	1.13	1.00	1.25	0.96	0.96	0.96	2336	5	7.16E+06	223.8	TYPE 1
3098	1639	1.13	1.00	1.25	0.96	0.96	0.96	2321	3	5.64E+06	176.2	TYPE 1
3060	1616	1.13	1.01	1.28	1.04	0.97	0.96	2158	0	3.20E+06	100	TYPE 1
3060	1616	1.13	1.01	1.28	1.04	0.97	0.96	2158	1	3.20E+06	100	TYPE 1
3060	1616	1.13	1.01	1.28	1.04	0.97	0.96	2158	1	3.20E+06	100	TYPE 1

Factors K_A , Z_W , $K_{H\alpha}$, and Z_X are equal to 1
* Duration is relevant to a satellite
Shot peening: TYPE 1 corresponds to 20A-0.7 / TYPE 2 corresponds to 18A-0.7 [5]

Table 2.7: FST test parameters.

FST	Sun steel	Sun torque [Nm]	Sun speed [rpm]	Total ratio [-]
3879	Ext. Supply	432	150	5.00
3436	18NiCrMo5	1109	208	6.92
3353	Ext. Supply	1000	180	6
3334	20MnCr5	537	145	4.85
3319	EN 353	1425	192	6.4
3268	18NiCrMo5	1250	241	6.4
3218	18NiCrMo5	1425	192	6.4
3098	Ext. Supply	1315	208	6.92
3060	Ext. Supply	1490	208	6.92

The model was created using a coaxial-shaft calculation module containing the sun shaft, the planet carrier and the outer ring, and a non-coaxial-shaft calculation module containing the planet pin. The load distribution factor $K_{H\beta}$ was calculated according to ISO 6336-1 Annex E [6] (manufacturing allowances were not taken into account). Shaft deflections were calculated from the shaft calculation modules, but for sun shaft only torque influence was taken into account (due to some instabilities of KISSsoft solver when bending deflection for sun shaft was considered).²

Each model permitted the evaluation of all the factors appearing in Equation 2.6 according to [3]. The factors are reported in the table 2.6. They are dependent on the FST's parameters (reported in Table 2.7) and on the lubricating conditions (see Table 2.8). Since the correction factors depend on the number of cycles [6, 3], they are different for inspection performed at different working hours even if the working conditions of the test are always the same.

2.4.2 Statistical analysis

The data reported in Table 2.6 were analyzed using the statistical approach similar to that presented in [7] and [8]. The statistical analysis was necessary to obtain design data at different risks and to compare the results with the allowable limits of the Standard, which reports only the curves

²KISSsoft AG is still working on a new release to fix the problems that were identified during this work

Table 2.8: Lubrication details of FSTs.

FST	Oil	Viscosity		Tooth flank Roughness
		40 °C	100 °C	
		[cSt]	[cSt]	[mm]
3879A	AGIP ROTRA MULTI THT 80W	65.6	10.1	1.0
3879B	AMBRA MULTI G	60	9.1	1.0
3879C	FUCHS TITAN EG HY-GARD	56	9.3	1.0
3879D	AGIP ROTRA MULTI THT 80W	65.6	10.1	1.0
3879E	AGIP ROTRA MP 80W-90	144	14.5	1.0
3436	AGIP ROTRA MULTI THT 80W	65.6	10.1	1.0
3353	AGIP ROTRA MULTI THT 80W	65.6	10.1	0.8
3334	SHELL DONAX TD 10W-30	70.4	11.2	1.2
3319	CAT TO-4 TX-7855 (SAE30)	100	11.1	1.0
3268	MOBILFLUID 424	55	9.3	1.0
3218	CAT TO-4 TX-7855 (SAE309)	100	11.1	1.0
3098	AGIP ROTRA MULTI THT 80W	65.6	10.1	1.0
3060	AGIP ROTRA MP 80W-90	144	14.5	1.0

at 99% of survival probability as shown in Figure 2.16. The standard recognizes three different steel qualities, from low quality (ML) to excellent quality (ME), with increasing allowable pitting fatigue limit $\sigma_{H\ lim}$. This allowable limit was defined as the pitting stress obtained on reference gears at the high-cycle knee of the curve (50,000,000 of cycles). In the picture also the inverse slopes of the portions of the fatigue curves (k) are reported. The stress reported in the y-axis ($\sigma_{H\ lim} Z_{NT}$) corresponds to the nominal hertzian contact stress between two tooth flanks. In the very high cycle region of the fatigue curve, the standard suggests to use an horizontal line only in the case of optimum lubrication, material, manufacturing and experience. Otherwise, an inclined line up to 10 billions of cycles is proposed. First of all, it is important noting that survival probability p and confidence level γ are two important parameters that must be considered when making statistical elaboration of data. From a set of data (stress and life) the statistical dispersion can be estimated once a statistical distribution is chosen. Since only a finite number of specimens are tested in the available set of data, the estimated dispersion cannot be directly applied to the entire population. The calculation of the dispersion is affected by an error, that must be considered. This is made using the confidence interval, which provides the error on the inference made using only a small amount of data.

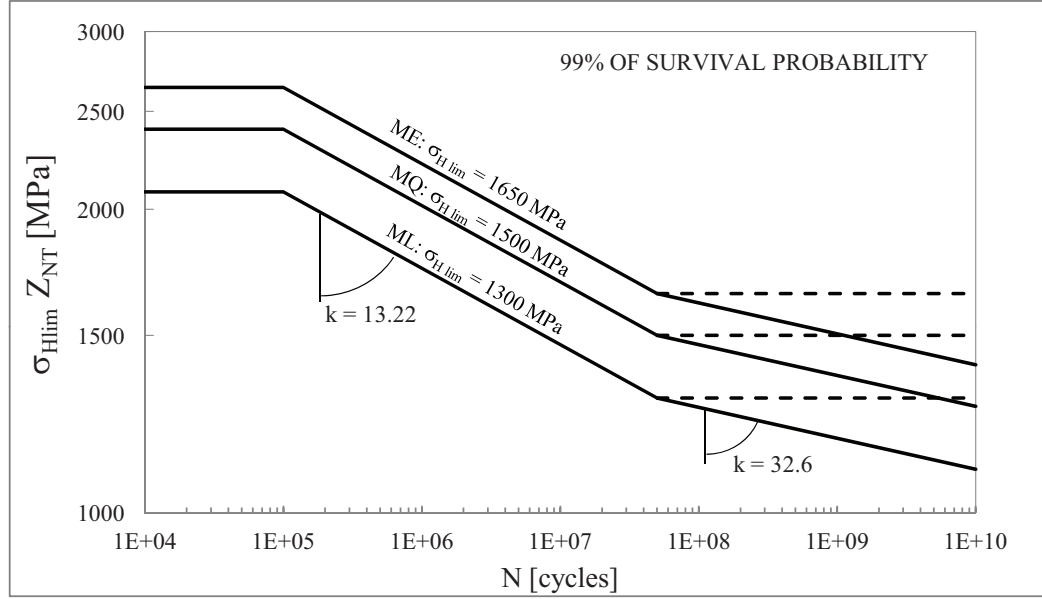


Figure 2.16: Nominal pitting fatigue curves reported in ISO 6336 standard for case-hardened reference gears [45].

The approach is based on the following expression:

$$\log N_{p,\gamma} = \log \bar{N} - qs \quad (2.7)$$

where $N_{p,\gamma}$ is the anticipated life for a survival probability of p % and a confidence level of γ %, \bar{N} is the mean life, s is the standard deviation and

$$q = f(p, \gamma, \nu) \quad (2.8)$$

where ν is the number of degrees of freedom of the statistical analysis (related to the sample size n). The value of q are listed in the Table 2.9. As it can be seen, the higher the confidence level and the survival probability required for inference, the higher the value of q . It must be noted that Table 2.9 is constructed for the case where $\nu = n - 1$. To use it for the case when $\nu = n - 2$ the values of the $(n - 1)$ -th line must be chosen (see more details in A.2).

The mean life \bar{N} was considered as the fitting curve at 50% of survival probability obtained using a least square regression (see equations from A.3 to A.10). Since the pitting stresses were evaluated using ISO6336 approach [10] and converted to a nominal condition accordingly, the fitting slope of the regression line was taken as 13.22, according to the Standard.

Table 2.9: Values of q assuming Normal Distribution [9].

n	$\gamma=50\%$				$\gamma=75\%$			
	$p=75\%$	90%	95%	99%	$p=75\%$	90%	95%	99%
4	0.739	1.419	1.830	2.601	1.256	2.134	2.680	3.726
6	0.712	1.360	1.750	2.483	1.087	1.860	2.336	3.243
8	0.701	1.337	1.719	2.436	1.010	1.740	2.190	3.042
10	0.694	1.324	1.702	2.411	0.964	1.671	2.103	2.927
12	0.691	1.316	1.691	2.395	0.933	1.624	2.048	2.851
15	0.688	1.308	1.680	2.379	0.899	1.577	1.991	2.776
18	0.685	1.303	1.674	2.370	0.876	1.544	1.951	2.723
20	0.684	1.301	1.671	2.366	0.865	1.528	1.933	2.697
25	0.682	1.297	1.666	2.357	0.842	1.496	1.895	2.647

n	$\gamma=90\%$				$\gamma=95\%$			
	$p=75\%$	90%	95%	99%	$p=75\%$	90%	95%	99%
4	1.972	3.187	3.957	5.437	2.619	4.163	5.145	7.042
6	1.540	2.494	3.091	4.242	1.895	3.006	3.707	5.062
8	1.360	2.219	2.755	3.783	1.617	2.582	3.188	4.353
10	1.257	2.065	2.568	3.532	1.465	2.355	2.911	3.981
12	1.188	1.966	2.448	3.371	1.366	2.210	2.736	3.747
15	1.119	1.866	2.329	3.212	1.268	2.068	2.566	3.520
18	1.071	1.800	2.249	3.106	1.200	1.974	2.453	3.370
20	1.046	1.765	2.208	3.052	1.167	1.926	2.396	3.295
25	0.999	1.702	2.132	2.952	1.103	1.838	2.292	3.158

The standard deviation was evaluated using the following expression:

$$s = \left[\frac{\sum (\log N - \log \bar{N})^2}{\nu} \right]^{0.5} = \left[\frac{\sum (\log N - \log \bar{N})^2}{n - 2} \right]^{0.5} \quad (2.9)$$

where it must be noted that the number of degrees of freedom ν was assumed equal to $n - 2$, to consider that the statistical analysis was performed using different pitting stress levels.

2.4.3 Statistical results

The fitting of data was made imposing a fixed slope because there was no possibility to define an experimental fitting slope. Available data were all concentrated around a particular pitting stress, that is very similar for every axle considered during the analysis. Every wheel hub drive was in the past designed using the same admissible pitting stress. For this reason, the calculated pitting stress were similar and therefore the data represented only the middle point of the pitting fatigue curve. However, for this point an estimation of the statistical scatterband was possible. Even if no information concerning the high-cycle and low-cycle knees of the curve was available, the fatigue knee was set at 5E7 cycles, while the low-cycle one was set at 1E5 cycles. This is in agreement with ISO 6336 standard, since the purpose of this analysis was to extrapolate pitting fatigue limits using its prescriptions. The aim was to obtain ISO 6336 pitting endurance limits to be implemented directly in calculation software. This approach permits to use the same solving algorithms of the Standard but using endurance limits closer to test evidence obtained in Company's Test Department, and adding the possibility to consider different survival probabilities and confidence levels.

The analysis did not distinguish the type of sun steel. This agree with [10] and was necessary in order to have a significant number of experimental points to analyze. However, the distinction between un-shot peened and shot-peened steels was made, but for shot peened steels the results were not distinguished on the type of shot peening treatment. In some cases (cfr. Table 2.7) the material of the sun gear was not known because of an external supply (some suppliers reserve the possibility to use different steels from batch to batch, on condition that the mechanical properties are respected). The analysis considered only the initial pitting stage, which was evaluated considering the cases where pitting level 1 or less was found on the sun gears. Pitting stage "0" was added to the standardized pitting level of [1] meaning that a surface pitted area lower than 5% of tooth area was found during test inspection. Level 0 and 1 were considered in the same way and used in the

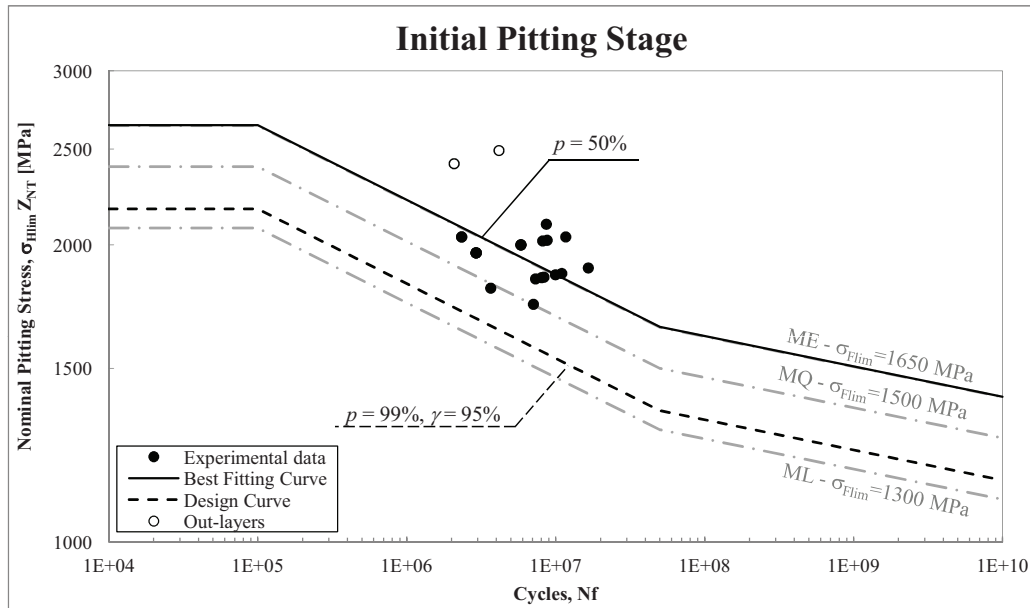


Figure 2.17: Nominal pitting curve for un-peened case-hardened steels compared to the pitting curves for different quality of steel proposed by ISO 6336.

definition of initial pitting curves.

Fitting curve of the experimental points corresponds to the curve of 50 % of survival probability. Using statistical approach presented in the previous paragraph, curves to different survival probability and confidence level were estimated. For un-peened steels 23 observations of pitting stage 0 and 1 were available, while for shot-peened steels 9 data were available (cfr. Table 2.6). However, the data of FST 3334 were excluded from the statistical analysis because they exhibited a very long pitting life for the calculated pitting stress. The pitting stresses resulted very high for this test because of the absence of crowning on sun gear teeth. This led to a numerical peak of contact stress that is difficult to consider representative of the real contact condition of the sun-planet gear pair. For this reason only 21 data were considered in the statistical elaboration of un-peened steels.

Figures 2.17 and 2.18 show the curves for 99% of survival probability and 95% of confidence level and compare them with the pitting curves reported in ISO6336. It can be noted that for a survival probability of 99% un-peened steels are well represented by the ML curve (which corresponds to a pitting stress of σ_{Hlim} of 1300 MPa) whereas shot peened steels are similar to the MQ curve.

Figure 2.19 shows the positive effect of the shot peening on the pitting performance. The increasing in pitting resistance can be estimated in 10%.

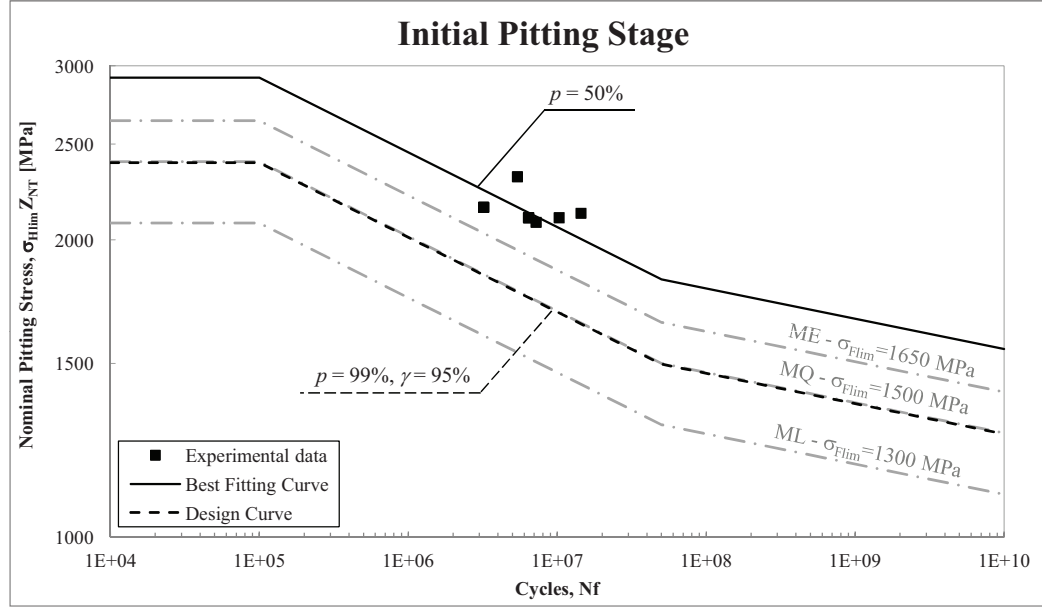


Figure 2.18: Nominal pitting curve for shot peened case-hardened steels compared to the pitting curves for different quality of steel proposed by ISO 6336.

Considering the statistical elaboration using a survival probability of 99% and a confidence level of 95%, the resulting scatterband is very large. If a symmetrical dispersion is assumed (normal distribution) the ratio between the pitting stress at 1% of survival probability and the one at 99% is:

$$T_{\sigma_H 1\%-99\%} = \frac{\sigma_{H1\%}}{\sigma_{H99\%}} = 1.48 \quad (2.10)$$

The value of $T_{\sigma_H 1\%-99\%}$ is not reported in ISO 6336 Standard. However, it can be compared to the corresponding value obtained analyzing available data of case-hardened steels reported in the literature. For instance, pitting data reported in [11] lead to a statistical dispersion $T_{\sigma_H 1\%-99\%}$ varying from 1.31 and 1.40, while data reported in [12] lead to a dispersion $T_{\sigma_H 1\%-99\%}$ varying from 1.45 to 4.32. AGMA2101-D04 Standard [13] presents a reliability factor $Y_Z = \frac{\sigma_{H99\%}}{\sigma_{H50\%}} = 0.7$. These values show that dispersion affecting pitting resistance can be much higher than that found in FST analysis.

It must be also noted that the corresponding dispersion in terms of life is much higher than in terms of stress, being the fitting slope 13.22.

Traditionally, Carraro's fatigue life predictions are made considering a survival probability of 90% and a confidence level of 70%. Table 2.9 gives the possibility to obtain curves for a survival probability of 90% and a confidence

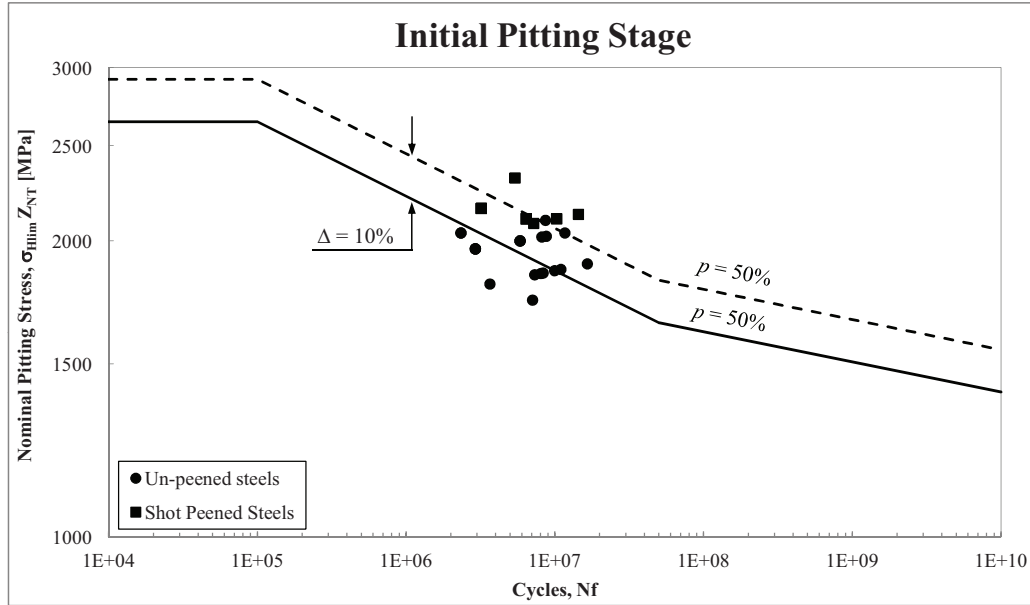


Figure 2.19: Comparison of nominal pitting curves for shot peened and un-peened case-hardened steels.

level of 75%, which were considered representative for Carraro's standards, since the corresponding curves (Figures 2.20 and 2.21) are on the safer side. For this condition $T_{\sigma_H 10\%-90\%} = 1.20$. It is important to notice that the pitting fatigue curve for un-peened steels according to Carraro's standard is coincident to the MQ curve reported in the ISO6336. However, the survival probability of the two approaches are different, being 90% for Carraro and 99% for ISO Standard.

Using all the approximations presented previously, the pitting endurance limits σ_{Hlim} that result from the analysis are reported in Table 2.10, where the limits suggested by [10] are reported too. Column for $p=50\%$ corresponds to best fitting of experimental data (no confidence considered), second column corresponds to Carraro Standards and third column corresponds to the safer life predictions (which should be comparable with ISO 6336 prescriptions). It must be noted that coefficient $Y_{NT} = 1$ at the fatigue knee.

It must be emphasized that [10] consider as initial pitting stage for case-hardened gears the failure by pitting of 0.5% of the total working flank area, or 4% of the working area of a single tooth. These failure criteria are slightly different from FST prescriptions.

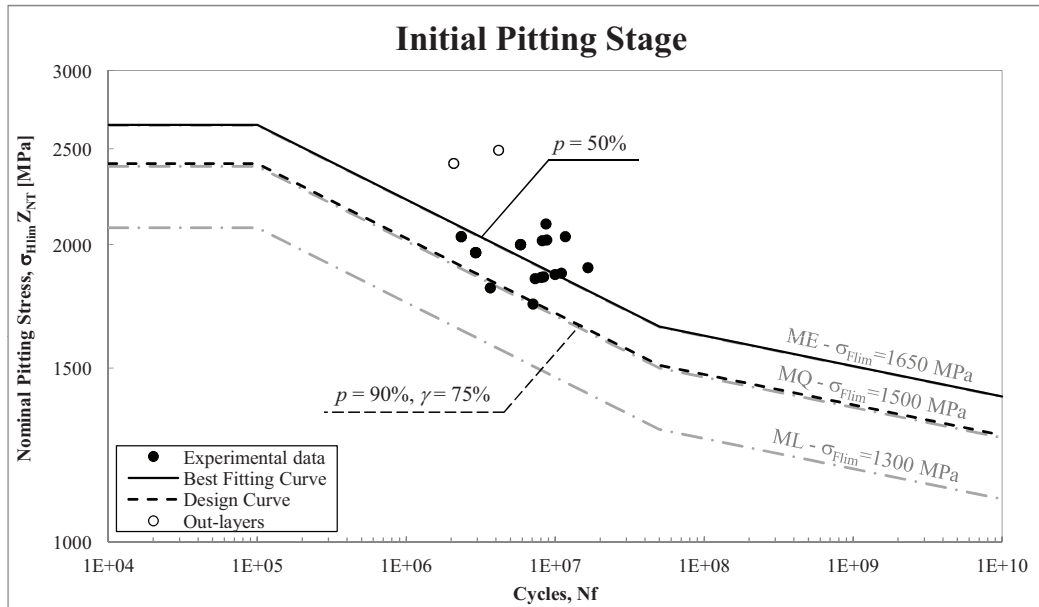


Figure 2.20: Nominal pitting curve for un-peened case-hardened steels according to traditional Carraro's statistical approach.

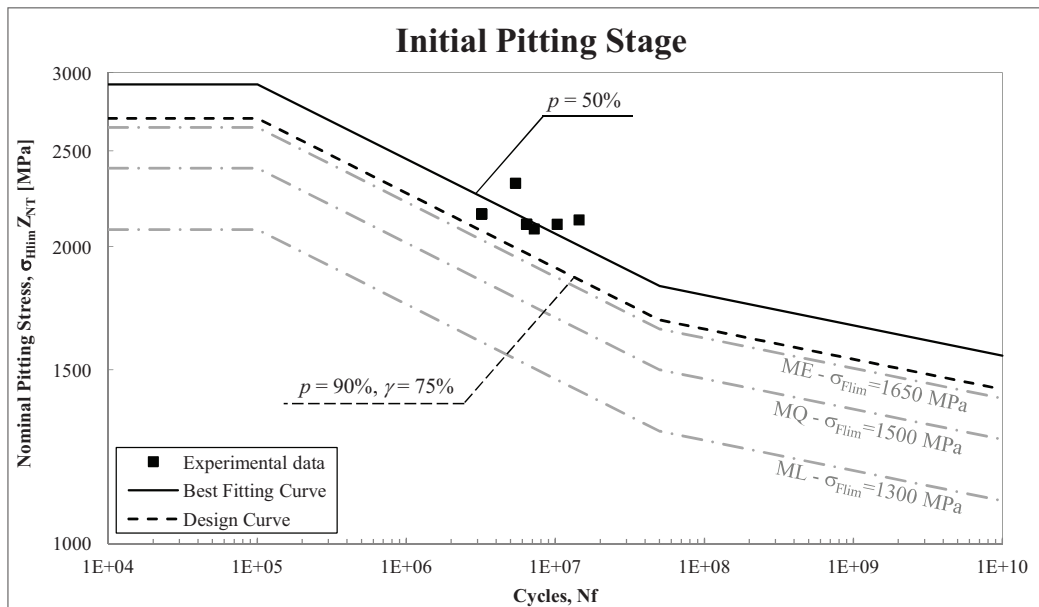


Figure 2.21: Nominal pitting curve for shot peened case-hardened steels according to traditional Carraro's statistical approach.

Table 2.10: Nominal pitting endurance limits (5E7 cycles) σ_{Hlim} [MPa] extrapolated from FSTs and limits reported in [10].

	$p=50\%$	$p=90\%$ $\gamma=75\%$	$p=99\%$ $\gamma=95\%$
Un-peened: $\sigma_{Hlim} =$	1652 MPa	1509 MPa	1359 MPa
Shot-peened: $\sigma_{Hlim} =$	1824 MPa	1685 MPa	1497 MPa
(ISO6336 ML quality: $\sigma_{Hlim} = 1300$ MPa)			
(ISO6336 MQ quality: $\sigma_{Hlim} = 1500$ MPa)			
(ISO6336 ME quality: $\sigma_{Hlim} = 1650$ MPa)			

2.4.4 Evolution of pitting

Using the data reported in Table 2.6 the pitting fatigue curves for pitting stages higher than 1 may be estimated as well. The statistical approach is the same but in this case less experimental points were available for each pitting stage, since FSTs are stopped when the target number of hours (400 hours in forward direction) is reached. In this way some information concerning the highest levels of pitting is lost, because these pitting stages did not happened before the end of the test. Therefore, it must be noted also that in this way the highest levels of pitting observed are relevant to the worst working cases, since the best cases were not observed due to the interruption of the FST before the highest levels of pitting happened. Moreover, if the velocity of pitting degradation was high, intermediate pitting stages were not observed between two inspections. For instance, if a pitting level 1 is observed at 200 hours and a pitting level 4 is observed at 300 hours, information concerning pitting levels 2 and 3 is lost and is not taken into account in the analysis. From this point of view, pitting curve drawn for pitting stage 1 (initial pitting stage) is more robust than the others presented in the following pages. For these reasons, the design curves for pitting levels higher than 1 are to be considered only exploratory curves, and in any cases less reliable than the initial pitting stage curve.

It must be noted that since few experimental points are available, the chosen confidence level affects significantly the position of the estimated *design* fatigue curve.

Statistical analysis was made using the traditional CDT design requirements, i.e. 90% of survival probability and 75% of confidence level³. The number of

³Actually, CDT requirements are relevant to 70% of confidence, but only the statistical coefficients q for 75% of confidence interval were available from the statistical tables

Table 2.11: Values of q for different pitting stages (un-peened steels)

Pitting Stage	No. of experimental points	q values	
		$p=90%$ $\gamma=75%$	$p=99%$ $\gamma=95%$
1	21	1.526	3.295
2	6	1.961	5.741
3	6	1.961	5.741
4	6	1.961	5.741
5	4	2.501	10.552

experimental points for each pitting stage are reported in Table 2.11, where the q values for $p = 99%$, $\gamma = 95%$ and $p = 90%$, $\gamma = 75%$ are also reported. It can be seen how few experimental data may lead to huge scatterbands, since the q values can be very high.

The curves obtained for the different pitting stages are reported in Figures 2.22, 2.23, 2.24 and 2.25 for pitting levels 2, 3, 4 and 5 respectively.

The overlap of the fatigue curves at $p=50%$ (see Figure 2.26) for the different pitting stages shows that the pitting phenomenon is progressive. It can be seen also from Table 2.12, where the nominal pitting endurance limits at $5E7$ cycles for each pitting stages are reported. Since to each pitting level is associated a percentage of pitted area (see Table 2.2), assuming an actual pitting stress it is possible to show the amount of pitted areas on the gear teeth versus the number of cycles. An example is shown in Figure 2.27, where an actual pitting stress of 1800 MPa is assumed. It is easy to see that the increase of pitted area is not linear, being the pitting progressively more damaging.

The overlap of the *design* fatigue curves for the different pitting stages (see Figure 2.28) may give to designers an idea of the pitting evolution to be taken into account during the design phase. It is easy to see that the phenomenon appears progressive again: the higher the pitting level, the higher the recorded number of cycles from the tests. In Figure 2.28 the no-pitting-allowed curves for different case-hardened steel qualities are reported only for reference, since they are relevant to 99% of survival probability.

A statistical analysis performed at $p = 99%$ and $\gamma=95%$ is actually meaningless, since the use of high values of q only for the pitting stages higher than 1 leads to lose the real nature of the phenomenon. In other words, the results are too much affected by the statistical model. Performing hard statistical

reported in the literature [9, 8, 14].

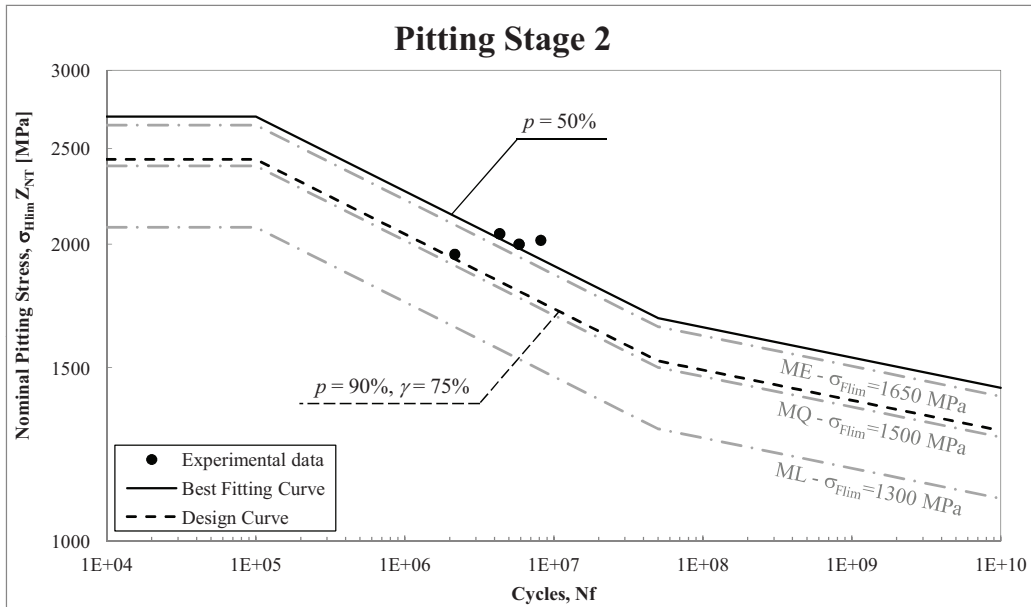


Figure 2.22: Nominal pitting curve for pitting stage 2 according to traditional Carraro's statistical approach (un-peened case-hardened steels).

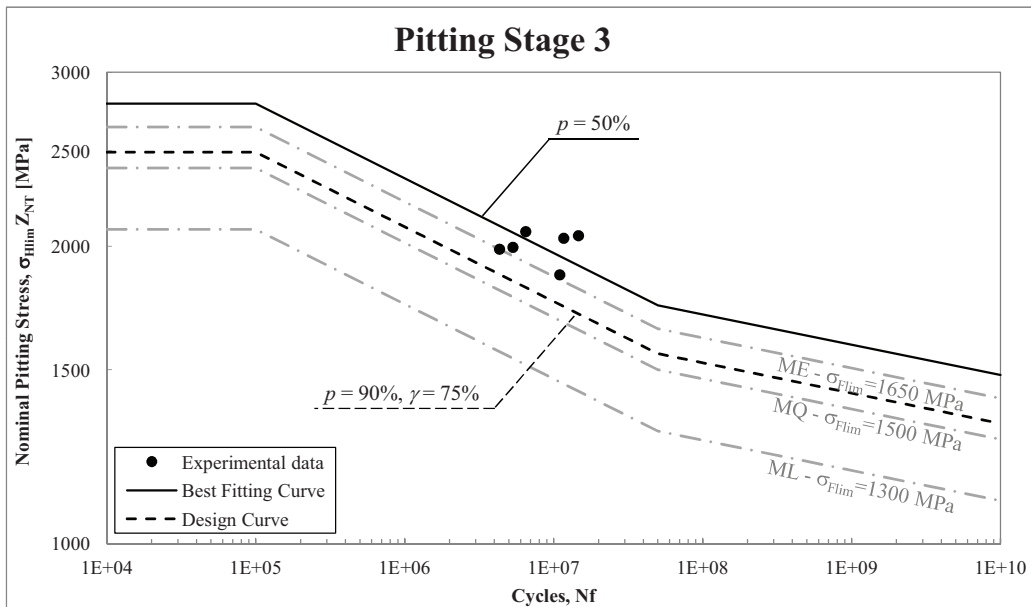


Figure 2.23: Nominal pitting curve for pitting stage 3 according to traditional Carraro's statistical approach (un-peened case-hardened steels).

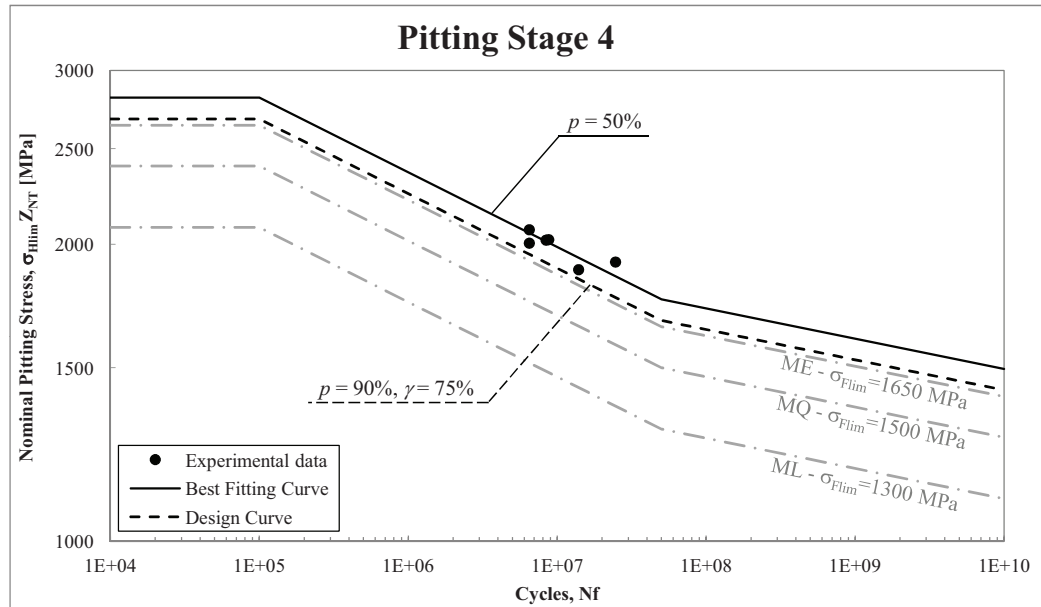


Figure 2.24: Nominal pitting curve for pitting stage 4 according to traditional Carraro's statistical approach (un-peened case-hardened steels).

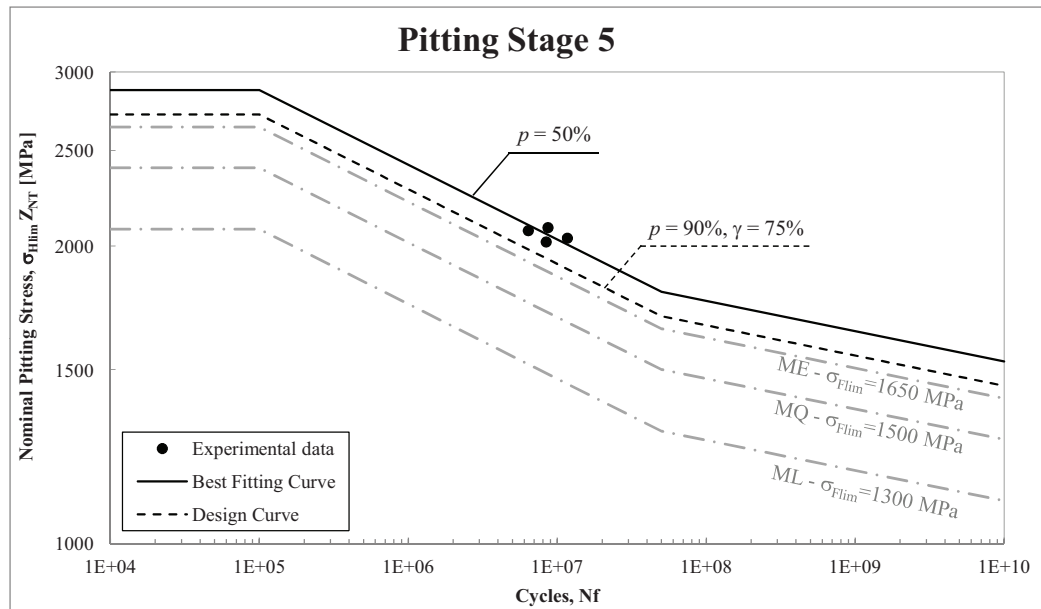


Figure 2.25: Nominal pitting curve for pitting stage 5 according to traditional Carraro's statistical approach (un-peened case-hardened steels).

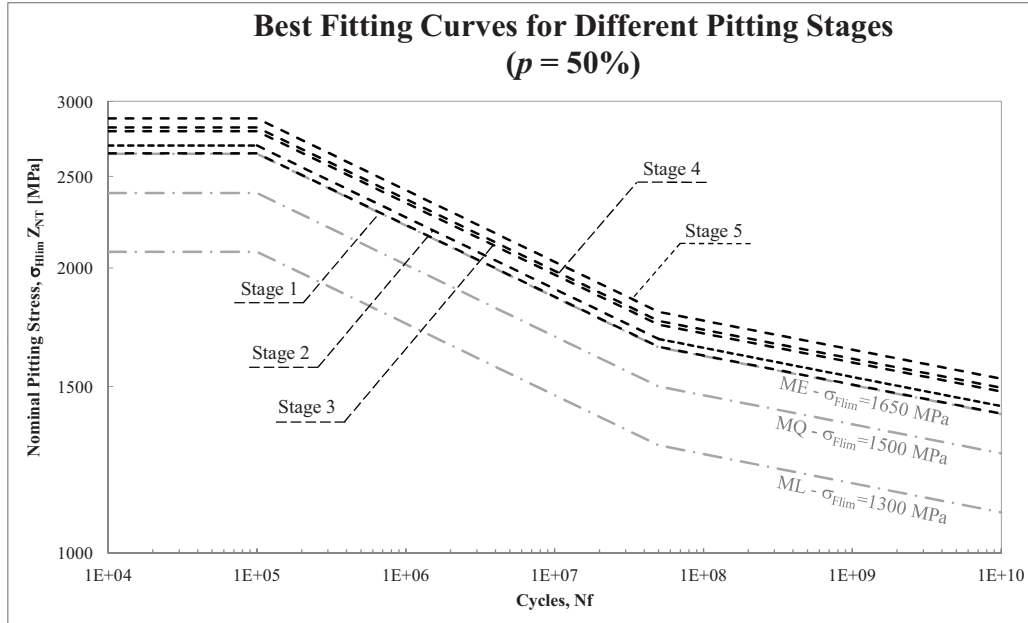


Figure 2.26: Overlap of the best fitting fatigue curves at different pitting stages (un-peened steels).

Table 2.12: Nominal pitting endurance limits ($5E7$ cycles) σ_{Hlim} [MPa] extrapolated from the best fitting on available experimental points of FSTs.

Pitting stage	σ_{Hlim} at $5E7$ cycles
1	1652 MPa
2	1683 MPa
3	1743 MPa
4	1760 MPa
5	1798 MPa
un-peened steels, $p=50\%$	

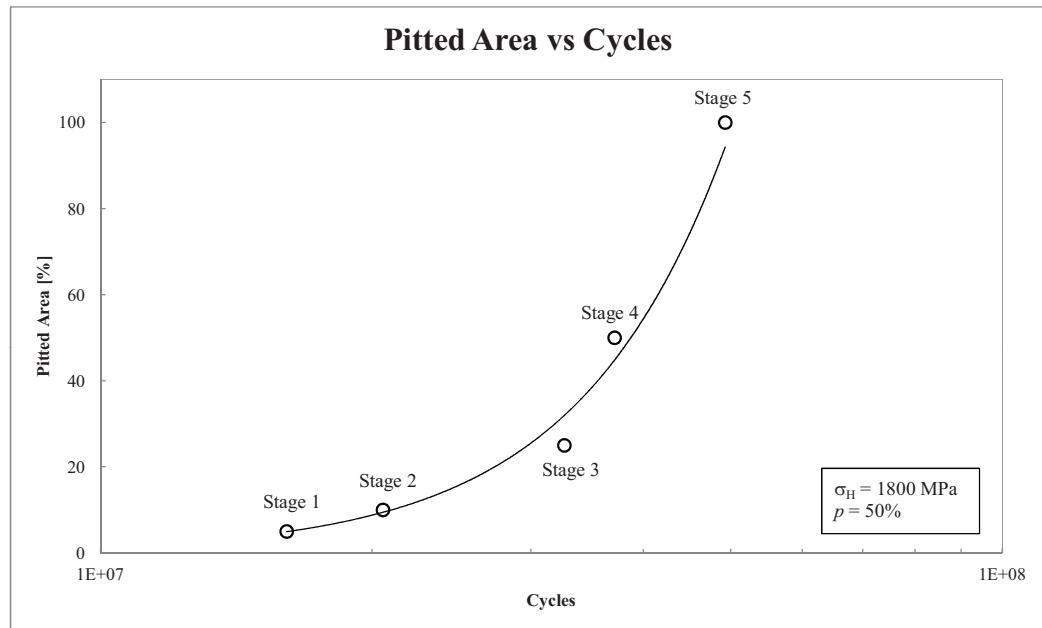


Figure 2.27: Pitted area versus number of cycles (simulation made assuming $\sigma_H = 1800$ MPa and using the best fitting curves for the different pitting stages).

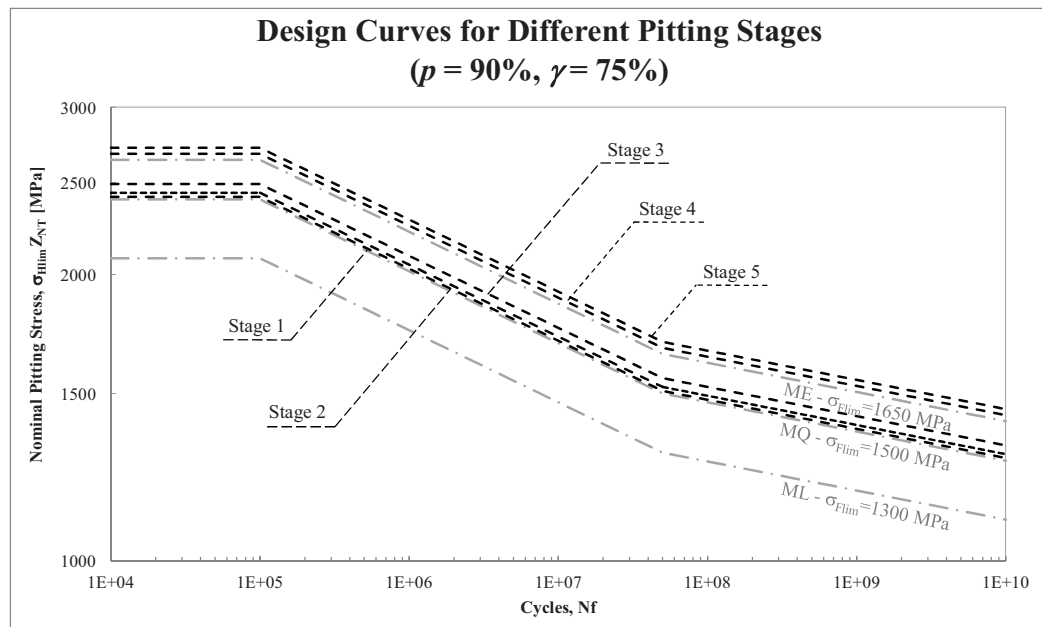


Figure 2.28: Overlap of the fatigue curves at different pitting stages (unpeened steels).

inference with small sample sizes is not a valuable approach. For these reasons, only the design curves for $p=90\%$ and $\gamma=75\%$ are here reported.

An alternative approach could be using the statistical scatter obtained for the pitting stage 1 for all the other pitting stages. In such a way, it is implicitly assumed that the different pitting stages have all the same statistical behavior and it is possible obtaining inferred design curves with a higher statistical significance.

It must be noted that for the estimation of the pitting curves at high pitting levels, a fixed slope (13.22) of the fatigue curve was adopted, even if ISO 6336 suggests a curve composed by different segments with variable slopes for limited flank pitting allowed. Since the number of available points for pitting levels major than 1 are few in this work, this kind of approach appeared too complex and useless, also because there is no indication of the amount of pitted area on gear teeth for "limited flank pitting allowed" condition in the Standard.

2.5 Bending performances of bevel gear sets

The analysis of CTs makes it possible the estimation of the bending fatigue performance of case-hardened steels. In CTs, the components more subject to failure are the bevel gear sets instead of cylindrical gears. This means that ISO 6336 cannot be used to calculate the bending tooth root stress, since it is only valid for cylindrical gears. Other calculation algorithms exist, and they are reported in:

- AGMA B97 [15]
- ISO 10300 [16]

Both the algorithms calculate the linear elastic stress peak at the tooth root, but using different approaches. AGMA B97 is based on the estimation of a coefficient called *J-factor* that summarizes the geometry of the gear contact, in terms of tooth shape, position at which the load is applied, the stress concentration due to tooth root fillet, the load sharing between adjacent pairs of teeth, the tooth thickness balance between the gear and mating pinion, and effective face width due to crowning. Both radial and tangential load components are included in the calculations. Since the calculation of J-factor is complex, several charts for its evaluation are available in the Standard for some reference configurations. Fortunately, gear calculation programs allow the designers to calculate the J-factor automatically in an easy way (that is

what was done in this work, using KissSoft Software [4]).

ISO 10300 is based on the transformation of the bevel gear set into a couple of mating virtual cylindrical gears⁴. On these gears, the tooth root bending stress is then calculated. The definition of the virtual cylindrical gears and the consecutive calculation of the bending stress can be automatically made using a calculation software ([4]).

Bevel gear sets are designed for Carraro by Gleason [17], which provides for each bevel gear set a data-sheet with all the geometrical dimensions necessary to produce the set. In this data-sheet the J factors for the pinion and the gear (calculated using [15]) are reported. Using KissSoft Software, a model for each tested bevel gear set was made and the tooth root bending stress was calculated using the two algorithms. Using the fatigue life recorded in the test report obtained from the Test and Prototype Department, experimental points representative of the bending fatigue performance of the bevel sets were defined and then overlapped on charts.

Two different activities were carried out using the results of the analysis. The data obtained from the application of AGMA B97 were used to check the reliability of the Gleason calculation method, that is used for fatigue life prediction inside the Company. The data obtained from the application of ISO 10300 were instead used to define the allowable bending fatigue curve by processing the data with statistical models.

The key aspects of making the models and the analysis activities are reported in the next paragraphs.

2.5.1 Bevel gear set models

The models of the bevel gear sets were made using KissSoft software [4]. The starting point was the Gleason data-sheet, where all the necessary data to build the model can be found. These data can be easily inserted in a specific window in KissSoft, see Figure 2.29, obtaining an approximate model of the bevel gear set. To refine the model the profile shift coefficient x_{smn}^* was adjusted in order to obtain the same mean circular thickness reported in the Gleason data-sheet.

The normal backlash of the gear set was then modeled as well. The backlash was assigned to the bevel pinion or gear checking that the J-factor calculated by the software was equal to the corresponding value reported in the data-sheet. If necessary, the tooth root fillet was modified from the default value of the software in order to achieve the right J-factor. The fine geometry of

⁴In this work the method B1 of ISO 10300 was used

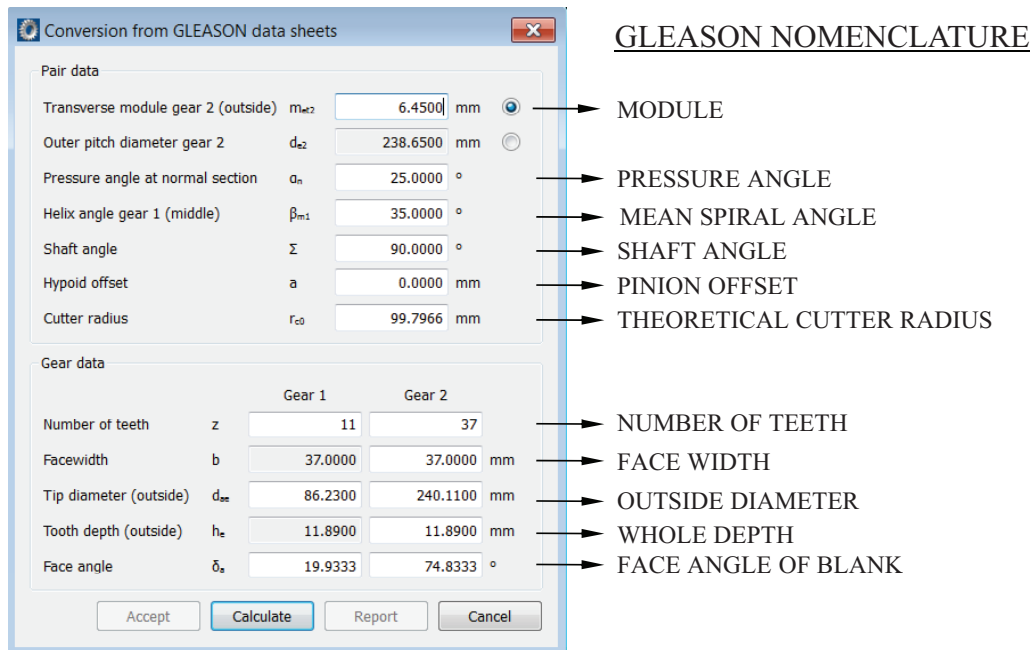


Figure 2.29: Main data required by KissSoft for the generation of the bevel gear set model.

the teeth was therefore found⁵. A 3D view of a bevel gear set obtained using KissSoft is reported in Figure 2.30.

Only the teeth of the pinion and gear were modeled, since ISO 10300 Standard [16] and the Gleason Method [18] do not allow to consider in the details the deflections of the shafts supporting the gear set. Deflections are taken into account using a mounting factor ($K_{H\beta-be}$ or K_m) depending on the assembly configuration of the bearings along the shafts (see Tables 2.13 and 2.14). The axle assembly configuration of the analyzed CTs was characterized by the bevel pinion overhung (cantilever mounted) and gear straddle mounted. In the following analyses the value $K_{H\beta-be} = K_m = 1.1$ was chosen, according to the mounting configuration of the set's members.

⁵A maximum error of 2.5% on the J-factors for pinion and gear was obtained.

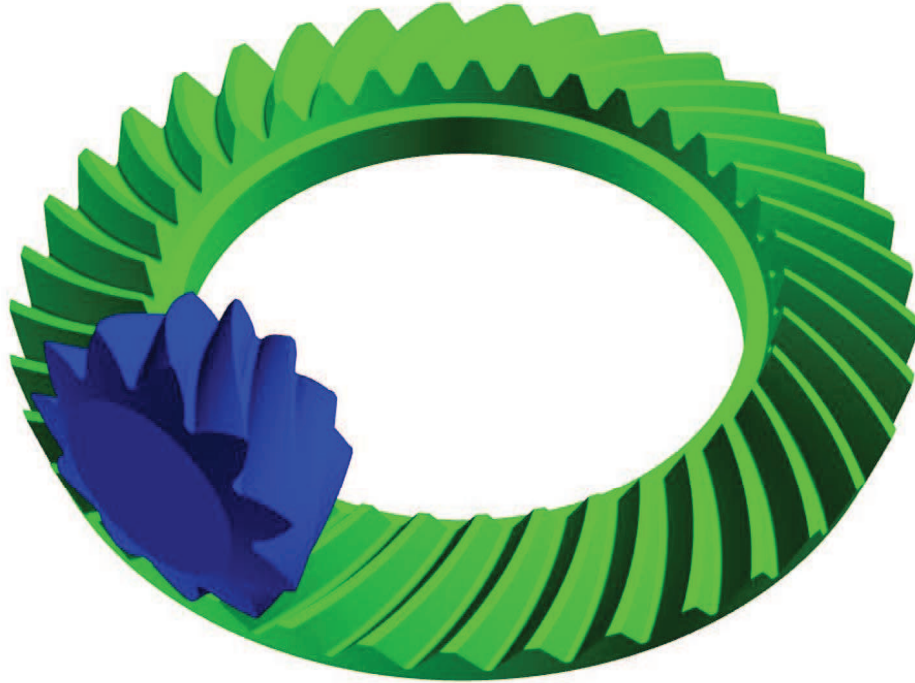


Figure 2.30: Model of a bevel gear set made in KissSoft (CT 3368).

Table 2.13: Mounting factor ($K_{H\beta-be}$) according to [16].

Contact pattern is checked for:	Cantilever mounted members:		
	Neither	One	Both
each gear set in its housing under full load	1.00	1.00	1.00
each gear set under light test load	1.05	1.10	1.25
a sample gear set and estimated for full load	1.20	1.32	1.50

Table 2.14: Load distribution factor (K_m) according to [18].

Application	Both members straddle mounted	One member stradde mounted	Neither member straddle mounted
General Industrial	1.00 to 1.10	1.10 to 1.25	1.25 to 1.40
Automotive	1.00 to 1.10	1.10 to 1.25	
Aircraft	1.00 to 1.25	1.10 to 1.40	1.25 to 1.50

2.5.2 Reliability of Gleason calculation method

The tooth root bending stress (s_t) according to Gleason method [18] can be calculated using the following expression:

$$s_t = \frac{F_t K_A P_d K_s K_m}{K_v b J K_x} \quad (2.11)$$

where:

- F_t is the tangential force [pounds].
- K_A is the overload factor, which accounts for the kind of application. Since testing conditions are constantly monitored and overloads did not take place, it was assumed equal to 1.
- K_v is the dynamic factor, which accounts for the effect of inaccuracies in profile, tooth spacing and runout. In the following analyses the K_v was evaluated according to diagrams relevant to bevel gears cut to good commercial quality with accurate spacing and concentricity, but free quenched (Curve 1A).
- P_d is the outer transverse diametral pitch.
- b is the net facewidth (inches).
- K_s is the size factor: $K_s = P_d^{-0.25}$.
- K_m is the mounting factor (see Table 2.14).
- J is the J-factor.
- K_x is the cutter radius factor: $K_x = 0.211 \left(\frac{r_c}{A} \right)^{\frac{0.2788}{\log \beta_m}} + 0.7889$, where r_c is the cutter radius, A is the mean cone distance and β_m is the mean spiral angle.

The allowable fatigue limit for the target life (s_w) can be estimated using the following expression:

$$s_w = \frac{s_{at} K_L}{K_T K_R} \quad (2.12)$$

where

- s_{at} is the allowable bending stress. For case-hardened steels Gleason suggests $s_{at} = 30 \text{ ksi} \approx 210 \text{ MPa}$.

Table 2.15: Safety factor K_R according to [18].

Requirements of Application	K_R
Maximum safety	2.0
Fewer than 1 failure in 100	1.0
Fewer than 1 failure in 3	0.8

Table 2.16: Life factor K_L according to [18].

Confidence Level	Low cycle ref. point		Endurance limit		Slope
	K_L	N	K_L	N	k
5%	4.6	1E3	1.0	6E6	5.68
50%	5.0	2E3	1.5	7E6	6.68
95%	5.0	1E4	2.2	7E6	7.97

- K_L is the life factor, which accounts for required number of cycles (see Table 2.16).
- K_T is the temperature factor, which is assumed to be equal to 1 under normal conditions. It can be calculated using $K_T = \frac{460+t}{620}$ (t is the temperature in Fahrenheit degrees) when, for case-hardened steel, the oil discharge temperature is between 70 and 150 °C.
- K_R is the safety factor, depending on the required reliability (see Table 2.15).

To design against bending fatigue, it must be verified that:

$$s_t \leq s_w \quad (2.13)$$

Generally the auxiliary strength factor Q is introduced. It is evaluated as follows:

$$Q = \frac{2P_d K_s}{bDJ} \quad (2.14)$$

where D is the external pitch diameter [inches] of the considered member of the gear set. The strength factor permits to simplify the expression of the bending stress leading to:

$$s_t = \frac{TQK_A K_m}{K_v K_x} \leq \frac{s_{at} K_L}{K_T K_R} = s_w \quad (2.15)$$

where T is the torque transmitted by the considered member of the gear set. Gleason method provides the endurance limit $s_{at} \approx 210$ MPa for case-hardened steels. Consequently it is possible to define the bending fatigue curve using the factors for the correction of the allowable endurance limit. Therefore, using the experimental data recorded from the CTs it is possible to compare the fatigue life predictions obtained using the Gleason method with the experimental evidence. Doing so, the reliability of the Gleason method may be investigated.

The test parameters of the analyzed CTs are reported in Table 2.17, where the torque applied at wheels, the speed ratios of the final drive and bevel gear set and the consequent input speed and torque at the bevel pinion are reported. The input values were estimated according to prescription reported in [1], i.e. considering an efficiency of 0.95 from the wheels to the input bevel pinion. For each CT, the failures and the corresponding fatigue lives are reported in Table 2.18. The Gleason calculation factors to define the tooth root bending stress are reported as well. In particular, the strength factor Q was taken directly from the data-sheet of the bevel gear set. The overload factor K_A was considered equal to 1, since the test conditions are controlled and monitored and therefore the test conditions can be considered constant. The mounting factor K_m was considered equal to 1.1. The temperature factor K_T was considered equal to 1 since CTs showed a temperature in the differential housing lower than 65 °C, as reported in Figure 2.31. The safety factor K_R was assumed equal to 1 as well. Analysis was restricted only to the axle under test and excluding the auxiliary axle that is used to close the power line. The reason is that the torque on bevel gear set on the auxiliary axle is lower than the tested axle due to all the power losses of the powerline. Looking at Table 2.18 it can be seen that the most frequent failure happened on pinions, since the design of the bevel sets is made in order to obtain a balanced stress between pinion and gear. Since the pinion rotates at higher speed than the gear, it is more probable that failures occur on it. The number of cycles to failure and the Gleason factors reported in the table are relevant to pinion or gear depending on where the failure takes place.

The overlap of the experimental results (bending stress evaluated using Gleason method and recorded life) and the fatigue curves suggested by Gleason is reported in Figure 2.32, where the data are classified in terms of test number. As it can be seen from the figure, the CTs lead to tooth root bending stresses that can be quite different from test to test. This is due to the different ratio of the bevel gear sets: even if the torque applied at the wheel is the same in two tests, the different number of teeth of pinions and gears lead to different input torque. This makes the investigation of a wider area of the fatigue curve possible, if compared to the FSTs results.

Table 2.17: Load and kinematic parameters of the analyzed CTs.

# CT	Wheel Torque	Final Drive Ratio	Bevel Set Ratio	Input Torque*	Input Speed
	[Nm]	[-]	[-]	[Nm]	[rpm]
3348	45000	6.4	2.500	2961.0	160
3348	45000	6.4	2.500	2961.0	160
3312	45000	6.4	2.750	2691.8	176
3312	45000	6.4	2.750	2691.8	176
3368	48600	6.4	2.750	2907.1	160
3420	45000	6.4	2.500	2961.0	160
3420	45000	6.4	2.500	2961.0	160
3420	45000	6.4	2.500	2961.0	160
3865	49000	6.4	2.667	3022.6	171
3865	49000	6.4	2.667	3022.6	171
3768	43000	6.923	3.364	1944.0	233
3768	43000	6.923	3.364	1944.0	233
3768	43000	6.923	3.364	1944.0	233
3384	43000	6.923	2.750	2377.8	190
3384	43000	6.923	2.750	2377.8	190
3384	43000	6.923	2.750	2377.8	190
3384	43000	6.923	2.750	2377.8	190
3384	43000	6.923	2.750	2377.8	190
3384	43000	6.923	2.750	2377.8	190
3384	43000	6.923	2.750	2377.8	190
3384	43000	6.923	2.750	2377.8	190
3667	45000	6.4	2.500	2961.0	160
3667	45000	6.4	2.500	2961.0	160
3412	41500	6.923	2.133	2958.2	148
2265	48600	6.4	2.750	2907.1	176
1835	48000	6.4	3.600	2193.3	230
2616	34000	6.923	2.538	2036.8	176
2616	34000	6.923	2.538	2036.8	176
2616	34000	6.923	2.538	2036.8	176
2616	34000	6.923	2.538	2036.8	176
3704	44000	6.4	3.182	2274.8	204
3704	44000	6.4	3.182	2274.8	204

* a total efficiency of 0.95 was considered

Table 2.18: Gleason calculation factors for the analyzed CTs.

# CT	Failure of	Steel	Fatigue Life		Q	K_A	K_m	K_v	K_x	s_t	
			[hours]	[cycles]						[psi]	[MPa]
3348	PINION	19CrNi5	55.2	5.30E+05	2.13729	1	1.1	0.96	1.017	62788	433
3348	PINION	19CrNi5	43.3	4.16E+05	2.13729	1	1.1	0.96	1.017	62788	433
3312	PINION	19CrNi5	14.9	1.57E+05	2.67180	1	1.1	0.97	1.004	72232	498
3312	PINION	19CrNi5	23.3	2.46E+05	2.67180	1	1.1	0.97	1.004	72232	498
3368	PINION	19CrNi5	36.5	3.50E+05	2.36298	1	1.1	0.97	1.017	68066	469
3420	GEAR	20MnCr5	5.8	2.23E+04	1.07570	1	1.1	0.97	1.004	79956	551
3420	GEAR	20MnCr5	7.2	2.76E+04	1.07570	1	1.1	0.97	1.004	79956	551
3420	GEAR	20MnCr5	7.4	2.84E+04	1.07570	1	1.1	0.97	1.004	79956	551
3865	PINION	18NiCrMo5	12.4	1.27E+05	2.98815	1	1.1	0.97	1.000	90953	627
3865	PINION	18NiCrMo5	11.8	1.21E+05	2.98815	1	1.1	0.97	1.000	90953	627
3768	PINION	18NiCrMo5	9.1	1.27E+05	5.43496	1	1.1	0.97	1.091	97703	674
3768	PINION	18NiCrMo5	2.1	2.93E+04	6.23201	1	1.1	0.97	1.000	122166	842
3768	PINION	18NiCrMo5	2.7	3.77E+04	6.23201	1	1.1	0.97	1.000	122166	842
3384	PINION	18NiCrMo5	6.9	7.88E+04	3.94474	1	1.1	0.97	1.000	94604	652
3384	PINION	18NiCrMo5	11.3	1.29E+05	3.94474	1	1.1	0.97	1.000	94604	652
3384	PINION	18NiCrMo5	18.4	2.10E+05	3.94474	1	1.1	0.97	1.000	94604	652
3384	PINION	18NiCrMo5	19.3	2.20E+05	3.94474	1	1.1	0.97	1.000	94604	652
3384	PINION	18NiCrMo5	20.6	2.35E+05	3.94474	1	1.1	0.97	1.000	94604	652
3384	PINION	18NiCrMo5	12.7	1.45E+05	3.94474	1	1.1	0.97	1.000	94604	652
3667	PINION	19CrNi5	31.1	2.99E+05	2.35688	1	1.1	0.97	1.004	70074	483
3667	PINION	19CrNi5	33.9	3.25E+05	2.35688	1	1.1	0.97	1.004	70074	483

Continues on next page

Table 2.18 – *Continues from previous page*

# CT	Failure of	Steel	Fatigue Life		Q	K_A	K_m	K_v	K_x	s_t	
			[hours]	[cycles]						[psi]	[MPa]
3412	PINION	18NiCrMo5	14.2	1.26E+05	2.76607	1	1.1	0.97	1.045	78976	545
2265	PINION	18NiCrMo5	6.7	7.08E+04	2.99602	1	1.1	0.97	1.042	84230	581
1835	GEAR	20MnCr5	14.8	5.68E+04	1.12409	1	1.1	0.97	1.000	89479	617
2616	PINION	18NiCrMo5	3.5	3.69E+04	4.66458	1	1.1	0.97	1.011	94633	652
2616	PINION	18NiCrMo5	8.8	9.28E+04	4.66458	1	1.1	0.97	1.011	94633	652
2616	PINION	18NiCrMo5	8	8.44E+04	4.66458	1	1.1	0.97	1.011	94633	652
2616	PINION	18NiCrMo5	3.5	3.69E+04	4.66458	1	1.1	0.97	1.011	94633	652
3704	PINION	18NiCrMo5	10	1.22E+05	2.87550	1	1.1	0.97	1.000	65958	455
3704	PINION	18NiCrMo5	14	1.71E+05	2.87550	1	1.1	0.97	1.000	65958	455

The experimental points are reported also in Figure 2.33, where the data are classified in terms of the case-hardened steel the broken component is made of.

As it can be seen from Figure 2.33, the curves proposed by Gleason Method envelope all the experimental points. This means that life predictions obtained by applying this methods seems to be satisfactory. It can be seen that points tend to be distributed along the curve at 50%. The failures obtained on 20MnCr5 members seems to take place at shorter lives than the other steels (it must be noted that in this case the broken components are gears and not pinions and only few points are available). The scatter of the failures obtained on 18NiCrMo5 members seems to be higher than those of the other steels. However, the experimental points of 18NiCrMo5 are also the most numerous. The scatter of 19CrNi5 steel is the lowest among the three steels instead. It must be considered that the Gleason calculation does not take into account all the real test parameters (e.g. the bearing preload, differential housing stiffness, tightening torque of screws used to fix the gear to the differential housing, ...) that may be different from test to test. Unfortunately the Gleason methods does not take into account these factors directly, therefore they cannot be distinguished in the calculations in an effective way.

2.5.3 Bending fatigue curves extrapolated from CTs

The CTs presented in Table 2.17 were also analyzed using the approach reported in ISO 10300 [16]. The fundamental expression for design against bending fatigue was the following:

$$\sigma_F \leq \sigma_{FP} \quad (2.16)$$

where σ_F is the actual tooth root bending stress and σ_{FP} is the corresponding endurance limit. Once the endurance limit is reached, i.e. the fatigue failure occurs, the expression can be written explicitly as follows:

$$\sigma_{F0} K_A K_V K_{F\beta} K_{F\alpha} = \frac{\sigma_{Flim} Y_{NT}}{S_{Fmin}} Y_{ST} Y_{\delta rel T} Y_{Rrel T} Y_X \quad (2.17)$$

where the term $\sigma_{Flim} Y_{NT}$ corresponds to the bending stress of the tested material under some nominal conditions. For this reason, it is independent from the geometry and working conditions of the analyzed gear. The stress $\sigma_{Flim} Y_{NT}$ can be evaluated from the experimental evidence once all the other

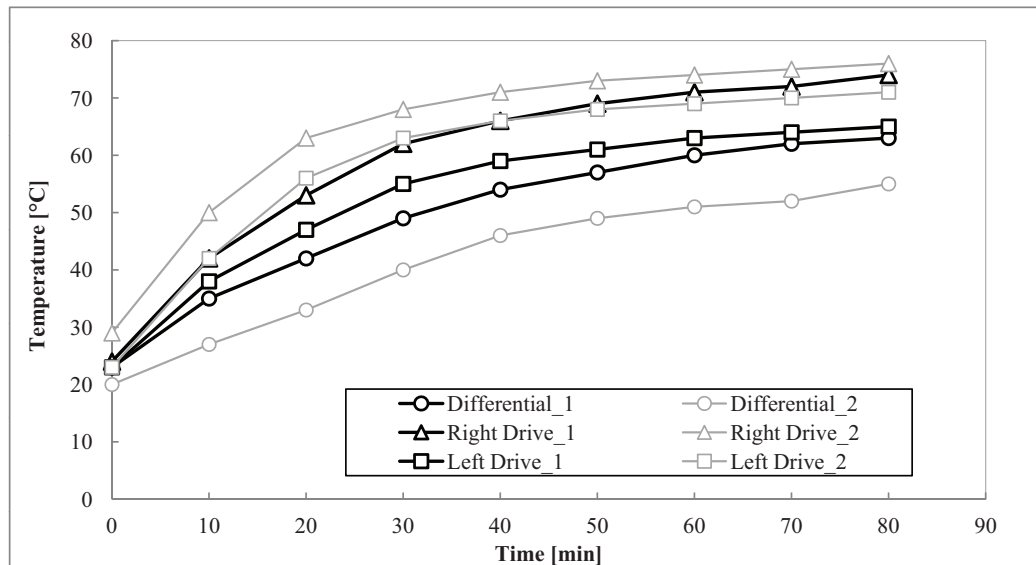


Figure 2.31: Profile temperature measured during a CT with no external fans or oil cooling. 1 = axle on test, 2 = auxiliary axle (FST 2075: Wheel torque = 16 kNm, Wheel speed 10 rpm).

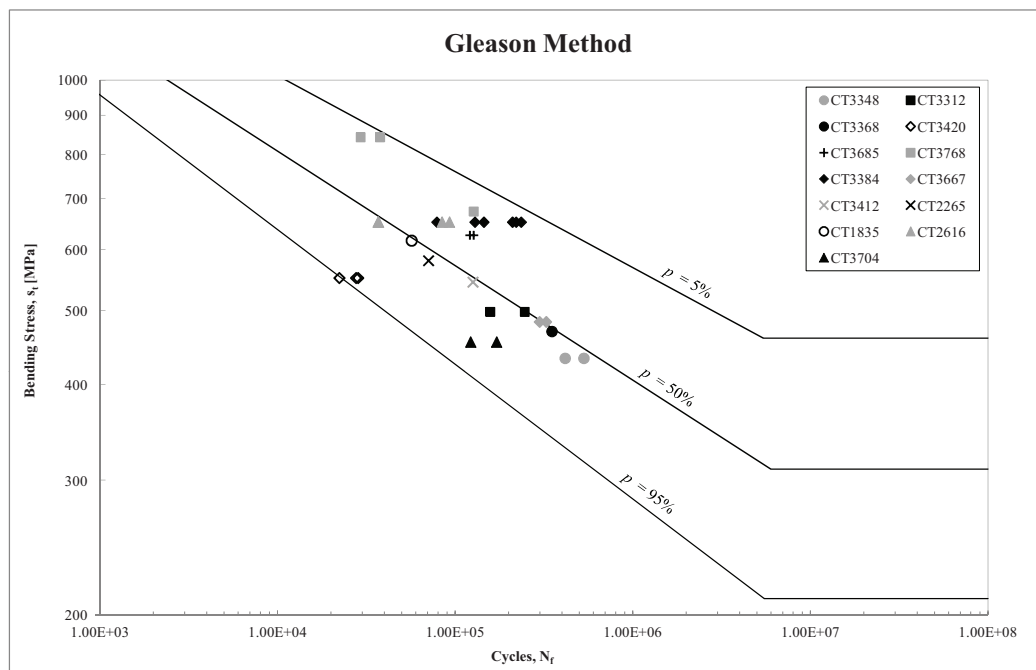


Figure 2.32: Experimental points of the analyzed CTs obtained applying Gleason Method. Differentiation is made on test number.

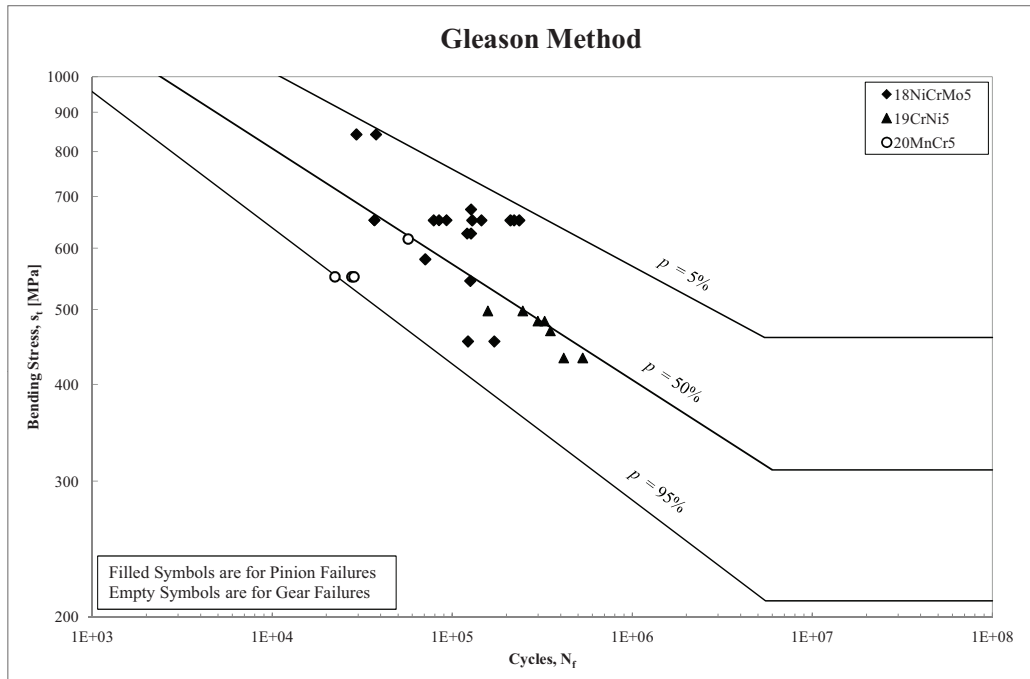


Figure 2.33: Experimental points of the analyzed CTs obtained applying Gleason Method. Differentiation is made on the material of the broken member of the set.

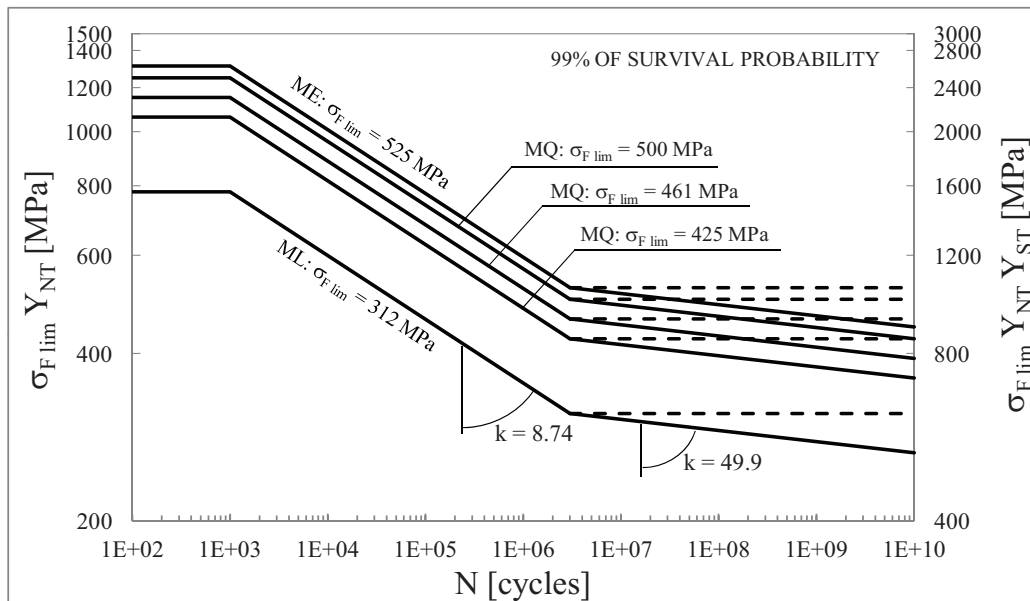


Figure 2.34: Nominal bending fatigue curves reported in ISO 6336 for case-hardened reference gears [45].

factors are estimated, obtaining ⁶:

$$\sigma_{Flim} Y_{NT} = \frac{\sigma_{F0} K_A K_V K_{F\beta} K_{F\alpha}}{Y_{ST} Y_{\delta rel T} Y_{Rrel T} Y_X} \quad (2.18)$$

The allowable bending fatigue curves reported in ISO 6336 for case-hardened steels are reported in Figure 2.34. The standard distinguishes three different qualities, from low (ML) to excellent (ME), passing through medium quality (MQ). Each steel qualities has an allowable endurance limit σ_{Flim} , which is defined as the maximum nominal bending stress at tooth root of a reference gear reached during a $R = 0$ fatigue cycle, at the endurance limit. The endurance limit is set to 3,000,000 cycles, and the fatigue curves are declared at 99% of survival probability only. To draw the entire fatigue curves, the standard uses a life factor Y_{NT} that practically provides the slope of the curve. Therefore the nominal fatigue curve is expressed in terms of $\sigma_{Flim} Y_{NT}$. Since the reference gears used to obtain the curves were characterized by a stress concentration factor $Y_{ST} = 2$, the curves may be expressed also in terms of linear elastic peak stress at tooth root, i.e. $\sigma_{Flim} Y_{NT} Y_{ST} = 2\sigma_{Flim} Y_{NT}$. The higher the steel quality, the higher σ_{Flim} . Within the medium quality, three different steel classes are presented, depending on the core and surface hardness of the gears. The higher the core and surface hardness, the higher the bending fatigue strength. Beyond the endurance knee, the fatigue curve may be declared horizontal up to 10 billions of cycles if there is experience on the endurance limit, and if material, manufacturing process and working conditions of the gears are optimum. Otherwise, the inclined line should be adopted.

The factors of Equation 2.18 were calculated using the KissSoft model that was built in order to match the Gleason data sheet of the bevel set. The obtained results are reported in Table 2.19. The fatigue life recorded during the CTs and the corresponding $\sigma_{Flim} Y_{NT}$ stress on the broken member of the bevel gear set can be plotted on a fatigue chart that can be used to estimate a nominal bending fatigue curve. This curve can be used for every bevel set, since it is theoretically independent from the working conditions and design configuration. The experimental points processed using ISO 10300 were analyzed using the prescription reported in Section 2.4.2. Since in the case of the bevel gear sets the bending stresses cover an higher stress range than in the case of pitting stresses of FSTs, it is theoretically possible to extrapolate an experimental slope of the fatigue curve. This experimental slope (inverse Wohler slope) results 4.31, while the suggested value in the Standard ISO 6336 was 8.738 (ISO 10300 suggests to design against fatigue using the same fatigue limit reported in ISO 6336).

⁶See Chapter 4 for the description of the calculation factors.

Table 2.19: Calculation factors according to ISO 10300 for the analyzed CTs.

# CT	Failure of	Steel	Fatigue Life		σ_{F0} [MPa]	K_V	$K_{F\beta}$	$Y_{\delta relT}$	Y_X	$\sigma_{Flim} Y_{NT}$ [MPa]
			[hours]	[cycles]						
3348	PINION	19CrNi5	55.2	5.30E+05	695	1.002	1.62	1.014	0.997	613
3348	PINION	19CrNi5	43.3	4.16E+05	695	1.002	1.62	1.014	0.997	613
3312	PINION	19CrNi5	14.9	1.57E+05	703	1.002	1.65	1.009	0.996	635
3312	PINION	19CrNi5	23.3	2.46E+05	703	1.002	1.65	1.009	0.996	635
3368	PINION	19CrNi5	36.5	3.50E+05	660	1.002	1.62	1.010	0.993	587
3420	GEAR	20MnCr5	5.8	2.23E+04	863	1.002	1.64	1.004	1.000	776
3420	GEAR	20MnCr5	7.2	2.76E+04	863	1.002	1.64	1.004	1.000	776
3420	GEAR	20MnCr5	7.4	2.84E+04	863	1.002	1.64	1.004	1.000	776
3865	PINION	18NiCrMo5	12.4	1.27E+05	849	1.002	1.65	1.009	0.996	767
3865	PINION	18NiCrMo5	11.8	1.21E+05	849	1.002	1.65	1.009	0.996	767
3768	PINION	18NiCrMo5	9.1	1.27E+05	1032	1.002	1.63	1.008	1.000	918
3768	PINION	18NiCrMo5	2.1	2.93E+04	1123	1.002	1.65	1.011	1.000	1009
3768	PINION	18NiCrMo5	2.7	3.77E+04	1123	1.002	1.65	1.011	1.000	1009
3384	PINION	18NiCrMo5	6.9	7.88E+04	860	1.002	1.65	1.009	0.999	774
3384	PINION	18NiCrMo5	11.3	1.29E+05	860	1.002	1.65	1.009	0.999	774
3384	PINION	18NiCrMo5	18.4	2.10E+05	860	1.002	1.65	1.009	0.999	774
3384	PINION	18NiCrMo5	19.3	2.20E+05	860	1.002	1.65	1.009	0.999	774
3384	PINION	18NiCrMo5	20.6	2.35E+05	860	1.002	1.65	1.009	0.999	774
3384	PINION	18NiCrMo5	12.7	1.45E+05	860	1.002	1.65	1.009	0.999	774
3667	PINION	19CrNi5	31.1	2.99E+05	716	1.002	1.64	1.013	1.000	639
3667	PINION	19CrNi5	33.9	3.25E+05	716	1.002	1.64	1.013	1.000	639

Continues on next page

Table 2.19 – *Continues from previous page*

# CT	Failure of	Steel	Fatigue Life		σ_{F0} [MPa]	K_V	$K_{F\beta}$	$Y_{\delta relT}$	Y_X	$\sigma_{Flim} Y_{NT}$ [MPa]
			[hours]	[cycles]						
3412	PINION	18NiCrMo5	14.2	1.26E+05	769	1.002	1.58	1.010	0.998	663
2265	PINION	18NiCrMo5	6.7	7.08E+04	892	1.002	1.58	1.016	0.998	765
1835	GEAR	20MnCr5	14.8	5.68E+04	921	1.002	1.65	1.005	1.000	832
2616	PINION	18NiCrMo5	3.5	3.69E+04	858	1.002	1.65	1.002	1.000	778
2616	PINION	18NiCrMo5	8.8	9.28E+04	858	1.002	1.65	1.002	1.000	778
2616	PINION	18NiCrMo5	8	8.44E+04	858	1.002	1.65	1.002	1.000	778
2616	PINION	18NiCrMo5	3.5	3.69E+04	858	1.002	1.65	1.002	1.000	778
3704	PINION	18NiCrMo5	10	1.22E+05	706	1.002	1.65	1.018	0.999	631
3704	PINION	18NiCrMo5	14	1.71E+05	706	1.002	1.65	1.018	0.999	631

$K_{F\alpha} = 1$ and $Y_{RelT} = 0.9103$ (tooth root roughness was assumed $R_a = 6.3 \mu\text{m}$)

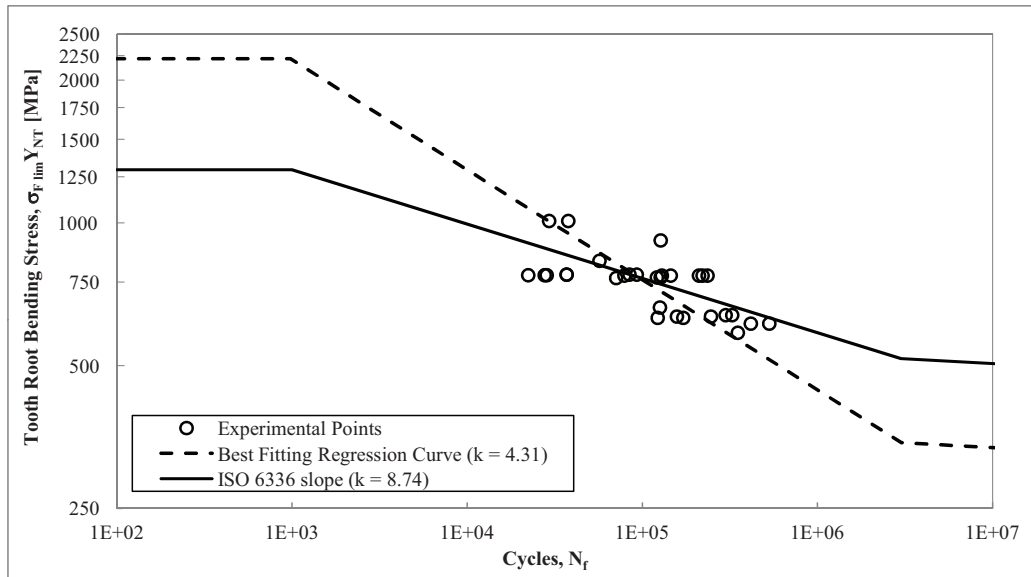


Figure 2.35: Fitting of CTs experimental points using least square regression line and ISO 6336 slope ($k=8.74$).

The fitting of the data using the least square regression line and the fitting made using the fixed slope of ISO 6336 is reported in Figure 2.35. In the picture, the low and high cycle knees of the fatigue curve are supposed to be located at $1E3$ and $3E6$ cycles respectively, according to ISO 6336 Standard. It is easy to see that there is a significant difference between the two curves. Since the purpose of this analysis is to estimate the allowable fatigue curve according to ISO Standard, the fitting based on the fixed slope of 8.738 was used.

Performing a statistical analysis of the experimental points presented in Table 2.19, the curves at different survival probability and confidence level can be estimated. The nominal fatigue curve obtained for $p = 99\%$ and $\gamma = 95\%$ is reported in Figure 2.36. The scatter index T_σ resulted:

$$T_{\sigma \ 1\%-99\%} = \frac{\sigma_{F1\%}}{\sigma_{F99\%}} = 1.91 \quad (2.19)$$

Notice that the design curve exhibits a lower fatigue strength than the MQ Quality. The endurance limit can be found in Table 2.20.

The nominal curve for Carraro's traditional requirements ($p = 90\%$ and $\gamma = 75\%$) is reported in Figure 2.37. In such a case the scatter index $T_{\sigma \ 10\%-90\%} = 1.36$ and the design curve corresponds to the curve proposed by ISO 6336-5 for the lowest level of the MQ quality (cfr. Table 2.20). It must be remembered that the curve proposed by ISO 6336-5 are at 99% of survival probability.

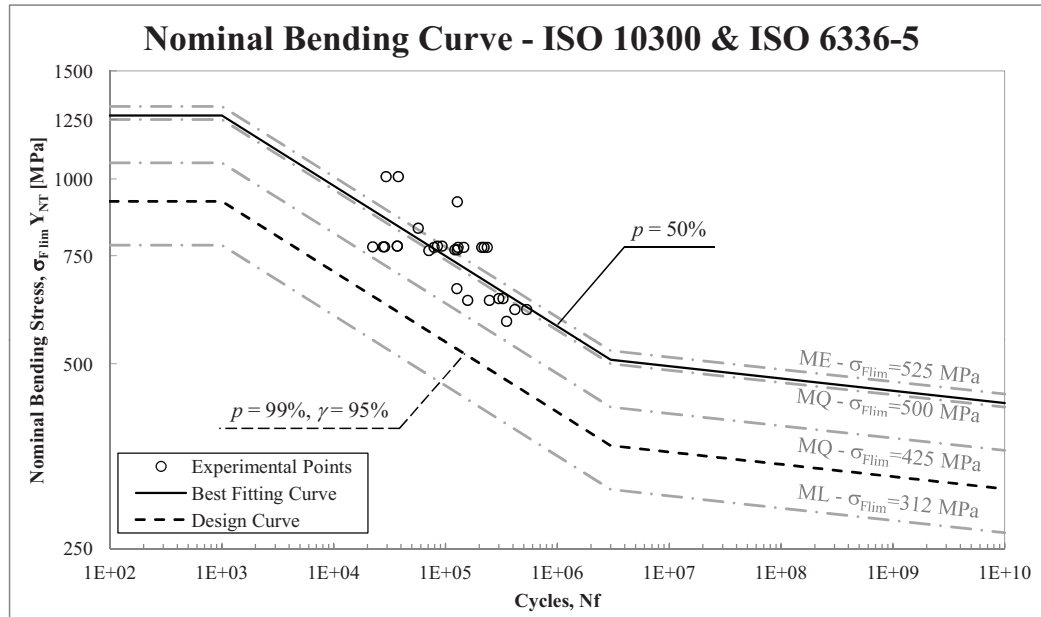


Figure 2.36: Nominal bending curve at $p = 99\%$ and $\gamma = 95\%$ for bevel gear sets compared to the bending curves for different quality of case-hardened steels proposed by ISO 6336-5.

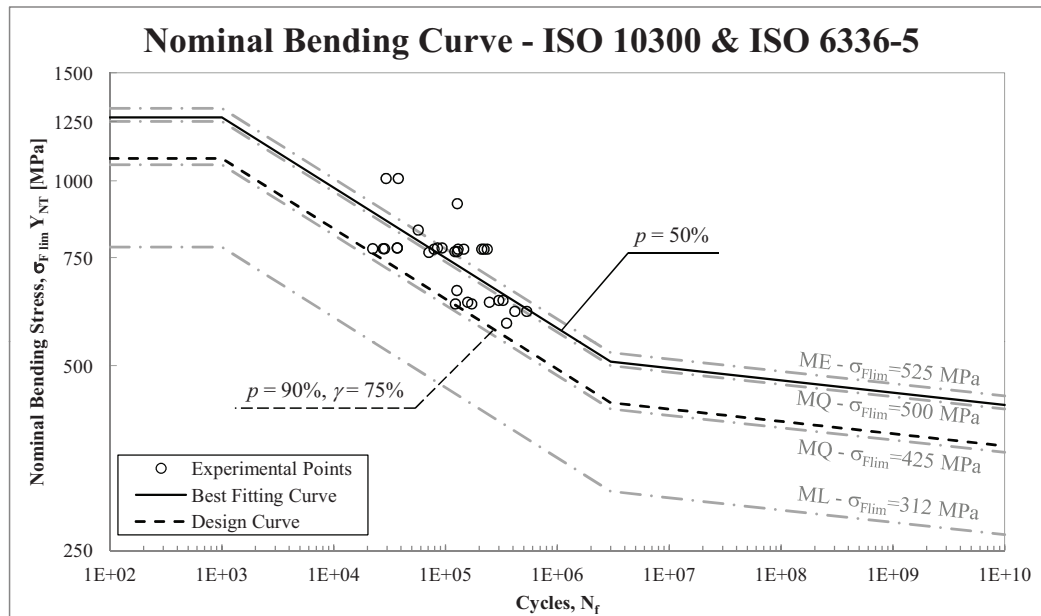


Figure 2.37: Nominal bending curve at $p = 90\%$ and $\gamma = 75\%$ for bevel gear sets compared to the bending curves for different quality of case-hardened steels proposed by ISO 6336-5.

Table 2.20: Nominal bending endurance limits (3E6 cycles) σ_{Flim} [MPa] extrapolated from CTs and limits reported in [10].

	$p=50\%$	$p=90\%$ $\gamma=75\%$	$p=99\%$ $\gamma=95\%$
$\sigma_{Flim} =$	508 MPa	435 MPa	368 MPa
	(ISO6336 ML quality: $\sigma_{Flim} = 312$ MPa)		
	(ISO6336 MQ quality: $\sigma_{Flim} = 425 \div 500$ MPa)		
	(ISO6336 ME quality: $\sigma_{Flim} = 525$ MPa)		

2.6 Conclusions

Several and complex tests are carried out inside CDT's Test Department. The purpose of these tests is to validate a finite product before releasing it to production. This necessarily requires complex bench tests, high amount of time, high costs. The advantage of such tests is that all the components of the product are validated in only one test. Moreover, every aspect of the problem is taken into account, since no simplifications are made. For instance, the ability of a supplier, in terms of in-field product life, can be easily checked. It can be said that the test carried out inside the Company are oriented to give a ready-to-use product to the customer.

However, this does not mean that the fatigue performances of driveline components is completely understood and can be precisely predicted. Actually, this approach has also some disadvantages. First, the knowledge of the single component of the entire product remains limited. Testing a single component using the entire finite product is very complex and expensive, since all the other components are to be assembled and controlled. Second, since only one configuration of product can be validated with a test, changes of suppliers or little design modifications require complete (and expensive) repetition of the test. Third, the testing time can be very long, due to all the complementary aspects that are related to the assembly and quality control of all the components of the finite product. Fourth, if something goes wrong during the test, not all the components can be validated, requiring other tests. Finally, it is very difficult to define the strength limit of the single component, because the influence of the whole system should be accurately considered and because it is not sure that the strength limit is reached during the test (since after a certain time, the test is interrupted even if no failure has taken place).

Since the testing of the finite product is necessary (and required by the customer), a solution may be the execution of other auxiliary tests on simplified

systems, in order to understand the behavior of the single component. Then, the experience collected on complex system should suggest how to correlate the single components one with the other. This approach requires initially an higher amount of assets, since new tests should be carried out on a lot of different components, but is more effective for the future, because a deep knowledge of every single part makes validation of different configurations faster. Naturally, the standards allow the designers to predict fatigue behavior even if specific tests are not carried out on the real component used by the Company. A verification of these design procedures could increase the comprehension of the product and of the failure modes. At least for gears. Making a transposition to FSTs, the analysis previously presented showed that FST's architecture resulted able to define the pitting performance of gear steels only partially. The reason is, again, that FST was thought to validate axles according to customers requirements. Experience collected during past years have shown that FST parameters are properly chosen to ensure no vehicle's failures on the field. However, this does not mean that the pitting performance of steels used in gear manufacturing by the Company is completely defined. Analyzing the FST, a lack of experimental data in the low-cycle and high-cycle region of the pitting curve was recognized. This means that there is no possibility to establish a slope of the pitting curve, and therefore calculating the pitting damage on test evidence. This is actually not a real problem for axles, where FST is standardized, but could be a problem for transmission, where applied duty cycles are very complex. In such a case, missing slope of the fatigue curves does not permit the evaluation of the total damage (using for instance the Miner rule). Moreover, there's no possibility to evaluate the real pitting fatigue limit of the several case-hardened steels used by the Company.

For these reasons, FST appears adequate to validate axles on the basis of experience, but is not an effective way to obtain pitting performance and to validate numerical models. Tests on gears at different torques (and contact stress consequently) seems to be necessary to understand real pitting fatigue limits. The analysis presented in this work allows to define the statistical scatter of the pitting phenomenon of the stress level applied during the FST. Increasing the number of experimental points may be a valuable approach to enhance the reliability of future life predictions.

The execution of test under different torques could be useful also for bevel gear sets, where, even if the stress range replicated with the CTs is higher than FSTs, experimental points seems to be too close to define in an effective way a fatigue slope. Experimental points obtained from the analyzed CTs are not enough to locate the low and the high cycle knee of the bending fatigue curve, making the extrapolation of a representative slope difficult. In

the case of bevel gear set the Gleason calculation method appeared safe, even if a large scatterband was found. The execution of tests on the same bevel gear set under different applied torque could reduce the scatter and create a sort of baseline to understand the influence of other influence factor of the system that are not taken into account by the Gleason approach.

Since CTs can be completed in short times, a test program of fatigue characterization at high and low torque of bevel gear sets appears feasible.

Experimental Tests on Case-Hardened Specimens

This chapter reports the experimental tests carried out on specimens made of different case-hardening steels, in order to obtain comparative results. Tests were carried out under plane bending loading conditions, in order to resemble the working conditions of the teeth of a real gear. Additional tests were carried out on specimens made of 20MnCr5, since this steel was considered strategically important by the Company. Specimens and tests were designed in order to investigate the effect of surface finishing, load type, mean stress and notch sensitivity. Further investigations on microstructure, microhardness, residual stresses and fracture surfaces are presented.

3.1 Introduction

Carraro Group has several manufacturing plants, located all over the world, e.g. in Italy, China, India and Brazil. From the point of view of *Local to Local* philosophy, the components assembled in a country should be supplied by local suppliers. Actually this means that for the Company it is necessary to investigate the fatigue properties of steels used abroad for the manufacturing of gears.

A test plan was defined in order to compare the most traditionally case-hardening steels used inside the Company and the other steels coming from foreign markets. The test plan involved 6 different case-hardening gear steels coming from Italy, China and India, as reported in Table 3.1. Due to some supply delays, the activity presented in this work focuses only on Italian and

Table 3.1: Steels defined for comparative tests.

Steel code	Steel name	Reference Standard	Country
1	20MnCr5	CARRARO 1-01-88 [19]	Italy
2	18NiCrMo5	CARRARO 1-12-88 [20]	Italy
3	19CrNi5*	CARRARO 1-00001/0 [21]	China
4	20CrMoH*	GB/T 5216-2004 [22]	China
5	EN 353	BS 970 [23]	India
6	815 H17	BS 970-1:1996 [23]	India

* results are not presented in this work

Indian steels ¹. The different steels were used to manufacture smooth specimens for static and plane bending fatigue tests. For steel 1 (20MnCr5) additional fatigue tests were carried out, since this steel was considered strategic (this steel is actually more inexpensive than 18NiCrMo5). Different geometries of specimens in 20MnCr5 were designed in order to investigate the effect of surface finishing, load type, mean stress and notch sensitivity.

¹tests on Chinese steels will be completed in the future.

Table 3.2: Data on case-hardened specimens collected from the literature.

Ref.	Material	Test Type*	Net section [mm ²]	K_{tn}	Notch Radius [mm]	Case Depth [mm]	Surface Hardness	Surface Res. Stress [MPa]	Surface Finishing
[24]	SAE8719	PB, R=0.1	□ 8.9x6.4	1.3	3.2	1.2	66 HRC	-	Polished
[25, 26]	SAE4320	PB, R=0.1	□ 8.9x6.4	1.3	3.2	1.1	61 HRC	0 / -138	Polished
[27]	SAE8219 (0.006% S)	PB, R=0.1	□ 8.9x6.4	1.3	3.2	1.38	63 HRC	-100	Polished
[27]	SAE8219 (0.015% S)	PB, R=0.1	□ 8.9x6.4	1.3	3.2	1.33	63 HRC	-100	Polished
[28]	SAE4118	PB, R=0.1	□ 8.9x6.4	1.3	3.2	0.9	680 HV	-290	Polished
[29, 30]	20MnCr5	PB, R=0.2	□ 21.6x19	1.63	7.62	-	-	-435	Ground
[29, 30]	SAE4320	PB, R=0.2	□ 21.6x19	1.63	7.62	-	-	-645	Ground
[29, 30]	SAE8822	PB, R=0.2	□ 21.6x19	1.63	7.62	-	-	-235	Ground
[29, 30]	PS18	PB, R=0.2	□ 21.6x19	1.63	7.62	-	-	-340	Ground
[31]	JIS SCr420	PB, R=0	□ 6x10	2.02	0.5	0.6	670 HV	100	Machined
[31]	JIS SCr420	PB, R=0	□ 6x10	1.59	1	0.6	670 HV	100	Machined
[31]	JIS SCr420	PB, R=0	□ 6x10	1.36	2	0.6	670 HV	100	Machined
[32]	AISI 8620 (1)	RB, R=-1	ϕ 6.3	1	-	0.4	860 HV	-	-
[32]	AISI 8620 (2)	RB, R=-1	ϕ 6.3	1	-	1	810 HV	-	-
[32]	AISI 8620 (3)	RB, R=-1	ϕ 6.3	1	-	1.1	820 HV	-	-
[32]	AISI 8620 (4)	RB, R=-1	ϕ 6.3	1	-	1.35	810 HV	-	-
[33]	SAE 8620 (E)	RB, R=-1	ϕ 6.0	1	-	0.39	740 HV	-551	Polished

Continued on next page

Table 3.2 – Continued from previous page

Ref.	Material	Test Type*	Net section [mm ²]	K_{tn}	Notch Radius [mm]	Case Depth [mm]	Surface Hardness	Surface Res. Stress [MPa]	Surface Finishing
[34]	Steel A ^a	RB, R=-1	ϕ 5.97	1	-	1.9	62 HRC	-	Ground
[34]	Steel B ^b	RB, R=-1	ϕ 5.97	1	-	1.9	59 HRC	-	Ground
[35]	SAE 8620 (A)	RB, R=-1	ϕ 6.0	1	-	0.86	760 HV	-586	Polished
[35]	SAE 8620 (B)	RB, R=-1	ϕ 6.0	1	-	1.2	762 HV	-490	Polished
[35]	SAE 8620 (C)	RB, R=-1	ϕ 6.0	1	-	0.76	702 HV	-131	Polished
[35]	SAE 8620 (D)	RB, R=-1	ϕ 6.0	1	-	1.49	742 HV	-131	Polished
[36]	Steel C ^c	RB, R=-1	ϕ 5.97	1	-	1.3	750 HV	-	Polished
[37]	SAE8620 (F)	AX, R=0.1	ϕ 9.0	1	-	0.8	770 HV	-370	Polished
[38]	SAE5120	AX, R=0	ϕ 6.0	1.2	6	0.7	693 HV	-270 / - 430	Ground
[38]	SAE5120	AX, R=0	ϕ 6.0	1.3	4	0.7	700 HV	-270 / - 430	Ground
[38]	SAE5120	AX, R=-1	ϕ 6.0	1.2	6	0.7	693HV	-270 / - 430	Ground
[38]	SAE5120	AX,R=-1	ϕ 6.0	1.3	4	0.7	700 HV	-270 / - 430	Ground

* AX=Axial, PB=Plane Bending, RB=Rotating Bending

a 0.19% C, 0.23% Si, 0.49% Mn, 0.015% P, 0.026% S, 1.56% Cr, 1.42% Ni, 0.05% Al, 0.0019% O, 0.011% N

b 0.19% C, 0.32% Si, 0.39% Mn, 0.005% P, 0.004% S, 1.35% Cr, 3.57%Ni, 0.03% Al, 0.0012% O, 0.009% N

c 0.21% C, 0.27% Si, 0.83% Mn, 0.009% P, 0.008% S, 1.16% Cr, 0,21% Mo, 0.0019% O, 0.011% N

3.2 Literature survey

Case-hardened steels are widely used to manufacture gears, since they lead to better bending and contact fatigue performance than normal alloyed steels. This is due to the effect of case-hardening, which results in an external layer characterized by high hardness and residual compressive stresses. The hardness is beneficial especially for the enhancement of contact fatigue strength, while the residual stress are beneficial especially for bending fatigue strength. Since only the external layer of the gear teeth is altered by case-hardened treatment, the core remains tough, having good behavior under overloads.

Several works can be found in the literature concerning the fatigue behavior of case-hardened steels. Fatigue properties of case-hardened steels can significantly vary, as it was shown by Cohen *et al.* [39], who collected from the technical literature several experimental results carried out under different test conditions and on different types of specimens. Results of tests on carburized steels specimens of smooth and notched geometries under prevailing plane and rotating bending loading conditions were presented, and a significant variability of the fatigue limit was observed. Several factors, such as the microstructure of the steels, the specimens size, the load type, the residual stress state, the specimens geometry, the population of defects and the presence of intergranular oxidation were identified as the main causes of experimental scatter [24, 25]. In particular, ref [25] analyzed the statistical scatter of experimental data, since it is fundamental to derive design fatigue curves.

Several data obtained on case-hardened steel specimens are available in the technical literature. However, those relevant to plane bending tests are of primary relevance, since such tests reproduce the real working conditions of gear teeth. Three and four point or cantilever design plane bending tests are mainly carried out under load ratio close to zero $R \approx 0$, being relevant to the teeth of a drive gear. Tests presented in refs [24, 25, 27, 28, 26] were carried out on cantilever specimens with rounded corners (see Figure 3.1) to avoid edge effects during the carburization, according to an evolution of the original specimen introduced by Brugger [40]. The specimens were characterized by a net-section stress concentration factor equal to $K_{tn} = 1.3$ and surfaces were chemically polished before case-hardening for all the considered specimens. All specimens of refs [24, 25, 27, 28, 26] were gas-carburized, quenched and then tempered, but with different temperatures and holding times in order to investigate their influence on fatigue properties. The data collected are reported in Table 3.2 (along with other data presented later on in the chapter), where the steel material, case depth, surface hardness and

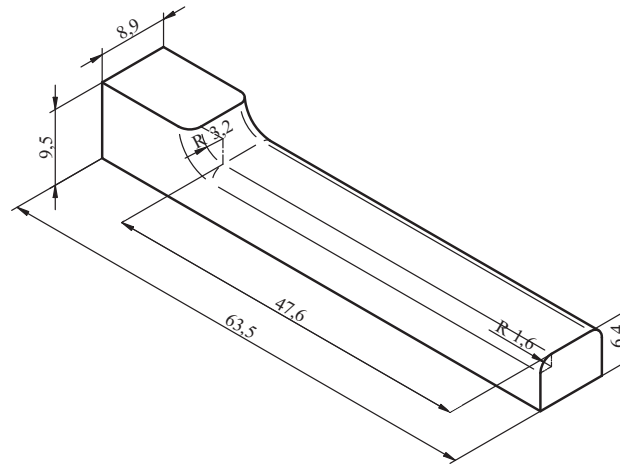


Figure 3.1: Specimen used for cantilever bending tests in [24, 25, 27, 28, 26].

surface residual stress are reported.

Additional data obtained on notched specimens were taken from [29, 30] and from [31], where in the latter case an electro-magnetic resonant machine operating at a load frequency of 70 Hz was used. The range of analyzed notch tip radii was from 0.5 to 7.62 mm. The experimental data concerning all plane bending tests taken from the literature [24, 25, 27, 28, 26, 29, 30, 31] are reported in Figure 3.2, where the net section nominal bending stress amplitude (σ_{an}) has been used to present the results. Figure 3.2 reports also four test series tested in the present work, namely A1, B1, C1 and X1, which will be considered later on in this chapter. The fatigue curves are very different since different steels, case-hardening parameters, specimen geometry and stress ratios are reported on the same chart. Except for [31], the fatigue knee is located between 50,000 to 400,000 cycles, that is at a relatively short life if compared to the fatigue curves proposed for case-hardened gears in ISO 6336 [41], where the endurance limit is set at 3,000,000 cycles. For most cases, the knee point can be clearly singled out and the statistical scatter may be very high. It should be noted that specimens taken from [31] were affected by tensile rather than compressive residual stresses and present the lowest values of the notch tip radius. In some cases [24, 25, 28, 26] the scatter on the results is very high not only in the proximity of the endurance limit, but also in the finite life region, where failures are spread almost over a whole decade. Differently from plane bending fatigue tests performed on standard servo-hydraulic machines, rotating bending tests often permit higher test frequency and therefore a reduced time to investigate the high-cycle fatigue behavior. Test data obtained from rotating bending on gas carburized smooth

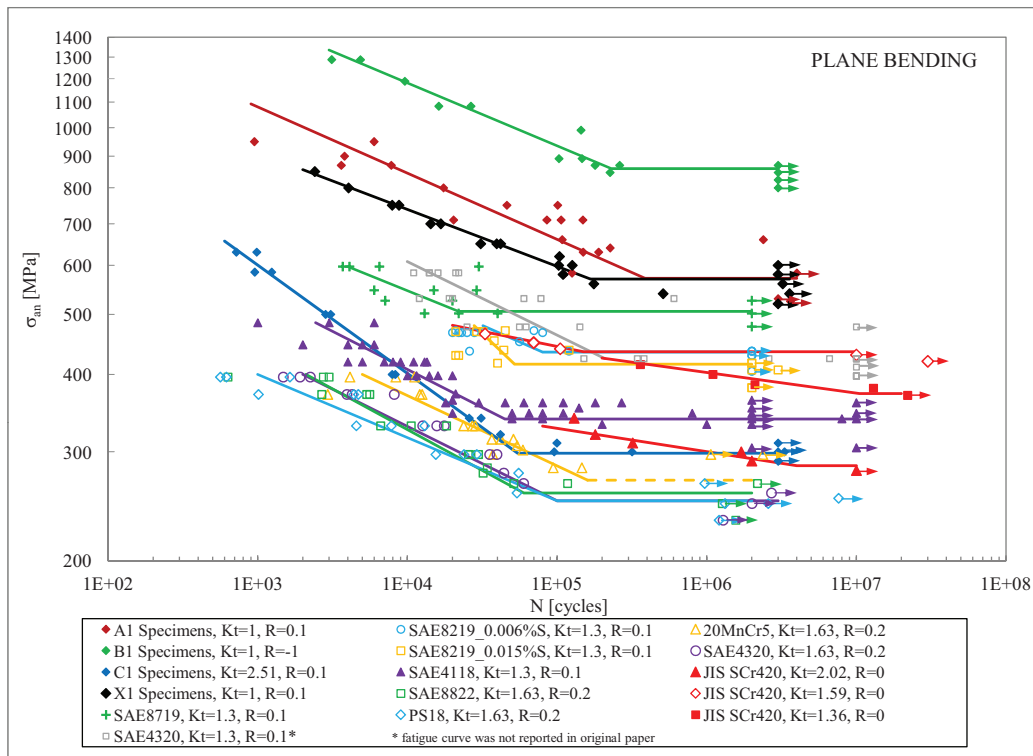


Figure 3.2: Plane bending fatigue test results on smooth and notched specimens of case-hardened gear steels.

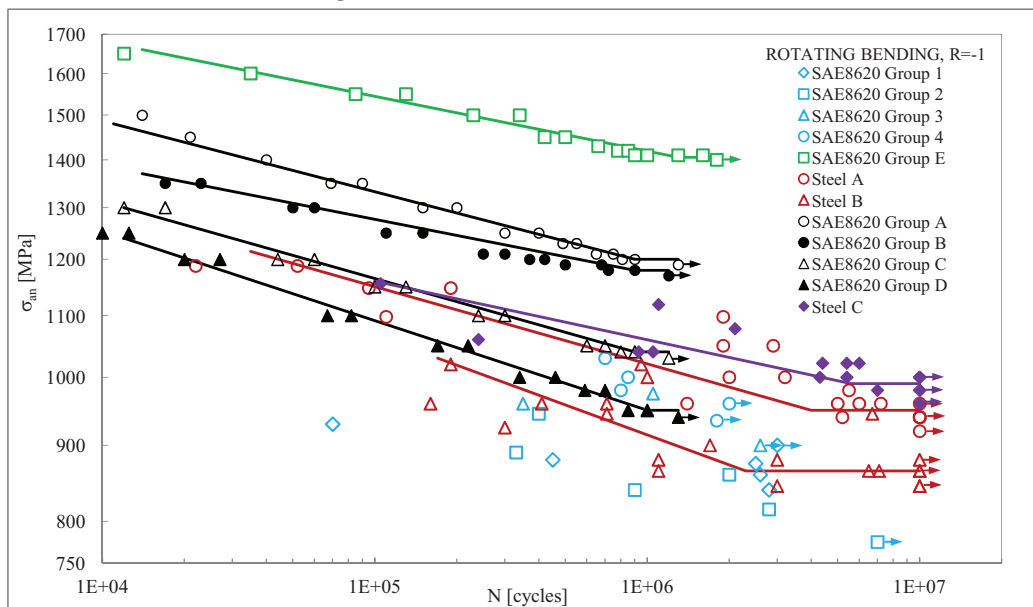


Figure 3.3: Rotating bending fatigue test results on smooth specimens of case-hardened gear steels.

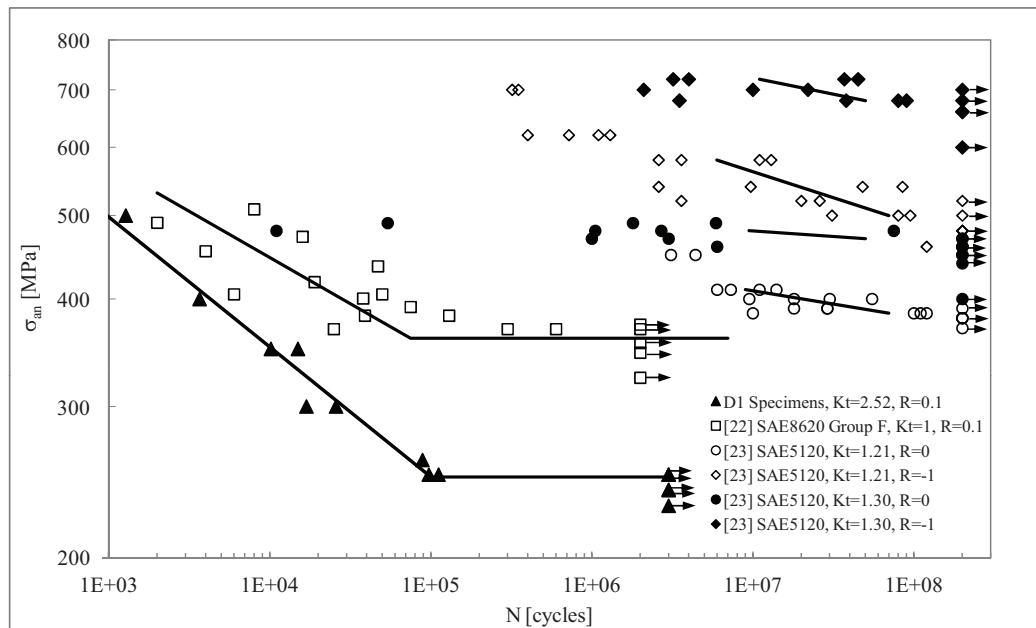


Figure 3.4: Axial fatigue test results on smooth and notched specimens of case-hardened gear steels.

specimens were taken from [32, 33, 34, 35, 36]. Details on the specimens are reported in Table 3.2, while the fatigue curves are shown in Figure 3.3. SAE 8620 data are presented for different groups of specimens characterized by different gas-carburizing parameters leading to case-depths ranging from 0.4 to 1.5 mm. It is easy to see that for rotating bending tests ($R = -1$) the curves do not show the fatigue knee in the medium cycle fatigue regime typical of the plane bending tests (see Figure 3.2), but the slope of the fatigue curves is constant up to some millions of cycles. It is interesting noting also that similar steels can exhibit very different endurance limit depending on the material state after the heat treatment process (case-depths, residual stress field, microstructure and in-depth hardness profile) [32, 33, 35]. The inverse slope of the fatigue curves was between 15 and 21 and the endurance limits ranged from 870 to 1410 MPa. According to the available test results, the scatter seems reduced as compared to that of the plane bending tests. In order to compare the bending to the axial fatigue behavior, additional sets of data were taken from the literature, relevant to plain case-hardened specimen under axial $R = 0.1$ stress ratio [37] and notched case-hardened specimens under push-pull and pulsating axial loading [38]. Details on the specimens are reported in Table 3.2, while the fatigue test results are shown in Figure 3.4 along with a set of data that will be presented later on in the

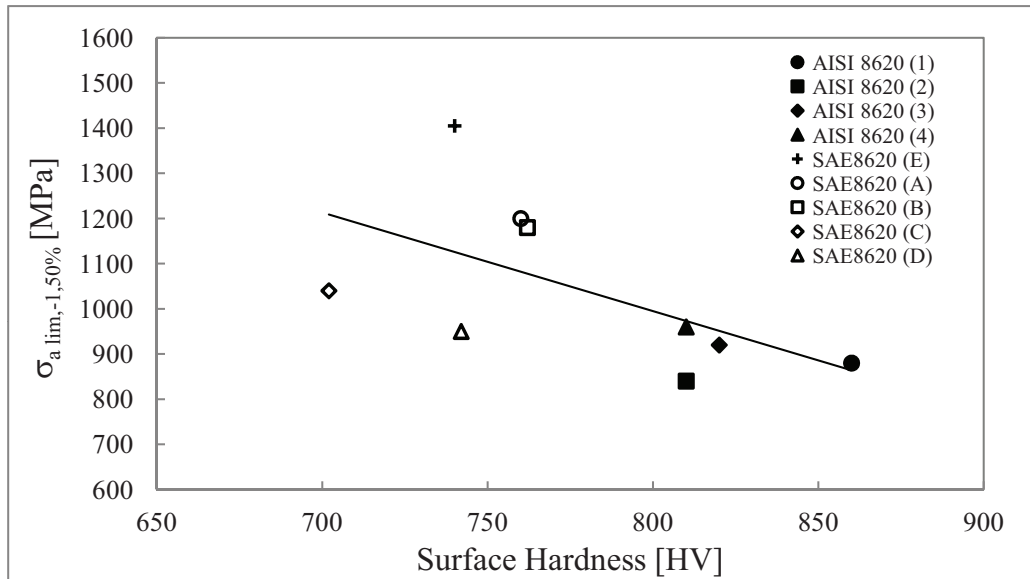


Figure 3.5: Endurance limit of case hardened steels from rotating bending tests against surface hardness.

chapter. It is seen that data published from Burkart et al. [38] showed failures in the very high cycle region, i.e. between 10 and 100 millions of cycles; such high numbers of cycles were made possible by the use of an electromagnetic resonant pulse system operating at 192 Hz. In some cases failures are distributed along a sort of horizontal band (e.g. the case $K_{tn} = 1.3$, $R = -1$ and $K_{tn} = 1.3$, $R = 0$), while in others the fatigue test results seem to follow a constant slope up to 100 millions of cycles (case $K_{tn} = 1.21$ and $R = -1$). Burkart showed that for a commercial case-hardening steel of normal cleanliness, the low cycle fatigue behavior is characterized by failures starting from the surface, while the high cycle one by failures originated from inclusions or from the internal matrix. Therefore, failure mechanism changes according to the applied stress level, being internal defects critical at long lives.

It is well known that the surface hardness can generally be beneficial for fatigue performance. However, it was shown by Burkart [38] that lower surface hardness may result in higher endurance limit. This trend is obtained also considering surface-fatigue limits reported in [32, 33, 35], as shown in Figure 3.5.

From the analyzed papers, three failure mechanisms are, generally speaking, in competition: (a) failures starting from inclusions, (b) failure starting from non-defects internal matrix crack initiation sites, typically at the interface

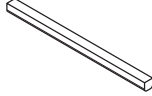

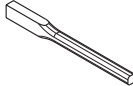
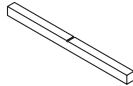
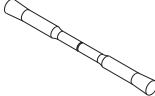
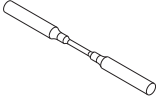
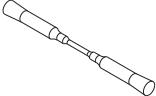
Table 3.3: Failure modes for axial fatigue tests (high cycle regime) [38].

Specimen variant	Notch radius	K_{tn}^*	Crack origin and frequency	
			$R = 0$	$R = -1$
D	6 mm	1.2	Surface: 1	Surface: 0
			Inclusions: 4	Inclusions: 5
			Non-defects: 10	Non-defects: 10
F	4 mm	1.3	Surface: 6	Surface: 2
			Inclusions: 1	Inclusions: 1
			Non-defects: 1	Non-defects: 6
* 2D ANSYS Axisymmetric analysis				

between case-hardened layer and core material, and (c) failures starting at specimen surface. The (a) failure mode depends on the statistical size distribution of inclusions in the steel. Concerning failure modes (b) and (c), Table 3.3 reports the crack initiation locations observed in axial fatigue tests of notched specimens with notch radii equal to 4 and 6 mm. Crack initiation from the surface was observed more frequently for the low than for the high notch radius. Therefore, it seems that the internal interface is weaker than the surface: if the stress field is sufficiently steep to compensate the higher strength of the surface, then initiation takes place there. A quantitative estimation can hardly be proposed because microstructure and residual stress effects are superimposed to the stress induced by the external load.

Since the fatigue behavior of case-hardened steels resulted significantly affected by the material and manufacturing process, fatigue tests on the commercial case-hardened steels used to manufacture gears of drivelines for tractors and earth-moving machines has been investigated. The purpose was to obtain useful data for gear design according to the specimen-based methods of ISO 6336. Therefore plane bending tests on smooth and notched specimens under $R = 0.1$ stress ratio constituted the major portion of the test plan. However, axial tests on notched components were also performed for comparison purposes. To complete the characterization of the steels, static tensile tests along with microstructure, hardness, residual stresses and fracture surfaces analyses were performed.

Table 3.4: Experimental test plan.

		Specimen geometry							
		A	X	B	C	D	E	ECH	
									
Manufacturing:		Ground	Machined	Machined	Ground	Ground	Machined	Ground	
Heat Treatment:		Carbur.	Carbur.	Carbur.	Carbur.	Carbur.	Un-treated	Carbur.	
#	Steel								Tot
1	20MnCr5	24	20	20	20	20	4	4	112
2	18NiCrMo5	20					4	4	28
3	19CrNi5*	20					4	4	28
4	20CrMoH*	20					4	4	28
5	EN353	20					4	4	28
6	815H17	20					4	4	28
Total:		124	20	20	20	20	24	24	252

* results are not presented in this work

3.3 Test plan

The test plan containing the number of specimens manufactured for the study of fatigue behavior of case-hardening steels is reported in Table 3.4. Each test series was identified by a code consisting of a group of letters which identifies the geometry of the specimens (A, X, B, C, D, E, ECH) and a number which indicates the steel type. Each specimen was then marked with a progressive number, separated from the previous code by ”_”. Thus, for example, A5_02 was the second specimens of the series with geometry A and made of steel 5, while ECH2_03 was the third specimen made of steel 2 of geometry ECH. Geometries A, B, C, D, X were used to perform fatigue tests, while geometries E and ECH were used for static tests. Comparative tests involving all the steels were carried out using variants A, E and ECH, while the other specimens’ variants were used to perform additional tests on steel 1 only. The type of tests carried out on the different kind of specimens are reported in Table 3.5.

3.4 Specimens

The design phase, the manufacturing process and microstructure investigations of specimens are here following reported.

3.4.1 Design of specimens

The specimens were designed first of all in order to make it possible the execution of tests using the available fatigue machines of the test laboratory of the University of Padova. The specimens were designed in order to simulate the material state of a real gear tooth, in terms of case-hardened layer, dimensions, and working conditions.

The specimens used for static tensile tests were defined following the prescriptions reported in ASTM E8 [42]. For both specimens E and ECH, calibrated diameter and gage length were assumed equal to 6 mm and 36 mm, respectively. The geometry of specimens used for static tests are reported in Figure 3.6 along with the other specimens used for fatigue tests. For ECH specimens, additional bushings made of a softer steel (C45 steel, quenched and tempered) are presented. The case-hardening treatment leads to a surface hardness of the specimens that is comparable to that one of the machine grips of the testing machine. In order to avoid slide under load and provide a surface where the machine grips can act effectively, the bushings were necessary. Exploratory tests were made on bar pieces of C45 steel that

Table 3.5: Testing conditions of the specimens.

Specimen	Steel	Surface finishing	Heat treatment	Test type
A1	20MnCr5	Ground	Case-hardened	P.B. fatigue, R=0.1
A2	18NiCrMo5	Ground	Case-hardened	P.B. fatigue, R=0.1
A5	EN 353	Ground	Case-hardened	P.B. fatigue, R=0.1
A6	815H17	Ground	Case-hardened	P.B. fatigue, R=0.1
B1	20MnCr5	Machined	Case-hardened	P.B. fatigue, R=-1
X1	20MnCr5	Machined	Case-hardened	P.B. fatigue, R=0.1
C1	20MnCr5	Ground*	Case-hardened	P.B. fatigue, R=0.1
D1	20MnCr5	Ground*	Case-hardened	AX. fatigue, R=0.1
E1	20MnCr5	Machined	Untreated	Static tensile
E2	18NiCrMo5	Machined	Untreated	Static tensile
E5	EN 353	Machined	Untreated	Static tensile
E6	815H17	Machined	Untreated	Static tensile
ECH1	20MnCr5	Ground	Case-hardened	Static tensile
ECH2	18NiCrMo5	Ground	Case-hardened	Static tensile
ECH5	EN 353	Ground	Case-hardened	Static tensile
ECH6	815H17	Ground	Case-hardened	Static tensile

P.B. = Plane Bending, AX. = axial

* only in the notch

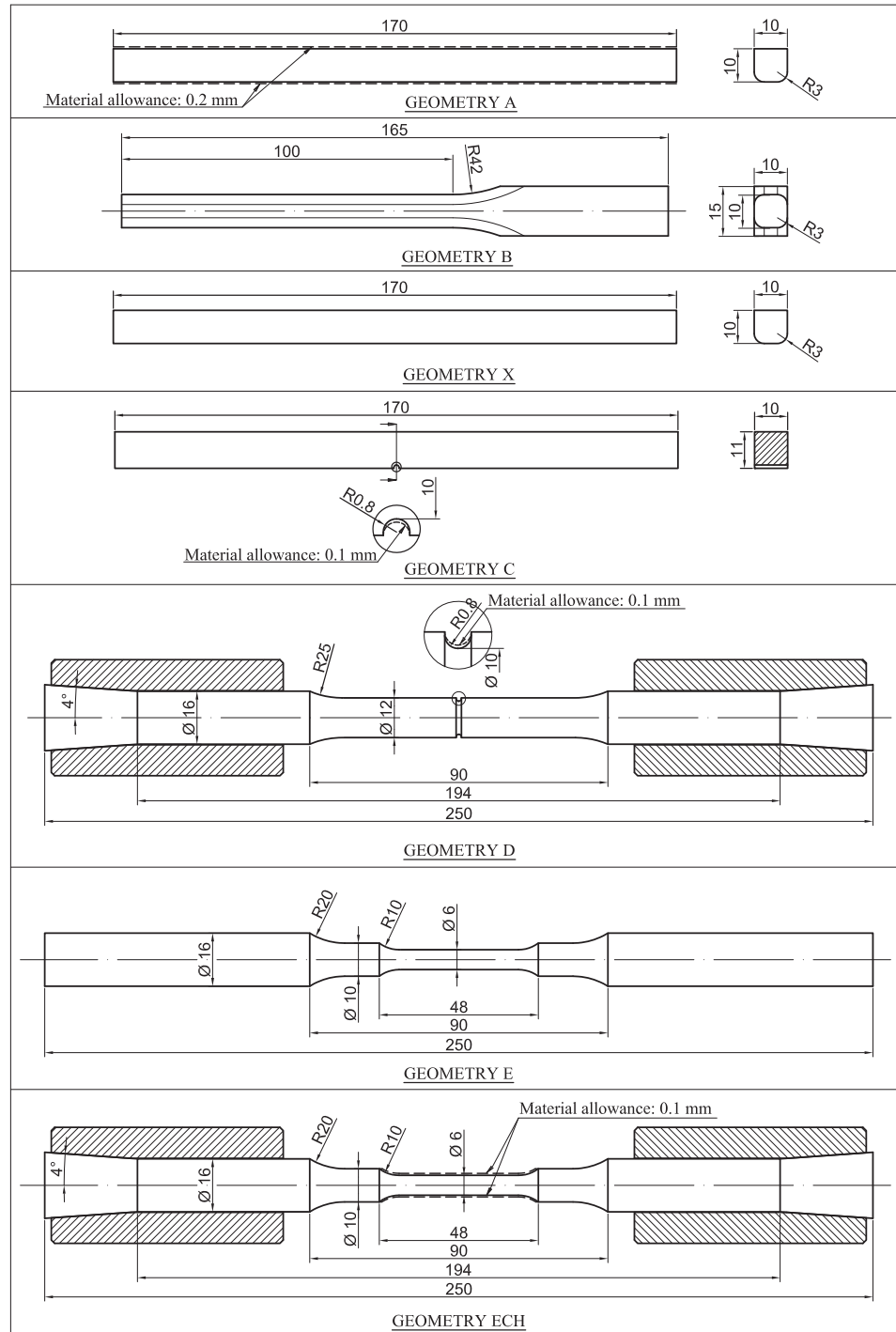


Figure 3.6: Geometries of the specimens.

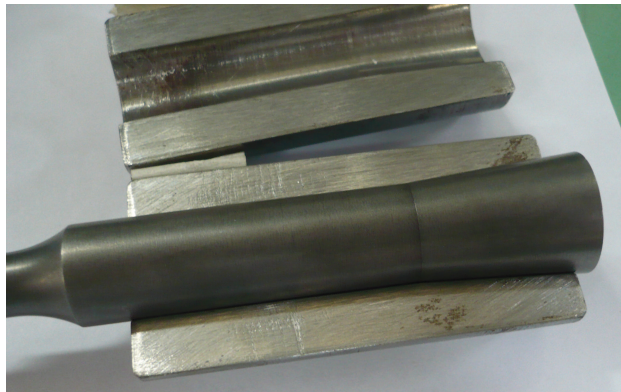


Figure 3.7: Auxiliary bushings used for tests of ECH and D specimens.

were loaded under axial static and fatigue loads. The tests showed the possibility to load cylindrical bushings statically up to 120 kN without sliding, while under fatigue loads ($R=0$) the tests were interrupted at 130 kN without showing sliding. Tested loads were enough for ensuring a correct execution of static and fatigue tests. Pressure of machine grips was set at 270 bar.

The introduction of the auxiliary bushings required tapered ends of ECH specimens. Inner profile of bushings was designed in order to match accurately the exterior profile of the specimens' ends (see Figure 3.7). The steps from the maximum diameter of the ends (minimum seizable diameter) to the calibrated 6 mm diameter were realized in order to maintain net stress concentration factors K_{tn} lower than 1.1. Calculations were made using ANSYS software [43] using 2D axisymmetric analysis, PLANE 82 elements. For case-hardened ECH specimens the calibrated area was ground by means of a grinding wheel designed specifically for this purpose. This was necessary to eliminate the slight deflections that are commonly obtained on long and thin specimens after the heat-treatment. Material allowance to be removed by grinding was of 0.2 mm.

The smooth specimens used for $R=0.1$ plane bending tests (geometries A and X, see Figure 3.6 for geometrical details) were designed in order to simulate the tooth thickness on the root circle of a gear. The height of the cross section was 10 mm, as well as the width, even if the face-width of a real gear is generally higher than this value. The same approach was used also to size the section of B specimens. It is important to notice that the corners of the cross sections of plain specimens (A, X and B) were rounded in the section side that underwent to tensile stresses under the fatigue tests. It was recognized by Cohen *et al.* [44] that sharp corners lead to lower fa-

tigue limits than rounded corners, since the carbon absorption is higher at corners than on flat surfaces. This led to different microstructure at corners after case-hardening treatment (higher amount of retained austenite) and 10% of lower fatigue limits for specimens with corners than specimens with fillets. Specimens A were ground after the case-hardening treatment on both the flat surfaces subject to maximum and minimum bending stresses, using a grinding wheel specifically designed. Material allowance was 0.2 mm. Grinding was necessary since ISO 6336 Standard [45] suggests to use polished test specimens for fatigue analysis. Grinding permitted to partly compensate the deflections of the specimens after the case-hardening treatment. Conversely to A specimens, X specimens were not ground. The purpose was to estimate in this way the surface finishing effects at fatigue limit K_l . This is an important aspect, since the tooth root fillet on gears can be either ground or not. Specimens B (for R=-1 plane bending fatigue tests) were designed in order to obtain a net stress concentration factor $K_{tn} < 1.05$ (ANSYS analysis, PLANE 82 elements, plane stress), in order to have a meaningless notch effect. A large radius (42 mm) was used in the change of section from thin to thick end, see Figure 3.6.

The notched specimens were designed in order to simulate with an easy geometry the notch effect of a tooth root fillet of a typical gear used in typical applications of the Company. A notch tip radius of 0.8 mm was adopted, for both C and D specimens (see Figure 3.6). The notch was firstly machined on the specimens, and then was finished by means of a grinding wheel specifically designed, in order to ensure a regular profile of the notch shape by removing a material allowance of 0.1 mm. Net section was maintained 10 mm x 10 mm like the plain A and X specimens. On specimens C, the net stress concentration factor K_{tn} using a 2D plane stress analysis (ANSYS, PLANE 183 elements) resulted $K_{tn,2D} = 2.52$, while using a 3D analysis (ANSYS, SOLID 186 elements) it resulted $K_{tn,3D} = 2.58$, as shown in Figure 3.8. For the 3D model, the maximum K_{tn} was located off-center along the width of the specimen, see Figure 3.9.

The notched axial specimens D were designed in order to obtain the same K_{tn} of specimen C. A series of 2D FE analysis (PLANE 82 axisymmetric elements) was performed in order to define the geometry of D specimens, maintaining a net section diameter of 10 mm. The final geometry obtained with FE analyses is reported in Figure 3.6 ($K_{tn} = 2.52$).

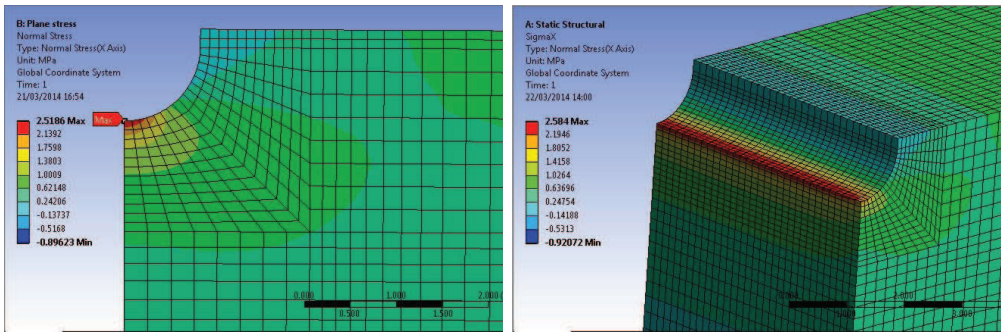


Figure 3.8: Results of 2D and 3D FE analyses of C specimen.

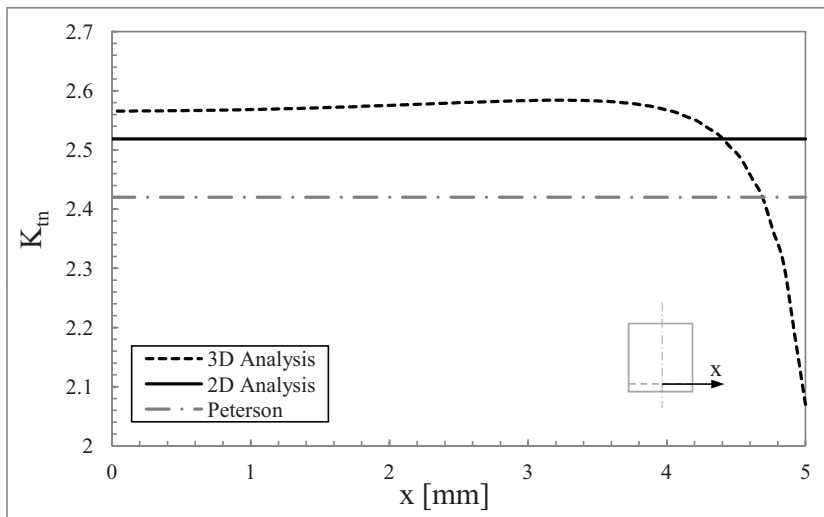


Figure 3.9: K_{tn} estimated using Peterson [46] and FE analyses.

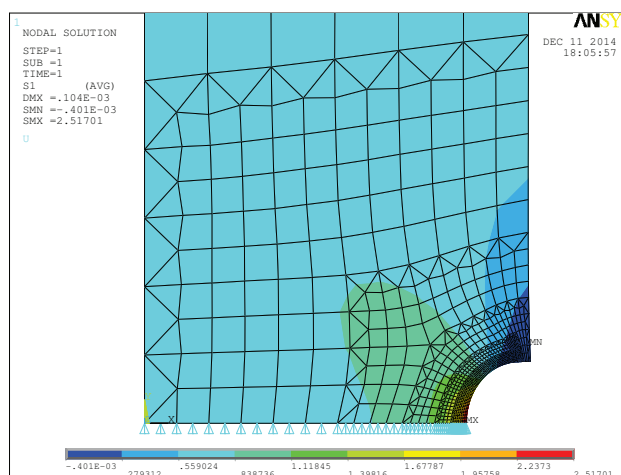


Figure 3.10: Results of 2D FE analysis of D specimen.

Table 3.6: Steel bars used to manufacture the specimens.

#	Steel	Steelworks	Section	Rolling ratio	Supply condition
1	20MnCr5	Acciaierie Bertoli Safau SpA	ϕ 70	15	Annealed
2	18NiCrMo5	Acciaierie Bertoli Safau SpA	ϕ 70	15	Annealed
5	EN 353	Shreeyam Power and steel industries limited	RCS 75	7	As rolled
6	815 H17	Aarti steels limited	RCS 75	7	As rolled

3.4.2 Manufacturing process of specimens

The specimens were obtained from hot rolled bars with the characteristics reported in Table 3.6, where also the name of steelworks are reported. In order to avoid defects located in the core and at the surface of the bars, the specimens were machined at 12.5 mm from the surface towards the core of the bars, according to prescriptions of EN 10083-1 [47] (see Figure 3.11 as an example for A specimens). After the machining process, the specimens were heat treated in order to obtain as similar as possible characteristics to those ones of a real gear of module $m = 3$ mm treated with a "Cm 7" case-hardening treatment (see Table 3.7). Before the heat treatment, the steels were controlled in order to record the chemical composition, finding the values reported in Table 3.8. On the basis of the chemical composition of the steels and the material allowance prescribed, some pilot tests were made in order to define the parameters of the case hardening process. Tests were necessary since the cross section of the specimens is significantly lower than that of a real gear. Thermal inertia was therefore smaller, and generally a weak quenching was necessary in order to avoid excessive hardness in the core of the specimens. As an example, the schematic heat treatment for A1 and X1 specimens is reported in Figure 3.12. Looking at picture, four different phases are distinguished: (1) heating in order to reach 920 °C, (2) carburization for more or less 6 hours, which consists in a first phase to increase the carbon content in the specimen surface and a second phase to stabilize this carbon content around 0.7 %, (3) quenching using thermal oil (at 120 °C) in order to avoid a strong cooling, and (4) tempering for two hours at 165 °C. Once the specimens were case-hardened, if required, they were ground. If grinding was not required (X1 and B1 specimens), the specimens were tested in the as-carburized conditions. Measurements of surface roughness of 10

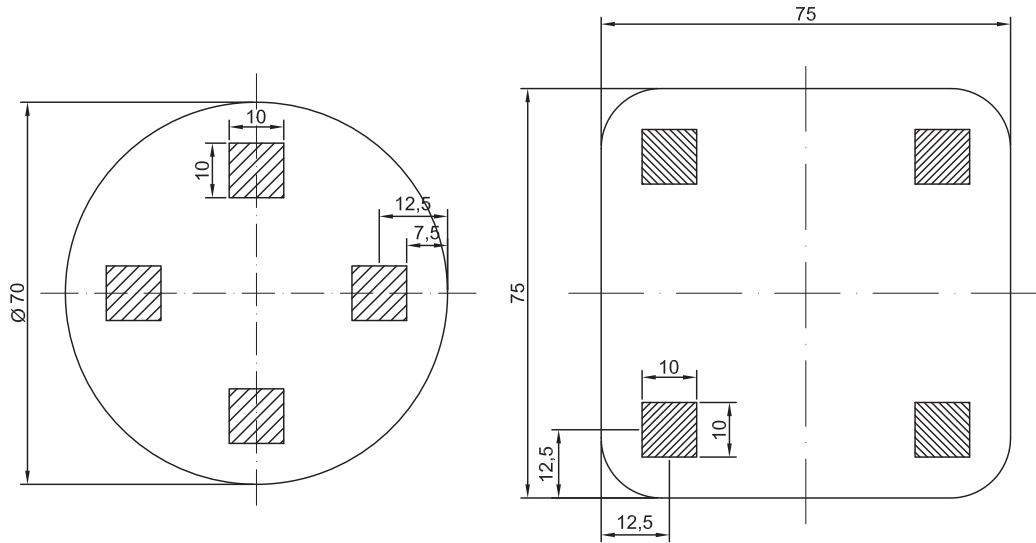


Figure 3.11: Positions of A specimens in the steel bars. On the left the case for A1 and A2 specimens, on the right the case of A5 and A6 specimens.

Table 3.7: Cm 7 case-hardening parameters on a gear ($m = 3$ mm).

Surface hardness	58÷62 HRC
Case-hardening depth	0.6÷0.8 mm
Hardness at case-depth	52 HRC
Tooth core hardness	36÷42 HRC
Tooth core strength	1150÷1300 MPa
Max retained austenite	20%

ground A1 and 10 machined as-carburized specimens were made, as reported in Table 3.9. Ground specimens exhibited a surface roughness of $R_z = 2.28 \pm 0.44 \mu\text{m}$ (mean value and standard deviation), while for machined as-carburized ones $R_z = 8.11 \pm 1.83 \mu\text{m}$. It is suitable using peak-wally roughness R_z to characterize surface finishing, since ISO 6336 [45] is based on it ².

3.4.3 Microstructure of steels

Some micrographs of the tested steels taken from A specimens are reported in Figures from 3.13 to 3.16. The micrographs were obtained by etching polished samples with Nital 4%. Case-hardening followed by quench-

²Experimental results show that $R_z/R_a \approx 6 \div 6.3$, that is in good agreement with prescriptions reported in ISO 6336-1 [6].

Table 3.8: Chemical compositions of the tested steels (percentage values).

Steel	C	Si	Mn	Ni	Cr	Mo	P	S	Cu	Al
1	0.20	0.21	1.23	0.12	1.17	0.03	0.010	0.024	0.20	0.024
2	0.20	0.24	0.81	1.32	0.94	0.19	0.010	0.021	0.17	0.020
5	0.20	0.27	0.83	1.06	1.10	0.18	0.020	0.023	0.12	0.023
6	0.19	0.23	0.84	1.29	1.17	0.18	0.020	0.013	0.20	0.029

Table 3.9: Surface roughness measured on specimens A1 and X1.

Specimen	R_a	R_z	Specimen	R_a	R_z
A1_02	0.2344	1.3138	X1_02	0.7282	5.9193
A1_04	0.3521	2.1385	X1_04	1.2196	8.6983
A1_05	0.4189	2.3895	X1_05	1.3082	7.6999
A1_06	0.3883	2.3157	X1_06	1.2183	8.0648
A1_08	0.3583	2.3576	X1_08	1.6679	9.2749
A1_09	0.3437	2.2158	X1_09	1.3436	9.1785
A1_10	0.3760	2.4804	X1_10	1.7632	11.2579
A1_11	0.5257	3.1994	X1_12	0.7478	4.3859
A1_12	0.3050	1.9928	X1_13	1.3812	7.4300
A1_14	0.3260	2.3627	X1_14	2.0837	9.2392
Mean	0.36	2.28	Mean	1.35	8.11
St. Dev.	0.07	0.44	St. Dev.	0.40	1.83

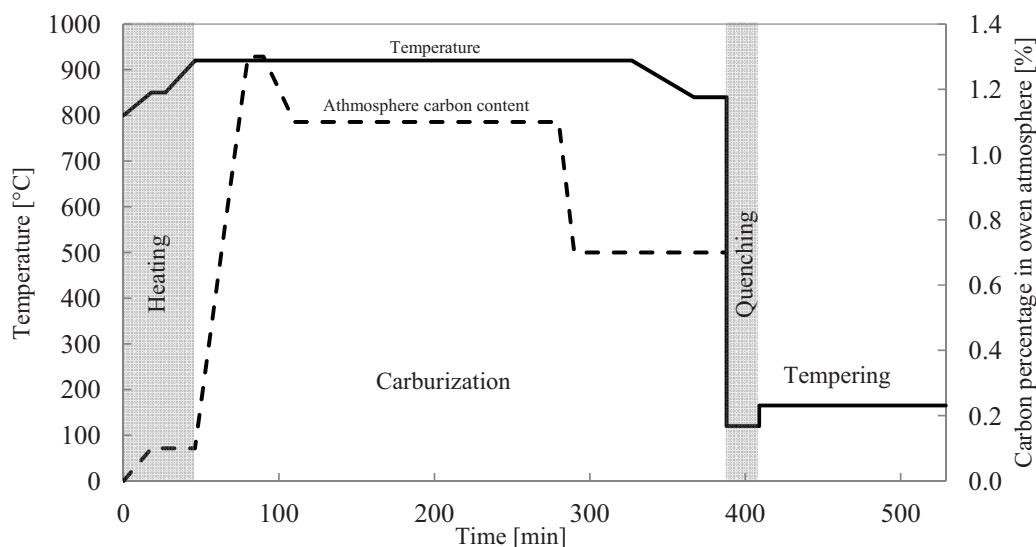


Figure 3.12: Schematic heat treatment of A1 specimens.

ing and tempering led to an external layer characterized by fine martensite and retained austenite, and to presence of Low Carbon Martensite (LCM) structure in the core of the specimens. The high level of carbon reached at the surface led to High Carbon Martensite (HCM) after quenching. Since the thermal gradient was very high at the surface, very fine martensite was obtained in the case-hardened layer. Moving towards the core the structure becomes slightly coarser. The difference in microstructure size was not marked, since the thickness of the specimens was limited to solely 10 mm. In the core, the presence of LCM was found along with bainite. Steels were supplied according to the prescriptions reported in Table 3.10 concerning inclusions and austenitic grain size. Inclusions were mainly sulfides, that were found to be elongated according to lamination direction, as shown in Figure 3.17, where a couple of examples for steels 5 and 6 are reported.

3.4.4 Micro-hardness profiles

The micro-hardness profiles from the surface towards the core of the specimens A and X were measured. The results are reported in Figure 3.18. Measurements were made using a micro-Vickers hardness tester, by applying a load of 2 N with a dwell time of 15 seconds. Both the indentation diagonals were measured, and then the HV0.2 hardness was calculated using the

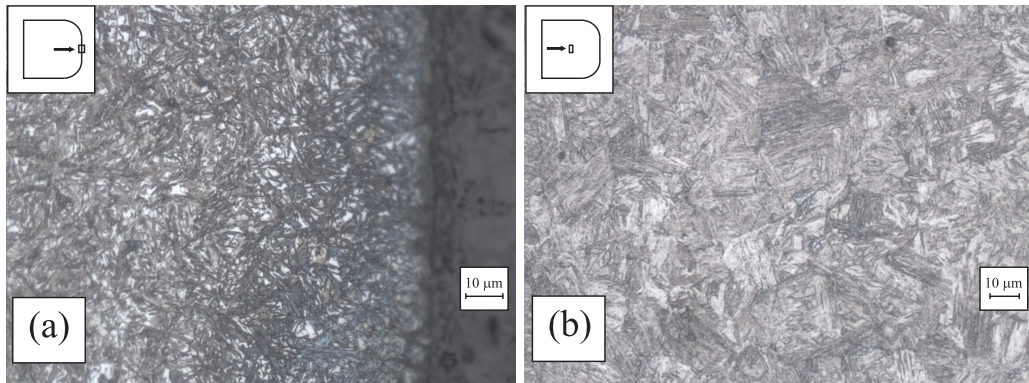


Figure 3.13: Microstructure of 20MnCr5 after case-hardening, quenching and tempering process: (a) external layer, (b) core (A1 specimens).

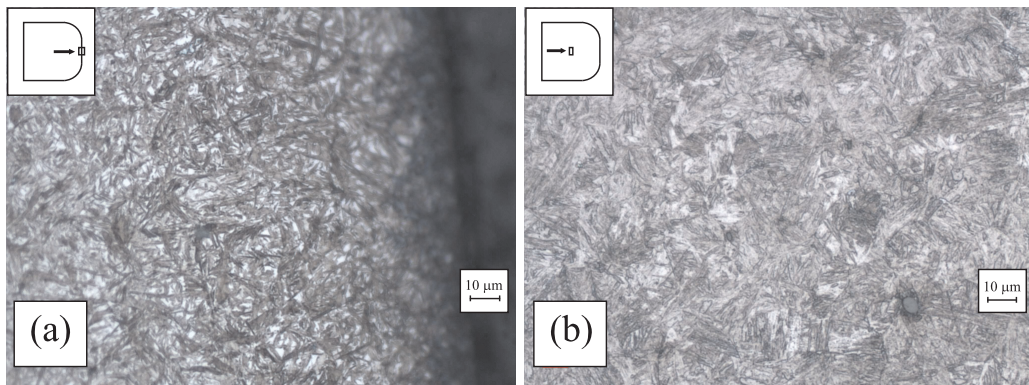


Figure 3.14: Microstructure of 18NiCrMo5 after case-hardening, quenching and tempering process: (a) external layer, (b) core (A2 specimens).

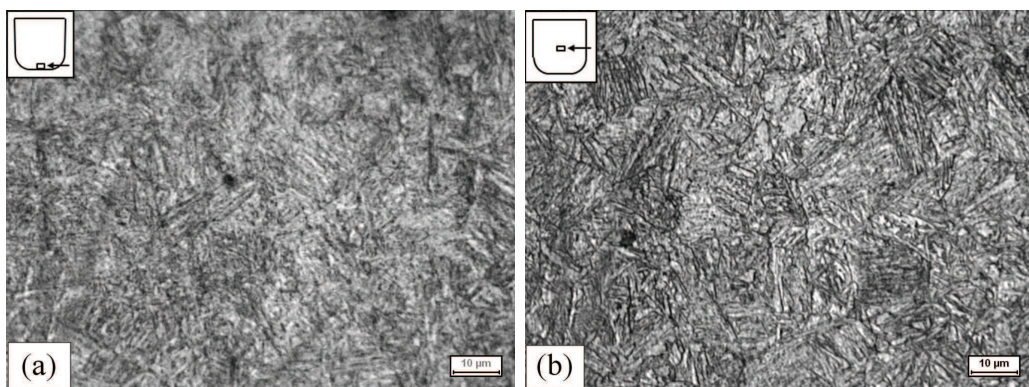


Figure 3.15: Microstructure of EN 353 after case-hardening, quenching and tempering process: (a) external layer, (b) core (A5 specimens).

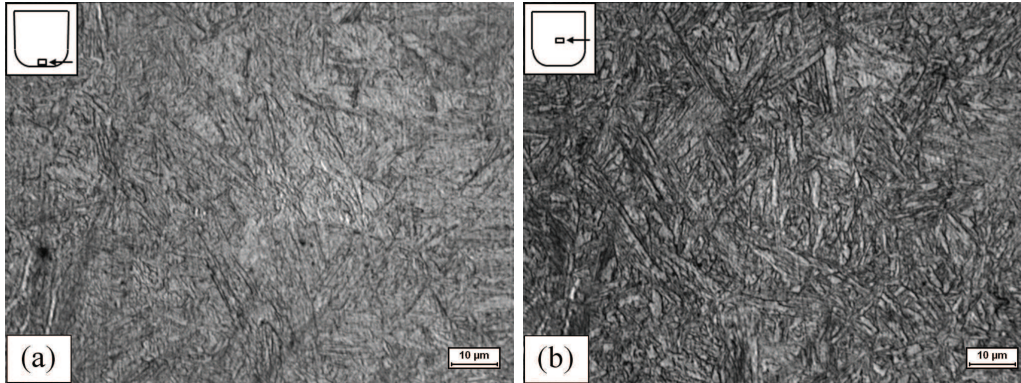


Figure 3.16: Microstructure of BS815 H17 after case-hardening, quenching and tempering process: (a) external layer, (b) core (A6 specimens).

Table 3.10: Metallurgical parameters of tested steels.

	Inclusions		Austenitic grain	
	Standard	Response	Standard	Response
20MnCr5	[48]	K4 - 0	[49]	MC QUAID: 6
18NiCrMo5	[48]	K4 - 0	[49]	MC QUAID: 6
EN 353	[50]	*	[51]	6.5/7.0
BS815 H17	[50]	*	[51]	7.5

* Inclusion rating according to ASTM E-45

	A		B		C		D	
	T	H	T	H	T	H	T	H
EN 353	2.0	-	1.5	-	1.0	-	-	1.0
BS815 H17	2.0	-	0.5	-	-	-	1.5	-

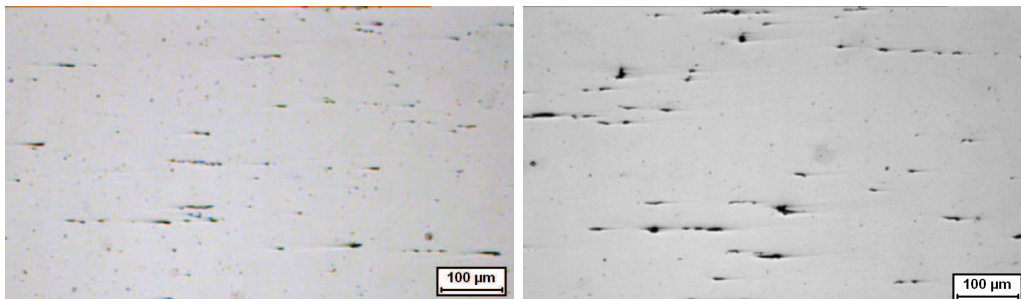


Figure 3.17: Inclusion observed for steel 5 (left) and 6 (right).

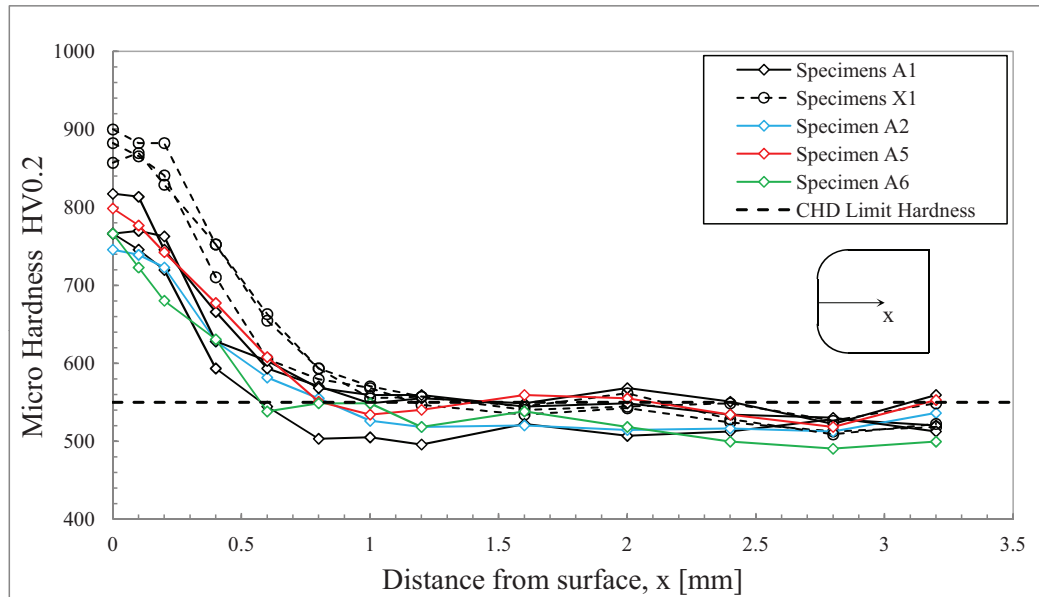


Figure 3.18: Micro-hardness profiles of specimens A and X1.

following expression:

$$HV0.2 = 0.1891 \frac{F}{d^2} \quad (3.1)$$

where F is the applied load (N) and d is the average of the two measured indentation diagonals.

As it can be seen in Figure 3.18, the surface hardness of the different steels obtained on A specimens is similar, being around $750 \div 820$ HV0.2. For steel 1, three hardness profiles were taken, while for the other steels only one. Moving towards the core, the hardness decreases, reaching a rather constant value at a depth of about 1 mm from the surface. It is common for case-hardened steels to define the Case-Hardened Depth (CHD) as the depth where the hardness is 550 HV [52]. It can be seen from Figure 3.18 that CHD resulted approximately in the range of $0.6 \div 1$ mm. Core hardness was actually constant and about 550 HV, thus making not clear the case-depth definition.

Looking at the hardness profiles obtained on X1 specimens, it can be seen that their surface hardness was higher than the ground specimens A. This was due to the removal of the hardest external layer by grinding. Actually, the hardness profiles of A1 and X1 specimens resulted shifted of approximately 0.2 mm, that corresponds to the material allowance removed by grinding. Furthermore, it can be seen that there was no significant difference on the scatter of the results obtained for X1 and A1 specimens. This suggest that

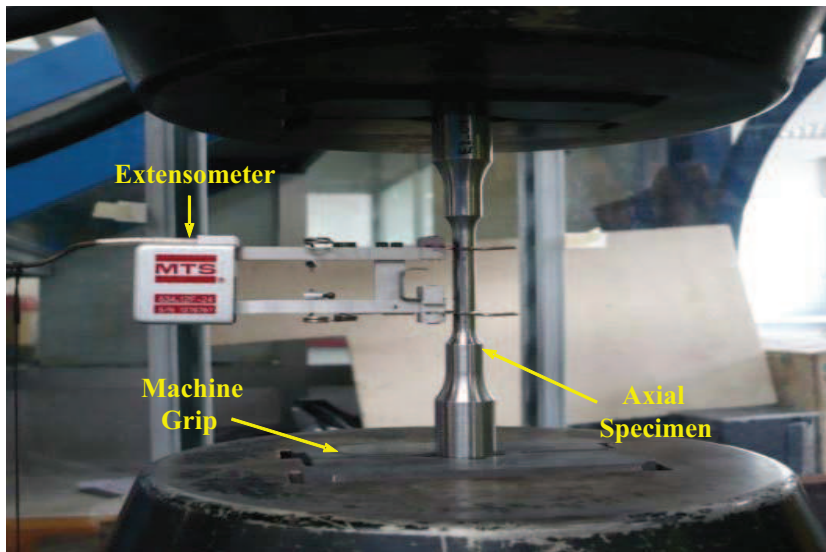


Figure 3.19: MFL axial testing machine and MTS extensometer during a static test on E1 specimens.

grinding should not have introduced scatter on material surface state. Even if a thermal oil was used to perform a weak quenching, the core hardness of the specimens resulted higher than that one prescribed for gears, being around $490 \div 550$ HV0.2, that can be roughly transformed in $48 \div 52$ HRC (higher than $36 \div 42$ HRC reported in Table 3.7).

3.5 Static tests

Experimental activity started with the execution of static tests on specimen variants E and ECH. Static tensile tests were carried out using a servo-hydraulic axial testing machine (MFL, 250 kN of load capacity) equipped of an MTS Testar IIm digital controller. During the test, a MTS extensometer (25 mm of gage length) was used to record in real time the deformations of the calibrated part of the specimens obtained by imposing a cross-head rate of 1 mm/min. A picture of the MFL machine during a tensile test is reported in Figure 3.19. For the execution of tests on ECH specimens, auxiliary bushings reported in 3.7 were necessary.

Table 3.11: Results of static tests on E and ECH specimens.

Specimen	S_u [MPa]	$S_{y,up}$ [MPa]	$S_{y,low}$ [MPa]	S_y [MPa]	$S_{p0.2}$ [MPa]	E [MPa]	A^* [%]	Z [%]
E1_01	552	316	285	308	-	201636	29.8	60
E1_04	559	316	284	312	-	201669	26.3	63
Average	556	316	285	310	-	201653	28.1	62
Deviation	5	0	1	3	-	23	2	2
E2_01	578	330	337	336	-	200987	26.8	58
E2_02	572	349	308	328	-	205957	27.6	65
E2_03	572	337	325	332	-	203867	28.6	64
Average	574	339	323	332	-	203604	27.7	62
Deviation	3	10	15	4	-	2495	1	4
E5_01	759	-	-	-	512	191948	18.2	59
E5_02	768	-	-	-	510	191330	17.8	56
E5_03	750	-	-	-	500	188017	18.8	57
Average	759	-	-	-	507	190432	18.3	57
Deviation	9	-	-	-	6	2114	1	2
E6_01	833	-	-	-	610	201816	16.8	65
E6_02	847	-	-	-	615	205201	16.3	62
E6_03	847	-	-	-	622	207796	15.7	63
Average	842	-	-	-	616	204938	16.3	64
Deviation	8	-	-	-	6	2999	1	1
ECH1_02	1649	-	-	-	1222	203658	1.32	~ 0
ECH1_03	1650	-	-	-	1169	203422	1.36	~ 0
ECH1_04	1660	-	-	-	1180	202469	1.34	~ 0
Average	1653	-	-	-	1190	203183	1.34	~ 0
Deviation	6	-	-	-	28	630	0.02	0
ECH2_01	1683	-	-	-	1215	202422	1.66	~ 0
ECH2_04	1716	-	-	-	1146	201099	1.84	~ 0
Average	1700	-	-	-	1165	201761	1.75	~ 0
Deviation	23	-	-	-	49	936	0.13	0
ECH5_01	1729	-	-	-	1165	200902	3.87	~ 0
ECH5_02	1730	-	-	-	1166	200147	3.04	~ 0
ECH5_03	1733	-	-	-	1163	199659	3.23	~ 0
Average	1731	-	-	-	1165	200236	3.38	0
Deviation	2	-	-	-	2	626	0.43	0

Continues on next page

Table 3.11 – *Continues from previous page*

Specimen	S_u [MPa]	$S_{y,up}$ [MPa]	$S_{y,low}$ [MPa]	S_y [MPa]	$S_{p0.2}$ [MPa]	E [MPa]	A^* [%]	Z [%]
ECH6_01	1678	-	-	-	1140	199648	2.07	∞ 0
ECH6_02	1675	-	-	-	1173	196702	1.8	∞ 0
ECH6_03	1724	-	-	-	1176	196201	2.29	∞ 0
Average	1692	-	-	-	1163	197517	2.05	∞ 0
Deviation	27	-	-	-	20	1862	0.25	0

* After failure.

For each type of specimen, generally three tests were performed. The sets of results were then used to calculate mean values of the following static mechanical properties (see Table 3.11):

- ultimate tensile strength S_u ;
- yield strength S_y (if the steel showed marked yielding);
- upper and lower yield stresses ($S_{y,up}$ and $S_{y,low}$ respectively);
- 0.2% offset yield strength $S_{p0.2}$ (if no marked yielding was exhibited);
- modulus of elasticity E ;
- elongation after failure A ;
- reduction of the cross section area due to necking Z ;

The curves obtained by testing the steels in their supply conditions (specimens E) are reported in Figure 3.20, where one curve for each steel is reported. The corresponding curves for case-hardened ECH specimens are reported in Figure 3.21 instead. As it can be seen from Figure 3.20, the stress-strain curves showed a marked necking accompanied by a significant reduction of the cross section area ($Z \approx 60\%$). Indian steels exhibited higher strength and lower ductility than the Italian steels. Furthermore, Indian steels did not exhibit a well-defined yielding, differently from the Italian ones. These differences were probably due to the different supply conditions of the steels, since Indian ones were as-rolled while Italian ones were annealed after rolling. After the case-hardening treatment (see Figure 3.21) S_u

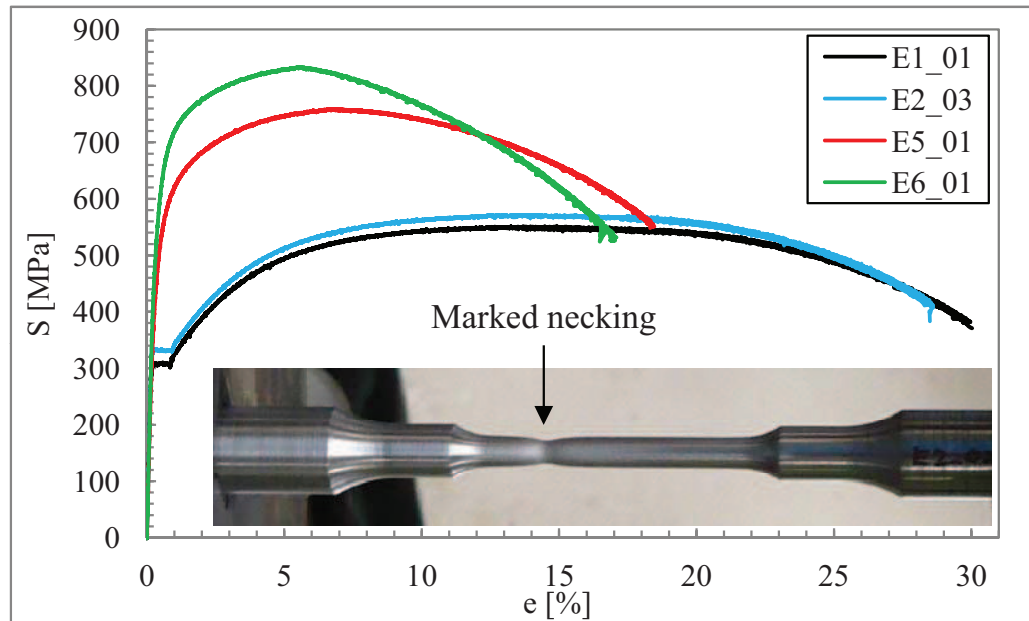


Figure 3.20: Engineering stress-strain curves for E specimens (supply conditions of steels).

resulted increased by a factor ranging from 2 to 3. The ductility was almost completely lost, since the elongation after failure was reduced from 30% to 1.4% for steel 1. ECH specimens did not exhibited necking ($Z \approx 0$), and the static curves appeared very similar for each steel investigated.

3.6 Fatigue tests

The test plan reported in Table 3.4 is constituted of several type of fatigue tests, that will be showed in the following section, focusing on the methodology, equipment, results and discussion.

3.6.1 Four point plane bending test, $R=0.1$

Most of the tests carried out to compare the different steels were performed under 4-point plane bending tests. The choice of using this test method was made in order to simulate the working conditions of a gear tooth, which is mainly subject to plane bending loads due to the action of the force transmitted by tooth contact. A generic tooth of a drive gear is subject to $R = 0$ load ratio, being unloaded when it is not meshing with the mating gears, and then (when the contact occurs) being loaded up to the

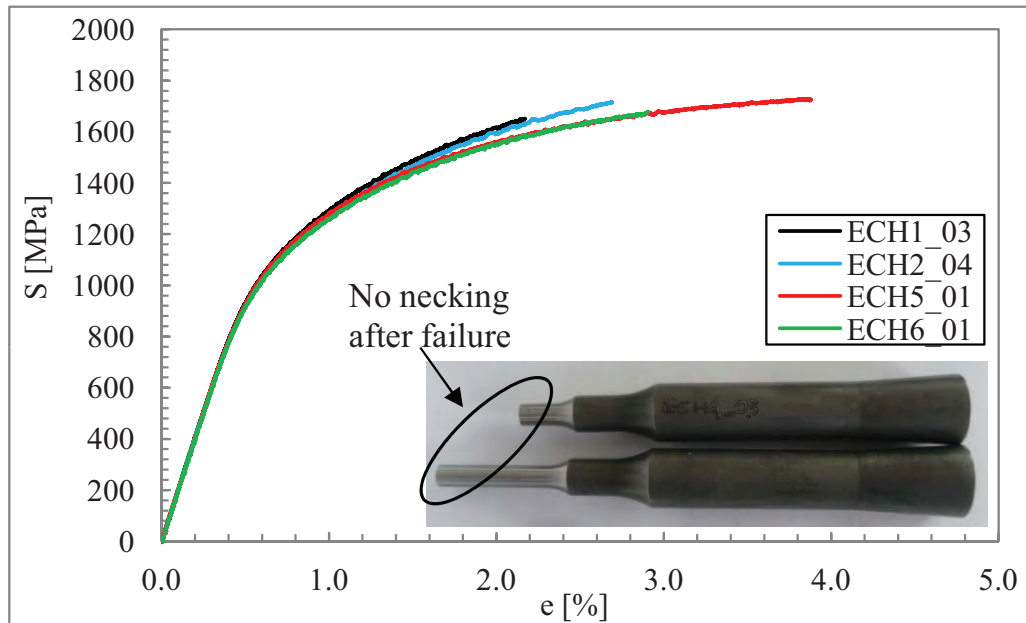


Figure 3.21: Engineering stress-strain curves for ECH specimens (case-hardened).

maximum force value.

Plane bending tests were carried out using a MTS MINIBIONIX servo-hydraulic axial machine (15 kN load capacity, MTS Testar IIIm digital controller) on A, X and C specimens. To apply bending loads, the axial machine was equipped with the equipment reported in Figure 3.22. The equipment was composed by:

- a lower and an upper beam
- reaction and loading punches
- two small forks on the specimen
- a fork for the upper beam
- a plastic pillow on the lower beam

The load was cyclically applied by the upper beam, by means of the load punches. All the punches were equipped with a roller made of quenched high-speed steel, characterized by high hardness. The load punches acted on the specimen, which was supported by the two reaction punches, in order to design a 4-point bending loading conditions which led to a maximum constant

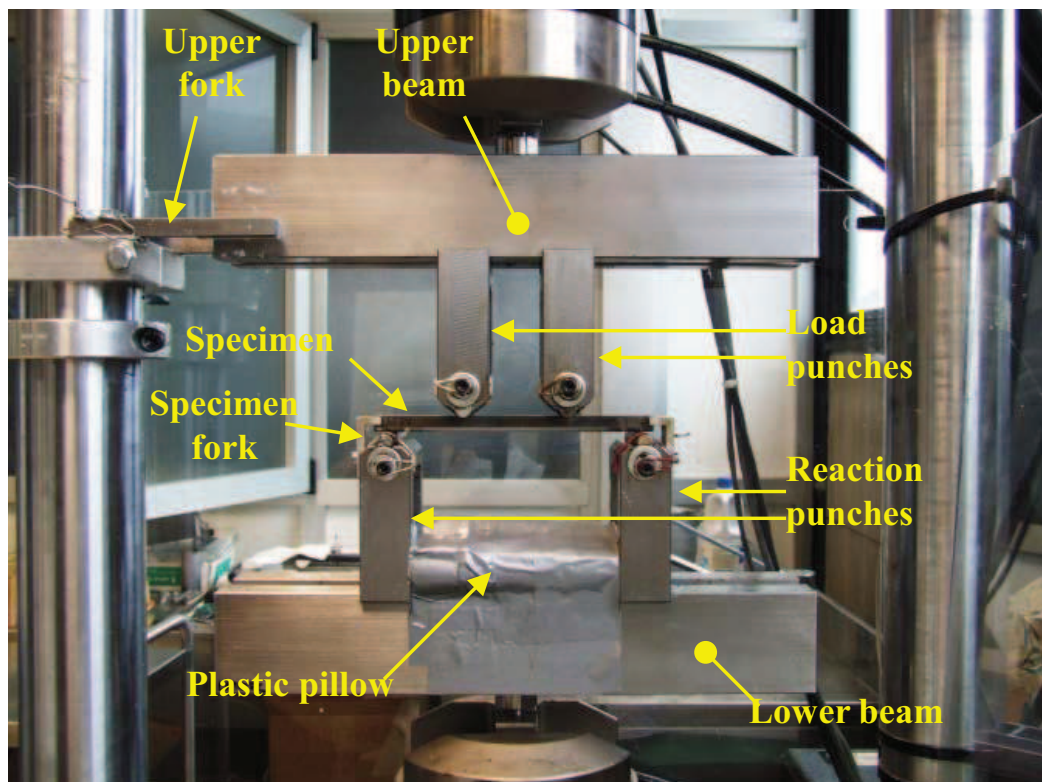


Figure 3.22: Equipment used to perform 4-point plane bending tests.

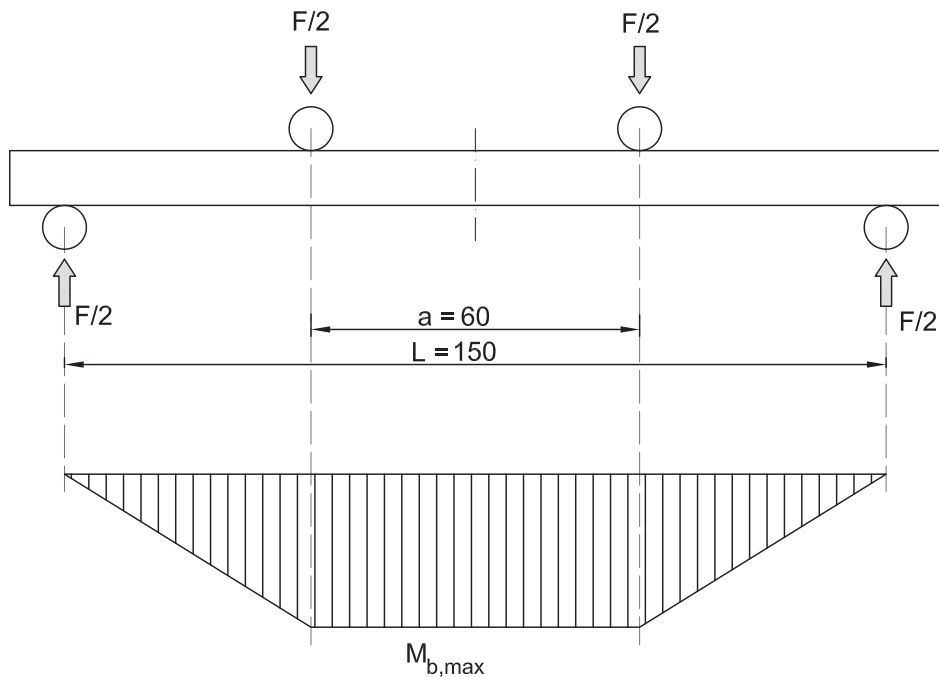


Figure 3.23: Schematic of four point plane bending tests (dimensions in mm).

bending moment $M_{b,max}$ in the portion of the specimen between the two loading punches (see Figure 3.23). The movement of the specimens on the rollers was prevented by two forks located at the ends of the specimens. To prevent the rotation of the upper beam during the load cycles, an additional fork acting on the upper beam was introduced. The fork was equipped with two Teflon inserts in order to allow the sliding between the upper beam and the fork. A plastic pillow was placed on the lower beam in order to collect the specimen after the fatigue failure. Two polycarbonate screens were used to protect the operator from being hit by the broken parts of the specimen after the fatigue failure.

The maximum bending moment for test configuration was:

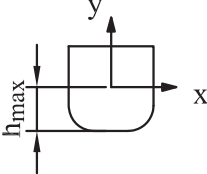
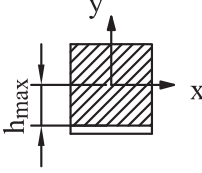
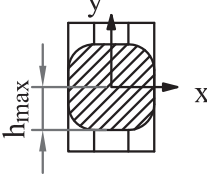
$$M_{b,max} = \frac{F}{2} \frac{L - a}{2} \quad (3.2)$$

and the corresponding bending stress:

$$\sigma = \frac{M_{b,max}}{J_{xx}} h_{max} \quad (3.3)$$

The geometrical parameters of A, X, C specimens are reported in Table 3.12, along with values of B specimens.

Table 3.12: Second moment of area and maximum height of the specimens.

Specimen	Section	J_{xx}	h_{max}
A, X		756.8 mm ⁴	5.17 mm
C		833.3 mm ⁴	5 mm
B		686.0 mm ⁴	5 mm

The heat treatment led to distortions of the specimens, since they were very long and thin. Before the tests, the deflections ($\text{Max}\Delta y$) of all the specimens were measured by means of a comparator, that was moved along the x direction of the specimens (see Figure 3.24). $\text{Max}\Delta y$ was found to be in the range of $0 \div 0.75$ mm. The most deflected A specimen was mounted on 4-point equipment, and two strain gages (see Figure 3.25) were applied on tensile fibers: one in the center of the specimen (1), and one at 15 mm of distance from it (2). Acquisitions of the two strain gages (see Figure 3.25) showed that the deformations were the same, meaning that the deflection of the specimens did not affected the execution of the tests. The details of the acquisitions are reported in [53]. Since a minimum pre-load was necessary to perform the tests, the stress ratio was fixed to $R = 0.1$. However, it was assumed that the fatigue limit (in terms of net stress amplitude σ_{an}) was practically the same for $R = 0$ and $R = 0.1$. The fatigue tests were performed at different frequencies, depending on the applied load. Test frequencies ranged from 2 Hz for high loads on specimens A to 35 Hz for load near the fatigue limit on specimens C.

The fatigue results obtained on the different specimens are reported in the Figures from 3.26 to 3.31 for specimens A1, A2, A3, A4, X1 and C1 respectively. Net stress amplitude σ_{an} was used to represent the results. In the

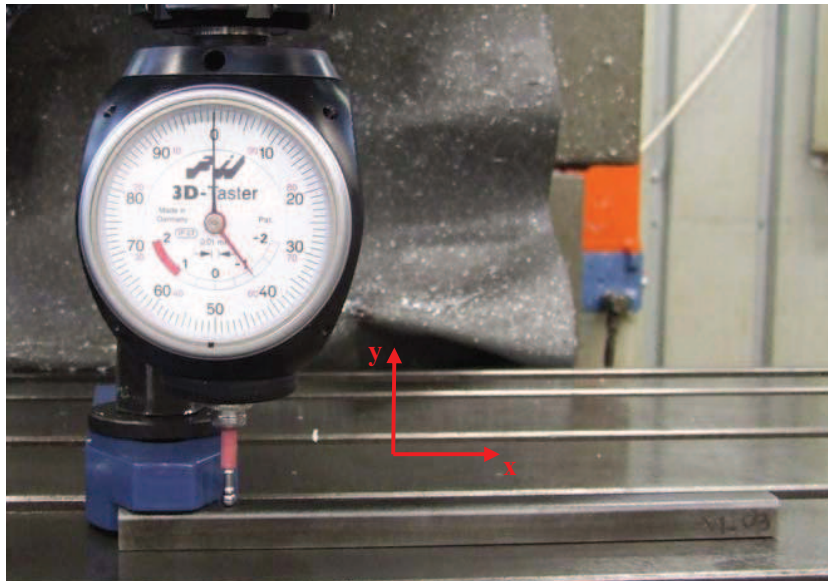


Figure 3.24: Measurement of specimens' deflections.

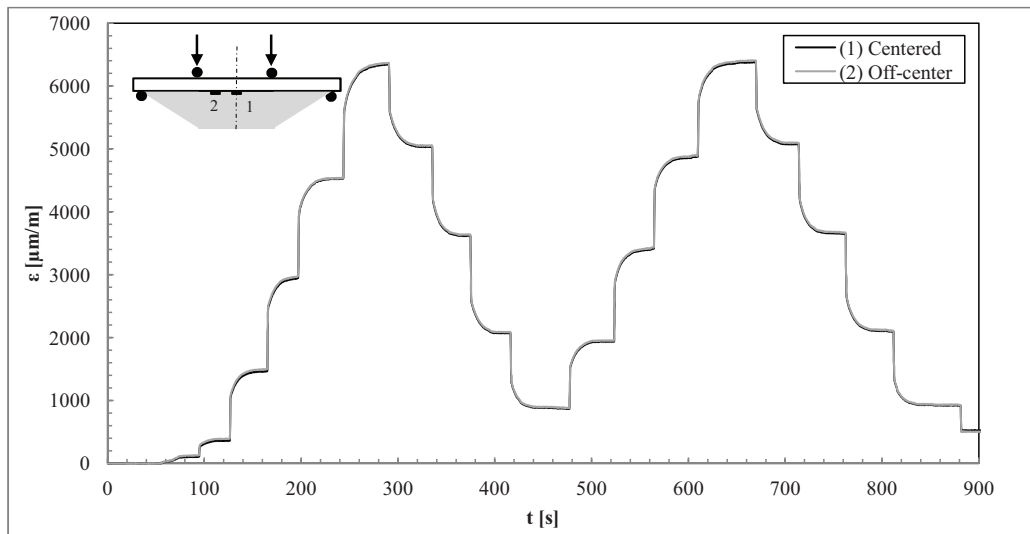


Figure 3.25: Strain gages' acquisitions on specimen A1_13: deformations are the same in the center of the specimen and off-center. Initial load was zero, then it was modified following the load sequence [kN] 0, 0.5, 2, 4, 6, 8, 6, 4, 2, 0.5, 2, 4, 6, 8, 6, 4, 2, 0.5, 0. Notice that a plastic deformation of about 500 $\mu\text{m}/\text{m}$ was recognized at the end of the test.

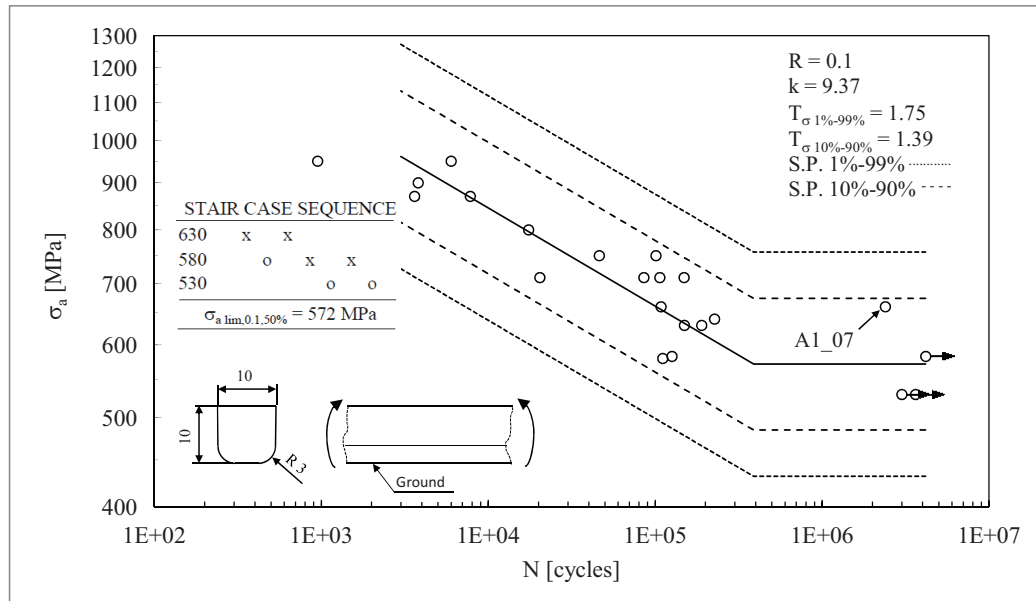


Figure 3.26: Fatigue results of A1 specimens.

figures, the curves obtained for a Survival Probability (S.P.) of 90% and 99% are also reported, along with the corresponding scatter indexes for the finite life region $T_{\sigma 10\%-90\%}$ and $T_{\sigma 1\%-99\%}$ and the inverse slope of the Wohler curve k . For the specimens made of 20MnCr5, the stair case sequence (target life 3 millions of cycle according to suggestions of ISO 6336-3) are reported. The statistical analysis of the curves was made using a software specifically developed³ (see Appendix A for the statistical basis of the approach). Looking at the fatigue curves, it is interesting to notice that the positions of the endurance knees of the plain specimens are located between 200,000 and 400,000 cycles, that is a relatively short number of cycles if compared to the 3,000,000 cycles suggested by ISO 6336-3. The endurance knee is located at a shorter number of cycles (around 50,000 cycles) for the notched C1 specimens. This is in agreement with most of the results found in the literature for plane bending and reported in Figure 3.2. However, a couple of specimens were found to fail over 1 million of cycles: specimens A1_07 and A5_02. These specimens failed from cracks originated in the subsurface, while the other specimens failed from cracks starting from the surface. This aspect will be treated in the section dedicated to the observation of the fracture surfaces. Another interesting aspect is that there is a significant scatter on the results, especially for A1 specimens. High scatter was found

³The software is described in [54].

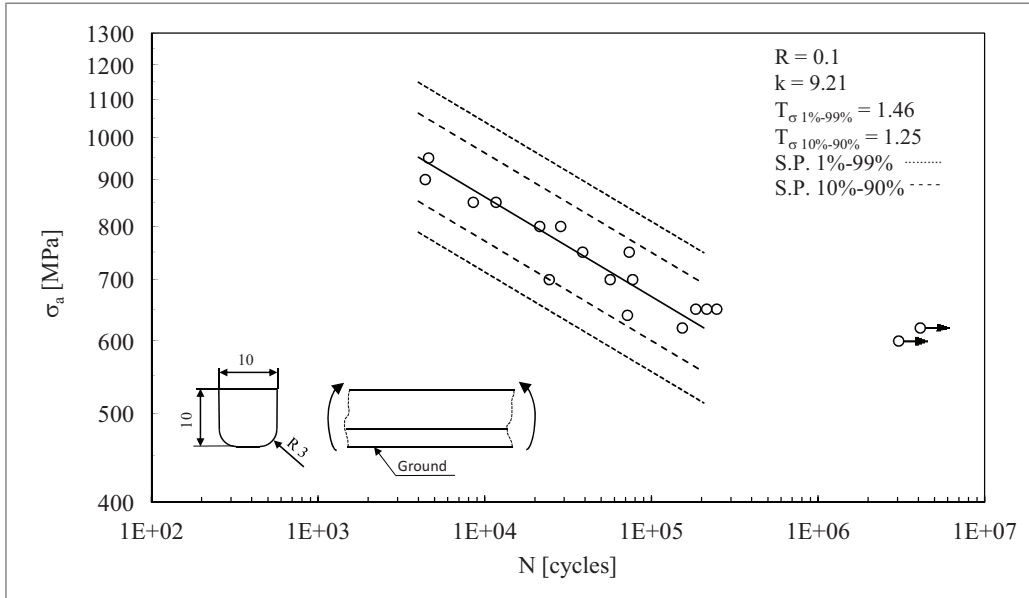


Figure 3.27: Fatigue results of A2 specimens.

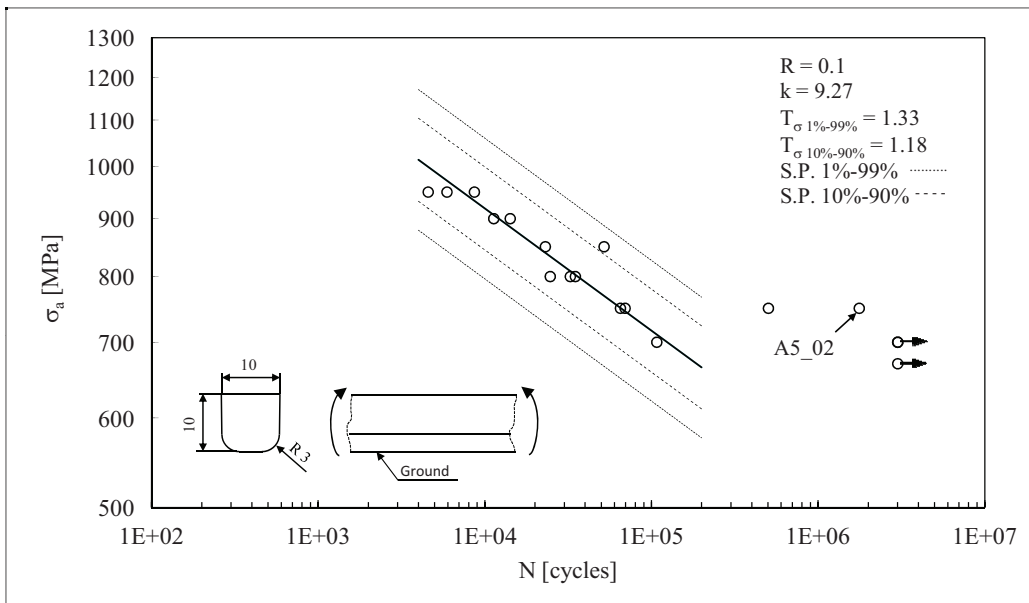


Figure 3.28: Fatigue results of A5 specimens.

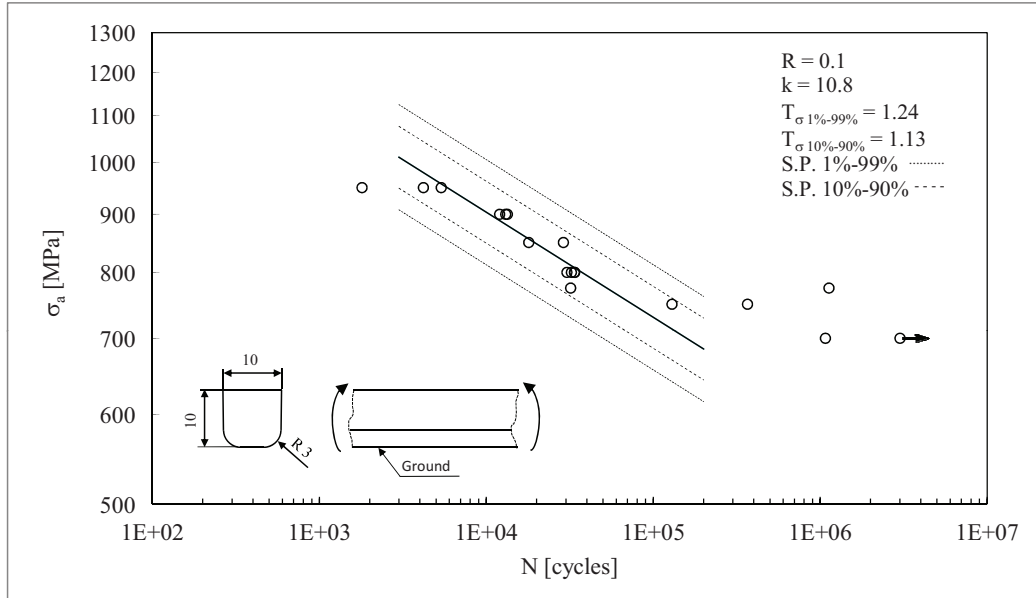


Figure 3.29: Fatigue results of A6 specimens.

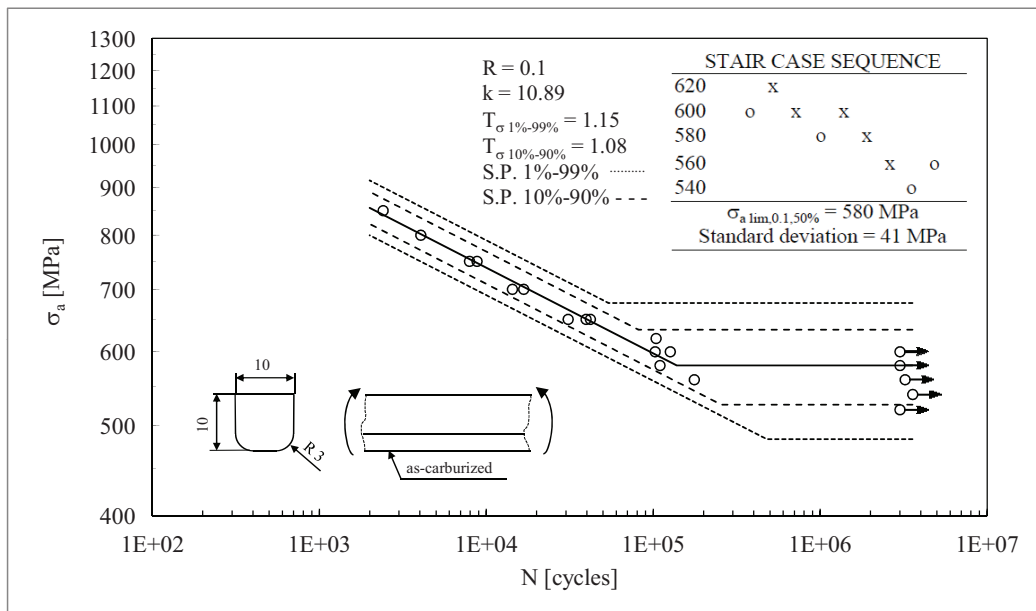


Figure 3.30: Fatigue results of X1 specimens.

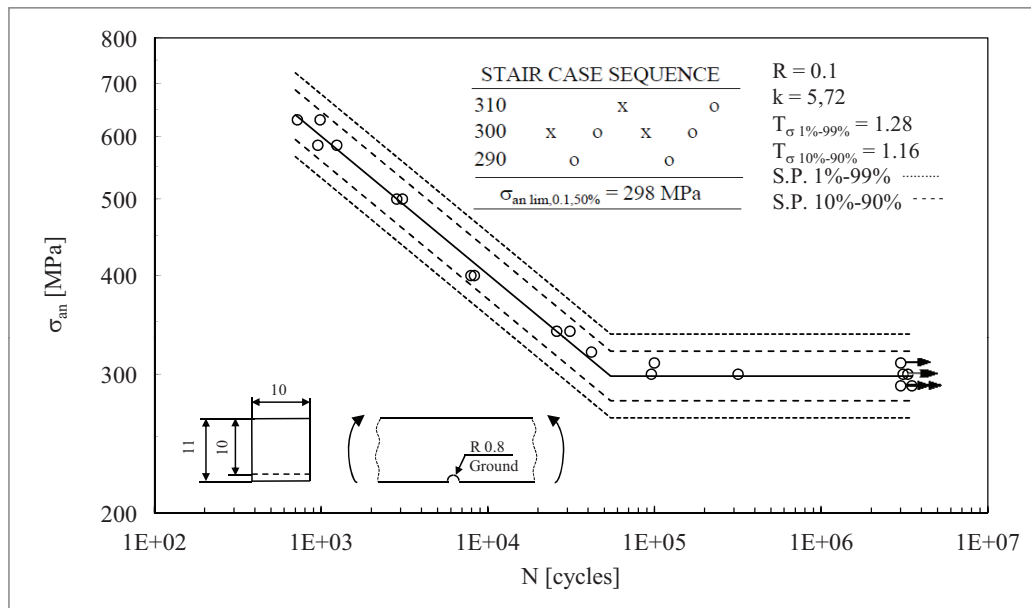


Figure 3.31: Fatigue results of C1 specimens.

also analyzing data from the literature [25]. The scatter was very high in the high-cycle region of the curves, as it is shown by the stair-case sequence of X1 specimens (Figure 3.30)⁴.

Additional dynamic acquisitions were made on A1 specimens, in order to investigate the cyclic behavior of 20MnCr5 steel during a fatigue test. Three levels of stress were investigated:

- $\sigma_a = 580 \text{ MPa}$ on specimen A1_13;
- $\sigma_a = 750 \text{ MPa}$ on specimen A1_16;
- $\sigma_a = 800 \text{ MPa}$ on specimen A1_17.

The applied force versus strain recorded during the fatigue test of A1_13 and A1_17 are reported in Figures 3.32 and 3.33, respectively. The pictures show that, during the fatigue test, the deformation increased significantly, meaning that plastic deformations took place not only at high loads but also near the fatigue limit. Near the fatigue limit the steel did not show a linear elastic hysteresis loop, at least in the range of cycles observed. The elastic modulus E remained the same during the test, but the higher the number

⁴When the stair case sequence was not sufficient to estimate the dispersion of the data according to Dixon method (see Appendix A) the dispersion of the low cycle region was extended to high-cycle region.

of cycles, the higher the minimum and maximum deformation of a load cycle. This means that even if the stress ratio remained constant and equal to $R = 0.1$, at long lives the strain ratio $R_\epsilon = \epsilon_{min}/\epsilon_{max}$ increased, as it is shown in Figure 3.34. There are perturbations of R_ϵ before 100 cycles because the desired minimum and maximum loads are reached and kept constant by the testing machine after about that number of cycles.

Hysteresis loops were not actually regular during the execution of the fatigue tests. An estimation of the energy dissipated in a load cycle could be made using the strain recorded by the strain gage and the theoretical linear elastic stress calculated from the applied load. This is not actually a precise calculation procedure, but it gives an idea and an index to measure the shape of the hysteresis loops versus the number of cycles. The plastic strain hysteresis energy density dissipated by the hysteresis loop in one cycle (W_1) versus the number of cycles is reported in Figure 3.35⁵ for specimens A1_13 and A1_17. Looking at the picture, it is not evident a well-defined trend of W_1 , since it appears particularly unstable.

3.6.2 Cantilever plane bending test, $R=-1$

On 20MnCr5 (steel 1) additional tests were made under $R = -1$ plane bending loading conditions. The idea was to simulate the fatigue behavior of the teeth of an idler gear, since they engage with the teeth of two gears during one rotation and result loaded with $R = -1$ stress ratio⁶.

The tests were carried using a MTS servo-hydraulic actuator equipped with a 15 kN load cell and a Flex Test GT 60 digital controller. A picture of the test bench is reported in Figure 3.36, where it can be seen that the actuator was fixed on the ground of the test bench and on the loaded end of the specimen by means of ball joints. This fixture mode was necessary in order to accomplish the arc-deformations described by the specimens under load, that resulted in radial forces on the actuator rod. Radial components of force may be detrimental for the seals mounted on the rod and lead to bending moments on the actuator.

A parafilm sheet was placed inside the specimen-bench clamping fixture in order to avoid fretting on the fixed end of the specimen. The use of the actuator limited sensibly the test frequency, that ranged from 4 to 9 Hz depending on the applied load.

⁵The area of the hysteresis loops was estimated using graphical integration.

⁶Actually, $R = -1$ only if the teeth of the two mating gears have the same geometry, and the two gears have the same center distances with respect to the idler gear. However, differences on these parameters are generally limited and real stress ratios are close to $R = -1$.

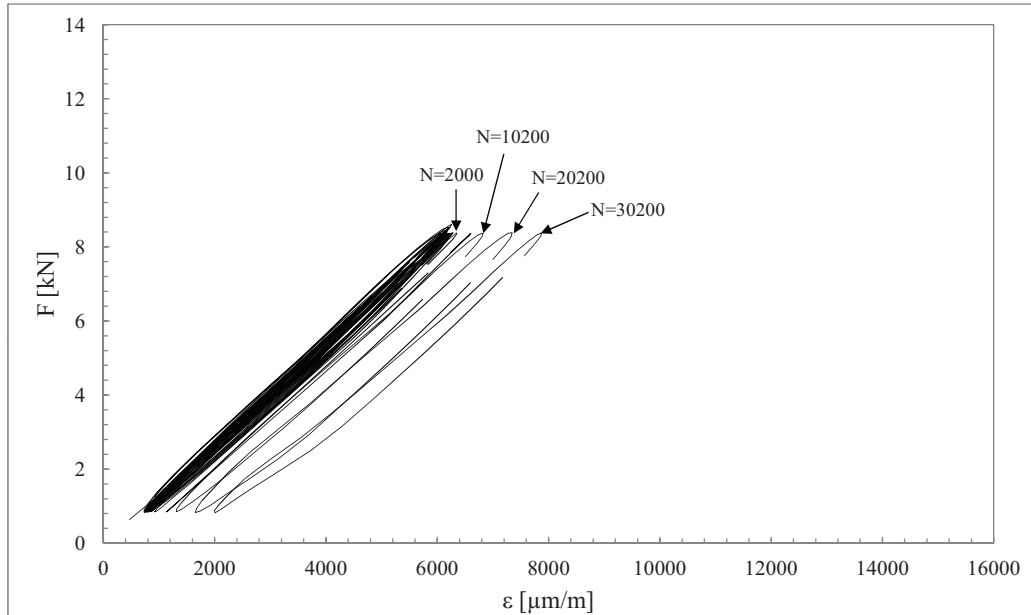


Figure 3.32: Force versus strain for A1_13 specimen for the first 30,200 cycles ($\sigma_a = 580$ MPa, failure at 110,839 cycles).

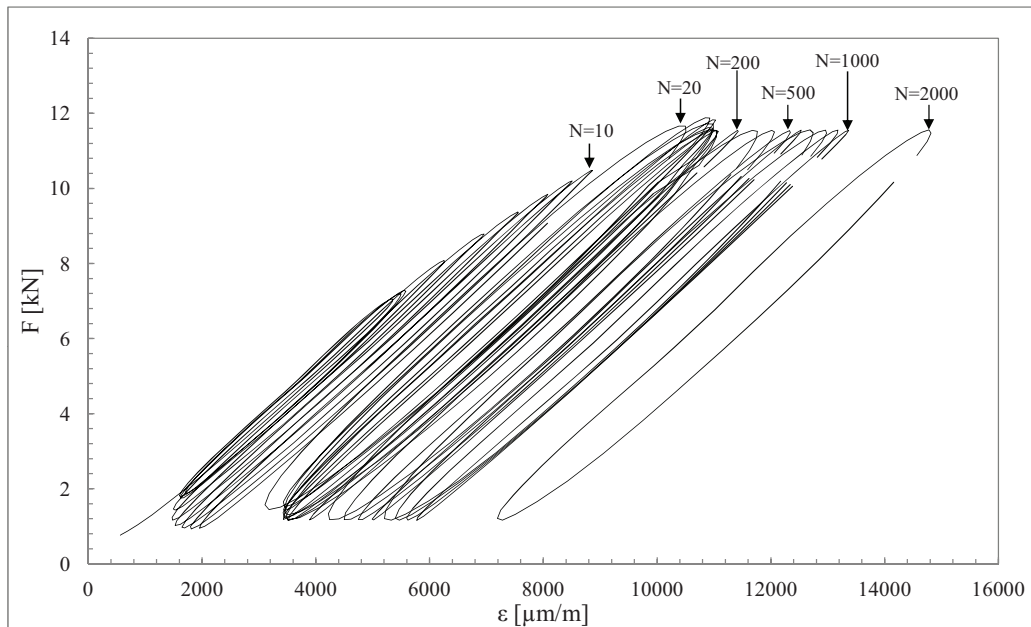


Figure 3.33: Force versus strain for A1_17 specimen for the first 2,000 cycles ($\sigma_a = 800$ MPa, failure at 17,429 cycles).

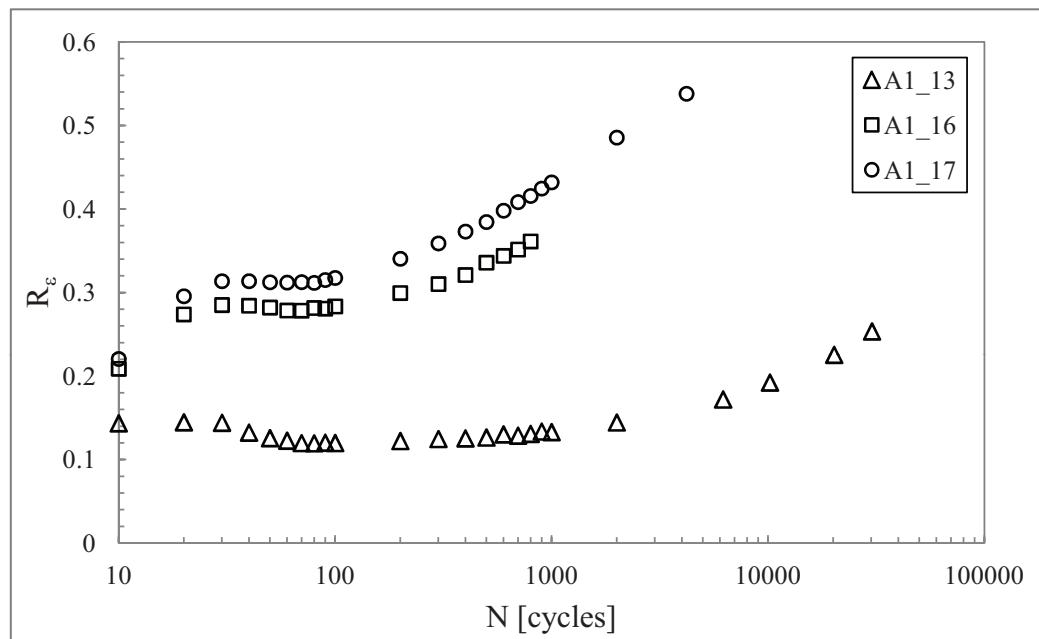


Figure 3.34: Strain ratios recorded during fatigue tests of specimens A1_13, A1_16 and A1_17.

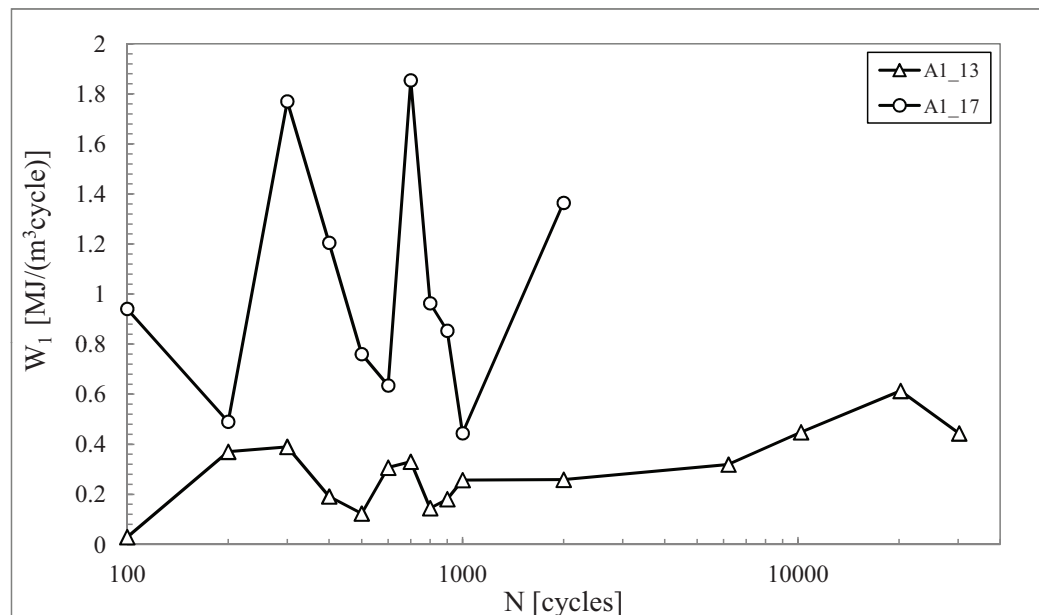


Figure 3.35: Energy dissipated in a load cycle during fatigue tests of specimens A1_13 and A1_17.

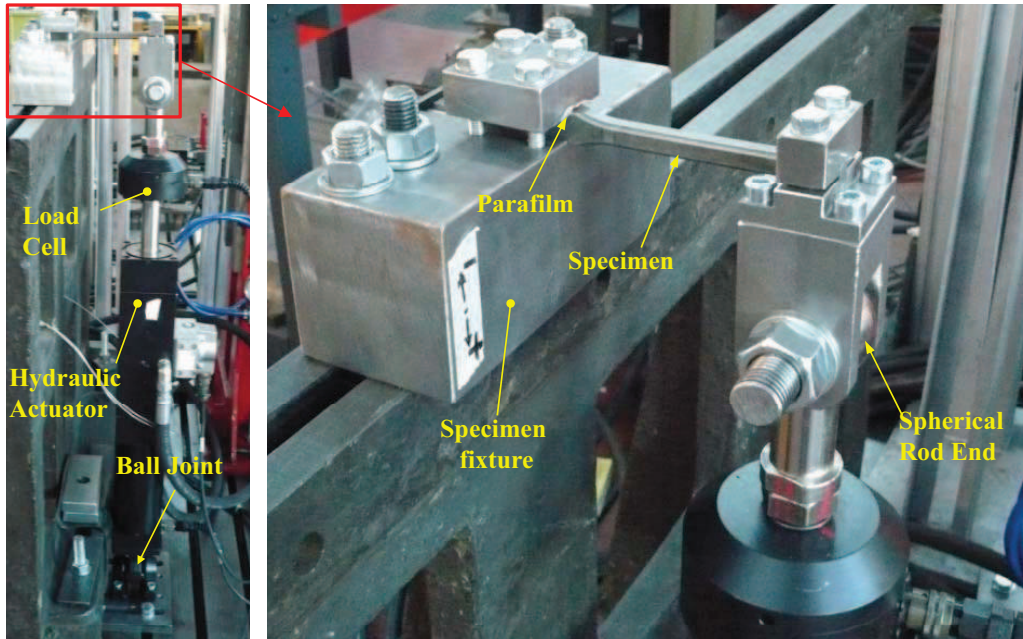


Figure 3.36: Equipment used to perform $R = -1$ plane bending tests.

The loading conditions of the test are schematically reported in Figure 3.37. The bending stress on the critical section of the specimen is:

$$\sigma = \frac{F \cdot L}{J_{xx}} h_{max} \quad (3.4)$$

where the value of the second moment of area J_{xx} and of h_{max} are reported in Table 3.12. In order to ensure that the stress on the critical section of the specimens was the desired one, a calibration of the test rig was made. For design reason, there was a distance from the loaded end of the specimen and the center of the spherical rod end of the actuator. This distance forms a bending arm b when the specimen is deformed under load, as shown in Figure 3.38, resulting in an undesired bending moment $M_{b,und}$ applied on the specimen. The higher the force applied by the actuator, the higher the deformation of the specimen and therefore the undesired bending moment. The bending moment is anticlockwise (with reference of Figure 3.38) for both pushing and pulling forces. Two strain gages were applied on the surface of a specimen: one located at 40 mm (1) from the theoretical point of application of the force, and one located on the critical section, i.e. 90 mm of distance from the force (2). Since the 20MnCr5 exhibited plastic deformation at relatively low stress levels (cfr. Figures 3.21 and 3.25), the application of strain gage 1 was necessary in order to remain in the elastic field under the

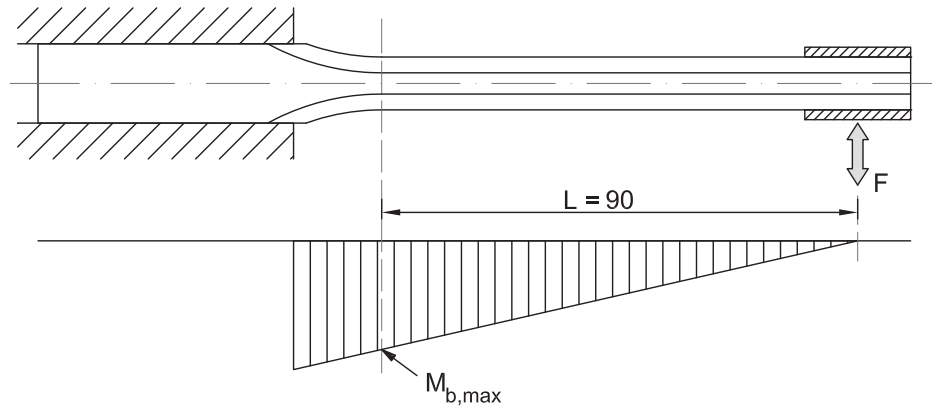


Figure 3.37: Schematic of cantilever bending tests and representation of theoretical bending moment (dimensions in mm).

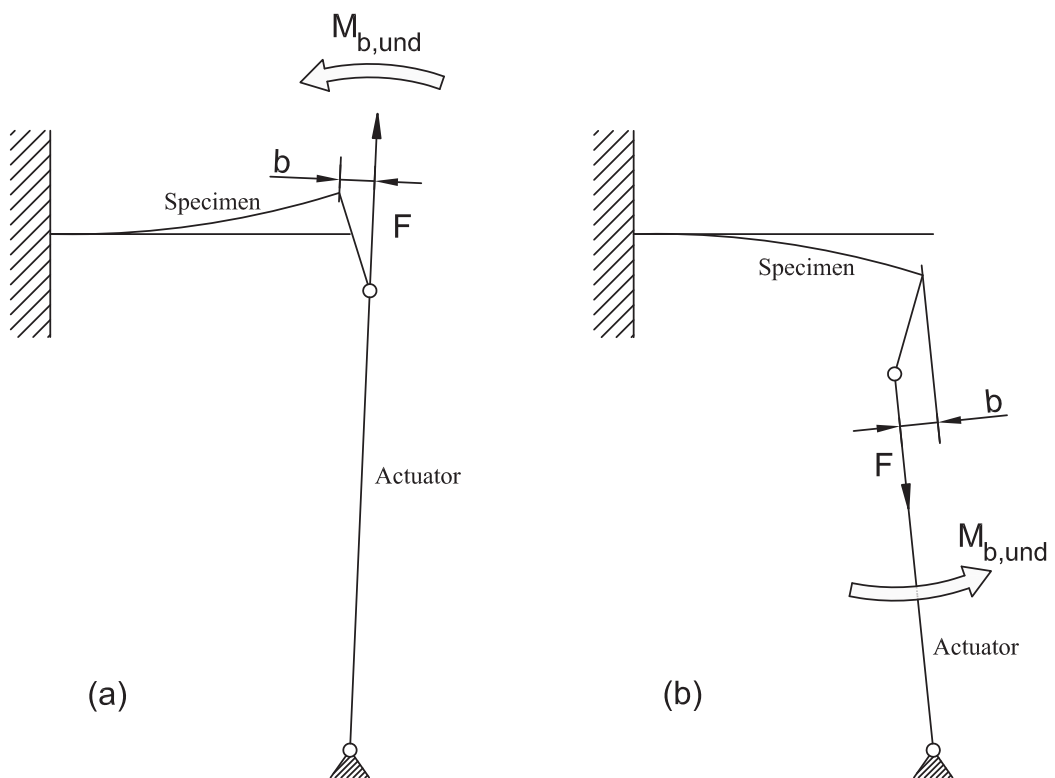


Figure 3.38: Schematic of the undesired bending moment $M_{b,und}$ on B1 cantilever specimens.

high levels of applied loads. Push and pull forces were applied increasing their value of steps of 2 kN, as shown in Figure 3.39. Between opposite values of force, the specimen was relaxed in order to investigate residual plastic deformation. From the picture, it can be seen that for load of about 1.6 kN there was a significant plastic deformation at the critical section. It can be also seen that strain gage 1 always remained in the elastic field. It can be noted that deformations obtained by applying pulling (+) forces was lower than those obtained by applying pushing (-) forces, in agreement with the effect of $M_{b,und}$.

Using the strain recorded for each applied load, it was possible to compare the true values of strains (ϵ_{1t} , ϵ_{2t}) read by the strain gages and their corresponding theoretical linear elastic values (ϵ_1 , ϵ_2)⁷. Comparison is reported in Figure 3.40, where the theoretical linear elastic strain was evaluated as:

$$\epsilon_{1,2} = \frac{FL_{1,2}}{EJ_{xx}}h_{max} \quad (3.5)$$

where $L_1 = 40$ mm and $L_2 = 90$ mm. Since only location 1 remained in the elastic field, the data recorded from strain gage 1 were used to estimate the difference (ΔM) between the real bending moment acting on the specimen and the theoretical one.

$$\Delta M = (\epsilon_{1t} - \epsilon_1) \frac{EJ_{xx}}{h_{max}} \quad (3.6)$$

ΔM evaluated in this way is composed by $M_{b,und}$ and by the clamping moment $M_{b,clamp}$ introduced when the specimen is fixed to the rod end, therefore:

$$\Delta M = M_{b,und} + M_{b,clamp} \quad (3.7)$$

ΔM is reported in Figure 3.41 and it was considered constant along the specimen, since it is a concentrated moment. The linear elastic bending stress obtained on the critical position of the specimen was therefore evaluated as:

$$\sigma_2 = \frac{(FL_2 + \Delta M)}{J_{xx}}h_{max} \quad (3.8)$$

σ_2 versus the force F applied by the actuator is reported in Figure 3.42, which constitutes the calibration curve of the test rig. Using the calibration curve, once the stress level was defined, the corresponding force to be applied during the fatigue test was automatically defined.

⁷Strain recorded for -0.2 kN was not considered in the analysis of data since the signals was not stable, see Figure 3.39.

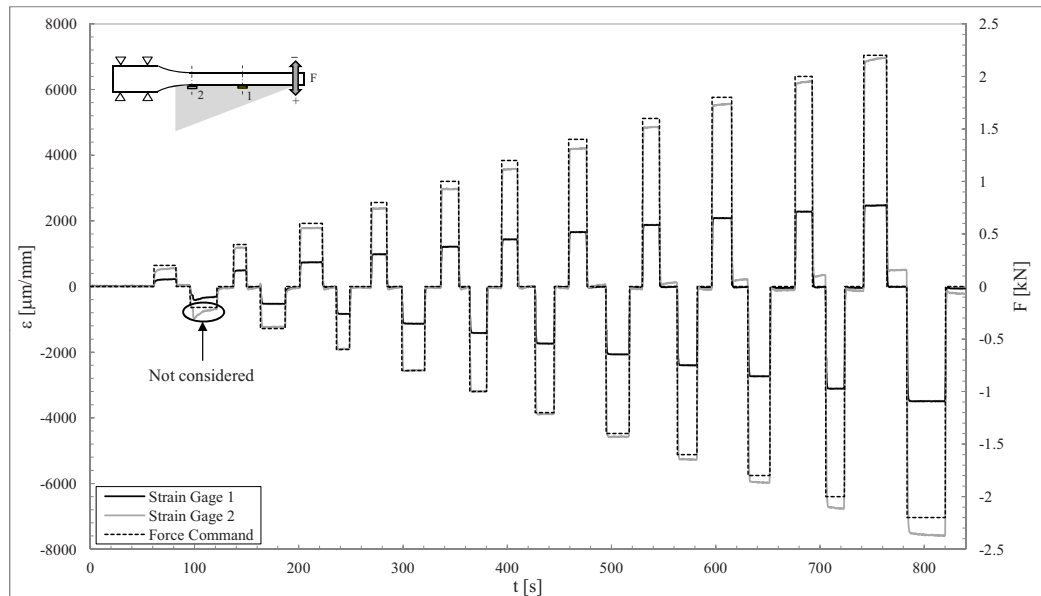


Figure 3.39: Strains under applied force command on the strain gages on a B1 specimen.

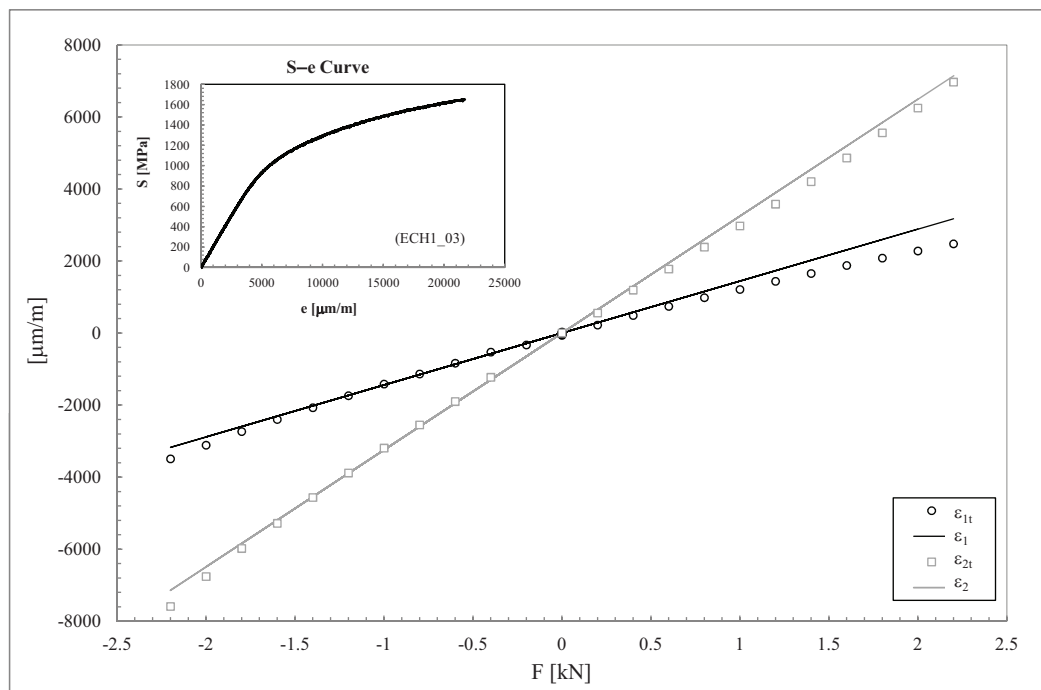


Figure 3.40: Comparison of true strain and theoretical linear elastic ones.

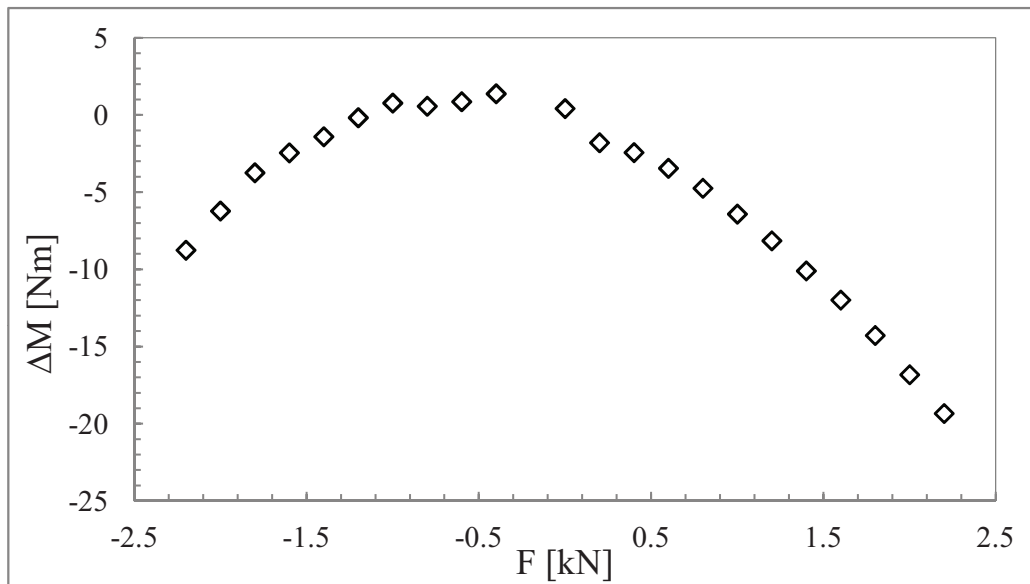


Figure 3.41: Undesired moment versus applied force acting on B1 specimens during the fatigue tests.

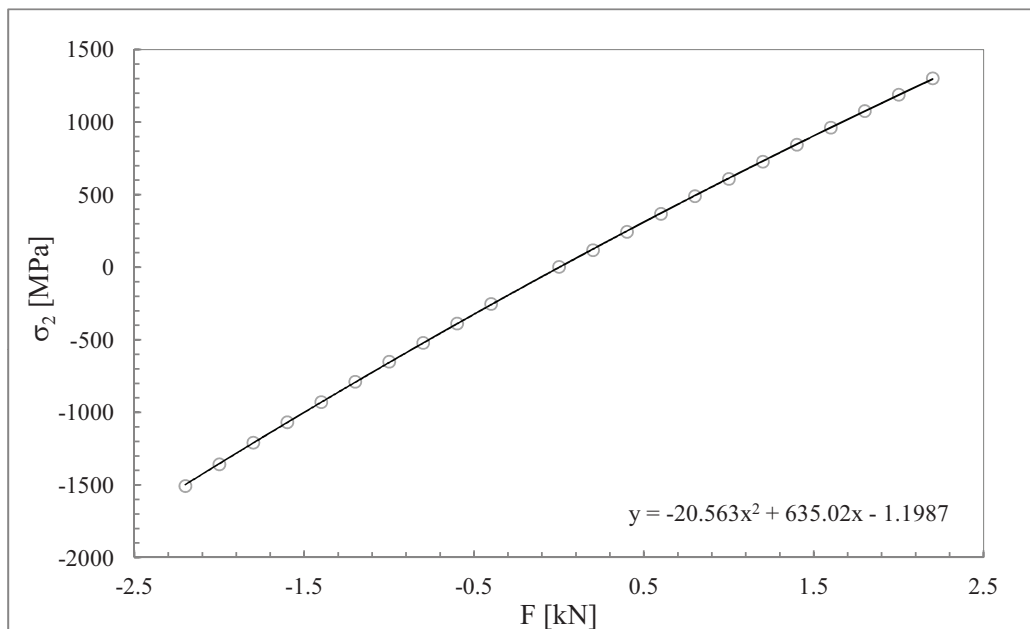


Figure 3.42: Calibration curve of cantilever plane bending tests (linear elastic bending stress on critical section σ_2 versus applied force F).

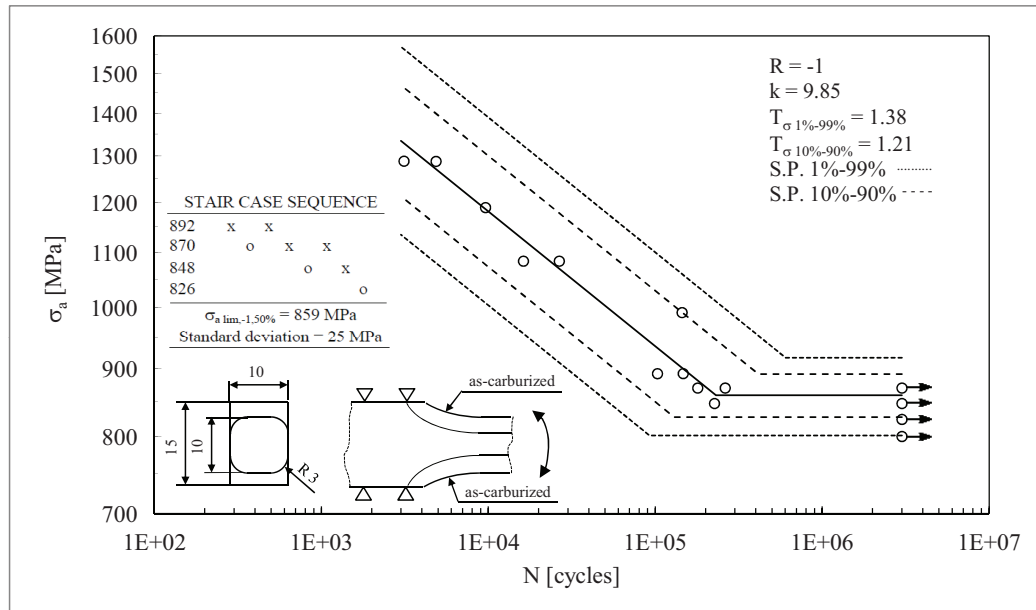


Figure 3.43: Fatigue results of B1 specimens.

The fatigue curves obtained from the tests are reported in Figure 3.43. As it can be seen the inverse slope of the curve k resulted similar to the slopes recorded for $R = 0.1$ plane bending tests. A stair case sequence was carried out with a target life of 3 millions of cycle, and was used to estimate the scatter on the endurance limit. As it can be seen, the scatter is significant, especially for the finite life region of the curve. The endurance knee is located, similarly to $R = 0.1$ plane bending tests, around 200,000 cycles.

3.6.3 Axial fatigue test, $R=0.1$

Axial fatigue tests were carried out on D1 specimens using the same MFL servo-hydraulic axial machine that was used also for the static tests (Figure 3.19). External bushings were used again to clamp the specimens into the machine grips. Test frequency ranged from 2 to 40 Hz, depending on the applied load amplitude: the higher the load applied by the testing machine, the lower the frequency used.

The fatigue curve obtained is reported in Figure 3.44, where the net stress amplitude σ_{an} is used to represent the results. Net stress was simply evaluated as:

$$\sigma_{an} = \frac{4F}{\pi d^2} \quad (3.9)$$

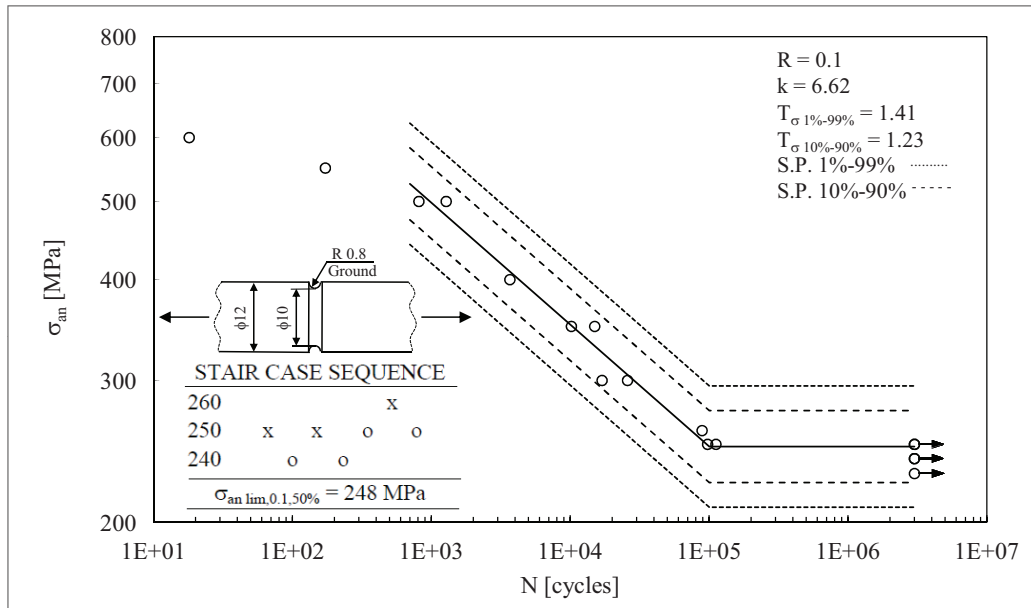


Figure 3.44: Fatigue results of D1 specimens.

where d is the net section diameter in the notched area ($d = 10$ mm) and F it the load applied by the testing machine.

It can be recognized that the position of the fatigue knee is located around 100,000 cycles, similarly to the previous fatigue tests. Tests carried out at very high stress showed that in the low cycle of the curve there is a modification of the inverse slope if compared to the medium life region, showing a sort of low-cycle fatigue knee.

3.7 Observation of fracture surfaces

The fracture surfaces of the broken specimens were observed using both the light microscope and the Electron Scanning Microscope (SEM).

After the fatigue failure of A, X and C specimens, in several cases the fracture surfaces resulted partly covered by the grase that was placed between the reaction and loading rollers and the specimens to avoid fretting phenomena. For this reason, the fracture surfaces of these specimens were firstly cleaned by brushing the surface with citric acid.

Since the number of tested specimens was considerable, not all the specimens were observed at the microscopes. For each test series three or four specimens were examined (totally, more than 20 specimens). Generally the observations were made on those specimens that showed a particular behav-

ior if compared to the others.

Two different failure modes were recognized on the specimens: failures starting from the surface and failure starting from the internal matrix, with completely different aspects and characteristics. Former failure mode was the most frequent, while the latter was observed only in two cases: A1_07 and A5_02 specimens. No failures starting from inclusions were found, although in the literature failure from inclusions is recognized as one of the most dangerous failure mode for high-strength steel [55].

3.7.1 Failures starting from surface

For both plain and notched specimens, fatigue failure of the specimens started prevailing from the surface.

The fracture surfaces exhibited well defined zones: light-grey zones corresponding to nucleation and stable crack growth, and dark-grey zones corresponding to unstable crack growth, that led to the final failure of the specimen. Extension and location of light-grey zones depend on the geometry of the specimens and load magnitude, according to Figure 3.45⁸ (the lower the applied load, the larger the light-grey zone). Nucleation sites are located at the surface, where the stress is higher. For A specimens the light-grey area is always located in the tension area of the cross section and generally has an asymmetrical shape, being wider towards one of the two rounded corner. For notched specimens C1 and D1, the light-grey zone always starts from the notch tip and is quite evenly distributed around the notch tip line, at least at high stress amplitudes. For D1 specimens, for high level of stress several crack initiation sites were found along the notch tip line, while for low stress only some sites became dangerous leading to crack propagation.

Fracture starting from surface of case-hardened specimens were already analyzed in the literature, especially from Krauss [56]. Krauss observed that under plane bending, the failures started from intergranular sites located on the surface (Figure 3.46). These sites involved only few grains (generally 3 or 4), and therefore they resulted very difficult to identify at the microscope, because of their limited dimensions. After the intergranular nucleation, the crack propagated in transgranular way, showing a regular and smooth appearance in an area described by a radius of few hundreds of microns. After this phase, the crack propagated by intergranular fracture again, showing irregular appearance. When crack reached the lower carbon portion of the case, the propagation became unstable, leading to a mainly ductile fracture. It resulted easier to identify the early crack propagation areas in notched

⁸The complete collection of the fracture surfaces is reported in [53].

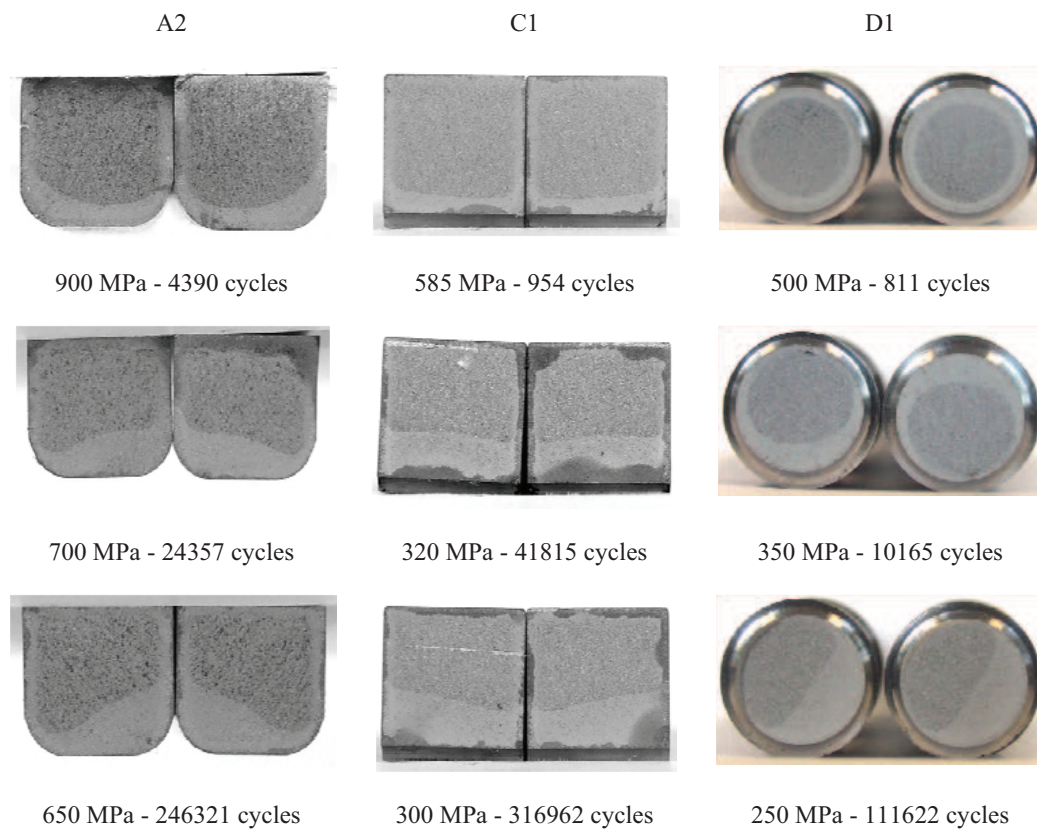


Figure 3.45: Fracture surfaces of specimens A2, C1 and D1 for different applied stress amplitudes.

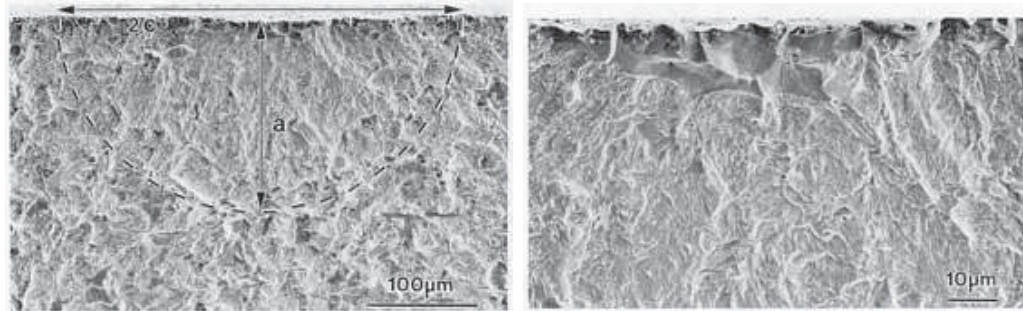


Figure 3.46: Fracture surfaces of a specimen in SAE 4320 steel tested under $R = 0.1$ plane bending [56]. On the top it is well visible the transgranular crack propagation zone (identified by dashed line); on the bottom there is a magnification of the intergranular nucleation site at the surface.

specimens than in plain ones, therefore an example of fracture surface of C1 specimen is reported in Figure 3.47. As it can be seen, near the crack nucleation sites (located at the notch tip) the surface appears more regular and smooth than the other zone, indicating that the fracture here was transgranular. The transgranular zones near the nucleation sites are highlighted by dashed lines in the magnification of the picture. Far away from the crack nucleation sites, the surface appears irregular and mainly intergranular. Sometimes also cleavages were observed. Moving towards the core of the specimen, ductility became predominant, as it is shown in Figure 3.48, taken from the core of specimen A1_15. In the observations made during the work here presented, intergranular initiations at surface observed by Krauss were not recognized.

Ratchet marks were often observed at the surface of both plain and notched specimens. In Figure 3.49 it is reported an example for notched C1 specimens, while in Figure 3.50 it is reported an example for notched D1 specimens. This feature was more visible for high applied stress, when the crack nucleation sites were numerous.

Inclusions seemed to not affect the fatigue behavior of the analyzed specimens, since no cases of failure starting from big inclusions located near the high-stress region were recognized. However, if even a small inclusion is located at the surface, it can lead to crack nucleation, as it is shown in Figure 3.51. Only this case was observed among the analyzed specimens. It is actually a particular case since the inclusion is located precisely at the surface, and there is low probability that this circumstance is frequently repeated. Therefore, inclusions for the analyzed specimens could not be considered as a prevailing failure mode.

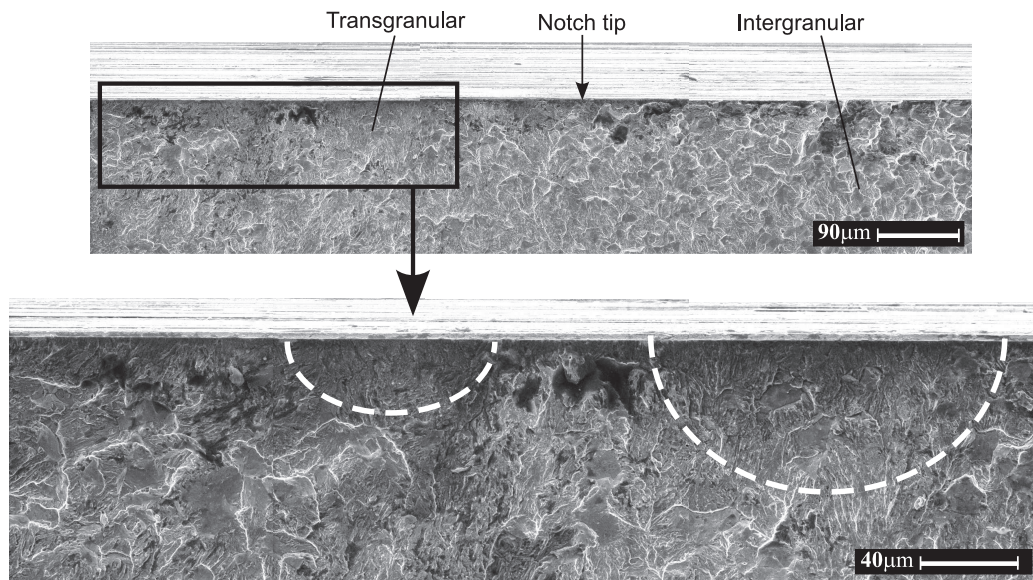


Figure 3.47: Fracture surface of C1_05 specimen ($N = 31,074$ cycles).

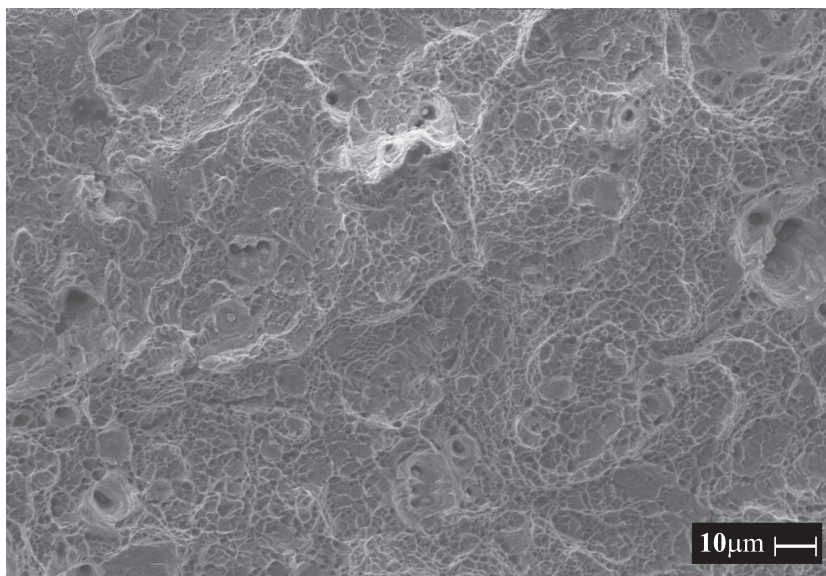


Figure 3.48: Detail of fracture surface in the core region of A1_15 specimen ($N = 38,612$ cycles). Dimples (visible everywhere in the picture) testify the high grade of ductility of unstable fracture.

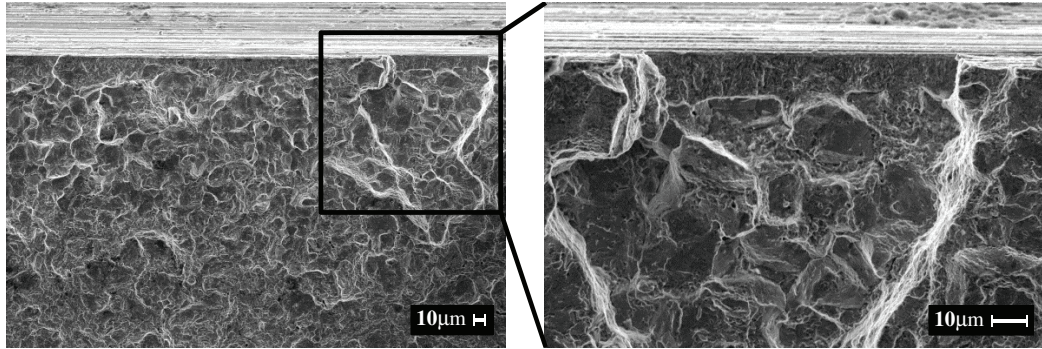


Figure 3.49: Ratchet marks observed on specimens C1_01 ($N = 954$ cycles).

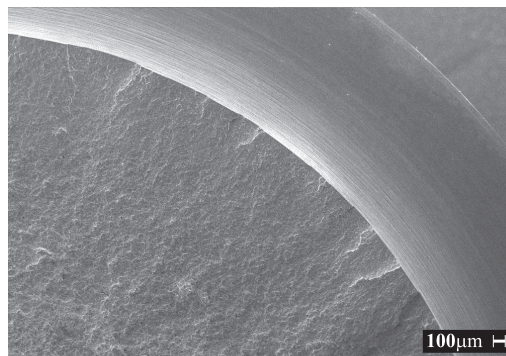


Figure 3.50: Ratchet marks observed on specimens D1_01 ($N = 10,156$ cycles).

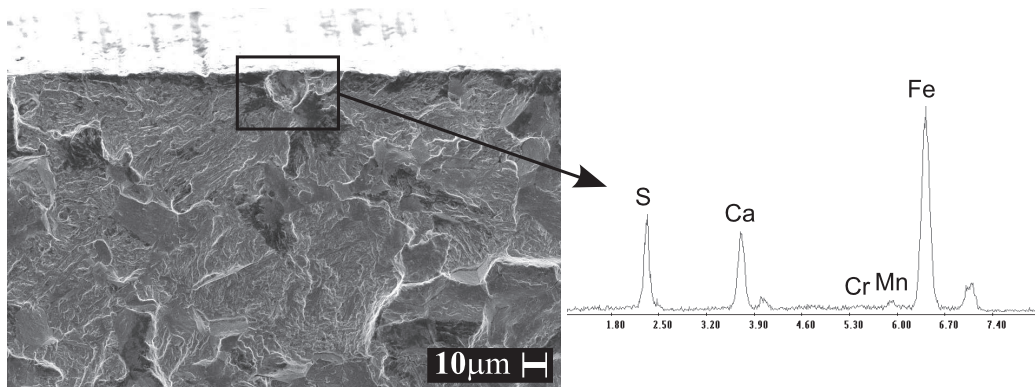


Figure 3.51: Crack nucleation site due to an inclusion located precisely at the surface of A2_18 ($N = 4,596$ cycles).

There is an important aspect to report concerning the impression of the identification code on the specimens. An electric pen was used, in order to avoid the cancellation of the codes on the specimen, since they were cleaned several times due to the use of grease during the plane bending tests. Few cases were found where the failures started (at least as secondary initiation site) from the corrosion pits created by the electric discharge induced by the electric pen (see Figure 3.52). If these pits were located in the most stressed zone or near it, they can lead to premature failure of the specimens. For this reason, if an electric pen is used to mark the specimens, attention must be paid. The specimens where the failure was recognized to start and propagate from corrosion pits were removed from the fatigue curve presented.

3.7.2 Non-defect internal matrix failures

Besides the fracture starting from surfaces, two cases of fractures starting from the subsurface were encountered during the plane bending tests on A specimens, see Figure 3.53. Failures involved specimens A1_07 and A5_02, that as it can be seen from Figures 3.26 and 3.28 failed at high number of cycles if compared to the other specimens where the failure started from the surface. The failures took place at about 1 mm from the surface, on the fibers subjected to tensile stress, as shown in Figure 3.53. This distance is comparable to effective case depth, thus the initiation sites took place at the interface between the external case-hardened layer and the lower-carbon interior zone, probably in the place where the residual stresses reached the highest tensile value [57].

SEM observations of the fracture origins are reported in Figure 3.54, where it is possible to see that there are no inclusions at the crack initiation sites.

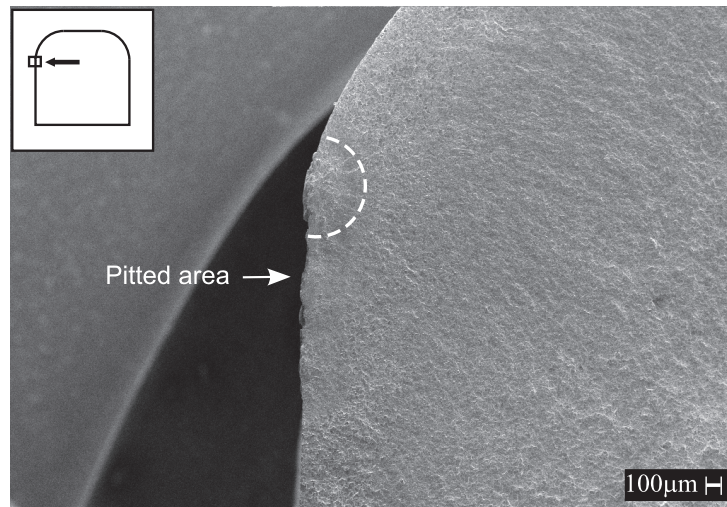


Figure 3.52: Crack nucleation site on lateral surface due to corrosion pits on X1_15 ($N = 511,007$ cycles).

This kind of failure was reported in the literature [58, 59, 60] as internal matrix non-defect failure, since the fracture starts in the internal matrix (at the interface between hardened layer and core) but in absence of defects. This kind of failure was not completely explained yet, but it seems that [58] it is related to the deformation mismatch of the different phases composing the microstructure. In the case-hardened specimens here presented, the microstructure is characterized by martensite near the external layer, that gradually becomes LCM structure (and also bainite) towards the core of the specimens. Martensite is more resistant than bainitic structure, therefore the deformations of the two phases are slightly different (see Figure 3.55, leading to fatigue damage at long lives (longer than 1,500,000 cycles in the present work). Burkart *et. al* [38] performed axial fatigue tests on notched specimens and demonstrated that internal matrix non-defect failures are very common for super-cleaned steels. For steels like those investigated in this work (normal cleanliness), the non-defects failures were more probable for specimens with low stress gradient near the surface, i.e. the lower the notch effect, the higher the probability to obtain a subsurface non-defect failure (and the lower the probability to fail from the surface). This is due to an intrinsic higher fatigue resistance of the surface than the core. When the applied stress is constant (axial stress), the failure should take place in the core of the specimens. When a notch effect is introduced, the highest stress is shifted towards the surface that becomes the critical initiation site. From these considerations, failures from subsurface internal matrix non-defect sites

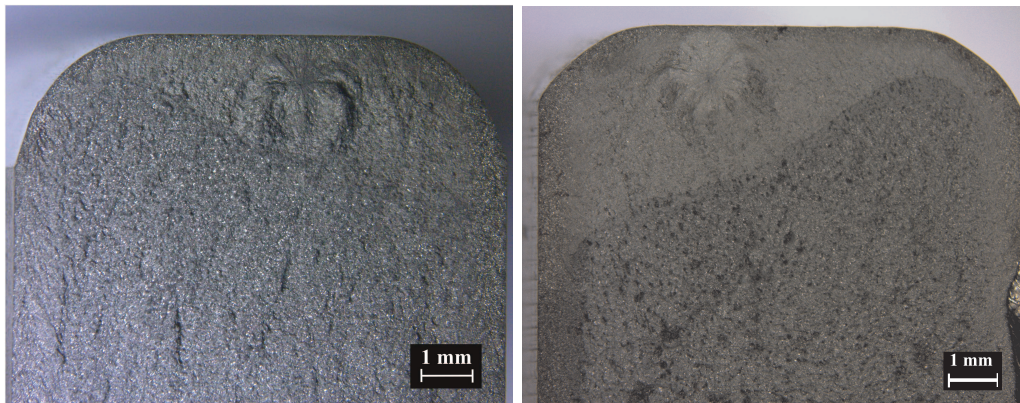


Figure 3.53: Non-defect internal matrix failure on A1_07 specimen ($N = 2,389,383$ cycles) (left) and A5_02 ($N = 1,762,734$ cycles) (right).

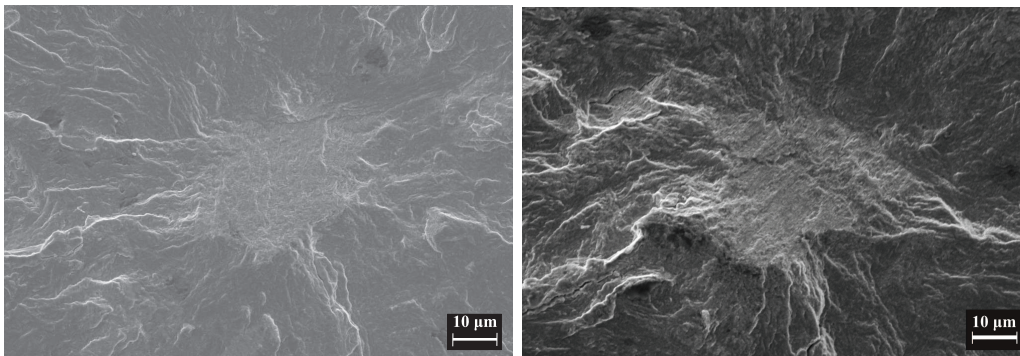


Figure 3.54: SEM observations of crack nucleation sites of A1_07 specimen (left) and A5_02 specimen (right).

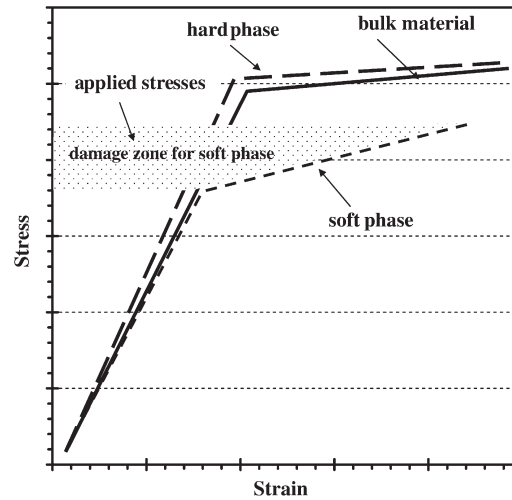


Figure 3.55: Schematic stress versus strain curves of single-phase alloys and two-phase alloy. Here the hard phases is much stronger than the soft phase [58].

should not be common in gears, since the notch effect induced by the tooth root fillet is generally high. On the contrary, if steel does not present high inclusions, gears should always fail (for bending loads) by fractures starting from the surface of the tooth root fillet.

3.8 Residual stresses

It is well known that case-hardening process leads to compressive residual stress in the surface case, which have a beneficial effect on fatigue behavior. Residual stress measurements were determined from X-ray using the $\sin^2\psi$ -method on ground and as-carburized specimens in 20MnCr5 steel (A1 and X1 respectively). Main characteristics of the X-ray measurements are reported in Table 3.13. Measurements were carried out on the surface where crack initiation took place and, more precisely, at the locations reported in Figure 3.56 for unloaded, failed and run-out specimens. Additional measurements were carried out in-depth in the carburized layer, more precisely at 0.03, 0.06, 0.1, 0.15, 0.2 and 0.3 mm from the surface of one specimen for each type (unloaded, run-out and failed). Residual stresses on the surface were evaluated for other 5 failed specimens, on position 1, since the specimens' ends could be considered not affected by previous load history (the bending moment in that position was zero). The results of residual stress measurements are listed in Table 3.14, and the corresponding residual stress fields are reported in Figure

Table 3.13: Characteristics of X-ray measurements.

Incident Radiation	Cr $K\alpha$
Filter	Vanadium
Detector type	Strip
Detector's angle range	40°
Elementary cell	Cubic
Miller's index (hkl)	(211)
2θ angle	156.3°
Young Modulus	208 GPa
Poisson coefficient	0.29
Tube tension	29 kV
Tube current	85 μ A
Collimator's diameter	1 mm

3.57. Electrochemical metal dissolution was used to remove the external layers of material, making it possible to measure the residual stress in-depth. It can be seen that in the unloaded specimens the maximum residual stress is reached at the surface (-380 \div -450 MPa and -520 \div -580 MPa for A1 and X1 specimens, respectively) and decreases rapidly within a 100- μ m-thick layer, reaching a value around -260 MPa (Figures 3.57a and 3.57b). By considering measurements made on unloaded positions on the specimen's surface, ground specimens (A-type) exhibited a mean residual stress at the surface of -402 MPa, while the as-carburized specimens (X-type) a mean of -534 MPa (see Figure 3.58). This difference of about 130 MPa is due to the removal of the external material allowance by grinding. The residual stress field of the specimens which underwent fatigue cycles resulted altered in the loaded area (point 2 of failed as well as run-out specimens, see Figure 3.56). This has been interpreted as due to the transformation of the retained austenite in martensite, corresponding to an increase of the compressive residual stress as reported from Figure 3.57c to 3.57f [24, 61, 62].

3.9 Discussion of experimental results

Static tests conducted on the four steels under the supply conditions showed that the Indian steels (EN 353 and BS 815 H17) had higher resistance and low ductility than the Italian ones (20MnCr5 and 18NiCrMo5). However, this difference was probably due to the different supply conditions of the steel bars: Indian bars were in as-rolled conditions, while Italian ones

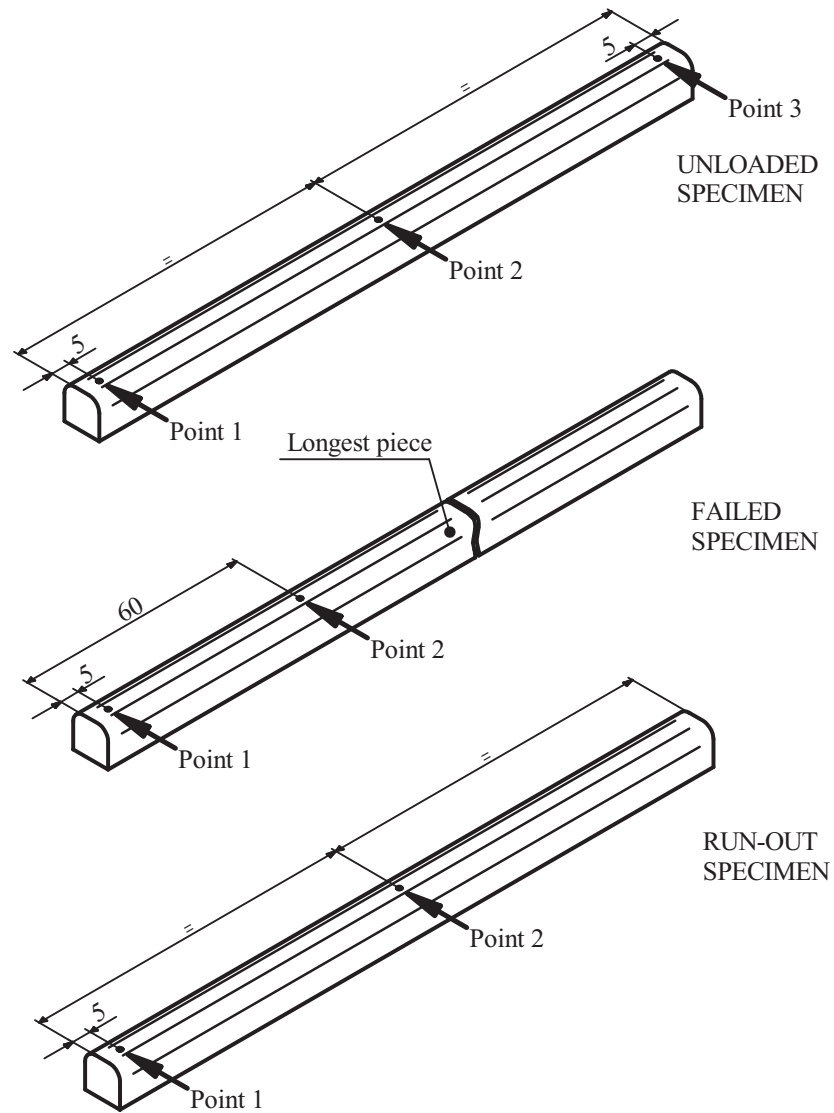


Figure 3.56: Measurement points for residual stress evaluation.

Table 3.14: Residual stresses [MPa] measured on A1 and X1 specimens.

Specimen	Type	Pos.	Depth from surface [mm]						
			0	0.03	0.06	0.1	0.15	0.2	0.3
A1_23	Unloaded	1	-435	-283	-274	-291	-267	-263	-265
		2	-453	-327	-221	-291	-289	-253	-255
		3	-384	-253	-289	-269	-275	-299	-263
A1_01	Run Out	1	-392	-245	-269	-244	-303	-298	-340
		2	-412	-322	-361	-298	-272	-395	-327
A1_09	Failed	1	-414						
A1_11	Failed	1	-334						
A1_13	Failed	1	-443						
A1_17	Failed	1	-368						
A1_22	Failed	1	-425						
A1_16	Failed	1	-374	-230	-293	-318	-294	-269	-267
		2	-322	-381	-394	-359	-406	-448	-453
X1_20	Unloaded	1	-574	-332	-267	-272	-184	-231	-293
		2	-520	-273	-209	-169	-213	-226	-239
		3	-550	-365	-190	-227	-198	-199	-261
X1_17	Run Out	1	-521	-267	-174	-224	-216	-254	-312
		2	-613	-463	-345	-405	-310	-263	-293
X1_04	Failed	1	-509						
X1_06	Failed	1	-535						
X1_09	Failed	1	-563						
X1_13	Failed	1	-495						
X1_19	Failed	1	-557						
X1_01	Failed	1	-516	-410	-290	-262	-140	-225	-271
		2	-544	-479	-396	-291	-392	-378	-372

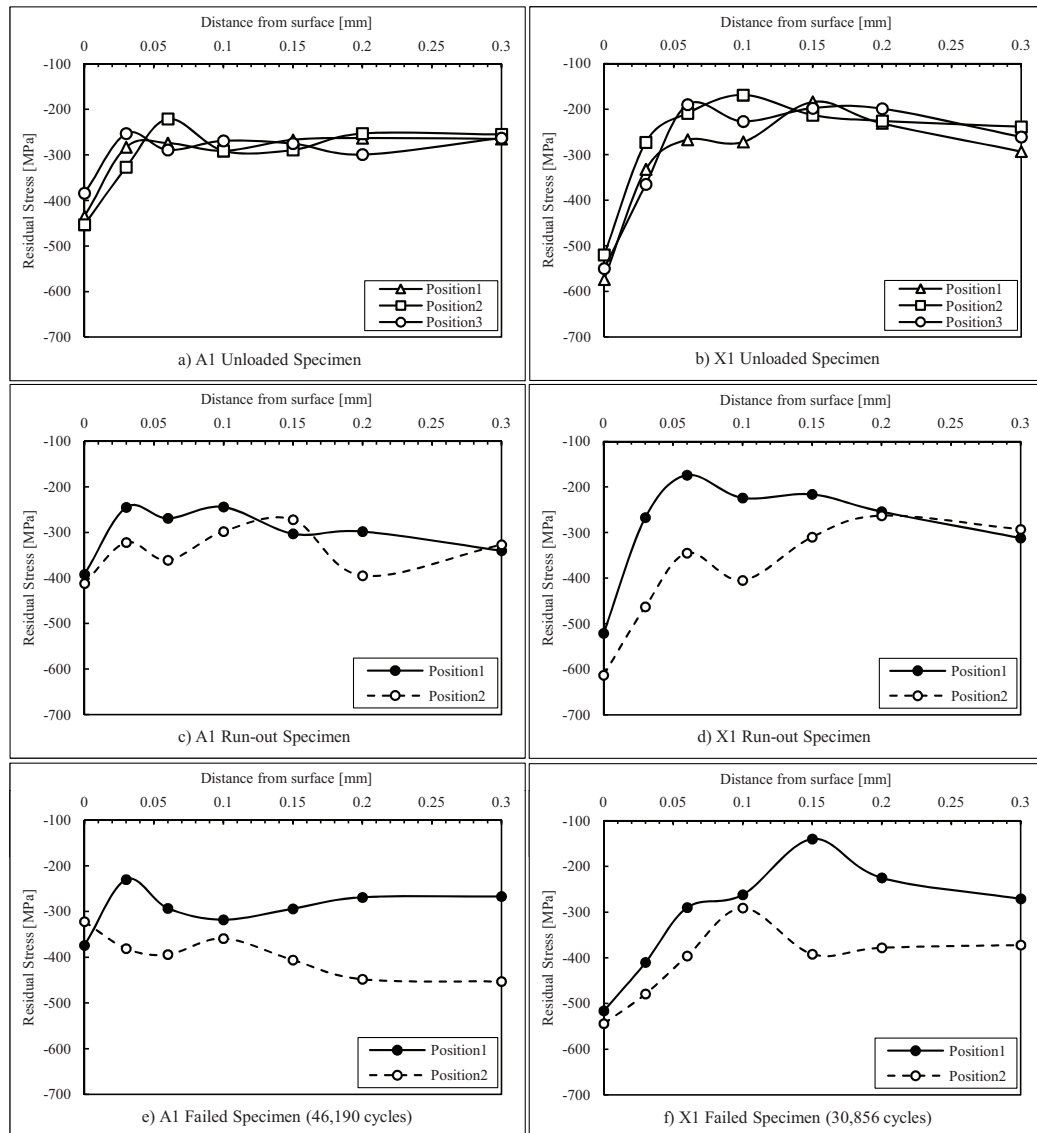


Figure 3.57: Residual stress fields of unloaded, run-out and failed specimens A1 and X1.

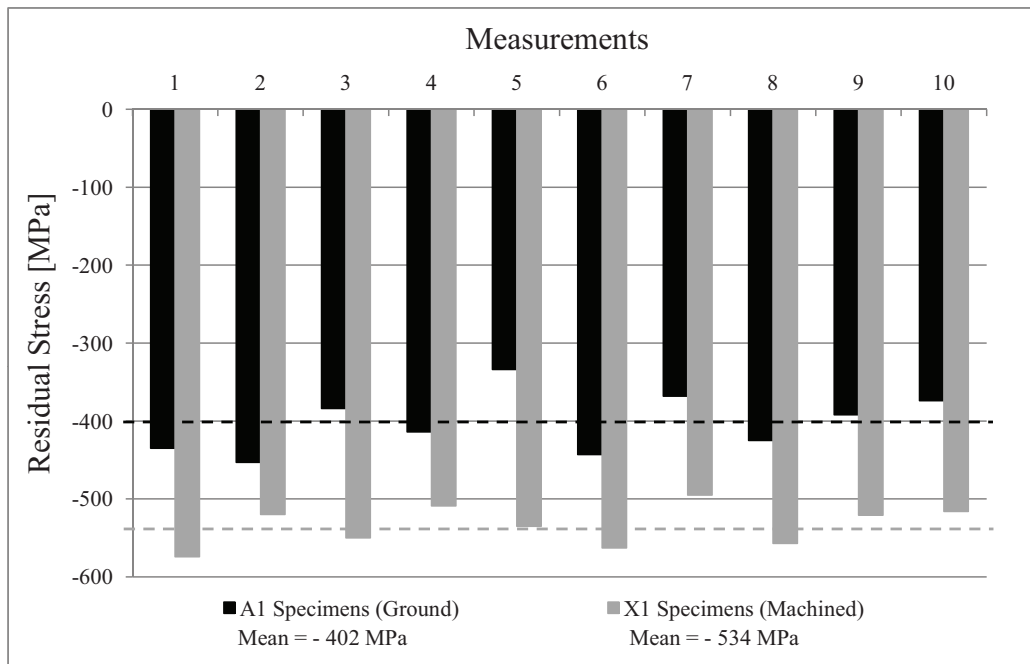


Figure 3.58: Surface residual stresses measured on A1 and X1 specimens (only locations 1 and 3).

were annealed (annealing eliminates work hardening due to plastic deformations). Even if the static behavior was different, the case-hardening treatment led to comparable static properties on 6-mm diameter specimens, in terms of tensile strength (S_u) and elongation after fracture (A). Case-hardening treatment led to an increase of S_u by a factor ranging from two for BS 815 17 steel to three for the Italian steels. Ultimate tensile strength reached values around 1700 MPa, that is a very high value for a steel. As expected, such strength increase was accompanied by a very severe reduction of ductility, that was almost lost.

The four steels were also compared in terms of fatigue resistance under plane bending $R = 0.1$ fatigue tests. Deep investigation of the fatigue limit was made only on 20MnCr5 (using stair case sequence), while for the other steels only few tests were made to locate the fatigue limit. The four point bending tests on ground A specimens revealed that there is an endurance limit around few-hundreds-thousand cycles, as it can be seen in Figure 3.59 where the results of the tests carried out on A specimens are reported. Failures taking place beyond 1,500,000 cycles were found to be due to internal matrix non-defect crack origins, while for shorter lives the fractures started from the surface. It can be seen that 20MnCr5 (steel 1) and 18NiCrMo5 (steel 2) have

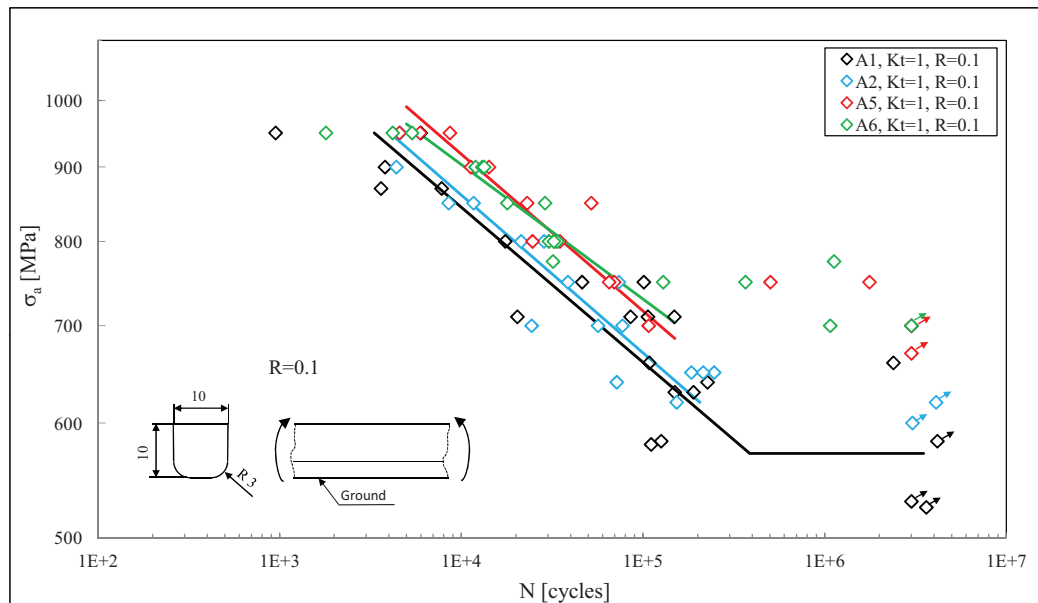


Figure 3.59: Experimental data and fatigue curves at S.P.=50% for all A specimens.

comparable fatigue curves in the finite life region, even if 18NiCrMo5 was affected by a slightly lower scatter ($T_{\sigma 1\ 10\%-90\%} = 1.39 > T_{\sigma 2\ 10\%-90\%} = 1.25$). Actually, no precise conclusions can be drawn on the endurance limit, since no staircase sequence was performed for 18NiCrMo5 steel. Even if run-outs of 18NiCrMo5 are located at slightly higher stress values, few trials were made around the endurance limits, therefore it is not possible to trust that endurance limit is higher for steel 2 than steel 1. The fatigue curves of the two Indian steels are comparable as well, but the curves are located above the curves of the Italian ones. Indian steels exhibited therefore better fatigue performances than Italian ones: the difference can be estimated in +5% of fatigue resistance in favor of Indian steels. Again, no precise information can be obtained on the endurance limit of the two Indian steels, even if the endurance limit seems to be located around the same value for both the steels. Run-outs on Indian steels were located at higher stresses than Italian steels. The scatter indexes ($T_{\sigma 5\ 10\%-90\%} = 1.18$, $T_{\sigma 6\ 10\%-90\%} = 1.13$) were similar and slightly lower than Italian ones.

The fatigue results obtained on the specimens in 20MnCr5 are reported in Figure 3.60. For each series the staircase sequences were performed, making it possible the determination of the endurance limits at least at S.P. = 50%. Comparing the results obtained from plain ground and machined as-carburized specimens (A1 and X1 respectively), the influence of grinding on

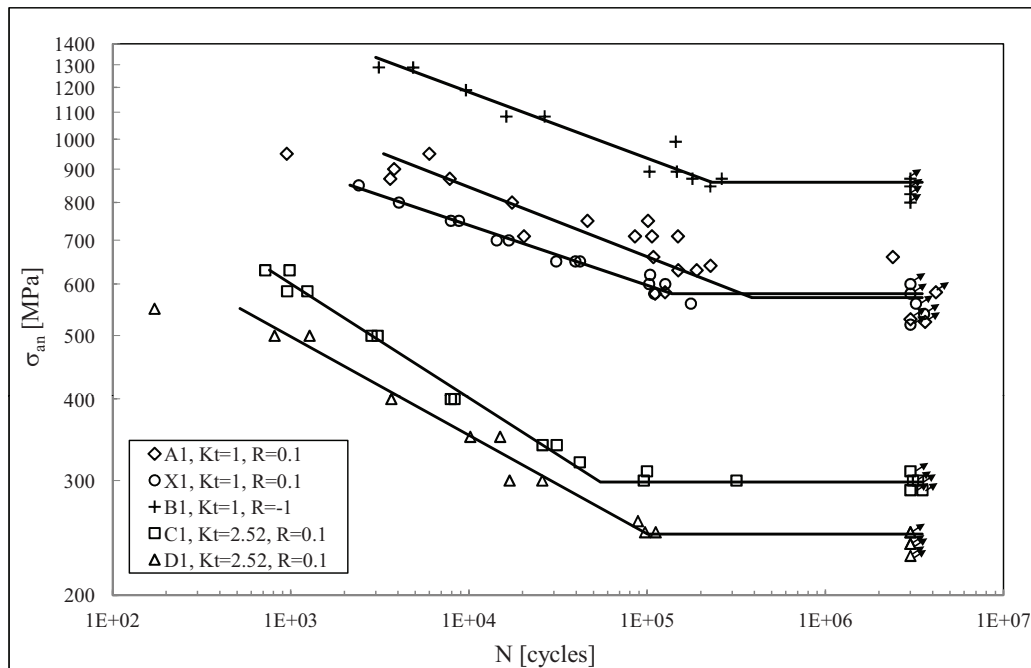


Figure 3.60: Experimental data and fatigue curves at S.P.=50% for all the specimens made of steel 1.

fatigue performances can be estimated. Grinding is generally made to improve the fatigue performance, since it leads to a better surface roughness, as it was shown also for the analyzed plain specimens (see Table 3.9). For the finite life region, ground A1 specimens showed a higher fatigue resistance than machined as-carburized X1 specimens. (around +10% in terms of stress). Actually, it must be considered that in the as-carburized X1 specimens, the external layer was affected by intergranular oxidation (IGO), that reduces the fatigue resistance of the surface. This oxidized layer was removed by grinding. However, the endurance limit was almost the same for the two types of specimens. This may appear strange, since generally the better the surface finishing, the higher the fatigue limit. But in this case, on one hand grinding improved the surface roughness and removed the IGO layer, but on the other it removed the external layer with the higher compressive residual stresses (and higher hardness). Surface compressive residual stress for specimens A1 resulted 130 MPa lower (as an average) than X1 specimens, as reported in Figure 3.58. Probably, for the specimens analyzed in this work, the beneficial and detrimental effects of grinding counterbalance themselves, resulting in almost the same endurance limit for both A1 and X1 specimens. That said, the surface finishing factor K_l for fatigue design from the experimental

results is:

$$K_l = \frac{\text{Endurance limit of A1 specimens}}{\text{Endurance limit of X1 specimens}} = \frac{572}{580} \approx 1 \quad (3.10)$$

even if this factor actually takes into account not only the effects of the surface finishing but also the presence of the IGO layer and of higher residual stress. Surface finishing factor reported in ISO 6336-3 [41] resulted instead:

$$K_{l,ISO} = \frac{1}{Y_R} = \frac{1}{1.49 - 0.471 (R_z + 1)^{0.1}} = 1.11 \quad (3.11)$$

Notch sensitivity of case-hardened 20MnCr5 steel could be estimated from the fatigue results. The K_f factor can be evaluated as:

$$K_f = \frac{\text{Endurance limit of A1 specimens}}{\text{Endurance limit of C1 specimens}} = \frac{572}{298} = 1.92 \quad (3.12)$$

Comparing the notch factor with the stress concentration factor, the support factor $Y_{\delta k}$ results:

$$Y_{\delta k} = \frac{K_t}{K_f} = \frac{2.52}{1.92} = 1.31 \quad (3.13)$$

The support factor equals 1 in case of full sensitivity to notch, while equals to K_t in case of complete insensitivity to notch. 20MnCr5 steel resulted therefore quite sensitive to notch, but not so much as what reported in ISO 6336, that suggests a support factor of $Y_{\delta k} = 1.09$, predicting therefore an higher sensitivity to notch with respect to that one found experimentally.

Using the data relevant to axial fatigue tests, the load type factor K_v (plane bending to axial) can be estimated for notched specimens:

$$K_v^* = \frac{\text{Endurance limit of C1 specimens}}{\text{Endurance limit of D1 specimens}} = \frac{298}{248} = 1.20 \quad (3.14)$$

meaning that axial loads are 20% more damaging than plane bending loads. Naturally, gear teeth are never subjected to axial fatigue loads. However, this data may be interesting if axial tests would be used to characterize different steels or suppliers. In fact, axial tests are faster and generally easier to perform than plane bending ones.

It must be noted that the fatigue factors previously evaluated are relevant to a $R = 0.1$ stress ratio, differently from reference conditions generally reported in the books ($R = -1$, [63]).

Finally, it is possible to estimate differences in fatigue performances of drive and idler gears, comparing results under $R = 0.1$ and $R = -1$ stress ratios.

Using the same approach suggested by ISO 6336 [45] it is possible to define the Y_M factor, defined using the maximum stress reached during the fatigue cycle (σ_{max}):

$$Y_M = \frac{\text{Endurance limit of B1 specimens } (\sigma_{max})}{\text{Endurance limit of X1 specimens } (\sigma_{max})} = \frac{870}{1289} = 0.67 \quad (3.15)$$

Experimental Y_M factor is in excellent agreement with the corresponding value according to ISO 6336, derived for a stress ratio $R = 0$, since $Y_{M,ISO} = 0.7$.

3.10 Conclusions

The chapter presented the experimental tests carried out to characterize the static and the bending fatigue behavior of four case-hardened steels widely used from the Company to manufacture gears. For comparison purposes, additional axial fatigue tests were performed on a series of notched specimens in 20MnCr5 steel. The microstructure, micro-hardness and residual stresses were also analyzed. As a results of the investigations, the following conclusions could be drawn:

- 1.** Concerning the static tests conducted on specimens of 6 mm diameter, case-hardening process increased from two to three times the tensile strength of the steels from the as-supplied conditions, but it caused the loss of ductility almost completely. Ultimate tensile strength around 1700 MPa were reached for all the steels.
- 2.** The fatigue curves showed a low number of cycles at the endurance limit as compared to 3,000,000 cycles reported in ISO 6336 Standard. The endurance limit was in the range of 50,000 to 400,000 cycles, the lower values being relevant to notched specimens. Irrespective of the load type (either bending or axial), the experimental data suggested clearly that a plateau at the endurance limit exists, at least up the 3 million fatigue cycles, which has been selected as the maximum number of cycles in the present fatigue tests. A similar behavior in plane bending has been reported in the literature for the same class of steels, while the existence of a flat plateau at the endurance limit in axial and rotating bending fatigue tests has not been uniformly observed in the literature. Approximately the same number of cycles at the knee point of the endurance limit was observed in the plane bending and axial tests carried out in this work.
- 3.** The use of specimens resulted an effective way to compare the fatigue behavior of different steels. Furthermore, it may be used to characterize the manufacturing capability of different suppliers under standardized supplying

conditions. From this point of view, testing some specimens could be a way to qualify suppliers or new steels available in the emerging markets.

4. The fatigue notch factor K_f and surface finishing factor K_l were evaluated from the experimental results and a 10 ÷ 20 % difference was found if compared with the corresponding factors calculated according to ISO 6336 Standard. Excellent agreement was found for the Y_M factor, defined as the fully reversed to pulsating bending endurance limit ratio, which resulted equal to 0.67.

5. The analysis of fracture surfaces indicated that failures started from the surface of the specimens, except for a couple of ground plain specimens, where a so-called non-defect internal matrix crack origin was found. Early crack propagation from the crack nucleation sites was characterized by transgranular fracture, while moving towards the interior of the specimens, the fracture showed an intergranular appearance, characterized by both ductility and cleavages. Inclusions were not found to be critical for the fatigue resistance of the tested specimens. Internal matrix non-defect crack origins seemed to be typical of low stress gradient, that is uncommon for gears, that for this reason should fail from crack starting from the surface.

6. Residual stresses were analyzed and were found to rapidly decrease within a 0.1-mm-thick layer starting from the external surface of the specimens. On the basis of X-ray measurements performed after the tests, it was found that the residual stress field varied after the application of the fatigue loads, probably due to retained austenite transformation. Case-hardening process led to a mean compressive stress at the surface of 530 ± 40 MPa. For specimens ground after case-hardening, the beneficial effect on fatigue behavior due to the improved surface finishing was found to be counter-balanced by the detrimental effect caused by the removal of the high compressive residual stress existing at the surface.

7. Since bending fatigue tests were carried out using the ISO 6336 recommendations, i.e. pulsating plane bending test on ground specimens, the 99% survival probability fatigue curves derived here for plain as well as notched specimens will be used to set-up the specimen-based methods mentioned by the ISO Standard.

ISO 6336-3 Analysis

This chapter analyzes the different gear design methods presented in ISO 6336. Theoretical derivation of the methods was faced: starting from the theoretical basis of local stress approach of German school, the expressions reported in ISO 6336 Standard were obtained. Specimen-based methods were firstly applied to data available in the literature, showing that a homogeneous set of data obtained on plain specimens, notched specimens and gears made of the same steel is necessary. Therefore, the data presented in Chapter 3 were completed presenting the fatigue curves obtained by pulsator tests on a gear geometry used on off-highway drivelines. ISO 6336 method B , B_p and B_k were applied using both the specimens' and gear data collected and results were commented. Attention was paid to the correction factors of the methods, focusing in particular on the support factors, that were identified as the most critical ones. Using experimental data, new expressions were proposed to improve the life predictions of the specimen-based methods.

4.1 Introduction

The design against bending fatigue of gears is reported in ISO 6336-3 [41]. The Standard reports four different methods for the design of a gear pair:

- Method A , based on the fatigue testing of fac-similes of the gears under design;
- Method B , based on the use of fatigue strength data obtained by testing reference gears;
- Method B_p , based on the use of fatigue strength data obtained using plain specimens;

- Method B_k , based on the use of fatigue strength data obtained using notched specimens.

The purpose of this chapter is to show the theoretical derivation of the design methods for bending design proposed by the Standard, and then apply them to some specific cases in order to investigate their reliability. Both data taken from the open literature and obtained from experimental tests were used in the analyses. The results are finally discussed and some improvements to fit well experimental results are proposed.

4.2 Derivation of methods B , B_p and B_k

4.2.1 Theoretical basis

The design approach used by ISO 6336 is based on the calculation of the linear elastic stress at the tooth root and on its comparison with the corresponding fatigue limit. This corresponds to a local-stress based approach, which is typical of the German school. It is used for example in the FKM-Guideline [64].

To explain the derivation of the design methods proposed in [41], it is useful to think to plain specimens first. Let's consider a plain specimen subject to $R=0$ plane bending. The fatigue design can be made using the fatigue limit obtained from uniaxial fatigue tests (under $R=0$) on plain specimens of 10 mm diameter and polished surface $\sigma_{a\infty,nom,ax}^{PLAIN*}$. This fatigue limit is corrected using the classical fatigue correction factors to take into account the load type (using K_V factor), the dimensions (using K_d factor) and the surface finishing (using K_l factor). The bending stress amplitude on the generic plain specimen ($\sigma_{a,nom,b}^{PLAIN}$) must be lower than the axial stress amplitude at fatigue limit of the reference plain specimen:

$$\sigma_{a,nom,b}^{PLAIN} \leq \frac{\sigma_{a\infty,nom,ax}^{PLAIN*}}{(K_V K_d K_l)^{PLAIN}} \quad (4.1)$$

The expression is still valid if the maximum nominal stress is used instead of the amplitude, i.e.:

$$\sigma_{max,nom,b}^{PLAIN} \leq \frac{\sigma_{max\infty,nom,ax}^{PLAIN*}}{(K_V K_d K_l)^{PLAIN}} \quad (4.2)$$

Let's consider now the influence of the dimensions of the specimens. Large dimensions increase the probability to find a defect in the most stressed zone,

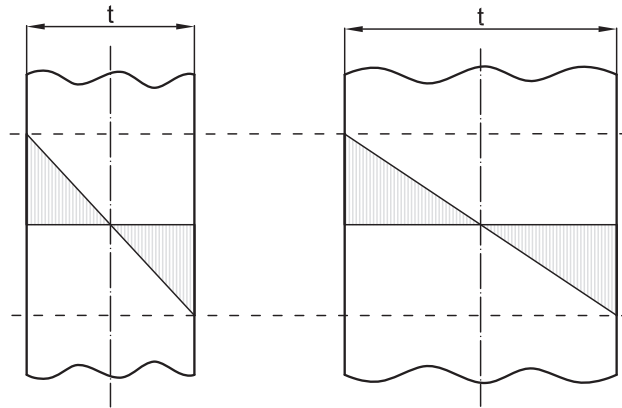


Figure 4.1: Effect of dimensions on stress gradient.

resulting in a higher probability of failure. The word *dimensions* means both thickness and width of the specimen (if the specimen is not a cylinder for example). Furthermore, big dimensions may lead to poor heat treatment results. Therefore, the bigger the specimen, the bigger K_d . But the dimensions actually affect also the shape of the stress gradient generated by the bending stress. Considering the same maximum nominal bending stress, the stress gradient is higher in a plain specimen with small thickness (t) than in a specimen with large thickness, see Figure 4.1. Since the stress gradient is an important factor in the local-stress design method, let's consider to divide the effects of dimensions of the specimen in two parts: one related to the statistical probability to find a defect and to the quality of the heat treatment ($K_{d,s}$), and one related to the influence on the stress gradient ($K_{d,g}$).

The support factor ν_0 can be introduced and defined as:

$$\nu_0 = \frac{1}{K_V K_{d,g}} \quad (4.3)$$

i.e. a factor that consider the different fatigue behavior of a plain polished specimen subject to plane bending and a plain polished specimen subject to axial loading. The support factor takes into account the effect of the materials fibers which are adjacent to the fiber that withstands the highest stress. The internal fibers, that are not subject to the highest load, help the most stressed fiber and "absorb" part of the stress. Practically, the internal fibers *support* the external one, moving stress from the exterior to the interior of the specimen. Therefore the name of *support factor*. This means that when a specimen is subject to bending load (or other load condition that leads to a stress gradient) the maximum local stress that can be reached without failure is higher than the case of an axial load, where all the fibers of the

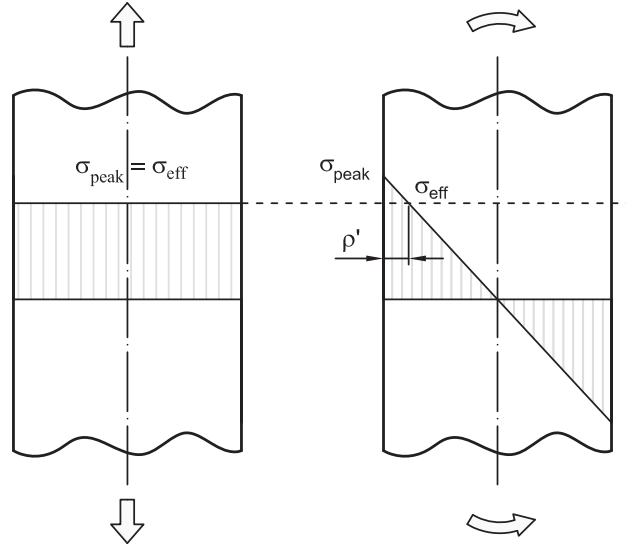


Figure 4.2: Schematic representation of Siebel parameters in plain specimens under axial and bending loads.

cross section are subject to the same maximum stress. In the case of axial load, the support effect cannot take place, since internal fibers are loaded like the external ones. It is therefore interesting to notice that the higher the stress gradient, the higher the possibility to redistribute stress on the internal fibers. This means also that for a given maximum local stress, the higher the stress gradient, the higher the capability to resist to loads by means of the re-distribution of stress.

The support factor can be estimated using the approach proposed by Siebel and Stieler [65]. They said that for a plain specimen (no notch):

$$\nu_0 = 1 + \sqrt{\rho' \chi_P^*} \quad (4.4)$$

where ρ' is the *slip layer thickness*, that is a property of the material, while χ_P^* is the relative stress gradient obtained in the plain specimen, defined as:

$$\chi_P^* = \left(\frac{1}{\sigma_{max}} \frac{d\sigma}{dx} \right)^{PLAIN} \quad (4.5)$$

The parameters of the local stress method proposed by Siebel are shown in Figure 4.2. The method proposed by Steiler is based in the definition of an effective stress σ_{eff} , which is evaluated for a particular distance ρ' from the surface, depending on the material. The slip layer thickness proposed by ISO 6336 Standard is reported in Table 4.1 for several materials ¹. As it can be

¹Other values for ρ' can be found in [66]

Table 4.1: Slip layer thickness ρ' according to [41].

Material	ρ'
GG, $\sigma_B = 150$ MPa	0.3124
GG, GGG (ferritic) with $\sigma_B = 300$ MPa	0.3095
NT, NV for all hardness	0.1005
St with $\sigma_S = 300$ MPa	0.0833
St with $\sigma_S = 400$ MPa	0.0445
V, GTS, GGG (perlitic, bainitic) with $\sigma_S = 500$ MPa	0.0281
V, GTS, GGG (perlitic, bainitic) with $\sigma_S = 600$ MPa	0.0194
V, GTS, GGG (perlitic, bainitic) with $\sigma_S = 800$ MPa	0.0064
V, GTS, GGG (perlitic, bainitic) with $\sigma_S = 1000$ MPa	0.0014
Eh, IF (root) for all hardness	0.0030

LEGEND

GG: Grey cast iron

GGG: Nodular cast iron (perlitic, bainitic, ferritic structure)

GTS: Black malleable cast iron (perlitic structure)

NT: Nitriding steels, nitrided

NV (nitr.): Through-hardening and case-hardening steel, nitrided

NV(nitricar.): Through- and case- hardening steel, nitrocarburized

St: Steel ($\sigma_B < 800$ MPa)V: through-hardening steel, through-hardened ($\sigma_B \geq 800$ MPa)

IF: steel and GGG, flame or induction hardened

Eh: case-hardening steel, case hardened

seen, the slip layer thickness can be very small. For case-hardened steels ρ' is of $3 \mu\text{m}$, much lower than typical grain size. The slip layer thickness was introduced by Stieler [67]. He said that to introduce a plastic deformation (i.e. to overcome the yield stress $\sigma_{p0.2}$) the critical shear stress $\tau_F = \sigma_{p0.2}/2$ must be exceeded over a certain finite structure volume. This means that the plastic deformation and therefore fatigue damage is generated only if the stress gradient leads to shear stresses higher than τ_F outside the slip layer thickness. In Figure 4.3 an example of damaging stress gradient is reported.

Once the support factor is defined, Equation 4.2 can be rewritten as:

$$\sigma_{max,nom,b}^{PLAIN} \leq \frac{\sigma_{max\infty,nom,ax}^{PLAIN*}}{(K_{d,s}K_l)^{PLAIN}} \nu_0 \quad (4.6)$$

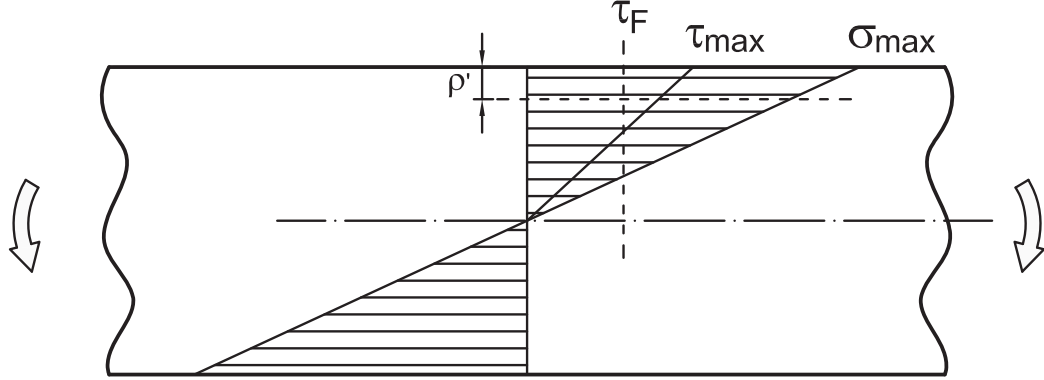


Figure 4.3: Damaging stress gradient: shear stress exceeds τ_F for a depth higher than the slip layer thickness.

In the Standard the influence of surface finishing and dimensions is taken into account using the factors $Y_R = 1/K_l$ and $Y_X = 1/K_{d,s}$, respectively. Therefore:

$$\sigma_{max,nom,b}^{PLAIN} \leq \sigma_{max\infty,nom,ax}^{PLAIN*} (Y_R Y_X)^{PLAIN} \nu_0 \quad (4.7)$$

It is easy to note that while K -factors are higher than 1, Y -factors are lower than 1.

Considering now a notched specimen of general dimensions and surface finishing, the design against fatigue is based on the following expression:

$$\sigma_{max,nom,b}^{NOTCH} \leq \frac{\sigma_{max\infty,nom,ax}^{PLAIN*}}{(K_V K_{d,s} K_{d,g} K_l K_f)^{NOTCH}} \quad (4.8)$$

where also the K_f factor appears, since in this case the notch effect must be taken into account. It is useful to insert the linear elastic concentration factor in the previous expression, leading to:

$$\sigma_{max,nom,b}^{NOTCH} \leq \frac{\sigma_{max\infty,nom,ax}^{PLAIN*}}{(K_V K_{d,s} K_{d,g} K_l K_f)^{NOTCH}} \left(\frac{K_t}{K_t} \right)^{NOTCH} \quad (4.9)$$

Now, like for the plain specimen, it is possible to define a support factor for the notched specimen which takes into account all the factors that affect the stress gradient:

$$\nu_d = \left(\frac{K_t}{K_V K_{d,g} K_f} \right)^{NOTCH} \quad (4.10)$$

Using the support factor for notched specimen ν_d , the Equation 4.9 becomes:

$$\sigma_{max,nom,b}^{NOTCH} \leq \frac{\sigma_{max\infty,nom,ax}^{PLAIN*}}{K_t^{NOTCH}} (Y_R Y_X)^{NOTCH} \nu_d^{NOTCH} \quad (4.11)$$

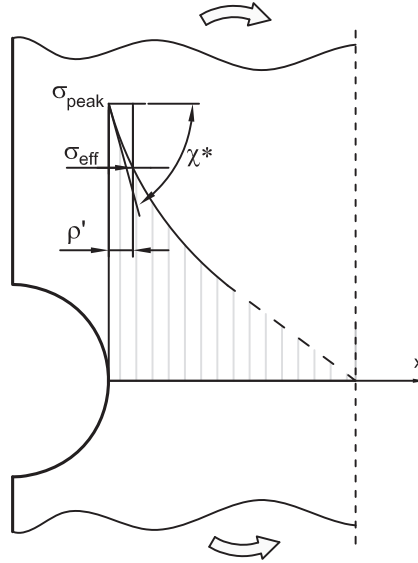


Figure 4.4: Schematic representation of Siebel-Stieler parameters.

which is very similar to Equation 4.7 for the plain specimen: formally the only difference is the presence of the stress concentration factor K_t .

The support factor for notched specimen ν_d can be defined again using the approach of Siebel:

$$\nu_d = 1 + \sqrt{\rho' \chi^*} \quad (4.12)$$

where χ^* is the relative stress gradient of the notched specimen, represented in Figure 4.4 along with the other parameters of Siebel and Steiler approach. From the picture it can be seen that the stress gradient is influenced by the notch shape.

Remembering the definition of ν_0 , Equation 4.10 can be rewritten as:

$$\nu_d = \nu_0 \left(\frac{K_t}{K_f} \right)^{NOTCH} \quad (4.13)$$

In ISO 6336 Standard, the effect of notch is taken into account using the *notch sensitivity* factor Y_δ , which is defined as the ratio between the stress concentration factor and the form factor of the notch:

$$Y_\delta^{NOTCH} = \left(\frac{K_t}{K_f} \right)^{NOTCH} \quad (4.14)$$

It is easy to see that when a material is completely insensitive to notch, i.e. $K_f = 1$, the notch sensitivity factor is equal to the stress concentration factor: $Y_\delta = K_t$. On the contrary, when a material is fully sensitive to notch,

i.e. $K_f = K_t$, then $Y_\delta = 1$. It must be noted that it is possible to explain Y_δ as a function of the support factors. Looking to Equation 4.13 it is easy to see that:

$$Y_\delta^{NOTCH} = \frac{\nu_d}{\nu_0} \rightarrow Y_\delta = \frac{1 + \sqrt{\rho' \chi^*}}{1 + \sqrt{\rho' \chi_P^*}} \quad (4.15)$$

4.2.2 Method B_p

Each design method reported in ISO 6336 is based on the following main equation:

$$\sigma_F \leq \sigma_{FP} \quad (4.16)$$

where σ_F is the linear elastic peak stress at the tooth root and σ_{FP} is the corresponding endurance limit at a target life. The calculation of σ_F is the same in each method, while the definition of σ_{FP} changes from method to method.

The peak stress at tooth root fillet is calculated using the following expression:

$$\sigma_F = \sigma_{F0} K_A K_v K_{F\beta} K_{F\alpha} \quad (4.17)$$

where:

- σ_{F0} is the maximum local stress at tooth root induced by error-free gear pair under a nominal and constant torque. The gear is assumed to be a driving gear, i.e. the stress ratio is $R=0$.
- K_A is the application factor, which takes into account the uniformity of the applied torque on the gear.
- K_v is the dynamic factor, which takes into account dynamic effects such as resonance.
- $K_{F\beta}$ is the face load factor which takes into account uneven distribution of load along the facewidth of the gear due to manufacturing inaccuracies and elastic deformations.
- $K_{F\alpha}$ is the transverse load factor which takes into account uneven distribution of load in the transverse direction due to, for example, pitch deviations.

The maximum local stress at tooth root σ_{F0} is defined as:

$$\sigma_{F0} = \frac{2T}{dbm_n} Y_F Y_\beta Y_B Y_{DT} \quad (4.18)$$

where:

- T is the nominal torque transmitted by the gear.
- d is the pitch circle diameter of the gear.
- b is the net facewidth of the gear.
- m_n is the normal module of gear teeth.
- Y_F is the form factor which transform the torque into nominal stress at tooth root. Depending on the design of the mating gears, more than one pair of teeth can engage during the rotation. Y_F factor refers to most critical case, i.e. when only a pair of teeth is engaged and the contact between them is located at the maximum possible external diameter of the gear under study. This condition leads to the highest bending moment arm, thus resulting in the highest stress at the tooth root fillet.
- Y_β is the helix factor, which takes into account that in helical gear the contact takes place along an oblique line.
- Y_B is the thickness factor, which takes into account the effect of thin rim under the teeth.
- Y_{DT} is the deep tooth factor, which corrects Y_F when more than two teeth are always engaged during the rotation.

The permissible fatigue bending stress σ_{FP} for method B_p is defined starting from the fatigue performance obtained by testing plain specimens. ISO 6336 states that pulsar bending stress must be used to obtain the bending fatigue curve from the specimens. This means that R=0 plane bending stress should be carried out.

The expression of the permissible bending stress can be obtained starting from the general equation for fatigue design of a notched component (Equation 4.11), that now is of course a gear:

$$\sigma_{max,nom,b}^{GEAR} \leq \frac{\sigma_{max\infty,nom,ax}^{PLAIN*}}{K_t^{GEAR}} (Y_R Y_X)^{GEAR} \nu_d^{GEAR} \quad (4.19)$$

where the axial fatigue limit of the plain specimen can be substituted with Equation 4.7, leading to:

$$\sigma_{max,nom,b}^{GEAR} K_t^{GEAR} \leq \frac{\sigma_{max,nom,b}^{PLAIN}}{(Y_R Y_X)^{PLAIN} \nu_0} (Y_R Y_X)^{GEAR} \nu_d^{GEAR} \quad (4.20)$$

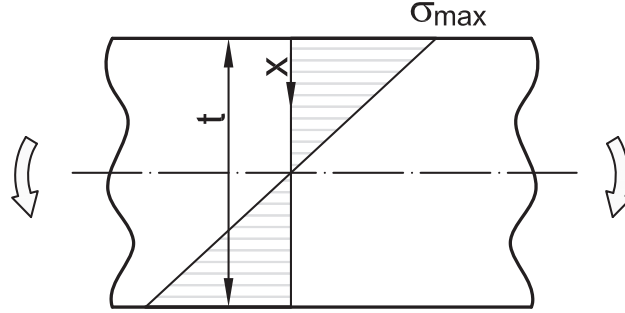


Figure 4.5: Stress gradient induced by bending load in a plain specimen.

that can be rearranged in the following expression:

$$\sigma_{max,pe,b}^{GEAR} \leq \sigma_{max\infty,nom,b}^{PLAIN} \frac{\nu_d^{GEAR}}{\nu_0} \frac{Y_R^{GEAR}}{Y_R^{PLAIN}} \frac{Y_X^{GEAR}}{Y_X^{PLAIN}} \quad (4.21)$$

where $\sigma_{max,pe,b}^{GEAR}$ is the linear elastic stress at tooth root of the gear under bending load (also called σ_F according to ISO 6336). Using the same notation of ISO 6336, remembering Equation 4.13 and noting that $\sigma_{max\infty,nom,b}^{PLAIN}$ is the bending fatigue limit of plain specimen (σ_{plim} according to ISO 6336):

$$\sigma_F \leq \sigma_{plim} Y_\delta Y_R \frac{Y_X^{GEAR}}{Y_X^{PLAIN}} \quad (4.22)$$

where:

- Y_δ is the notch sensitivity factor of the gear referred to the plain specimen;
- Y_R is the surface factor of the gear referred to the polished plain specimen;

It is important to notice that ISO 6336 states that the relative stress gradient of the plain specimens is $\chi_P^* = 0.2 \text{ mm}^{-1}$. Actually, the value of χ_P^* should be related to the dimension and shape of the specimens used to obtain the fatigue data. This suggests to use a specimen of thickness (or diameter) equal to 10 mm (cfr. Figure 4.5), since:

$$|\sigma(x)| = \frac{2\sigma_{max}}{t} x \quad (4.23)$$

$$|\chi_P^*| = \frac{1}{\sigma_{max}} \frac{d}{dx} \left(\left| \frac{2\sigma_{max}}{t} x \right| \right) \rightarrow 0.2 = \frac{2}{t} \rightarrow t = 10 \text{ mm} \quad (4.24)$$

Since 10 mm is a sort of "reference dimension" for specimens, it could be thought that for this dimensions $Y_X^{PLAIN} = 1$ and therefore also for notched specimens of the same dimension $Y_X^{NOTCH} = 1$.

At the fatigue limit the first term of the equation 4.22 is equal to the second one. Using the same notation of ISO 6336 and remembering that $Y_X^{PLAIN} = 1$ we obtain that:

$$\sigma_{FP} = \sigma_{plim} Y_{\delta} Y_R Y_X \quad (4.25)$$

where $Y_X = Y_X^{GEAR}$ is the size factor of the gear of interest.

Expression 4.25 is presented in ISO 6336 also with a safety factor S_{Fmin} (used to reduce the fatigue limit) and a life factor Y_{Np} (used to permit the evaluation of the permissible bending stress for a target life that is shorter than the number of cycles of the high-cycle knee of the fatigue curve). Expression reported in ISO 6336 for method B_P is therefore:

$$\sigma_{FP} = \frac{\sigma_{plim} Y_{Np}}{S_{Fmin}} Y_{\delta} Y_R Y_X \quad (4.26)$$

It should be noted that the factor $\sigma_{plim} Y_{Np}$ is actually the real fatigue curve obtained from the plain specimens, since the life factor is used to obtain the shape of the fatigue curve for every number of cycles (σ_{plim} is only the value of the fatigue limit). In other words, σ_{FP} is dependent on the number of cycles and therefore analyses at different target lives have different values of σ_{FP} . Method B_p is not limited to the correction of the nominal bending stress of the polished plain specimen at the fatigue limit. Also the nominal bending stress of the low-cycle knee (σ_{pstat}) must be corrected in the same way. It means that there could be a different value of the correction factors Y_{δ} , Y_R and Y_X for the low- and the high-cycle knee.

4.2.3 Method B_k

The permissible bending fatigue stress for method B_k is obtained from tests on notched specimens. ISO 6336 does not suggest a predefined geometry of the specimens, but states only that tests must be carried out under R=0 plane bending. Net section of the specimens and notch radius should be therefore chosen close to the desired tooth geometry.

Considering a notched specimen and remembering Equation 4.15, at the fatigue limit, the Equation 4.11 can be rewritten as:

$$\sigma_{max,nom,b}^{NOTCH} = \frac{\sigma_{max\infty,nom,ax}^{PLAIN*}}{K_t^{NOTCH}} (Y_R Y_X Y_{\delta})^{NOTCH} \nu_0 \quad (4.27)$$

The same thing can be made on Equation 4.19, which at the fatigue limit becomes:

$$\sigma_{max,nom,b}^{GEAR} = \frac{\sigma_{max\infty,nom,ax}^{PLAIN*}}{K_t^{GEAR}} (Y_R Y_X Y_\delta)^{GEAR} \nu_0 \quad (4.28)$$

Inserting Equation 4.27 into Equation 4.28 the following expression is obtained:

$$\sigma_{max,nom,b}^{GEAR} K_t^{GEAR} = \frac{\sigma_{max\infty,nom,b}^{NOTCH} K_t^{NOTCH}}{(Y_X Y_R Y_\delta)^{NOTCH}} (Y_R Y_X Y_\delta)^{GEAR} \quad (4.29)$$

Rearranging:

$$\sigma_{max,pe,b}^{GEAR} = \sigma_{max\infty,nom,b}^{NOTCH} K_t^{NOTCH} \frac{Y_\delta^{GEAR}}{Y_\delta^{NOTCH}} \frac{Y_R^{GEAR}}{Y_R^{NOTCH}} \frac{Y_X^{GEAR}}{Y_X^{NOTCH}} \quad (4.30)$$

Using the notation of ISO 6336 ($\sigma_{max\infty,nom,b}^{NOTCH} = \sigma_{klim}$ and $K_t^{NOTCH} = Y_{Sk}$) and assuming that specimens are of reference dimensions ($Y_X^{NOTCH} = 1$), the following expression is obtained:

$$\sigma_{FP} = \sigma_{klim} Y_{Sk} Y_{\delta relk} Y_{Rrelk} Y_X \quad (4.31)$$

Introducing the safety factor S_{Fmin} and the life factor Y_{Nk} like in method B_p :

$$\sigma_{FP} = \frac{\sigma_{klim} Y_{Nk} Y_{Sk}}{S_{Fmin}} Y_{\delta relk} Y_{Rrelk} Y_X \quad (4.32)$$

where:

- σ_{klim} is the maximum nominal bending stress on the specimens obtained during a load cycle;
- Y_{Nk} is the life factor for notched bending specimen;
- Y_{Sk} is the stress concentration factor of notched specimen;
- $Y_{\delta relk}$ is the notch sensitivity factor of the gear of interest relevant to notched specimen;
- Y_{Rrelk} is the surface roughness factor of the gear relevant to notched specimen;
- Y_X is the size factor of the gear;
- S_{Fmin} is the minimum safety factor to be used for design.

Correction factors $Y_{\delta relk}$, Y_{Rrelk} and Y_X reported in Equation 4.32 are evaluated in different way for the low- and high-cycle region of the fatigue curve.

4.2.4 Method B

The permissible bending stress for method B is obtained from tests on reference gears. The reference gears were characterized by the following items² [10]:

- Helix angle $\beta = 0$;
- Module $m = 3 \div 5$ mm;
- Stress concentration factor $Y_{ST} = 2$;
- Notch parameter $q_{ST} = 2.5$;
- Roughness $R_z = 10\mu\text{m}$;
- Gear accuracy grades from 4 to 7 according to ISO 1328-1;
- Basic rack according to ISO 53
- Facewidth b from 10 mm to 50 mm;
- Load factors $K_A = K_V = K_{F\beta} = K_{F\alpha} = 1$.

Equation 4.11 applied to a reference gear can be rewritten as:

$$\sigma_{max,nom,b}^{REF.GEAR} = \frac{\sigma_{max\infty,nom,ax}^{PLAIN*}}{K_t^{REF.GEAR}} (Y_R Y_X Y_\delta)^{REF.GEAR} \nu_0 \quad (4.33)$$

Inserting Equation 4.33 into Equation 4.28 the following expression is obtained:

$$\sigma_{max,nom,b}^{GEAR} K_t^{GEAR} = \frac{\sigma_{max\infty,nom,b}^{REF.GEAR} K_t^{REF.GEAR}}{(Y_X Y_R Y_\delta)^{REF.GEAR}} (Y_R Y_X Y_\delta)^{GEAR} \quad (4.34)$$

that can be rearranged in the following way:

$$\sigma_{max,pe,b}^{GEAR} = \sigma_{max\infty,nom,b}^{REF.GEAR} K_t^{REF.GEAR} \frac{Y_\delta^{GEAR}}{Y_\delta^{REF.GEAR}} \frac{Y_R^{GEAR}}{Y_R^{REF.GEAR}} \frac{Y_X^{GEAR}}{Y_X^{REF.GEAR}} \quad (4.35)$$

Using the notation of ISO 6336 ($\sigma_{max\infty,nom,b}^{REF.GEAR} = \sigma_{Flim}$ and $K_t^{REF.GEAR} = Y_{ST}$) and assuming that for reference gears $Y_X^{REF.GEAR} = 1$, the following expression is obtained:

$$\sigma_{FP} = \sigma_{Flim} Y_{ST} Y_{\delta rel T} Y_{R rel T} Y_X \quad (4.36)$$

²Tests carried out on gears with different characteristics were adjusted and referred to reference ones.

Introducing the safety factor S_{Fmin} and the life factor Y_{NT} like in methods B_p and B_k :

$$\sigma_{FP} = \frac{\sigma_{Flim} Y_{NT} Y_{ST}}{S_{Fmin}} Y_{\delta relT} Y_{RrelT} Y_X \quad (4.37)$$

where:

- σ_{Flim} is the maximum nominal bending stress at the tooth root of the reference gears (the highest value obtained during a load cycle);
- Y_{NT} is the life factor for fatigue curves of reference gears;
- Y_{ST} is the stress concentration factor of reference gears ($Y_{ST} = 2$);
- $Y_{\delta relT}$ is the notch sensitivity factor of the gear of interest relevant to reference gears;
- Y_{RrelT} is the surface roughness factor of the gear relevant to reference gears;
- Y_X is the size factor of the gear of interest;
- S_{Fmin} is the minimum safety factor to be used for design.

Correction factors $Y_{\delta relT}$, Y_{RrelT} and Y_X reported in Equation 4.37 are evaluated in different way for the low- and high-cycle region of the fatigue curve.

4.3 Application of methods to literature data

In order to investigate the reliability of the design methods against bending fatigue of ISO 6336, methods B_p , B_k and B were applied to data available in the literature. Data of plain and notched specimens made of case-hardened steels similar to those of CDT's applications were taken from published papers. The methods were used to predict the fatigue life of a gear subject to pulsating fatigue tests. The fatigue data concerning this gear were taken from the published literature as well.

4.3.1 Results of pulsator tests on gears

Actually, few works in the literature report enough data to apply the calculation methods presented in ISO 6336. The application of method B for example needs not only the detailed geometry of the gear, but also the position of the load applied during the pulsator test. Handschuh *et al.* published a complete set of data in [68] for a standardized geometry of gear [69] used by

Table 4.2: Gear data used for calculation [68, 69].

Number of teeth	z	28
Module (mm)	m	3.175
Pitch diameter (mm)	d	88.9
Tooth width (mm)	b	6.35
Circular pitch (mm)	p	9.975
Addendum (mm)	h_a	3.175
Dedendum (mm)	h_f	4.445
Tooth height (mm)	h_w	7.620
Pressure angle ($^\circ$)	α	20
Tip Diameter (mm)	d_a	95.250
Root Diameter (mm)	d_f	80.010
Base Diameter (mm)	d_b	83.539
Root fillet radius (mm)	ρ	1.02-1.52
Measurement over pins (mm)	M_{dk}	96.03 to 96.30
Pin diameter (mm)	D_M	5.5
Hob tip radius (mm)	ρ_{aP0}	1.1176
Surface roughness (μm)	R_{ms}	0.4

Gear tolerances: AGMA class 11, which
corresponds to ISO 1328 class 5.

NASA. The data of the gear are reported in Table 4.2. The gears were made of AISI 9310 case-hardened steel, having the chemical composition reported in Table 4.3. In the table are reported also the chemical compositions of the other steels taken from the literature and analyzed in this section.

Since ISO 6336 uses peak-to-valley surface roughness (R_z), the root-mean-squared surface roughness R_{ms} reported in [68] was converted using the following expressions, taken from [70] and [45] respectively:

$$R_{ms} = 1.25R_a \quad (4.38)$$

$$R_z = 6R_a \quad (4.39)$$

The pulsator test rig used in [68] was made of two loading rods acting on a couple of teeth, see Figure 4.6. The fixture of the test rig permitted an angular rotation of the gear along its axis. This permitted to adjust the diameter where the tooth under test contacts the loading rod. The diameter used in the tests was that one identifying the Highest Point of Single Tooth Contact (HPSTC) of two identical gears. This is an important aspect, since the tooth root peak stress is calculated under the HPSTC conditions according

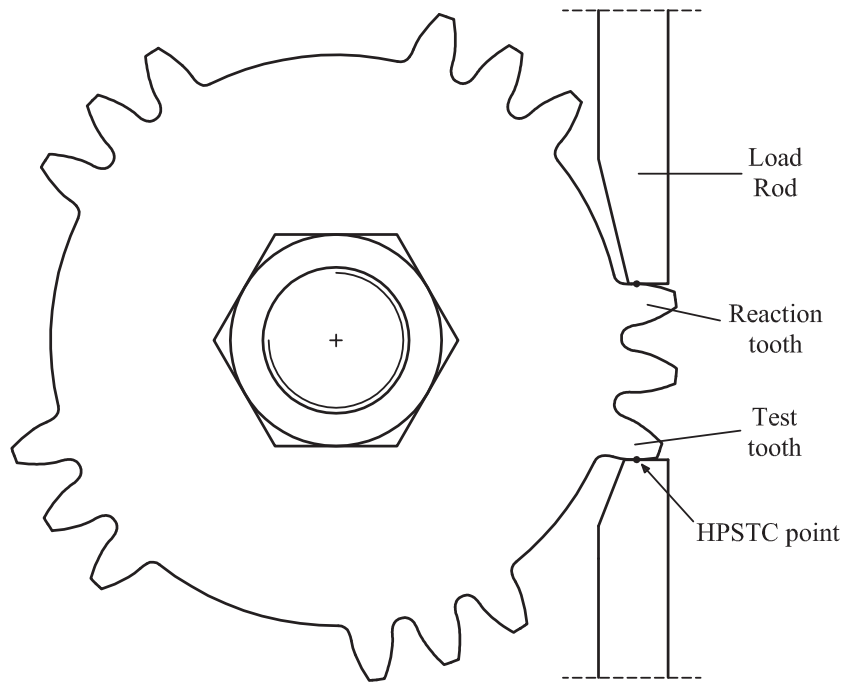


Figure 4.6: Schematic picture of the pulsator test rig used in [68].

to method *B* of ISO 6336. This means that the σ_F calculated using method *B* can be associated to the experimental life obtained during the pulsator test without any adjustment.

The contact on the reaction tooth took place on a diameter smaller than the HPSTC diameter. This meant that failure happened always on the tooth under test. The HPSTC diameter resulted 90.117 mm. Since the tooth profile was an involute, each point along the tooth flank had the property to have a normal tangent to the base circle. This means that independently from the position of the contact point between tooth and rod, the applied load generated a torque T of:

$$T = F_N \frac{d_b}{2} \quad (4.40)$$

where F_N is the pushing force applied by the rods and d_B is the base circle diameter. The bending stress at tooth root fillet σ_{F0} was evaluated according to ISO 6336 [41], taking advantage of a KissSoft model of a gear pair where two identical gears (see Table 4.2) were modeled (according to original paper [68]). The calculations were made by imposing an input torque evaluated with Expression 4.40 on one gear.

Table 4.3: Chemical composition of case-hardened steels declared in original papers.

Steel	Source	C	Ni	Cr	Mo	Cu	Mn	Si	S	P
AISI 9310	[68]	0.10	3.22	1.21	0.12	0.13	0.63	0.27	0.005	0.005
SAE 8620	[71]	0.18	0.6	0.59	0.24	-	0.72	-	-	-
SNC 21	[72]	0.15	2.05	0.35	-	0.19	0.61	0.26	0.008	0.017
20CrMo4*	[36]	0.21	-	1.08	0.27	-	0.8	0.27	0.008	0.007
20MnCr5	[29, 30]	-	-	-	-	-	-	-	-	-
SAE 4320	[29, 30]	-	-	-	-	-	-	-	-	-
SAE 8822	[29, 30]	-	-	-	-	-	-	-	-	-
PS 18	[29, 30]	-	-	-	-	-	-	-	-	-
JIS SCr420	[31]	0.19	0.07	1.02	-	0.18	0.69	0.24	0.014	0.024
SAE 5120	[38]	0.205	0.216	1.21	0.043	0.157	1.21	0.281	0.031	0.0095

*Steel designation was gathered from chemical composition and was not reported in [36]

Table 4.4: Calculation factors for bending stress calculation.

Application factor	K_A	1
Dynamic factor	K_V	1
Face load factor	$K_{F\beta}$	1
Transverse load factor	$K_{F\alpha}$	1
Form factor	Y_F	1.74
Stress correction factor	Y_S	1.74
Helix factor	Y_β	1
Rim thickness factor	Y_B	1
Deep tooth factor	Y_{DT}	1

Since the pulsator test was made on a fixed gear (no rotation and no shaft deflections), the evaluation of the actual bending stress σ_F was made setting the multiplying K-factors of Equation 4.17 equal to 1. All the calculation factors are reported in Table 4.4. During the pulsator test, rod forces were applied with a load ratio very close to zero ($R \approx 0$). The loads applied during the pulsator test are reported in Table 4.5 along with the corresponding stress ratio, torque used for calculations, bending stress at tooth root and fatigue life. The failure criterion used by the authors to determine the fatigue life was the detection of a crack of the same dimensions of the case-hardened layer.

The authors evaluated the linear elastic bending stress at the tooth root using a 2D FE-model developed by themselves. The bending stress σ_F evaluated using ISO 6336 was in good agreement with values obtained by the authors, being 3.7% the maximum difference.

Since ISO 6336 provides life predictions at 99% of survival probability, the experimental fatigue points were elaborated accordingly, under the assumptions of constant scatter band and Log-normal distribution of fatigue life. The experimental points, the regression line and the lower-bound curve at 99% of survival probability are reported in Figure 4.7. The statistical analysis was made considering all the available points. It is easy to see that only the low-cycle portion of the curve was investigated. To built a complete fatigue curve, the prescriptions of ISO 6336 were used: the Standard states that the slope of the curve is constant and that the low-cycle and high-cycle knees are located at 1,000 and 3,000,000 cycles respectively. The Wohler inverse slope resulted $k = 7.28$.

Table 4.5: Pulsar test parameters and fatigue lives [68].

Max load	Min load	Stress ratio	Torque	σ_F (ISO 6336)	Fatigue life
[N]	[N]	[-]	[Nm]	[MPa]	[cycles]
15569	222	0,01	650	2203	4721
15618	512	0,03	652	2210	6679
18260	187	0,01	763	2584	855
18153	89	0,00	758	2569	1208
16734	111	0,01	699	2368	2181
15542	351	0,02	649	2199	2235
15507	343	0,02	648	2194	2108
16401	316	0,02	685	2321	4524
16347	271	0,02	683	2313	4170
16369	311	0,02	684	2316	3426
17735	276	0,02	741	2510	2151
17722	240	0,01	740	2508	1163
16534	165	0,01	691	2340	1095
16525	209	0,01	690	2338	2000
16530	173	0,01	690	2339	1638
16681	218	0,01	697	2360	1752
18656	133	0,01	779	2640	1900
18678	191	0,01	780	2643	1242
18878	440	0,02	789	2671	462
18905	445	0,02	790	2675	348
20969	311	0,01	876	2967	190
21129	262	0,01	883	2990	638
22308	529	0,02	932	3157	460
22250	325	0,01	929	3148	498
13318	187	0,01	556	1885	14800
13362	178	0,01	558	1891	16400

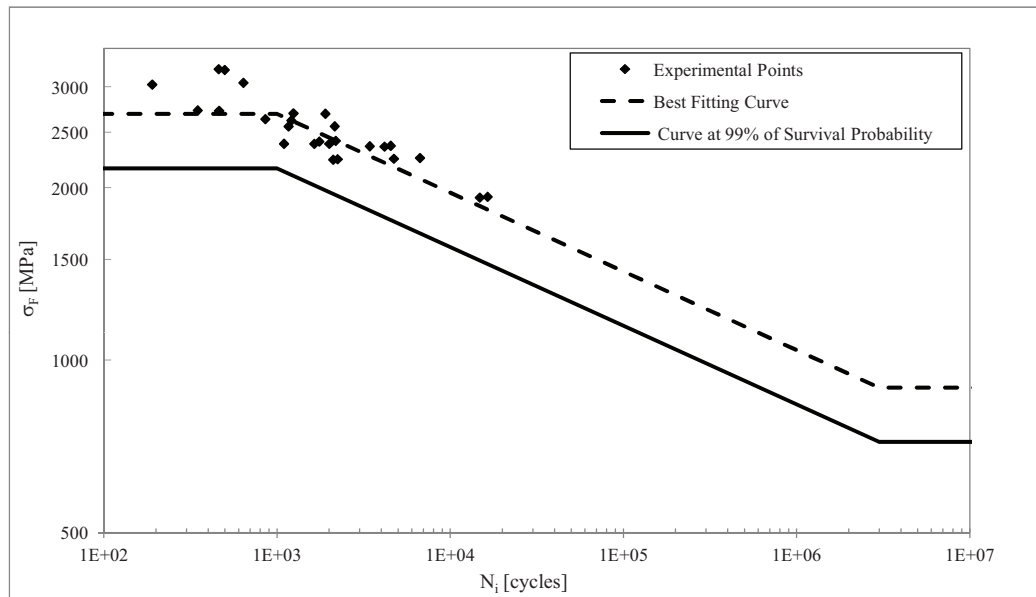


Figure 4.7: Experimental points of pulsator test [68] and statistical curves at 50% and 99% of survival probabilities.

Table 4.6: Plain specimens geometry and original bending fatigue limit for a survival probability of 99% (K_V , K_l and K_d factors are referred to $R = -1$) [71, 72, 36].

Steel	Test type	K_V	Surface finishing	K_l	d [mm]	K_d	σ_R [MPa]	$\sigma_{plim,a,R=-1}^\circ$ [MPa]	N_{lim} [cycles]	Inverse slope
SAE 8620	RB	1.25	Polished	1	\emptyset 10	1	1596	756	1E6	15.4
SNC 21	PB	1.00	Machined	1.3	\square 14x3,5	1	-	596	1E6	6.9
20CrMo4	RB	1.25	Polished	1	\emptyset 5.97	1	-	868	6E6	22.8

PB = Plane Bending; RB = Rotating Bending; d = section diameter

Table 4.7: Notched specimens geometry and original bending fatigue data at 99% of survival probability (K_V , K_l and K_d factors are referred to a stress ratio $R = -1$).

Steel	Test type	R	K_V	Surface finishing	R_z [μ m]	Notch	$\sigma_{klim,a,R}^\circ$ [MPa]	N_{lim} [cycles]	Inverse slope
20MnCr5	PB	0.2	1	Ground	<i>4.8</i>	X	226	1.5E5	8.33
SAE 4320	PB	0.2	1	Ground	<i>4.8</i>	X	230	1.0E5	8.94
SAE 8822	PB	0.2	1	Ground	<i>4.8</i>	X	232	6.0E4	7.99
PS 18	PB	0.2	1	Ground	<i>4.8</i>	X	202	1.0E5	11.2
JIS SCr420	PB	0	1	Machined	12	Y1	245	6.0E6	19.3
JIS SCr420	PB	0	1	Machined	12	Y2	336	1.0E7	34.96
SAE 5120	A	0	1.4	Ground	3.6	Z	325	7.0E7	17.57
SAE 5120	A	-1	1.4	Ground	3.6	Z	398	7.0E7	15.62

A = Axial test. Italic values were assumed because not explicitly reported in original papers.

4.3.2 Fatigue data of plain specimens

For the application of method B_p the fatigue curves of polished plain specimens under $R = 0$ plane bending tests are needed. Curves like these were not found in the literature for case-hardened steels commonly used to manufacture gears. Therefore, the transformation of fatigue curves obtained under different testing conditions was necessary to obtain curves suitable for the application of B_p method. The Table 4.6 reports the details of the fatigue tests taken from the literature [71, 72, 36] and considered in the present chapter. Steel, test type, surface finishing, section shape, ultimate tensile stress (if available) and fatigue properties for a survival probability of 99% (number of cycles of high-cycle knee N_{lim} , fatigue limit $\sigma_{plim,a,R=-1}^\circ$, inverse slope of the curve) are reported.

The apex $^\circ$ refers to original fatigue data under given test conditions (surface roughness R_z , geometry of the specimens and load type). For the original data reported in Table 4.6 the stress ratio was equal to $R = -1$. All selected results were relevant to widely adopted case-hardened steels and common case-hardening processes (gas carburization, direct quenching and tempering), while materials having special chemical compositions or special treatments were discarded from the analysis here presented. Chemical compositions of the steels is reported in the previous Table 4.3.

In the original papers, only the high-cycle portion of the fatigue curves was reported, so that the low-cycle knee of the curves had to be estimated. The knowledge of the $(\sigma_{pstat}, N_{stat})$ coordinates of the low-cycle knee is an important aspect, since the algorithm for the estimation of the allowable fatigue curves involves the correction of both the allowable stresses of the high- and low-cycle knees (σ_{plim} and σ_{pstat}) by means of some correction factors (cfr. Sections 4.2.2, 4.2.3 and 4.2.4).

The low-cycle knee was set differently depending on whether the ultimate tensile strength σ_R was reported or not. The process for the definition of the low-cycle knee $(N_{stat}, \sigma_{p,stat,a,R}^\circ)$ at 99% of survival probability is reported in Figure 4.8. If σ_R was explicitly reported, the low-cycle knee of the fatigue curve was set at the intersection between the sloping part of the curve evaluated for a survival probability of 50% and σ_R . $\sigma_{pstat,a,R}^\circ$ was then determined as the stress at the low-cycle knee of the curve with a survival probability of 99%. If σ_R was not reported, the low-cycle knee was fixed at 1000 cycles on the 99% survival probability curve, according to ISO 6336. The ultimate tensile stress for a survival probability of 99% ($\sigma_{R,99\%}$) was then determined using the following equation:

$$\sigma_{R,99\%} = \frac{2\sigma_{p,stat,a,R}^\circ}{1 - R} \quad (4.41)$$

The 99% survival probability curve was determined under the hypothesis of constant scatter with respect to the applied stress amplitude. Results were then converted to ISO 6336 nominal conditions by modifying the fatigue limits obtained during the original tests, with a number of correction coefficients to take into account: surface roughness and manufacturing process (K_l factor), dimensions (K_d factor), test type (K_V factor) [73], and stress ratio (R). The following equation was used to pass from as-tested conditions to polished, net section size dimension lower than 10 mm, and plane bending conditions:

$$\sigma_{plim,a,R=-1} = \sigma_{plim,a,R=-1}^{\circ} K_l K_V K_d \quad (4.42)$$

where $\sigma_{plim,a,R=-1}$ is the fatigue limit in terms of stress amplitude for the just mentioned conditions, but for $R = -1$. Conversion to $R = 0$ was then made using Haigh equation:

$$\sigma_{plim} = 2\sigma_{plim,a,R=0} = 2 \cdot \frac{\sigma_{R,99\%} \cdot \sigma_{plim,a,R=-1}}{\sigma_{R,99\%} + \sigma_{plim,a,R=-1}} \quad (4.43)$$

Concerning the low-cycle knee, σ_{pstat} was determined according to Equation 4.41, considering that no correction factors were applied to low-cycle knee stress:

$$\sigma_{pstat} = 2\sigma_{pstat,a,R}^{\circ} \quad (4.44)$$

The fatigue curves obtained connecting the low-cycle and high-cycle knees are reported in Figure 4.9, where the maximum stress (and not the stress amplitude) is adopted, according to ISO 6336. As it can be seen from the picture, the curves are very different. This is a consequence of taking data from different case-hardened steels and of transforming the curves by means of K_l , K_d and K_V factors. It must be precised that the curves are drawn following the prescription of ISO 6336 where the experimental data were not sufficient to draw the curves. The fatigue limit is reported as an horizontal line up to 1E10 cycles (cfr. Figure 4.10) even if the staircase sequences reported in the original papers were terminated at lower lives. Since the purpose of the analysis here presented is to check the reliability of ISO 6336, the curves are built following ISO prescriptions where no data were available.

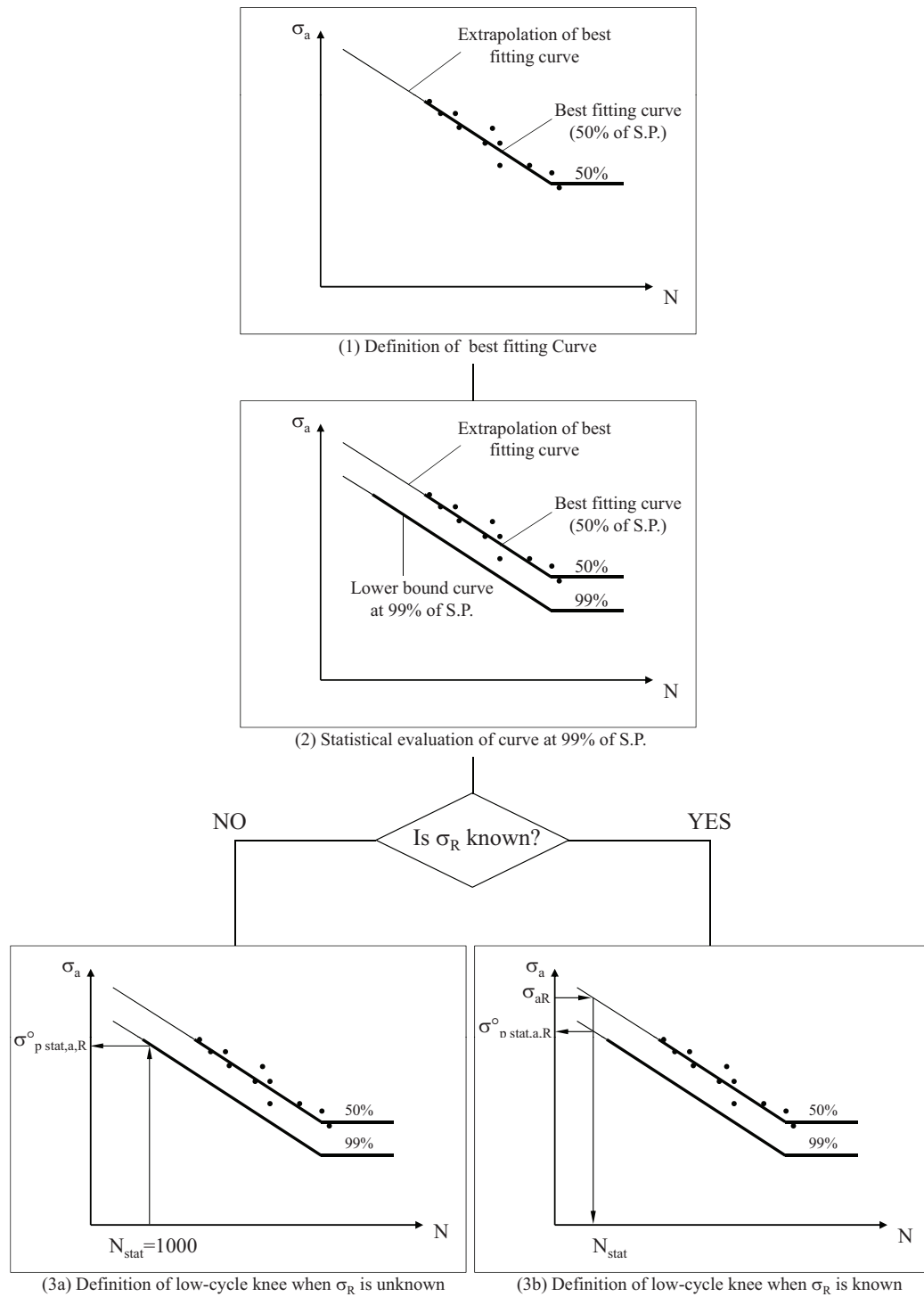


Figure 4.8: Definition of the low-cycle knee of specimens' fatigue curves. The curves are relevant to a generic stress ratio R .

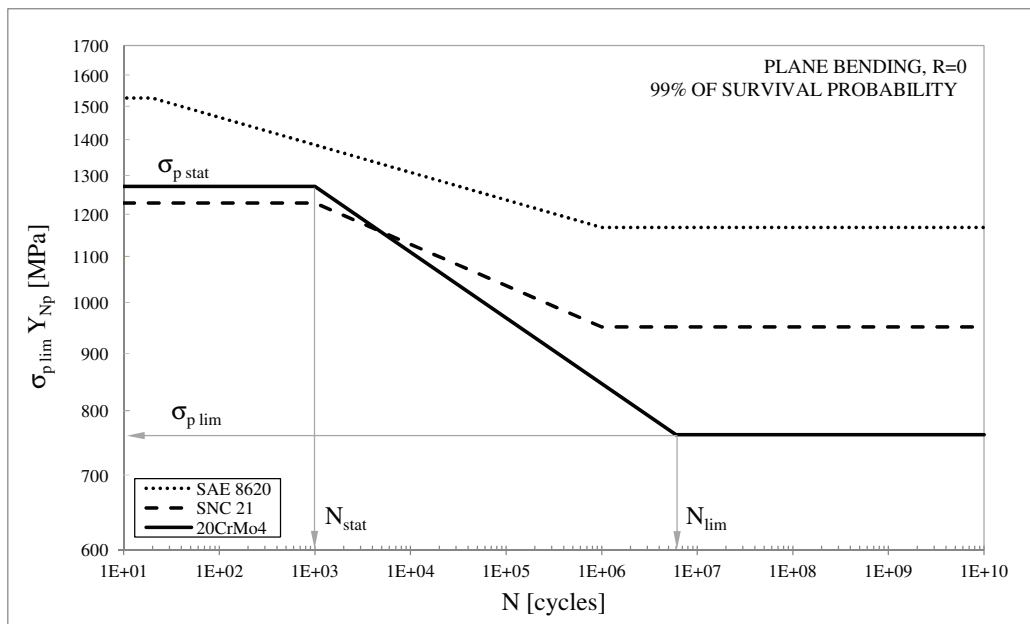
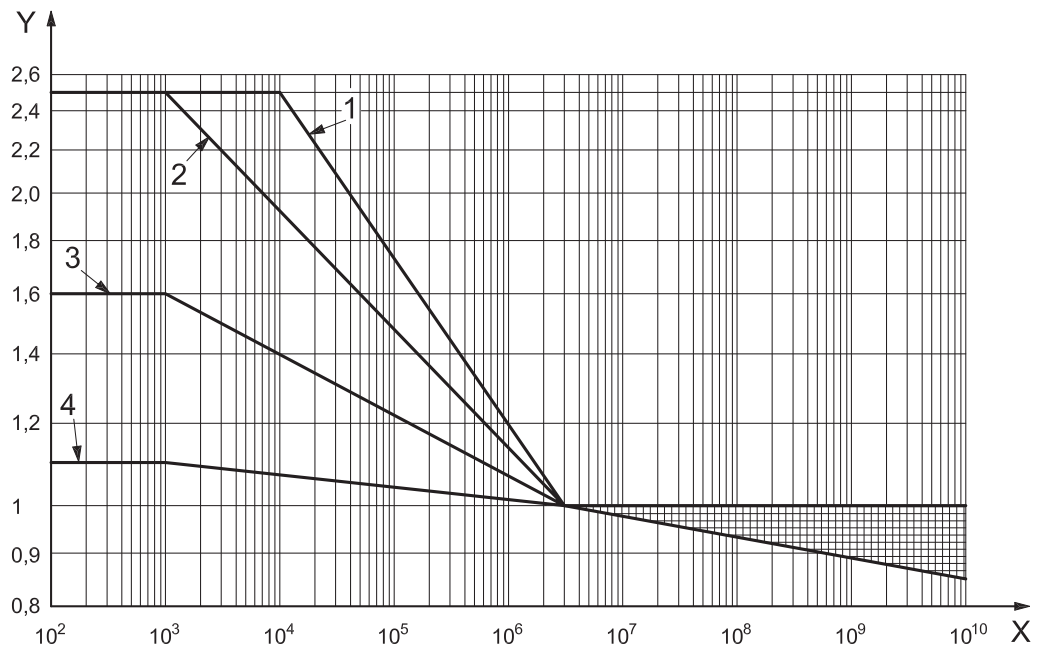


Figure 4.9: Bending fatigue curves of plain specimens under reference conditions (plane bending, polished condition, specimen size around 10 mm, $R = 0$) estimated from the original papers [71, 72, 36]

**Key**

X number of load cycles, N_L

Y life factor, Y_{NT}

1 GTS (perl.), St, V, GGG (perl. bai.)

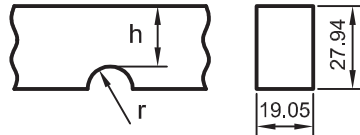
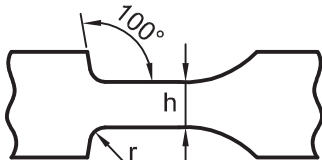
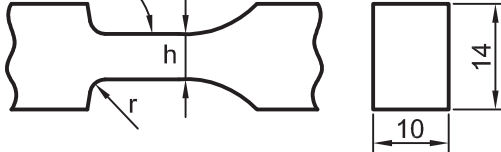
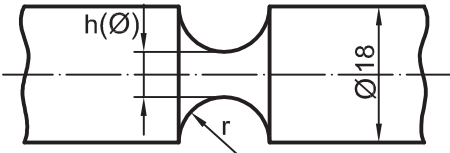
2 Eh, IF (root)

3 NT, NV (nitr.), GGG (ferr.), GG

4 NV (nitrocar.)

Figure 4.10: Standardized fatigue curves suggested for gears by ISO 6336 [41]. The meaning of material symbols are reported in Table 4.1.

Table 4.8: Notch and section geometries of the specimens tested in [29, 30, 31, 38].

Notch	Geometry and section dimensions	r [mm]	h [mm]	K_d	Y_{Sk}
X		7.62	21.59	1.11	1.63
Y1		0.5	6	1	2.02
Y2		2	6	1	1.36
Z		6	6	1	1.20

4.3.3 Fatigue data of notched specimens

Method B_k starts from pulsating ($R = 0$) bending fatigue tests of notched, flat test pieces. Surface roughness and notch geometry of the specimens are not defined by the standard. However, it should be noted that ISO 6336 suggests that specimens with a notch factor similar to that of the gear should be adopted in experimental fatigue tests.

The data taken from the literature and here analyzed are reported in Table 4.7, while the details of notch geometries of the specimens are reported in Table 4.8.

Due to uncertainties concerning notch sensitivity in static strength, the low-cycle knees of the original fatigue curves were assumed at 1000 cycles even if σ_R from a tension test on plain specimens was explicitly given in the original papers. By so doing, the values of $\sigma_{kstat,a,R}^\circ$ were determined on the 99% survival probability curve obtained from original fatigue data. $\sigma_{R,99\%}$ was then estimated according to Equation 4.41, where $\sigma_{pstat,a,R}^\circ$ must be substituted now by $\sigma_{kstat,a,R}^\circ$. The low-cycle knee stress σ_{kstat} was set equal to $\sigma_{R,99\%}$. Since different test conditions were used in the original papers, conversion to ISO 6336 requirements was necessary for the fatigue limit. To take into account the specimen's dimensions and the load type of the original tests, K_d and K_V factors were used. Since K_d and K_V are provided in the literature for $R = -1$ stress ratio [73], the fatigue curve of the original papers was firstly converted to $R = -1$ (if necessary), using the Haigh equation:

$$\sigma_{klim,a,R}^\circ = \frac{1}{\sigma_{klim,a,R=-1}^\circ} + \frac{1+R}{1-R} \frac{1}{\sigma_{R,99\%}} \quad (4.45)$$

where $\sigma_{klim,a,R=-1}^\circ$ is the fatigue limit estimated for $R = -1$ starting from that reported in Table 4.7, taken from the original papers. K_d and K_V factors were then applied using the following equation:

$$\sigma_{klim,a,R=-1} = \sigma_{klim,a,R=-1}^\circ K_V K_d \quad (4.46)$$

where $\sigma_{klim,a,R=-1}$ is the estimated bending fatigue limit of the notched specimens for alternating stress. The bending fatigue limit as defined by ISO 6336 for pulsating stress ($R = 0$) was finally determined using the following equation:

$$\sigma_{klim} = 2\sigma_{klim,a,R=0} = 2 \frac{\sigma_{R,99\%} \cdot \sigma_{klim,a,R=-1}}{\sigma_{R,99\%} + \sigma_{klim,a,R=-1}} \quad (4.47)$$

Resulting curves obtained connecting low-cycle and high-cycle knees are reported in Figure 4.11, where the maximum nominal bending stress is adopted, according to ISO 6336.

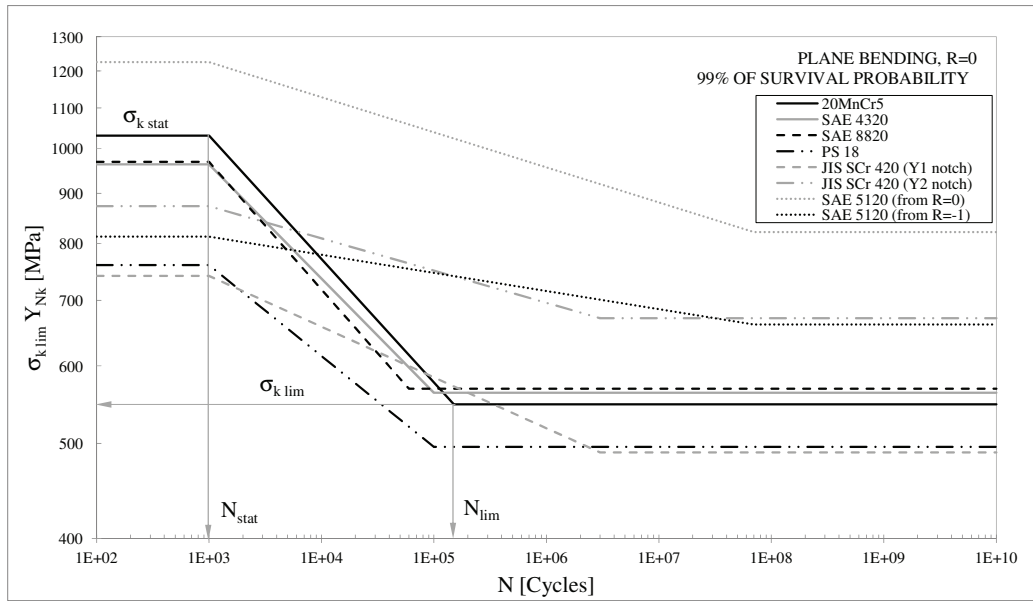


Figure 4.11: Bending fatigue curves nominal bending stress (in terms of $\sigma_{klim} Y_{Nk}$) of notched specimens under reference conditions (plane bending, specimens' size around 10 mm, $R=0$). Curves were estimated from notch fatigue data reported in the original papers [29, 30, 31, 38].

It must be precised that the fatigue limits are reported as an horizontal line up to 1E10 cycles (cfr. Figure 4.10) even if the staircase sequences reported in the original papers were terminated at lower lives. Since the purpose of the analysis here presented is to check the reliability of ISO 6336, the curves were built following ISO prescriptions.

Table 4.9: Correction factor using Method *B*.

Factor	Low-cycle knee	High-cycle knee
S_{Fmin}	1	1
Y_{ST}	2	2
$Y_{\delta relT}$	0.886	0.992
Y_{RrelT}	1	1.058
Y_X	1	1

Table 4.10: Correction factor using Method B_p .

Factor	Low-cycle knee	High-cycle knee
S_{Fmin}	1	1
Y_δ	1.562	1.026
Y_R	1	0.972
Y_X	1	1

Table 4.11: Correction factors using Method B_k .

Steel	Low-cycle knee		High-cycle knee	
	Y_{Sk}	$Y_{\delta relk}$	$Y_{\delta relk}$	Y_{Rrelk}
20MnCr5	1.628	1.068	1.004	1.040
SAE 4320	1.628	1.068	1.004	1.040
SAE 8822	1.628	1.068	1.004	1.040
PS 18	1.628	1.068	1.004	1.040
JIS SCr420(Y1)	2.02	0.887	0.967	1.096
JIS SCr420(Y2)	1.36	1.242	1.003	1.096
SAE 5120(R0)	1.14	1.434	1.017	1.026
SAE 5120(R-1)	1.14	1.434	1.017	1.026

$Y_{Rrelk} = 1$ for each steels for low-cycle knee
 $S_{Fmin}, Y_X = 1$ for both low-cycle and high-cycle knees

4.3.4 Application of methods B , B_p and B_k to literature data

Methods B , B_p and B_k were applied to estimate the fatigue strength of the gears tested in [68]. The correction factors to evaluate the allowable bending stress σ_{FP} are reported in Tables 4.9, 4.10 and 4.11 (distinguishing for the low- and high-cycle knees) for methods B , B_p and B_k respectively. The expressions used to calculate the factors are reported in ISO 6336-3 [41]. The fatigue curves obtained using method B are reported in Figure 4.12 along with the experimental results and the corresponding curve at 99% of survival probability obtained from pulsator tests on the analyzed gear [68]. The curves are referred to the best quality of case-hardened steels (ME: $\sigma_{Flim} = 525$ MPa), the worst quality (ML: $\sigma_{Flim} = 312$ MPa), and the near-worst condition of the medium quality (MQ: $\sigma_{Flim} = 430$ MPa). It is worth noting that method B leads to curves with the same slope, while the fatigue limit decreases according to the quality of the steel. ISO 6336 distinguishes the steel classes solely on the basis of a number of quality controls that must be carried out on the steel and the gear, but not explicitly on the basis of the material fatigue properties. Figure 4.12 shows that the slope of experimental and estimated fatigue curves are quite different. However, if the worst steel quality is adopted in fatigue design, method B provides estimations on the safe side. It is worth recalling that experimental results were generated only in the low-cycle portion of the curve, so that a robust comparison in the high-cycle regime cannot actually be made.

The fatigue curves obtained using method B_p are reported in Figure 4.13. They estimate the experimental results of the pulsator test more closely than the curves derived from method B . It is worth noting that the notch sensitivity factor Y_δ referred to the low-cycle knee (see Table 4.10) is significantly greater than 1, i.e. the gears were supposed to be notch insensitive in low-cycle region. The most important peculiarity of this method is that specific fatigue properties determined by material, manufacturing process and heat treatment can be directly taken into account in the calculations, as demonstrated by the variability of slopes and positions of the three fatigue curves estimated using this method.

Results obtained by applying method B_k are reported in Figure 4.14. It can be recognized that the fatigue curves estimated from SAE 5120 steel specimens were very different from the other ones. SAE 5120 specimens were indeed cylindrical and tested with an axial load, while the specimens made of the other steels were flat and tested in plane bending (as recommended by the Standard). Original test conditions (stress ratio, notch geometry and load type) can thus strongly affect the results of this method, depending on

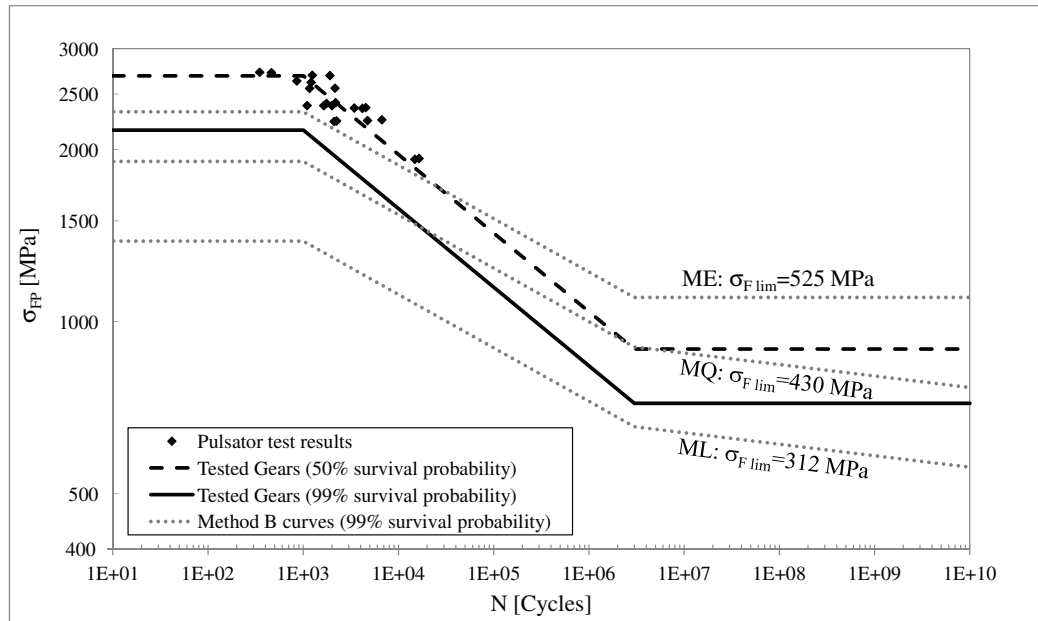


Figure 4.12: Experimental points [68] and fatigue curves calculated by applying ISO 6336 method *B*.

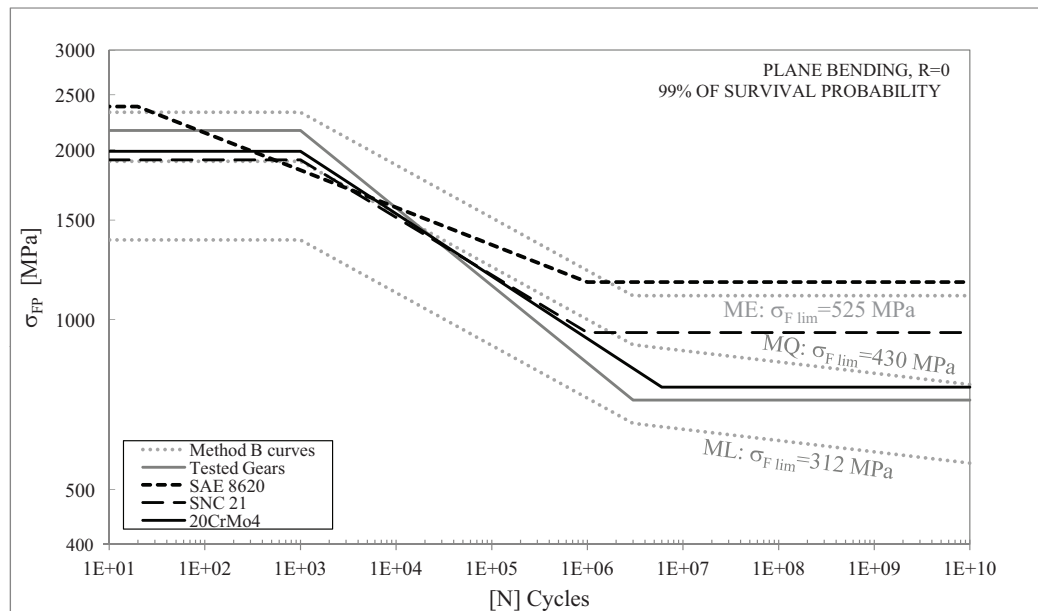


Figure 4.13: Fatigue curves calculated by applying method *B_p* and comparison with experimental results of pulsator tests [68] and method *B*.

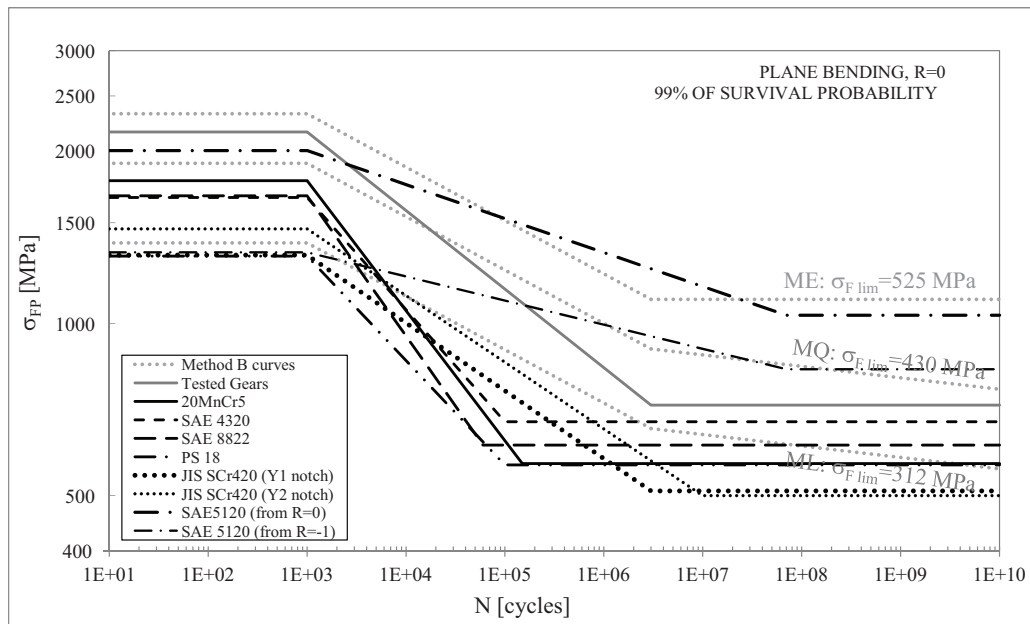


Figure 4.14: Fatigue curves calculated by applying method B_k and comparison with experimental results of pulsator tests [68] and method B .

the correction coefficients considered in the estimation of the fatigue curves for ISO 6336 reference conditions. Figure 4.14 shows that the curves resulting from method B_k (with the exception of SAE 5120) are steeper than the curves predicted by method B , and that the slope of the tested gears is roughly between those predicted by methods B_k and B . Fatigue curves using method B_k are much more in the safe side than either methods B and B_p . The distribution of the resulting fatigue curves in Figure 4.14 shows that method B_k can effectively take into account the notch fatigue behavior of different case-hardened steels. It is interesting to note that Table 4.11 shows that the reference fatigue curves reported in Figure 4.11 were modified by the correction factors more in the low-cycle than in the high-cycle regime.

4.3.5 Summary of the exploratory analyses

Starting from fatigue data taken from the literature, the application of methods B , B_p and B_k actually led to scattered results. It must be remembered that the analysis here reported is based on fatigue data relevant to different type of specimens and loading conditions, along with few experimental points available for gears. For these reasons, the analysis here presented should be considered as only an exploratory study, with the purpose

to highlight macro characteristics of the methods and identify the critical aspects. The study was limited by the lack in the open literature of homogeneous and complete sets of fatigue data of smooth specimens, notched specimens and gears made of the same steel. In fact, the application of the methods reported in ISO 6336 Standard requires lots of data concerning the geometry of the gear and the loading conditions, since ISO 6336 assumes to estimate linear elastic peak stress in the tooth root fillet when the HPSTC loading conditions are applied. If it is not the case, the stress on tooth root fillet declared in the articles cannot be compared directly to ISO predictions. This aspect strongly limited the number of works available in the literature to the unique work here analyzed [68].

Even with the just mentioned limitations, the analysis based on literature data showed the importance of following the testing procedures suggested by the Standard, since the conversion of the data from test made under different loading conditions leads to unreliable results. The use of data coming from specimens can highlight differences in terms of fatigue properties from one case-hardened steel to another. For example, the fatigue knee position obtained using data obtained from specimens can be significantly different in terms of number of cycles from the standardized fatigue knee of the Standard, which is located at 3,000,000 cycles.

The application of ISO methods to literature data showed the necessity of further investigations, using a homogeneous sets of fatigue data obtained from $R=0$ plane bending tests on specimens and gears made of the same steel. For this reason, pulsator bending tests were carried out on a gear used on CDT applications. The gear was made of the steel 1 (20MnCr5) presented in Chapter 3. Results are shown in next sections.

4.4 Fatigue tests on gears

The application of the design methods reported in ISO 6336-3 [41] did not lead to satisfactory results starting from literature data. Several approximation were necessary in such analysis, and therefore there was poor reliability on the results. To overcome this limitation, it was decided to draw the bending fatigue curve of a gear used by the Company made in 20MnCr5 (steel 1). In such a way, all the data necessary for the application of methods B , B_p and B_k were available and homogeneous, making it possible to investigate to which extent the different methods match the experimental results.

In order to satisfy the prescriptions of ISO 6336, and to be consistent with the loading conditions imposed on specimens in Chapter 3, pulsator tests (plane bending) were carried out on the gear teeth. A minimum pre-load

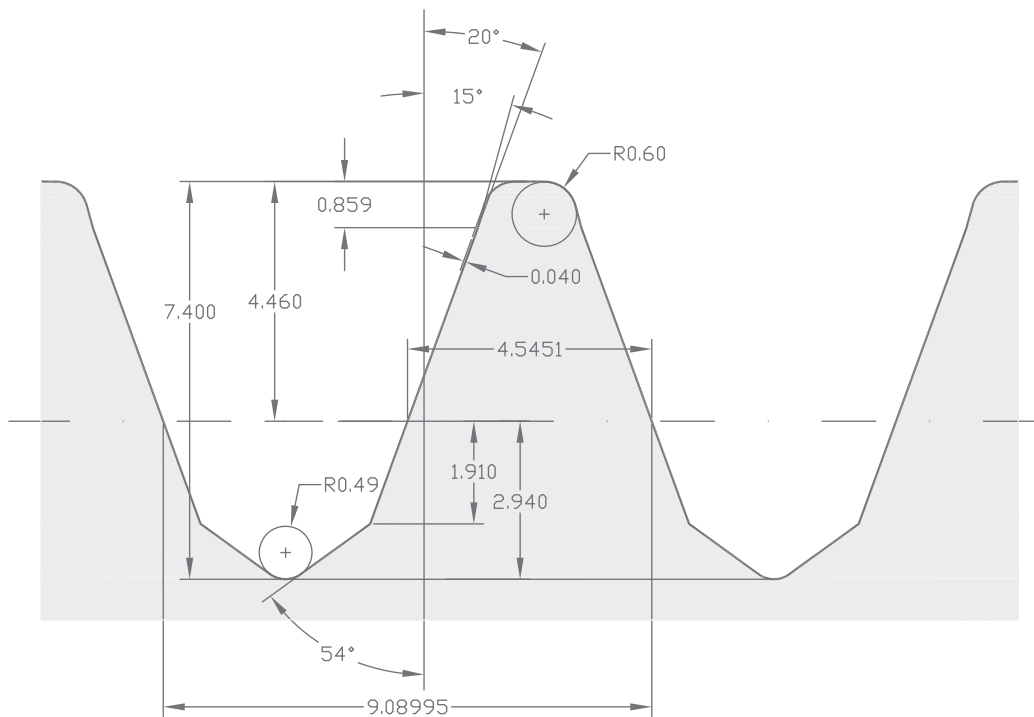


Figure 4.15: Hob used to manufacture the gears (module $m = 2.89342$ mm). Dimensions are in millimeters.

was necessary to perform the fatigue tests, therefore the stress ratio during the tests was $R = 0.1$. Actually, ISO 6336 prescribes to apply a stress ratio equals to $R = 0$. However, the differences on the stress amplitude at endurance limit under the two working conditions was considered negligible in this work.

4.4.1 Pulsator tests on 20MnCr5 gears

The geometrical dimensions of the 20MnCr5 gears under test are reported in Table 4.12. The real hob dimensions (see Figure 4.15) were used to model the final geometry of the 20MnCr5 gear, using KissSoft Software [4]. The corresponding geometry of the gear is reported in Table 4.12. It is interesting to note that the pressure angle of the gear is different from that of the hob. This is due to the hob has a pitch diameter that is different from the primitive circle of the gear. Only if the theoretical rolling circle of the hob and the gear are the same, then pressure angles, modules and pitches of hob and gear coincide. If the rolling circle of the hob is different from that one of the

Table 4.12: Geometrical parameters of tested gears.

Number of teeth	z	23
Module (mm)	m	3
Pressure angle ($^\circ$)	α	25
Profile shift coefficient	x^*	0.4422
Pitch diameter (mm)	d	69
Face width (mm)	b	30
Tip diameter (mm)	d_a	77.6
Root diameter (mm)	d_f	63.277
Root form diameter (mm)	d_{Ff}	65.193
Base diameter (mm)	d_b	62.535
Root fillet radius (mm)	ρ_F	0.8
Diameter of pins (mm)	d_m	6
Measurements over pins (mm)	M_{dk}	80.391
Crowning (μm)	C_b	$8 \div 18$
Root surface roughness (μm)	R_z	11.25
Inner diameter (mm)	d_{bi}	42.4

gear, the geometrical parameters of the hob must be adjusted. Probably, the suppliers had a 20° -pressure-angle hob, and decided to use it to manufacture the gear. The base diameter of the hob and of the gear must be the same in order to keep the tooth profile constant. The rolling diameter of the hob resulted therefore:

$$d_{HOB} = \frac{d_b}{\cos \alpha_{HOB}} = \frac{62.535}{\cos 20^\circ} = 66.5448 \text{ mm} \quad (4.48)$$

This means that the pitch of the hob is:

$$p = \frac{\pi d_{HOB}}{z} = \frac{66.5448\pi}{23} = 9.08994 \text{ mm} \quad (4.49)$$

that corresponds to a module of:

$$m_{HOB} = \frac{p}{\pi} = \frac{9.08994}{\pi} = 2.8934 \text{ mm} \quad (4.50)$$

The gear was forged before being cut by the hob. This is the reason why in specimens' test plan high values of rolling ratio (15 in the case of 20MnCr5) were required for the steel bars. The idea was to try to simulate the forged status of gear fibers, even if it is only an approximation, since forging leads to a different disposition of fibers in gear teeth from that one of the specimens.

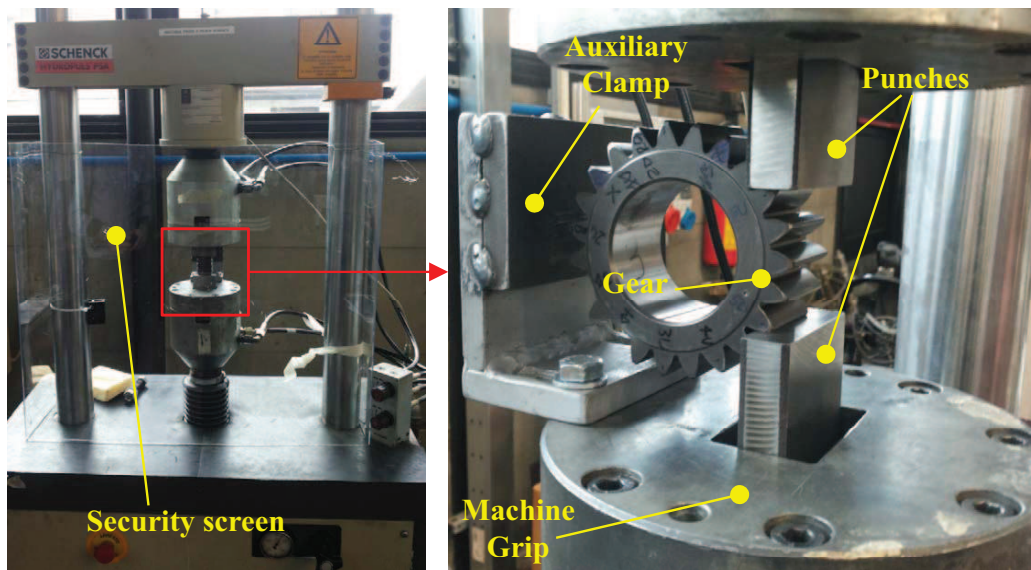


Figure 4.16: Equipment used to perform the pulsator tests.

Pulsator tests were carried out using a SCHENCK axial testing machine (load capacity 100 kN, TRIO SISTEMI RT3 digital controller) that was equipped with two punches acting on a couple of gear teeth (see Figure 4.16). The punches were made in 49CrMo4 quenched and tempered steel, in order to be have a good contact resistance. However, case-hardened gear teeth resulted harder than the punches, therefore after some tests the punches were ground on the surfaces in contact with the teeth in order to ensure a good contact quality. The equipment used to perform the test was constituted also of polycarbonate screens to protect the operator from being hit by the teeth broken during the test. For safety reasons and to help the operator to place the gear between the punches, an auxiliary clamp was used.

The tests were carried out under a stress ratio $R = 0.1$ to simulate the working conditions of a drive gear. Test frequency was in the range of $2 \div 18$ Hz, depending on the applied load. A schematic of the loading conditions is reported in Figure 4.17: the lower punch applies the load cyclically, while the upper punch is fixed. The punches touch the teeth at a nominal diameter of contact equals to $d_{cont} = 74.94$ mm. This is an important datum, since the position of load application is important in the definition of the tooth root bending stress. The normal to the flank profiles of the teeth passing through the contact points is tangent to the base diameter.

Up to 5 tests were performed on a single gear, changing the teeth under test paying attention to leave an un-tested tooth before and after each new tooth to test. Each couple of tested gear was marked with a code consisting of a

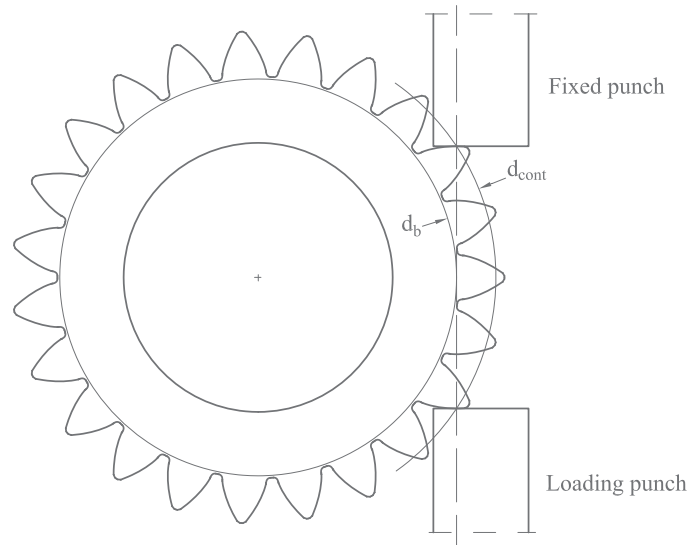


Figure 4.17: Schematic working conditions of the pulsator tests on gears ($d_b = 62.535$ mm, $d_{cont} = 74.94$ mm).

number (that identifies the gear), “_”, and another number identifying the couple of teeth. The upper tooth of a couple of teeth was then marked with “U”, the lower with “D”. Therefore, 5_3U indicates the upper teeth of the couple of teeth number 3 of the gear number 5.

The fatigue curve obtained from pulsator tests as maximum compressive load versus number of cycles to failure is reported in Figure 4.18. Staircase tests were carried out according to the sequence reported in the picture, using a target life of 3 millions of cycles. The results show again that the fatigue knee is located around 100,000 cycles, as it was shown from notched specimens C1 under plane bending tests (see Chapter 3). The scatter is higher at the fatigue limit than the finite life region, as it was show from specimens X1.

It is interesting to analyze the stiffness of the gears recorded by the testing machine during the tests. Maximum and minimum applied forces (F_{max} , F_{min}) and displacements (f_{max} , f_{min}) were acquired during the test at prefixed number of cycles, and at the last loading cycle, when failure occurred. The stiffness of the gear during the test was estimated by the ratio $\Delta F/\Delta f$. Some examples of stiffness versus the number of cycles are reported in Figure 4.19 for tests carried out at high, medium and low load level. The stiffness remains approximately constant up to the crack nucleation. Then the crack propagates and lead to failure, leading to a very low value of stiffness in the graphs. The picture shows that the time spent to nucleate the crack is

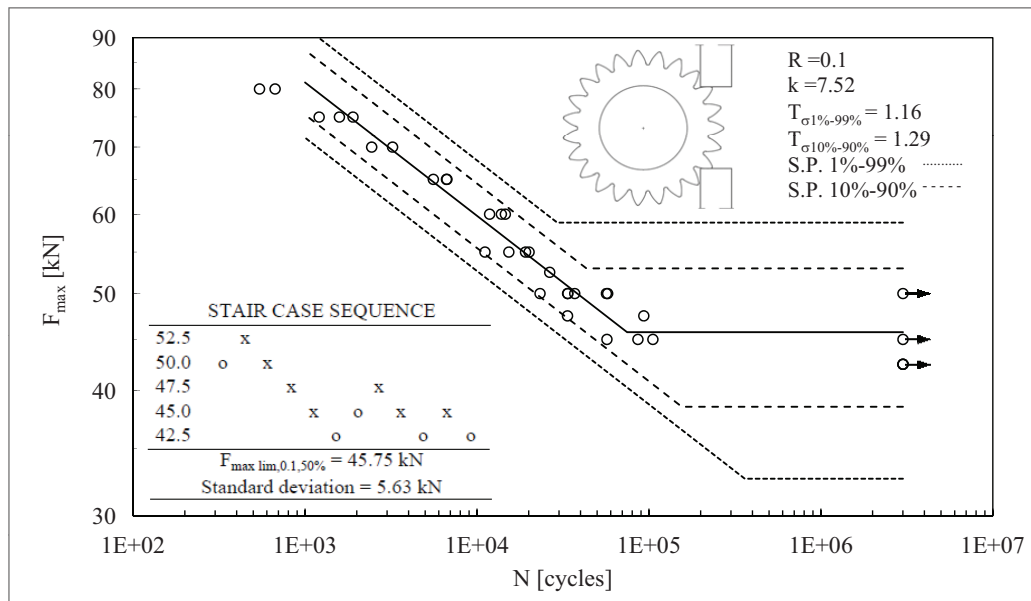


Figure 4.18: Fatigue results of pulsator tests on 20MnCr5 gears.

the major amount of the total life of the gear, being the propagation time limited to short number of cycles. The gear teeth failed, as expected, at tooth root. Initiation sites were located approximately in the middle zone of the facewidth, where the corresponding ratchet marks are generally visible (see Figure 4.20). The fracture surfaces showed, like the specimens, a light-grey area that corresponds to initiation and stable propagation phase, and a dark-area that corresponds to unstable crack propagation phase. The shape of these areas along the tooth facewidth is representative of the contact quality realized during the test. Good contact conditions led to symmetrically distributed light-grey areas, while poor contact conditions led to strong asymmetrical light-grey areas (respect to the middle plane passing trough half the facewidth of the gear). Examples of good contact quality are reported in Figure 4.21, where it can be seen also that the lower the applied load, the wider the light-grey zone. Since both the teeth under test were loaded in the the same way, the fractures took place randomly on both upper and lower teeth.

4.4.2 Calculation of tooth root bending stress

The forces applied by the punches on the gear teeth induce a bending stress (σ_F) at the tooth root of the teeth. The calculation of σ_F is dependent on the method used for calculation. Since the purpose of this chapter is to

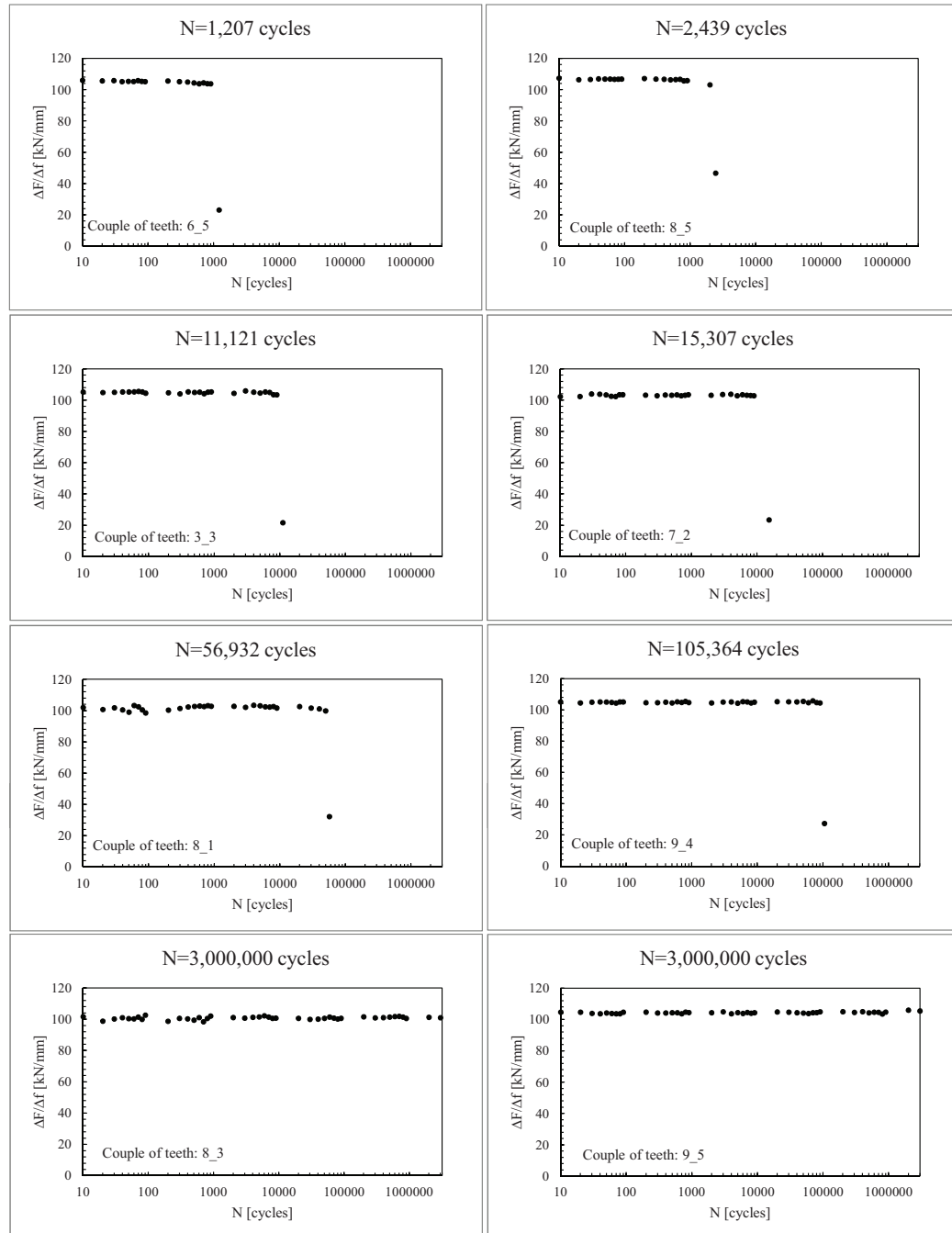


Figure 4.19: Stiffness recorded during the fatigue pulsator tests of some couples of gear teeth.

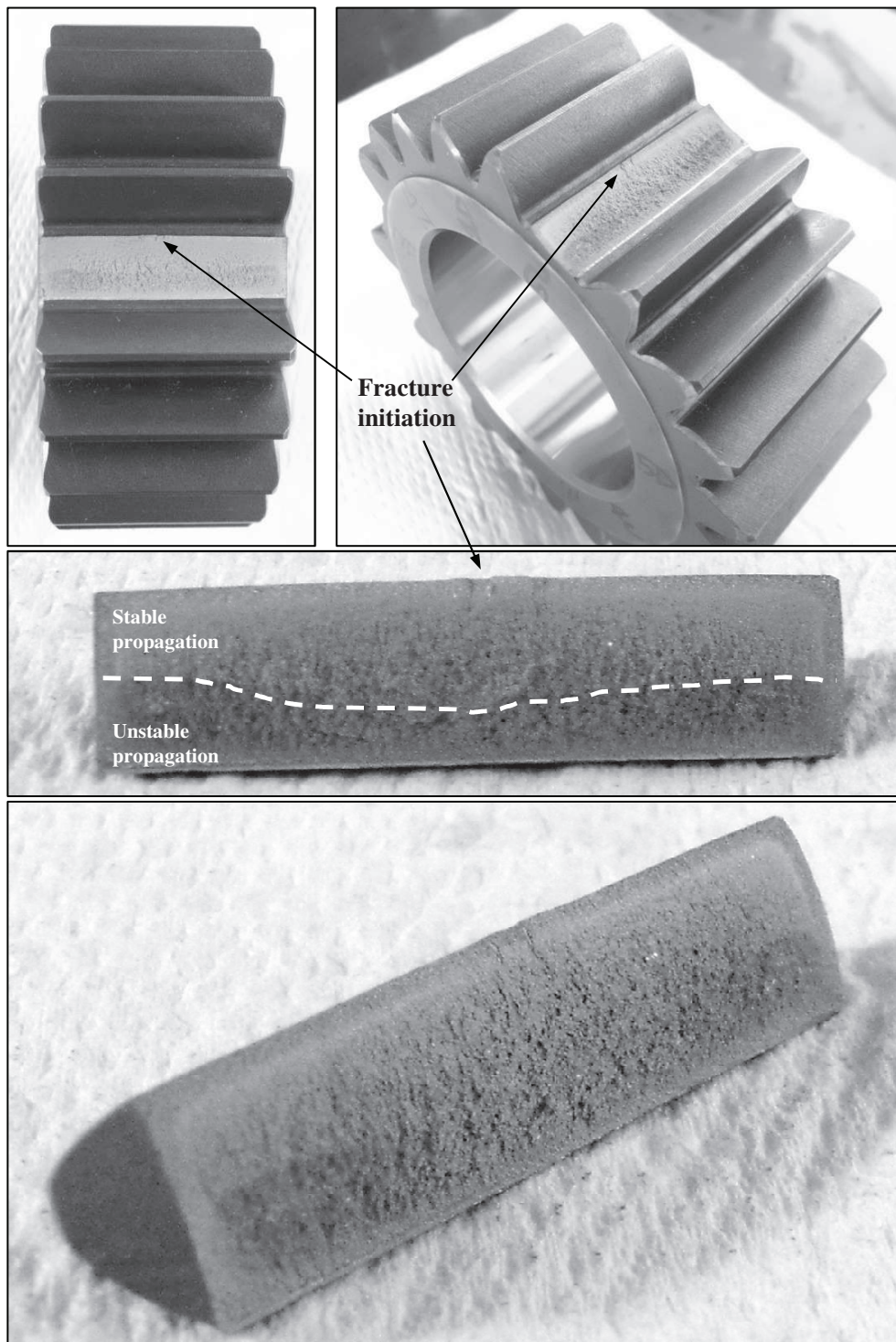


Figure 4.20: Fracture surfaces of 7_5U gear tooth ($N = 33,586$ cycles).

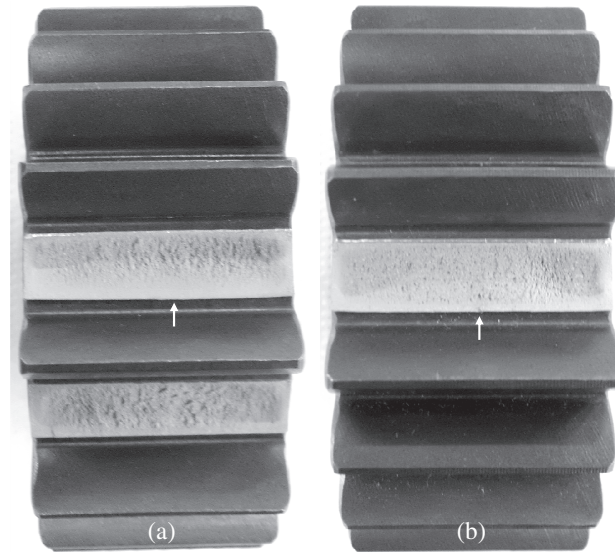


Figure 4.21: Fracture surfaces: (a) 9_4D gear tooth, $F_{max} = 45$ kN, $N = 105,364$ cycles, (b) 9_1D gear tooth, $F_{max} = 75$ kN, $N = 1,899$ cycles. The arrows indicate the probable initiation site.

investigate and analyze the design methods of ISO 6336, the calculation of σ_F was done using the calculation algorithm reported in the Standard [41]. However, calculations using Finite Element Analyses (FEA) were performed as well, in order to investigate the differences of the two methods.

The calculation according to ISO 6336-3 were made using KissSoft software³. In the ISO 6336-3 calculation algorithm, also the data of a mating gears must be inserted. These data are needed to define the position of the contact force (along the tooth flank) that produces the highest tooth root bending stress. The data of the mating gear reported in Table 4.13 were used in the model, and the center distance between the two gears was adjusted in order to obtain a diameter of Highest Point of Single Tooth Contact (d_{HPSTC}) equals to the theoretical contact diameter d_{cont} of the punches on the teeth in the pulsator test. In this way, the results of the KissSoft model and of the pulsator test are directly comparable. The torque used for ISO calculation corresponding to the pulsator test loading condition was determined using Equation 4.40 and was inserted in the KissSoft model.

Under a maximum compressive load $F_{max} = 50$ kN of the pulsator test, which corresponds to a torque on the gear $T = 1563$ Nm according to ISO Standard, the linear elastic tooth root bending stress resulted $\sigma_F = \sigma_{F0} =$

³The results were verified by implementing manually all the expressions of the Standard in an Excel file [74].

Table 4.13: Geometrical parameters of mating gear used in KissSoft model.

Number of teeth	z	12
Module (mm)	m	3
Pressure angle ($^{\circ}$)	α	25
Profile shift coefficient	x^*	0.3328
Pitch diameter (mm)	d	36
Face width (mm)	b	30
Tip diameter (mm)	d_a	44
Root diameter (mm)	d_f	30.678
Root form diameter (mm)	d_{Ff}	32.855
Base diameter (mm)	d_b	32.627
Root fillet radius (mm)	ρ_F	0.83
Diameter of pins (mm)	d_m	6.5
Measurements over pins (mm)	M_{dk}	48.226
Center distance (mm)	a	54.642

Table 4.14: Calculation parameters involved in the calculation of σ_F according to ISO 6336.

Tooth form factor	Y_F	1.51
Stress concentration factor	Y_S	2.45
Notch parameter	q_s	4.64
Relative stress gradient at tooth root	χ^*	2.06
Bending moment arm (mm)	h_F	4.90
Working angle ($^{\circ}$)	α_{Fen}	31.2
Tooth thickness at root (mm)	s_{Fn}	7.42
Tooth root radius (mm)	ρ_F	0.8

PRES-NORM
134.804

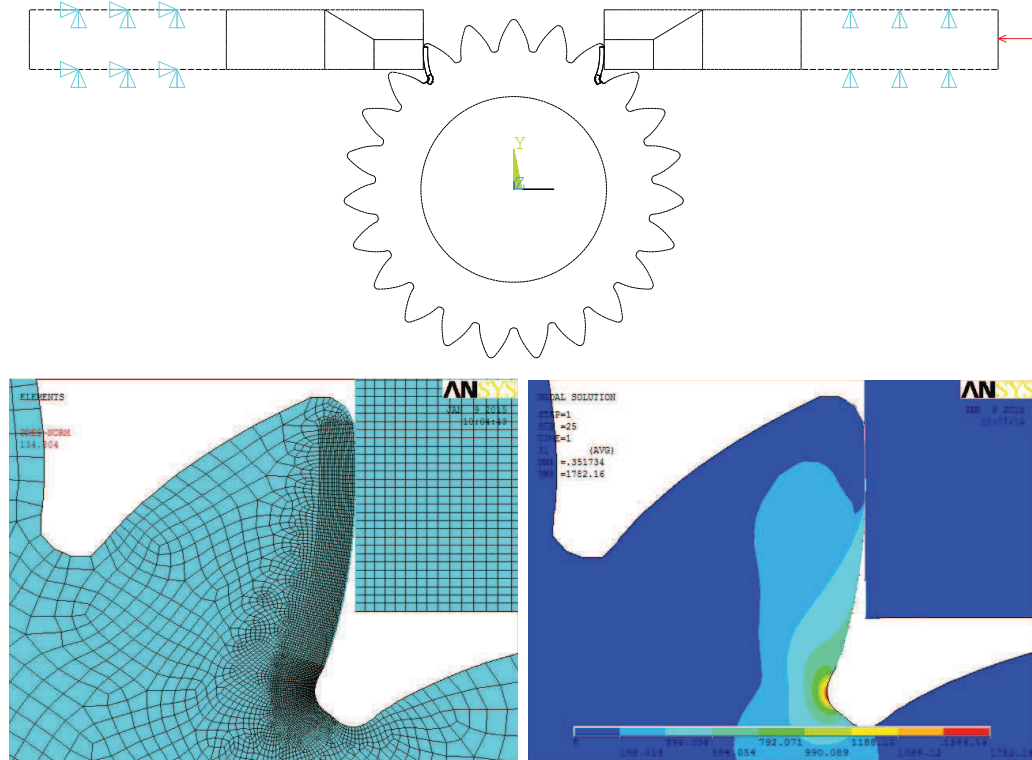


Figure 4.22: 2D model constraints, mesh and results.

1865 MPa. The auxiliary calculation parameters are reported in Table 4.14. For comparison purposes, linear elastic FE analyses were performed as well. 2D and a 3D models were realized, modeling the contact between the punches and the gear teeth (no friction was considered). 2D analysis were made using both plane stress and plane strain conditions. The entire gear was modeled, but for the 3D analysis, a submodel was used to reduce the calculation times and to consider a fine mesh. Constrains were applied only on punches for the analysis. The 2D and 3D models are reported in Figures 4.22 and 4.23 respectively.

Under the same applied force of $F_{max} = 50$ kN, the maximum linear elastic first principal stress resulted:

- 2D plane stress model: $\sigma_F = \sigma_{1,max} = 1620$ MPa
- 2D plane strain model: $\sigma_F = \sigma_{1,max} = 1624$ MPa
- 3D model: $\sigma_F = \sigma_{1,max} = 1700$ MPa

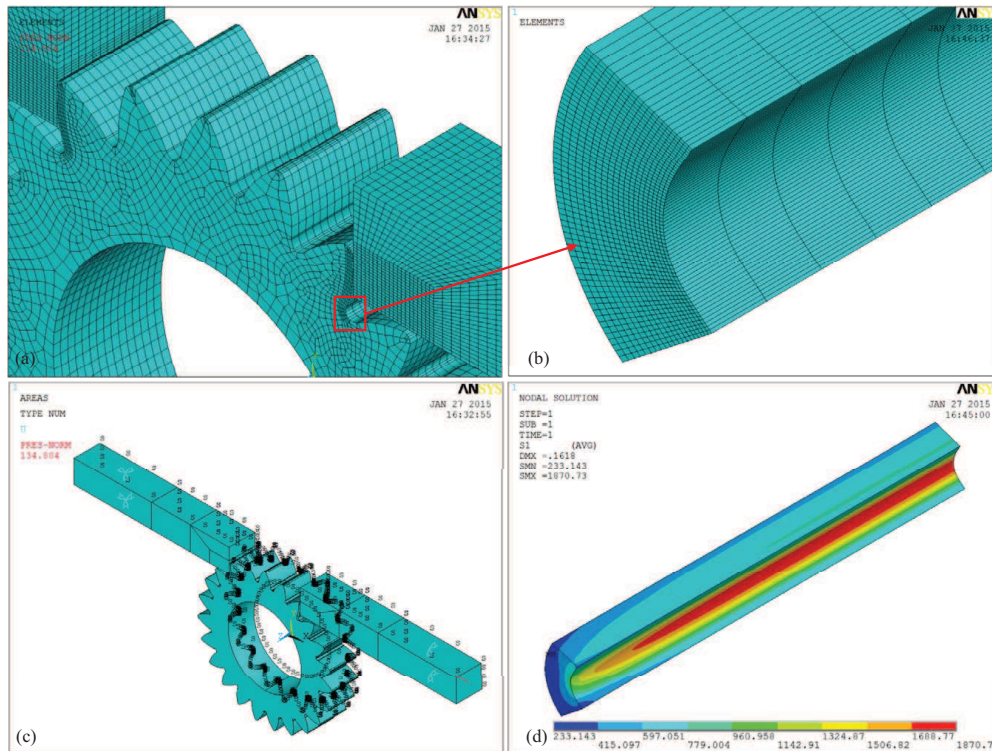


Figure 4.23: Details of 3D FE analysis: (a) mesh of coarse model; (b) mesh of the submodel; (c) constraints; (d) submodel results ($F = 55$ kN).

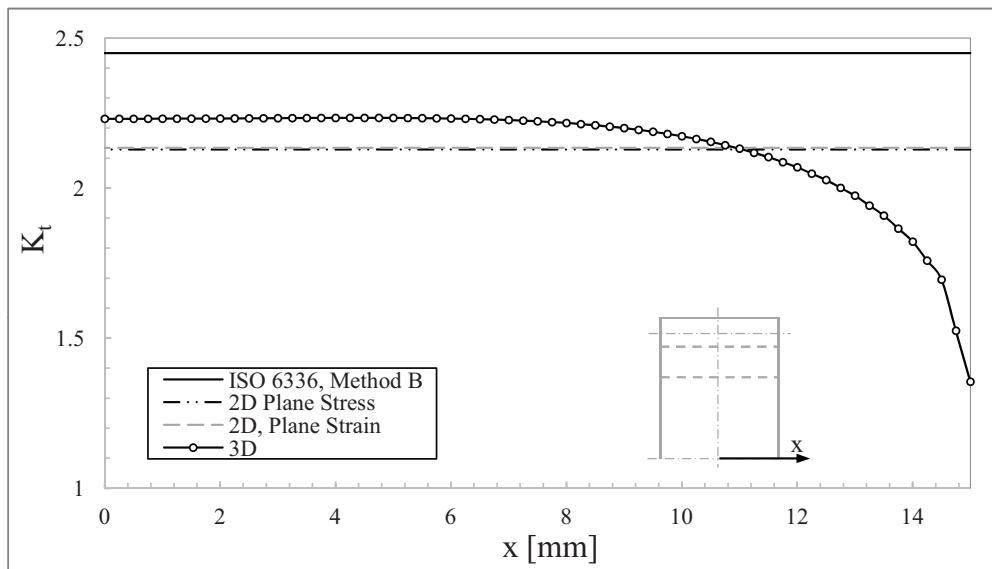


Figure 4.24: K_t resulting from 2D and 3D analyses compared to Y_S obtained by applying ISO 6336.

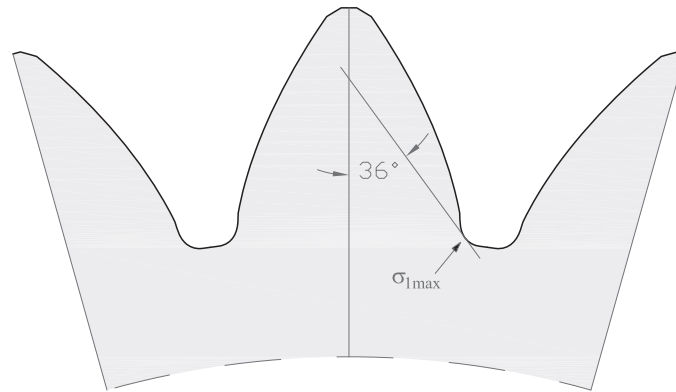


Figure 4.25: Location of σ_{1max} according to FE analyses.

As it can be seen from the results, the calculations made using FE analyses led to tooth root bending stresses lower than the ISO 6336 predictions. The difference was of 15% for 2D models and of 10% for the 3D models. Tri-axial effect due to facewidth is reported in Figure 4.24, where the K_t values of 3D analysis was compared to the corresponding value obtained from ISO 6336 and from 2D analyses. K_t was defined as:

$$K_t = \frac{\sigma_{1max}}{\sigma_F/Y_S} \quad (4.51)$$

The position of the maximum first principal stress (σ_{1max}) on the root tooth fillet described a tangent inclined of 36° respect to the tooth axis, as reported in Figure 4.25. This value is in good agreement with the Standard, since ISO 6336 takes as reference position for calculation the point on the root located at an angle of 30° .

4.4.3 SN curve of 20MnCr5 gears

The fatigue curves (P.S. 50%) of the 20MnCr5 gears in terms of maximum tooth root bending stress are reported in Figure 4.26, where both the stress evaluated using ISO method and 3D FEM analyses are used to represents the experimental points ($\sigma_{max,pe}$ is the maximum linear elastic stress at tooth root). The two curves relevant to 20MnCr5 gears are shifted as a consequence of the different stress obtained using the ISO and 3D FEM methods. In the picture, also the data of the notched specimens C1 presented in Chapter 3 are reported (the K_{tn} used was 2.58, according to 3D FE analysis). It is interesting to notice that the the specimens and the gears behaved similarly, but not exactly the same. The difference may be related to the slightly different residual stress field of the specimen notch root and tooth

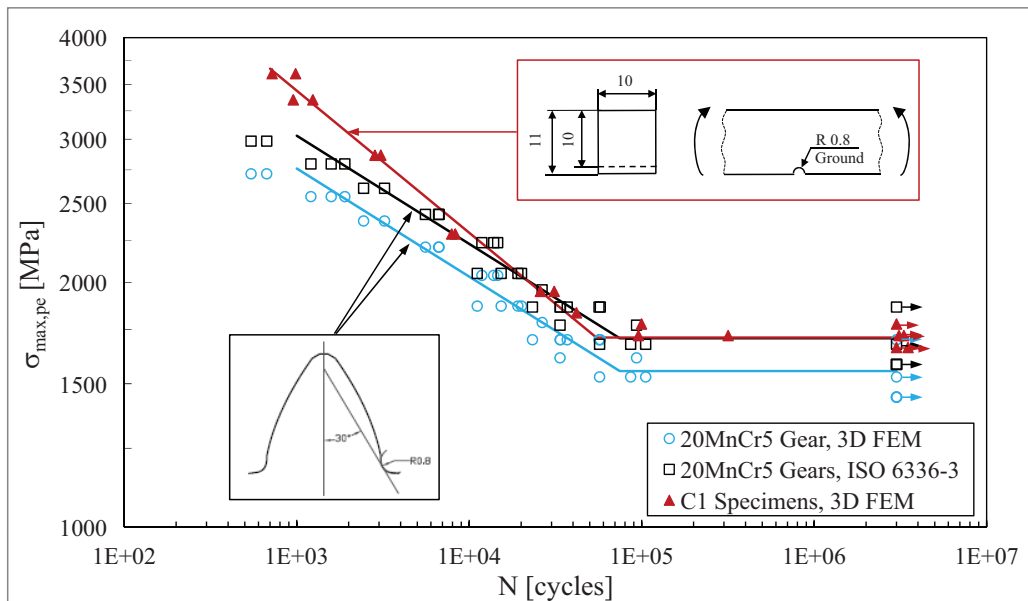


Figure 4.26: Fatigue curves (P.S. 50%) of 20MnCr5 gears and C1 notched specimens, represented in terms of maximum linear elastic bending stress at notch root ($R = 0.1$).

root fillet of the gears. In fact, the heat treatment was different for specimens and gears, since the mass of the gears is higher than that of the specimens. Therefore, locally the material strength could be different. There was not the possibility to measure the residual stress field on the gears in this work, therefore no further considerations can actually be made. Small difference was recognized also in the inverse slopes of the curves, that resulted $k = 7.52$ for the gears and $k = 5.72$ for the specimens. The difference between the two fatigue limits resulted about 10%, that can be considered a good result from an engineering point of view.

In Table 4.15 the fatigue stress according to ISO 6336-3 calculations in terms of maximum tooth root bending stress and in terms of maximum and amplitude of nominal bending stress at tooth root are reported. For completeness, the curves at different S.P. of the 20MnCr5 gears in terms of maximum tooth root bending stress evaluated according to ISO 6336 are reported in Figure 4.27. The curve is the same of Figure 4.18, except for the y-axis.

4.4.4 Pulsator tests on EN 353 gears

Experimental activity involved also fatigue tests on gears made of EN 353 (steel 5). The gears had the same geometry of 20MnCr5 ones, but were

Table 4.15: Stress on low-cycle ($N = 1000$ cycles) and high-cycle knees of 20MnCr5 gear curve obtained according to ISO 6336 calculations (50% S.P.).

Stress parameters	Symbol	Low-cycle	High-cycle
Maximum bending stress	σ_F	3029 MPa	1706 MPa
Maximum bending nominal stress	$\sigma_{Fnom,max}$	1236 MPa	696 MPa
Amplitude of nominal bending stress	$\sigma_{Fnom,a}$	556 MPa	313 MPa

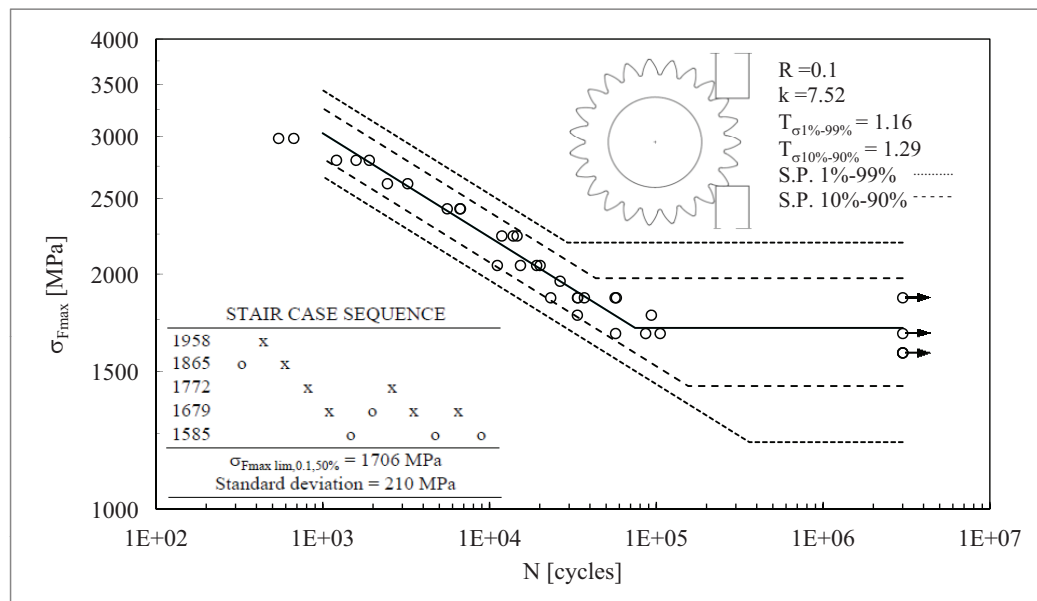


Figure 4.27: Fatigue curves of 20MnCr5 gears in terms of maximum tooth root bending stress calculated according to ISO 6336.

manufactured by another supplier. The purpose was to investigate the possibility to use simply fatigue tests to estimate differences between different suppliers.

EN 353 gears have the same drawing, and therefore the same nominal characteristics, of gears in 20MnCr5. However, each supplier use its own hob to cut the gears, placing the real profile of the gear teeth in a different zone of the tolerances range prescribed on the drawing. For this reason, even if the nominal drawing of the gear is the same, the real profile of the teeth may be slightly different between two different suppliers. Since the purpose here was to highlight differences from the 20MnCr5 gears, the fatigue results only in terms of applied force versus number of cycles to failures is reported, and then compared to 20MnCr5 results.

The fatigue curve is reported in Figure 4.28. The slope of the curve ($k = 7.00$) resulted very similar to that one obtained from the 20MnCr5 gears ($k = 7.52$). The scatter indexes in the finite life region were higher than those of 20MnCr5 gears, but this was a consequence of the fewer tests performed. Staircase sequence did not permit the estimation of the experimental scatter on the endurance limit using Dixon method. Looking at the experimental points, the scatter seemed to increase moving towards the high-cycle region of the fatigue curve.

Comparing the results of pulsator tests carried out on the two typologies of gears (see Figure 4.29), EN 353 gears showed better fatigue performances than 20MnCr5 gears in the low-cycle region of the curve, where the difference can be estimated in +15% in terms of stress. However, the endurance limit of the two typologies of gears are very similar. It is difficult to state that endurance limit of EN 353 gears is lower than 20MnCr5 gears as shown in Figure 4.29, since the staircase sequence of the former was shorter than that one of the latter, and thus less precise. Further investigations should be made in order to understand the residual stress field, hardness and microstructure of both the gears, in order to understand in a deeper way the origins of the different fatigue performances in finite life region.

4.5 Application of methods to experimental data

The experimental tests performed on A1, X1, C1 and 20MnCr5 gears constitute a homogeneous set of data that permits the application of the different life prediction methods presented in ISO 6336. Using these data is

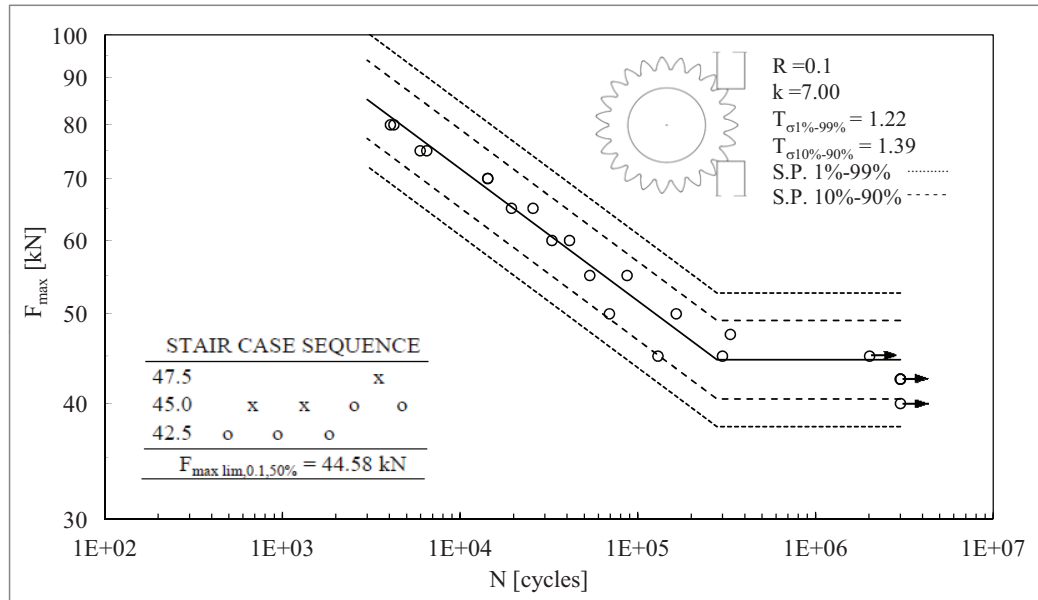


Figure 4.28: Fatigue results of pulsator tests on EN353 gears.

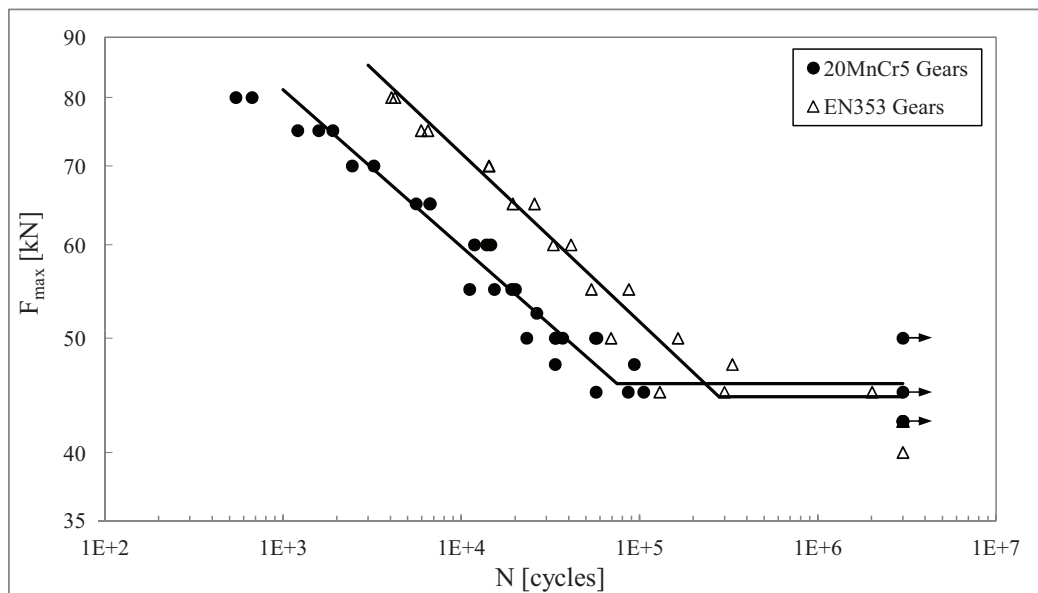


Figure 4.29: Fatigue results of 20MnCr5 and EN353 gears (50% S.P.).

therefore possible to investigate to which extent the methods are reliable. The methods were applied on the fatigue curves drawn for a S.P. of 99%, in order to be consistent with the prescriptions of the Standard, that suggests fatigue limits for this survival probability. Tests were performed under $R = 0.1$ plane bending, according to Standard prescriptions⁴. The maximum linear elastic stress $\sigma_F = \sigma_{1,max}$ was used to represent the results, since the Standard is based on fatigue limits defined in such a way.

The methods of ISO 6336 are based on the modification of the *static* (low-cycle) and the *reference* (high-cycle) fatigue knees. Method B places these knees at 1,000 and 3,000,000 of cycles respectively, since it describes a standardized approach to draw the fatigue curves. Methods B_p and B_k are based on the real curves obtained on specimens, instead. If the knees are not well defined, it is necessary to fix them before applying the methods. The high-cycle knees of the tests here presented were well defined by means of stair case sequences for each series. The low-cycle knee instead was not singled out, since only few tests were carried out at low number of cycles. The static knee of the method for each fatigue curve was then conventionally placed at 1,000 cycles, in accordance with method B .

For the notch sensitivity factor, related to the notch sensitivity of the gears, the methods give some expressions valid up to crack initiation. The fatigue curve reported in this work are relevant to complete failure of the gears. However, Figure 4.19 shows that the crack propagation phase is reduced in terms of life percentage. Therefore considering the data at complete failure is actually a good approximation.

Application of method B leads to a set of parallel fatigue curves with different endurance limit at 3,000,000 cycles. These endurance limits depend on the steel quality. The results here presented are relevant to ME quality ($\sigma_{F\ lim} = 525$ MPa), MQ quality ($\sigma_{F\ lim} = 500$ MPa and $\sigma_{F\ lim} = 425$ MPa) and ML quality ($\sigma_{F\ lim} = 312$ MPa). The correction factors of method B are reported in the Table 4.16 for low-cycle and high-cycle fatigue knees. The expressions used to calculate the factors can be found in ISO 6336-3 [41]. The allowable bending stresses can be calculated using expression 4.37, and applying it to low- and high-cycle fatigue knees. The results are reported as dotted lines in the Figure 4.30. ISO 6336 states that beyond the endurance limit at 3,000,000 cycles either an horizontal or an inclined line can be drawn. In the picture, the solution of the inclined line was chosen, being on the safe side. As it can be seen from the Figure 4.30, the allowable fatigue curves obtained using method B exhibited the same slope of the experimental pulsator

⁴Actually ISO 6336 prescribes $R = 0$ plane bending tests, but for test realization reasons a minimum pre-load of 10% was necessary.

Table 4.16: Correction factors of method *B* for 20MnCr5 gears.

Factor	Low-cycle knee	High-cycle knee
Y_{NT}	2.5	1
S_{Fmin}	1	1
Y_{ST}	2	2
$Y_{\delta rel T}$	1.198	1.017
$Y_{Rrel T}$	1	0.994
Y_X	1	1

tests. The $\sigma_{F lim}$ that led to a curve coincident to the experimental one (in the finite life region) evaluated for a S.P. of 99% resulted $\sigma_{F lim} \approx 450$ MPa. Although the method resembled very well the shape of the curve, actually the position of the endurance knee, located at 3 millions of cycle, seemed to be inadequate. Experimental results showed an endurance knee located at a significantly lower number of cycles (about 100,000 cycles). From this point of view, all the curves obtained using method *B* lead to bending fatigue life prescriptions on the safe side.

Method B_p is based on the fatigue data obtained on plain specimens under pulsating bending stresses. The application of method B_p was made on both the fatigue curves at a S.P. of 99% obtained on ground A1 and machined as-carburized X1 specimens. Although A1 and X1 specimens are not surface polished (as theoretically prescribed from ISO Standard), they can be used in the application of B_p method. The expression used for the endurance limit was:

$$Y_{Rrel p} = \frac{Y_R}{Y_{Rp}} \quad (4.52)$$

that substitutes the classic surface factor Y_R reported in Equation 4.26. The surface factor of the gear was calculated taking into account the real value of Y_S ⁵. The Standard provides only the following approximated expression:

$$Y_R = 1.49 - 0.471 (R_z + 1)^{0.1} \quad (4.53)$$

that is theoretically valid only for a tooth root stress concentration factor $Y_S = 2$, that it is not the case here presented, being $Y_S = 2.45$ for the gears tested in this work. The Standard provides the expression used to correctly

⁵The surface on a notch actually constitutes a notch-in-a-notch problem. Therefore the effect of the surface roughness is somewhat reduced considering the stress concentration factor Y_S [41].

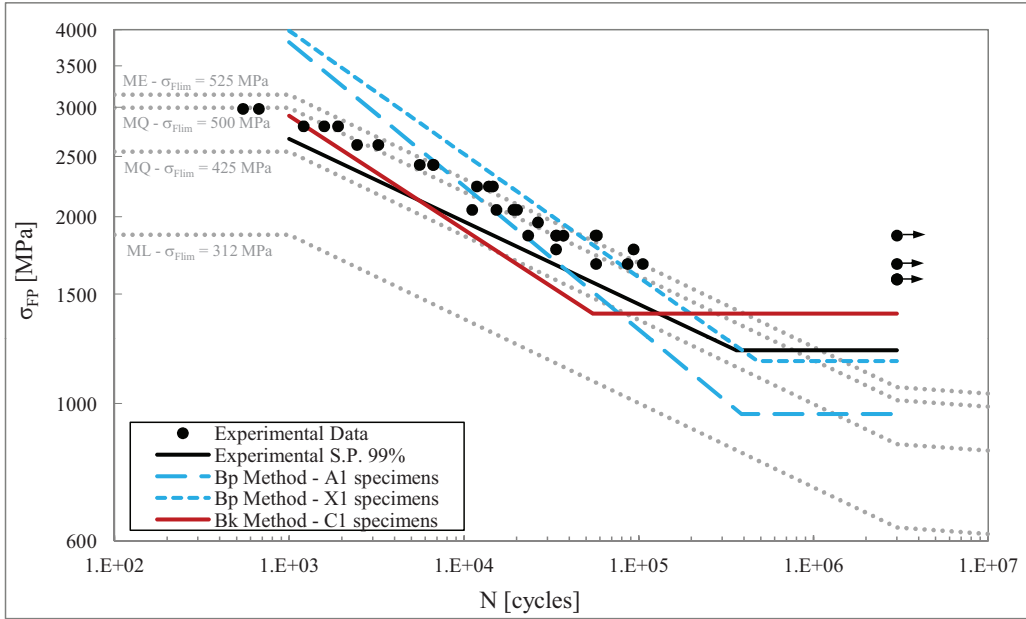


Figure 4.30: Allowable fatigue curves obtained by applying B , B_p and B_k methods to 20MnCr5 gears (S.P.=99%).

take into account the presence of a notch, that is:

$$Y_R = Y_{R0} + (1 - Y_{R0}) \left(\frac{Y_S - 1}{Y_S} \right)^2 \quad (4.54)$$

where Y_{R0} is the *absolute* surface factor of an un-notched specimen having the same roughness of the gear. Therefore it represents the surface finishing factor without any reducing effect due to notch.

Considering the two Equations 4.53 and 4.54 and assuming the reference value $Y_S = 2$ it is possible to derive the expression of the absolute surface factor:

$$Y_{R0} = 1.653 - 0.628 (R_z + 1)^{0.1} \quad (4.55)$$

where the surface roughness used may be either that of the gear or of both plain and notched specimens. Using a notation according to ISO 6336, Y_{R0} is the absolute surface factor of the gear (evaluated using R_z), Y_{R0T} is the absolute surface factor of the reference testing gear (evaluated using R_{zT}), Y_{R0p} is the absolute surface factor of the plain specimen (evaluated using R_{zp}) and Y_{R0k} is the absolute surface factor of the notched specimen (evaluated using R_{zk}).

The absolute surface factor of the gear was used to evaluate the effective Y_R factor using Equation 4.54 where $Y_S = 2.45$. Then, the relative surface factor

to be used in the general expression of method B_p (Equation 4.21) was:

$$Y_{Rrel p} = \frac{Y_R^{GEAR}}{Y_R^{PLAIN}} = \frac{Y_R}{Y_{R0p}} \quad (4.56)$$

The surface factors obtained by applying method B_p are reported in Table 4.17, along with the other factors calculated according to the Standard. As it can be seen from the table all the factors are near to 1, except the value of the notch sensitivity factor Y_δ that resulted around 2 for the static knee of the curve. This factor modifies sensibly the shape of the fatigue curves predicted by the method, that are reported in Figure 4.30. The curves obtained using method B_p resulted significantly different from the experimental evidence. In particular, the curves resulted steeper than the experimental one, due to the static support factor, that appears inappropriate for the analyzed cases. The endurance limits resulted lower than the experimental one using A1 specimens but very close to experimental limit using X1 specimens. The use of the specimens permitted to locate the endurance knee at a shorter value than 3 millions of cycles proposed by the standardized approach of method B . The curves obtained from A1 and X1 specimens resulted different, mainly because of the difference existing on the original curves of the specimens. The high scatter of A1 specimens in fact led to fatigue curve at 99% of S.P. that was lower than the curve of X1 specimens, even if theoretically A1 specimens should be more resistant than X1 specimens.

The application of method B_k was made starting from the fatigue curve at 99% of S.P. obtained on the notched C1 specimens. To correctly consider the surface factor Y_{Rk} , the roughness of the notch tip surface should be measured. This measurement was not available, therefore the same roughness obtained on the ground A1 specimens was considered, since the grinding was made using a similar grinding wheel. The effect of the notch of the surface factor was considered for both the notched specimens and the gears. The calculation factors of method B_k are reported in Table 4.18. In such a case, all the factors are similar to 1, meaning that the notched specimens are very similar to gear teeth and therefore that it is not necessary to modify significantly the original fatigue curve. The fatigue curve resulting from the application of method B_k is reported in Figure 4.30. As it can be seen the method B_k led to an endurance limit (at 99% of S.P.) higher than the other methods, located at a very short number of cycles. The slope of the curve resulted slightly different from the experimental one, but in the high cycle regime the curve resulted on the safe side. To summarize the results, the parameters of the low- and high-cycle knees of the curves obtained by applying the different methods are reported in Table 4.19.

Table 4.17: Correction factors of method B_p for 20MnCr5 gears.

Factor	Low-cycle knee	High-cycle knee
S_{Fmin}	1	1
Y_δ	2.107	1.053
$Y_{Rrel p}$ (from A1 specimens*)	1	0.952
$Y_{Rrel p}$ (from X1 specimens*)	1	1.035
Y_X	1	1
* $R_{zp A1} = 2.28 \mu\text{m}$, $R_{zp X1} = 8.11 \mu\text{m}$		

Table 4.18: Correction factors of method B_k for 20MnCr5 gears.

Factor	Low-cycle knee	High-cycle knee
Y_{Sk}	2.58	
S_{Fmin}	1	1
$Y_{\delta rel:k}$	0.955	0.989
$Y_{Rrel k}^*$	1	0.932
Y_X	1	1
* $R_{zk} = 2.28 \mu\text{m}$		

Table 4.19: Results of the application of methods B , B_p and B_k (S.P. = 99%).

Method	Low-cycle knee		High-cycle knee		k
	σ_{FP} [MPa]	N_{stat} [cycles]	σ_{FP} [MPa]	N_{lim} [cycles]	
Experimental	2667	1000	1218	360,837	7.52
B (ME)	3145	1000	1062	3,000,000	7.38
B (MQ - 500 MPa)	2995	1000	1012	3,000,000	7.38
B (MQ - 425 MPa)	2546	1000	860	3,000,000	7.38
B (ML - 312 MPa)	1869	1000	631	3,000,000	7.38
Bp - A1 spec.	3820	1000	961	387,651	4.32
Bp - X1 spec.	3988	1000	1170	478,277	5.03
Bk - C1 spec.	2908	1000	1395	54,642	5.45

Each method actually showed some limitations to predict the effective fatigue curve obtained experimentally on gears. Method B led to a slope very similar to the experimental one, but failed in defining the position of the high-cycle knee, that resulted significantly shifted towards long lives (however, in this way it resulted on the safe side). Furthermore, the method requires the knowledge of a proper steel quality in order to obtain reliable results, and generally this information is not well known in the design phase of the gear. Method B_p permitted to estimate better than the other the position of the endurance knee (at 99% of S.P.), especially using X1 specimens as starting point. However, the slope of the curve resulted sensibly different from the experimental one, and the method provided higher fatigue strength in the finite life region of the curve. Significant differences were found between A1 and X1 specimens. Method B_k led to an higher endurance limit than gears, but showing a similar curve to gears in the finite life region. Summarizing, all the methods resulted quite imprecise on some aspects. However, it must be emphasized that the application of the methods on curves obtained by means of statistical inference at very high survival probability may be actually misleading in the evaluation on the real capabilities of the methods to resemble correctly the experimental evidence. The tests carried out on both specimens and gears showed significantly different scatter in the low-medium and high cycle region of the curve. When the staircase sequences were able to estimate the statistical scatter, this resulted very large if compared to that of finite life. This means that making statistical inference at higher survival probability actually shift the position of the endurance knee, leading to curves that are significantly different from the case where the scatter on the finite region was extended also in the high cycle region. In other words, to compare effectively the effectiveness of the methods, it is more convenient to consider the curves at 50% of S.P.. For this reason, methods B_p and B_k were applied on fatigue curves obtained for this survival probability, obtaining the curves reported in Figure 4.31. Method B was here not reported since no information on the scatter is provided by ISO 6336, therefore making impossible to define the endurance limit for S.P. equal to 50%. From the picture, it can be seen that method B_k is actually more effective than method B_p , in both the low and high cycle region of the curve. It led to an endurance limit close to the experimental one obtained on gears, both in terms of stress and position. On the contrary, method B_p led to curves sensibly different from gears, being imprecise in both the low and high-cycle knees definition. From this analysis, it can be stated that method B_k resulted actually better than method B , even its capabilities are hidden when a strong statistical inference is made.

To make a better comparison of the methods under a S.P. of 99%, the

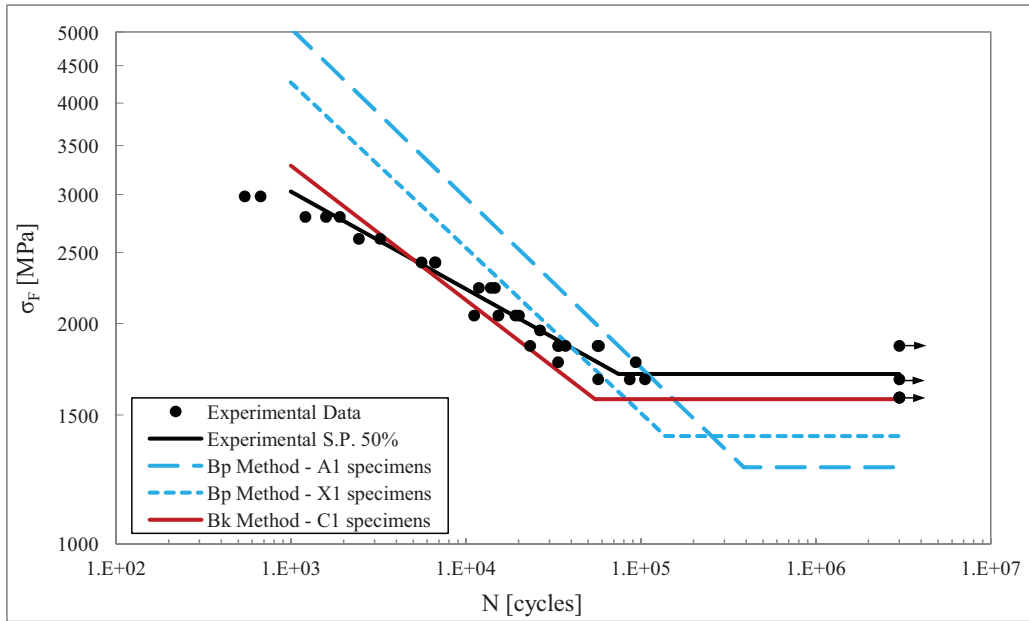


Figure 4.31: Fatigue curves obtained by applying B_p and B_k methods to 20MnCr5 gears (S.P.=50%).

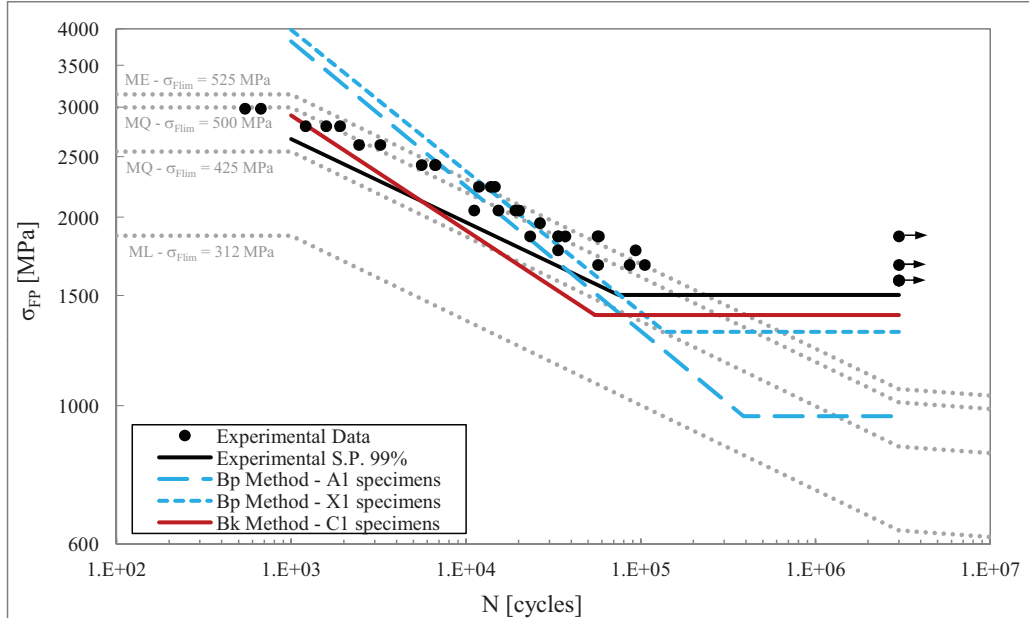


Figure 4.32: Allowable fatigue curves obtained by applying B , B_p and B_k methods to 20MnCr5 gears (S.P.=99%, imposing on endurance limit the same scatter of the finite life region).

original sets of data were compared using the finite life scatter also for the endurance limit. In this way, the scatter is accounted in the same way for all the starting test series (included gears). The results are showed in Figure 4.32, where it can be seen again that method B_k is better than B_p and that method B is good only if the right value of $\sigma_{F\lim}$ is known.

4.6 Improvement of specimen-based methods

From the application of the methods to the experimental sets of data, the notch sensitivity factor requires more attention, especially for method B_p , where the notch sensitivity must be evaluated directly for the gear, without using a relative value referred to similar notched test pieces. In the following section the analysis of the notch sensitivity factors will be presented, and some improvements for methods B_p and B_k will be discussed.

At the endurance limit, the notch sensitivity factor was evaluated with the Siebel and Steiler approach [65] (see Section 4.2):

$$Y_\delta = \frac{1 + \sqrt{\rho' \chi^*}}{1 + \sqrt{\rho' \chi_P^*}} \quad (4.57)$$

The relative stress gradients are evaluated using the following equation (valid for gears and notched specimens):

$$\chi^* = \chi_P^* (1 + 2q_s) \quad (4.58)$$

where $\chi_P^* = 0.2 \text{ mm}^{-1}$ is the relative stress gradient of a plain specimen (section of height 10 mm) under plane bending, and q_s is a geometrical parameter taking into account the notch geometry at tooth root:

$$q_s = \frac{S_{Fn}}{2\rho_F} \quad (4.59)$$

where S_{Fn} is the tooth thickness at root and ρ_F is the tooth root fillet radius. The same expressions can be evaluated for the notched specimens C1 (see Figure 3.6), but using:

$$q_{sk} = \frac{h}{2r} \quad (4.60)$$

For notched specimens reported in this work, the the net height of the specimen was $h = 10 \text{ mm}$ and the notch tip radius $r = 0.8 \text{ mm}$.

For comparison purposes, the relative stress gradient was evaluated using a 2D plane stress FE analysis. The first principal stress at tooth root (notch tip) was plotted towards the interior of the gear (notched specimens), along

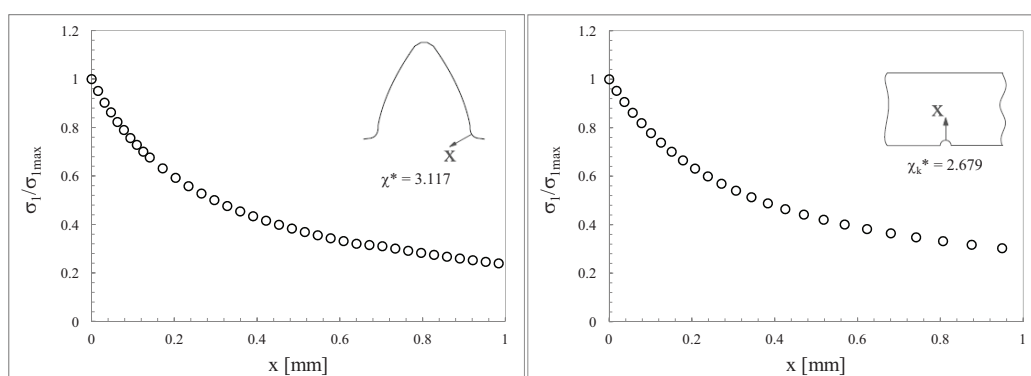


Figure 4.33: Relative stress gradients for gears (left) and notched specimens (right) evaluated by means of 2D plane stress analyses.

Table 4.20: Comparison among numerical and ISO 6336-3 notch sensitivity parameters.

Gear			Notched specimen		
	FEM	ISO		FEM	ISO
χ^* (mm^{-1})	3.117	2.056	χ_k^* (mm^{-1})	2.679	2.700
$Y_\delta = 1 + \sqrt{\rho' \chi^*}$	1.097	1.079	$Y_{\delta k} = 1 + \sqrt{\rho' \chi_k^*}$	1.090	1.090

the normal to the surface. The results for 20MnCr5 gears and C1 specimens are reported in Figures 4.33. As it can be seen, the stress field is steeper for the gear than the specimens. Therefore the stress gradient is higher for the gear than the specimen. The comparison between numerical and analytical values of the notch sensitivity parameters required from the Standard are reported in Table 4.20. The Table shows that the relative stress gradient is significantly different only for the gear, while for the specimen there is a good agreement. Actually, the support factors resulted very similar, meaning that the use of FE analyses does not permit to sensibly improve the fatigue curves predicted by the specimen-based methods.

The use of the experimental data collected by the tests on gears and specimens is more interesting, since it permits to evaluate experimentally the support factors to be used in the methods. In section 4.2 it was observed that the notch sensitivity factors are the ratio of the stress concentration factors over the notch factors at the endurance and the low-cycle knee. From the experimental tests presented in Chapter 3 and the pulsator test results presented in this Chapter, it is possible to define the following parameters

(using the nominal stress amplitudes in MPa and considering a S.P. of 50%):

$$K_{f,stat}^{NOTCH} = \frac{\text{Fatigue strength at 1000 cycle of A1 specimens}}{\text{Fatigue strength at 1000 cycle of C1 specimens}} = \frac{1080}{600} = 1.80 \quad (4.61)$$

$$K_{f,lim}^{NOTCH} = \frac{\text{Endurance limit of A1 specimens}}{\text{Endurance limit of C1 specimens}} = \frac{572}{298} = 1.92 \quad (4.62)$$

$$K_{f,stat}^{GEAR} = \frac{\text{Fatigue strength at 1000 cycle of A1 specimens}}{\text{Fatigue strength at 1000 cycle of gears}} = \frac{1080}{556} = 1.94 \quad (4.63)$$

$$K_{f,lim}^{GEAR} = \frac{\text{Endurance limit of A1 specimens}}{\text{Endurance limit of gears}} = \frac{572}{313} = 1.83 \quad (4.64)$$

These parameters may be used to estimate the support factors for gears and notched specimens at low- and high-cycle knees of the fatigue curve:

$$Y_{\delta,stat} = \frac{Y_S}{K_{f,stat}^{GEAR}} = \frac{2.45}{1.94} = 1.261 \quad (4.65)$$

$$Y_{\delta,lim} = \frac{Y_S}{K_{f,lim}^{GEAR}} = \frac{2.45}{1.83} = 1.341 \quad (4.66)$$

$$Y_{\delta k,stat} = \frac{Y_{Sk}}{K_{f,stat}^{NOTCH}} = \frac{2.58}{1.80} = 1.433 \quad (4.67)$$

$$Y_{\delta k,lim} = \frac{Y_{Sk}}{K_{f,lim}^{NOTCH}} = \frac{2.58}{1.92} = 1.344 \quad (4.68)$$

Using these support factors, the fatigue curves reported in Figure 4.34 were obtained. It was preferred to consider the curves at 50% of S.P. to avoid the undesired effect that the statistical inference has on results, hiding the real capabilities of the methods. As it can be seen from the picture, the methods produced curves more similar to the experimental one obtained on gears. In particular, B_p method improves sensibly, especially for A1 specimens. The curves obtained using the experimental notch sensitivity factors differ from the gear one only due to the roughness factors. If the surface factors are imposed equal to 1, than there is a perfect coincidence on the endurance limits of gears and both plain and notched specimens.

A useful approach to estimate the fatigue life of gears may be based on the use of the experimental data obtained on both plain and notched specimens. In such a case, to predict the bending fatigue life of a gear, the test of plain specimens and of notched specimens (with notch similar to tooth root notch) is required, without using any data coming from gear tests. From the experimental results it is possible to estimate the notch factor K_f^{NOTCH} for

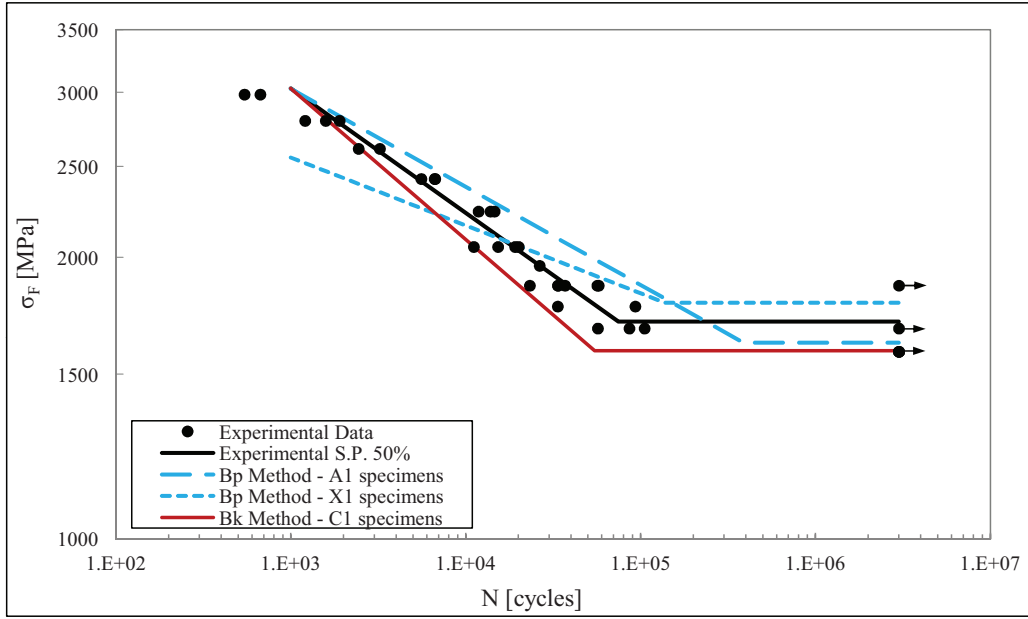


Figure 4.34: Fatigue curves obtained by applying B_p and B_k methods using experimental notch sensitivity factors to 20MnCr5 gears (S.P.=50%).

the notched specimens for both the low- and high-cycle knees. For the high-cycle region of the curve it is then possible to define an experimental value of the slip layer thickness ρ'' to insert in the Siebel-Steiler notch support factors to match better the experimental evidence on specimens. The relative stress gradient χ_k^* to be used in the equations is that one obtained by means of FE analysis on the specimens.

The following expression must be satisfied:

$$Y_{\delta k,lim} = \frac{K_t^{NOTCH}}{K_{f,lim}^{NOTCH}} = \frac{1 + \sqrt{\rho'' \chi_k^*}}{1 + \sqrt{\rho'' \chi_P^*}} \quad (4.69)$$

Using the data obtained in this work ($K_t^{NOTCH} = Y_{Sk} = 2.58$, $K_{f,lim}^{NOTCH} = 1.92$, $\chi_k^* = 2.679 \text{ mm}^{-1}$), the expression can be numerically solved obtaining:

$$\rho'' = 0.110 \text{ mm} \quad (4.70)$$

This value is significantly higher than the value suggested by ISO 6336 for case-hardened steels ($\rho' = 0.003 \text{ mm}$), meaning that the notch sensitivity showed by the experimental tests was significantly lower than that predicted by the Standard.

For the low-cycle knee of the fatigue curve, the approach proposed by ISO

6336 to define the support factor is based on the following expression:

$$Y_{\delta k,stat} = 0.77Y_{Sk} + 0.22 \quad (4.71)$$

This value is dependent on the stress concentration factor of the notched specimen. From the test presented in this work it is not possible to propose a new expression, since only a notched geometry was tested. For this reason, the use of the support factor experimentally obtained on notched specimens is here proposed instead of the value obtained from ISO 6336 prescriptions. Therefore:

$$Y_{\delta,stat} = Y_{\delta k,stat} = \frac{Y_{Sk}}{K_{f,stat}^{NOTCH}} = \frac{2.58}{1.80} = 1.433 \quad (4.72)$$

meaning that gears and notched specimens are supposed to behave in the same way in the low-cycle region of the curve ($Y_{\delta rel k,stat} = 1$). It is therefore important that the specimens have a notch geometry close to the real tooth-root fillet of the gear under study. The new value $Y_{\delta k,stat}$ here presented is significantly lower than the original one proposed by ISO 6336, where $Y_{\delta k,stat} = 2.207$. This means that notch sensitivity at low-cycle knee is much higher than that predicted by the Standard.

Using ρ'' in the equations relevant to the specimen-based methods B_p and B_k for the endurance limit and $Y_{\delta k,stat} = 1.433$ the curve reported in Figure 4.35 are obtained (for a S.P. of 50%). Calculation were made using the relative stress gradient of the gear obtained using FE analysis ($\chi^* = 3.117 \text{ mm}^{-1}$). The fatigue curves obtained in Figure 4.35 provides fatigue life predictions more similar to the experimental curve obtained on gears, especially for the plain specimens (method B_p). The endurance limits are more similar to the value observed on the gears for both notched and plain specimens, and the low cycle region of the curves based on plain specimens is significantly improved (from the application of the original method B_p of ISO 6336). For completeness, also the curve at S.P.=99% are reported in Figure 4.36, where it must be considered again that the scatter on the endurance limits of notched specimens, plain specimens and gears are evaluated using different statistical models. To estimate to which extent the original specimen-based methods (B_p and B_k) and the improved versions based on the experimental data of gears and specimens or only on specimens, the following error indexes may be defined:

$$\Delta\sigma_{FP lim} = 100 \frac{\sigma_{FP lim,method} - \sigma_{FP lim,gears}}{\sigma_{FP lim,gears}} [\%] \quad (4.73)$$

$$\Delta k = 100 \frac{k_{method} - k_{gears}}{k_{gears}} [\%] \quad (4.74)$$

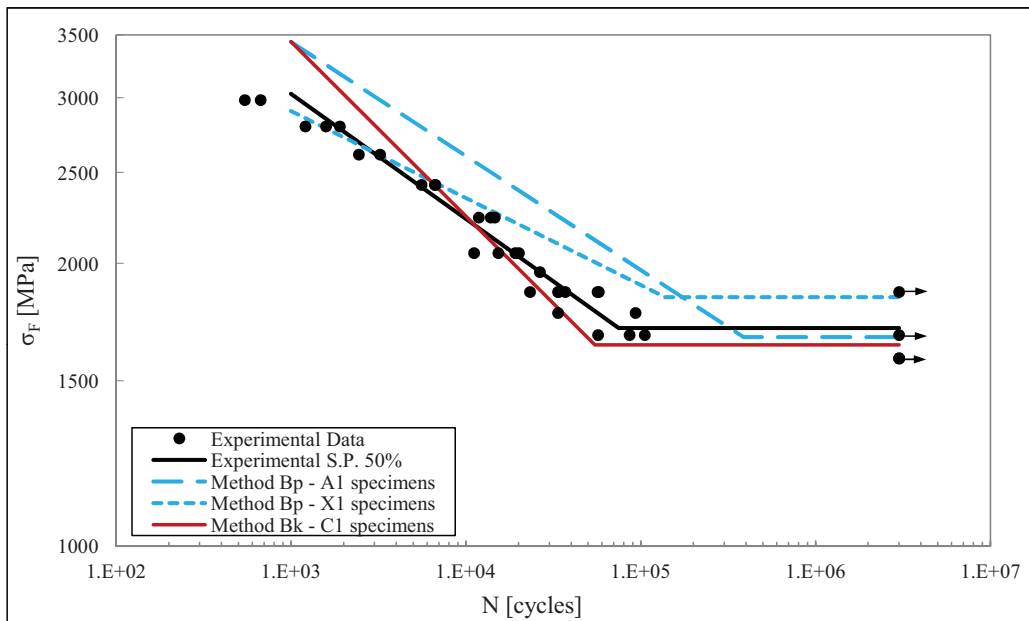


Figure 4.35: Fatigue curves obtained by applying B_p and B_k methods using $\rho'' = 0.110$ mm and $Y_{\delta,stat} = Y_{\delta k,stat} = 1.433$ (20MnCr5 gears, S.P.=50%).

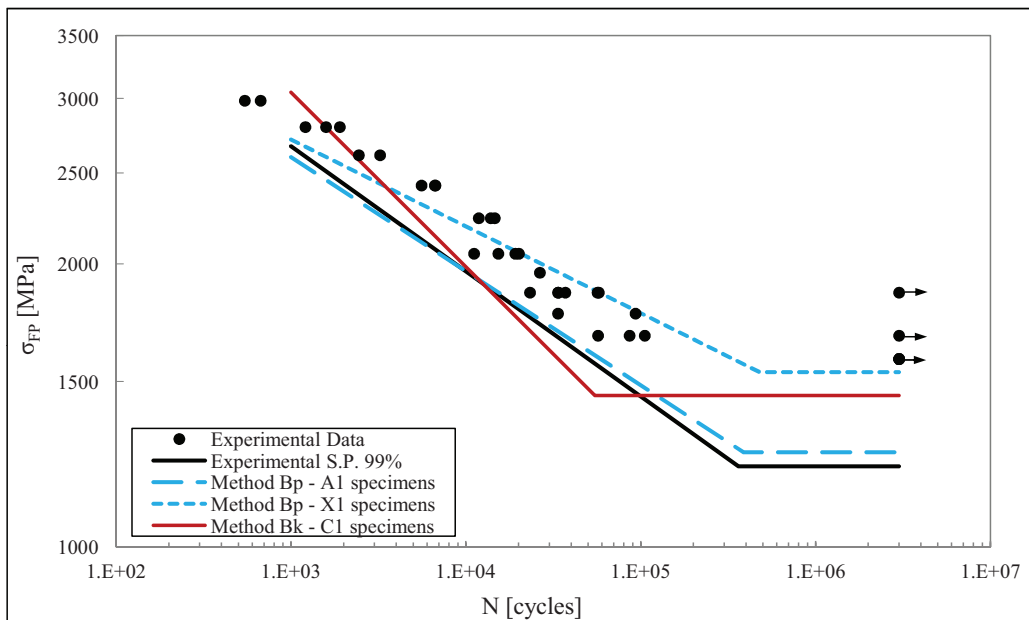


Figure 4.36: Allowable fatigue curves obtained by applying B_p and B_k methods using $\rho'' = 0.110$ mm and $Y_{\delta,stat} = Y_{\delta k,stat} = 1.690$ (20MnCr5 gears, S.P.=99%).

Table 4.21: Error indexes for method B_p and B_k (S.P.=50%).

Method	Version *	$\Delta\sigma_{FP\ lim}$	Δk
B	O	**	-1.9
Bp - A1	O	-25.4	-42.6
Bp - X1	O	-17.7	-41.1
Bk - C1	O	-7.6	-27.5
Bp - A1	G+S	-5.0	26.9
Bp - X1	G+S	4.8	83.4
Bk - C1	G+S	-6.9	-17.6
Bp - A1	S	-2.2	9.6
Bp - X1	S	8.0	43.9
Bp - C1	S	-4.0	-28.3

* O = Original version of ISO 6336-3
G+S = Using exp. data of gears and specimens
S = Using experimental data of specimens

** Not available at S.P.=50%

where the predicted allowable bending endurance limit and the slope of the resulting curves of the methods are compared to the corresponding values obtained from pulsator tests on 20MnCr5 gears (S.P.=50%), i.e. $\sigma_{FP\ lim, gears} = 1706$ MPa and $k_{gears} = 7.52$ as reported in Table 4.19. The error indexes are reported in Table 4.21. As it can be seen, the improved versions of the specimen-based methods permit better predictions of the endurance limit of the gears, reducing from 25% to less than 10% the error on the endurance limit. Error indexes of B_p method are particularly high when X1 specimens are used as starting point. It must be noted also that method B is the best method in predicting the slope of the curve.

4.7 Conclusions

The methods for bending fatigue design reported in ISO 6336 were analyzed starting from the theoretical basis and then applying them to some sets of data available in the literature. Since heterogeneity on data was huge and results scattered, methods were applied to fatigue curves obtained by experimental tests on plain, notched and gears made of the same steel (20MnCr5). Homogeneous sets of data were not found in the open literature, since the lack of some essential data in the papers made the application of the methods

impossible. However, it was found that method B_k gave safer results than method B_p , and it was confirmed that it is convenient that the specimens are tested under loading conditions as similar as possible to those of the gear teeth to have meaningful results.

In order to build a homogeneous set of fatigue data on specimens and gears, experimental tests were carried out on a typical gears used in Off-Highway applications. Pulsator tests were chosen to draw the fatigue curve, testing two different case-hardened steels: 20MnCr5 and EN353. The pulsator test resulted an effective way to properly show the fatigue behavior of gears, and permitted also to clearly show the difference in terms of fatigue performance of the two steels. The latter resulted more resistant in the finite life region than the former, according to results obtained from specimens and reported in Chapter 3. The endurance limits resulted very similar for the two steels, and resulted located around 100,000 ÷ 300,000 cycles (shorter than the 3,000,000 of cycles reported in ISO 6336 and in agreement with notched and plain specimens). The pulsator tests may be a valuable approach to characterize components inside the Company, at least for spur cylindrical gears, since their execution is easier and faster than testing real gears on complete drivelines and since the difference on fatigue behavior can be clearly exhibited.

The tooth root bending stress obtained on the gears using ISO 6336 and FE analysis were compared, showing that ISO 6336 method B predicted a tooth root stress 10% higher of 3D analyses and 15% higher of 2D analyses. From this point of view the Standard seemed to operate on the safety side, overestimating the tooth root bending stress.

Method B , based on fatigue limits obtained in the past on reference gears, resulted more precise than the other methods in the estimation of the fatigue curve slope, but the endurance limit resulted located at 3,000,000 of cycles, that resulted significantly higher than experimental results. Experimental fatigue bending tests showed instead that the endurance limit was located around 100,000 cycles for the case-hardened steel used by the Company to manufacture gears. Method B fitted very well the experimental curve of gears at 99% of S.P. (in the finite life region) for $\sigma_{F\ lim} = 450$ MPa.

Method B_p , starting from plane bending fatigue tests on plain specimens, was actually imprecise in the prediction of the fatigue life of the gears, showing a deviation of 25% on the endurance limits and around 40% on the slope, considering data at 50% of S.P..

Method B_k , starting from plane bending fatigue tests on notched specimens, was found a good compromise to resemble the real fatigue behavior of gears. The curve obtained resulted similar to that of gears in terms of endurance limits (8% of deviation) and of position of the endurance knee. However, the

curve was significantly steeper than the gear one (30% of deviation on the slope).

Using the experimental endurance limits found on gears and specimens the methods B_p and B_k may be improved, by evaluating the support factors on the experimental evidence. It was chosen to improve the effectiveness of method B_p and B_k using the data obtained on plain and notched specimens only, since generally the possibility to test gears is precluded in the design phase, while fatigue data of specimens may be already available from the literature or from previous tests. A new value of the slip layer thickness ($\rho'' = 0.110$ mm) based on the endurance limits of plain and notched specimens was proposed. This parameter resulted significantly higher than the value suggested from ISO 6336-3, since the notch sensitivity of the case-hardening steels tested in this work was found to be much lower than that one proposed by the Standard at the endurance limit. For the static knee, a new value of the support factor was proposed from the experimental evidence ($Y_{\delta k,stat} = 1.433$). This experimental value suggests that the notch sensitivity in the low-cycle region of the fatigue curve is higher than that predicted by ISO 6336. The proposed values of slip layer thickness and support factor led to a significant improvement of the methods, leading to endurance limits similar to the experimental one of gears (2 ÷ 4% of difference using notched and ground specimens). The slope of the curves resulted imprecise, but it must be remembered that in the power transmission field the design of gears is generally made to ensure infinite life.

It was found that attention must be paid to statistical scatter, that may be significantly different from plain specimens and notched components. For ground plain specimens the scatter index in the finite life was $T_{\sigma 1\%-99\%,A1} = 1.75$ while for notched components it resulted sensibly lower ($T_{\sigma 1\%-99\%,C1} = 1.28$ and $T_{\sigma 1\%-99\%,gears} = 1.29$). This means that using plain specimens may not be a good way to characterize gears. From the previously showed results, the use of notched specimens is suggested instead.

The use of specimens allows to directly show the endurance limit of the case-hardened steels easily and rapidly than testing real gears, and permits to build, test after test, a database of fatigue limits useful for future design of gears.

Conclusions

Case-hardened steels are widely used to manufacture gears, since they provides higher bending and pitting fatigue performances than common steels, due to the peculiar microstructure induced by the case-hardening treatment, characterized by high compressive residual stresses and high surface hardness. Even if the design of gears against fatigue is analyzed in many international standards, actually the raise of new markets in emerging world areas forces the companies dealing with the design of power transmissions systems to investigate the fatigue performances of alternative steels. Furthermore, the study of the fatigue limits of case-hardened gears is necessary to improve the calculation and validation processes of new products inside the R&D offices. The data available in the gear standards are sometimes too generic to be satisfactory for transmissions manufacturer. The allowable fatigue limits are provided for families of materials, where it is sometimes difficult to choose the right value, since only quality controls that do not consider the fatigue performances are involved in the definition of the steel quality. Moreover, sometimes experimental tests are not well depicted by allowable limits reported in the standards, and some data are missing to make statistics and thus to evaluate design risks.

An analysis of the test archive of Carraro Drive Tech was made focusing on gears. It was found that, for an axle, the critical components are the sun gears located in the final drives (inside the wheel hub) and the bevel gear pinions located in the differential housing. Sun gears failed by pitting, while bevel gear pinions by bending. Using the data collected in many years of tests, the allowable limits for pitting and bending fatigue were identified according to ISO 6336 standard. The approach used in the analyses allowed the estimation of the nominal fatigue limit of steel according to ISO 6336-5, independently from the gear geometry, shaft stiffness, lube, surface finishing and applied torque. The cloud of experimental points were fitted using

the slopes reported in the standard ($k = 13.22$ for pitting and $k = 8.74$ for bending), and the corresponding stress at fatigue knee of the curve was defined. Statistical analysis was performed on experimental results, assuming a log-normal distribution of life and constant scatter along the stress levels. By so doing, the allowable pitting limits for cylindrical sun gears resulted $\sigma_{H \text{ lim},50\%} \approx 1650$ MPa with a scatter index $T_{\sigma_H,1\%-99\%} = 1.48$, while for bevel gear pinions the allowable bending limits (maximum nominal stress, $R = 0$) resulted $\sigma_{F \text{ lim},50\%} \approx 508$ MPa with a scatter index $T_{\sigma,1\%-99\%} = 1.91$. The allowable values at 99% of survival probability resulted lower than values reported in ISO 6336-5 for a medium quality of case-hardened steel, that was the quality expected for the analyzed gears. For pitting the estimated allowable limits was $\sigma_{H \text{ lim},99\%} = 1359$ MPa versus 1500 MPa of the standard, while for bending $\sigma_{F \text{ lim},99\%} = 370$ MPa versus 500 MPa. For pitting, approximately, the allowable limits declared by ISO 6336 at 99% of S.P. corresponded to values at 90% of S.P. found in the analyses. The scatter was high for both the phenomena, but in line with what reported in the literature for case-hardened steels. Further investigations on fatigue life predictions according to Gleason method showed its capability to envelope the whole cloud of experimental points within the confidence bands declared by the method. The scatter index estimated experimentally was $T_{\sigma 5\%-95\%} = 2.00$ versus the suggested value of the method $T_{\sigma 5\%-95\%} = 2.19$. The analysis showed that the tests currently performed inside the Company cannot cover the whole range of life, making not possible the definition of a whole fatigue curve, but actually only the scatter around a fixed point. This was true especially for pitting. Alternative testing procedures should be adopted by the Company to completely characterize fatigue behavior of gears.

The globalization and the necessity of product localization of multinational corporations require the knowledge also of the materials of emerging areas where the production is localized. A test plan involving six different case-hardening steels was defined. Due to some supply problems, only four steels were compared: 20MnCr5 and 18NiCrMo5 (from Italy) and EN 353 and BS 815 H 17 (from India). Static tensile tests showed that after case-hardening the steels behaved very similarly, with ultimate tensile strength around 1700 MPa (on 6-mm-diameter specimens) and very low ductility (around 2% of elongation after failure). Plane bending fatigue tests under $R = 0.1$ stress ratio on ground plain specimens showed fatigue limits around 570 MPa for Italian steels, in terms of stress amplitudes. Indian steels showed fatigue curves 5% higher of Italian ones. The effect of surface finishing was investigated by comparing fatigue results of ground (after case-hardening) and machined (as-carburized) plain specimens. The fatigue limits resulted the same, since on one hand grinding improved the surface finishing and re-

moved the IGO-layer, but on the other hand it removed also the external layer with the highest compressive residual stress. Additional fatigue tests on notched specimens in 20MnCr5 steel were carried out under plane bending and axial loads. Tests on notched specimens exhibited much lower scatter than ground plain specimens, and the notch sensitivity at endurance limit resulted 20% lower than that one predicted by ISO 6336. Considering all the tested specimens, the endurance limit was found to be located in the range of 50,000 ÷ and 400,000 cycles, that is a much shorter number of cycles than the 3,000,000 of cycles proposed by the standard. Only a couple of failures on plain specimens occurred at long lives (higher than 1,500,000 cycles). In such cases, the fracture started in the internal matrix, approximately near the interface of external case-hardened layer and internal core. Such a failure mode is probably due to the deformation mismatch of the two different phases constituting the microstructure (martensite and bainite) in that area. The fracture of the other specimens was found to start from the surface, and inclusions were not found to be critical for the analyzed cases. Internal matrix crack origins are supposed to be typical of low stress gradients, that is not the case of gear teeth, where the presence of the tooth root fillet moves the most probable crack initiation site from the core to the surface.

To investigate to which extent the methods proposed by ISO 6336 for bending fatigue design are reliable, a 20MnCr5 gear used on off-highway axles was tested under $R = 0.1$ plane bending tests. The three different design methods of the standard starting from fatigue data of reference gears (method B), plain specimens (method B_p) and notched specimens (method B_k) were applied to the experimental data collected in this work. Results showed that method B was able to predict very well the slope of the bending curve of the real gears, but it placed the endurance limit at 3,000,000 of cycles, that is not consistent with experimental evidence, since also gears showed the endurance limit around 100,000 cycles, like the specimens. The specimen based methods led to steeper fatigue curves, but they took into account the real position in terms of number of cycles of the endurance limit. Method B_k resulted more accurate than method B_p to estimate the endurance limit. Since the notch sensitivity found experimentally was significantly different from that predicted by the standard, the specimen-based methods were calibrated using the experimental results obtained by specimen and gear tests. A new value of the slip layer thickness to be used in the calculation of notch sensitivity factors was proposed on the basis of experimental evidence. Results improved sensibly, especially in the definition of the endurance limit, since error on its definition was reduced from 7% to 4% for method B_k and from 25% to 8% for method B_p . The use of fatigue data taken from specimens allows to take into account differences on fatigue performance of different steels. It resulted

more convenient using data taken from notched specimens, since correction factors evaluated in such a way are more similar to gears, that are notched components as well. From the point of view of calculation, the application of ISO 6336 standard led to tooth root stresses 10% higher than the corresponding values obtained using 3D FE analyses. From this point of view the standard operates on the safe side, overestimating the tooth root bending stress. The use of pulsator tests to characterize bending fatigue performance of gears was found to be more effective, faster and easier than performing tests on complete axles or drivelines (as reported in the testing procedures of the Company), at least for cylindrical gears. Such a test permitted the estimation of statistical scatter and was able to clearly show differences on fatigue performances of gears coming from different suppliers.

Statistical Analysis of Fatigue Data

A.1 Introduction

When dealing with fatigue experimental tests, statistical analysis becomes a key aspect to be taken into account. The design against fatigue must be based on fatigue curves where certain levels of reliability and risk are considered. This means that in most cases, designing using the best fitting fatigue curve obtained directly from experimental tests it is not sufficient. For particular application, for example naval and aeronautic industry, the reliability of the design component under service must be very high, in order to avoid injury to people as a consequence of a failure.

The statistical scatter obtained during fatigue tests can be originated by several different sources, such as the correct alignment of the specimens on the testing machines, some inhomogeneity in the material properties, differences in the surface conditions of the specimens, different temperatures and many other factors. However, fatigue is inherently affected by statistical scatter, and this aspect must be necessarily considered in the design phase of a component.

Different approaches and techniques are reported in the literature, depending for instance on the statistical distribution adopted and the number of variables considered during the test. Statistical treatment of data is reported in technical standards such as ASTM E739-1[75], JSME S 002 [76] and ISO 12107 [7], where prescriptions for the execution of the fatigue test and techniques for the statistical analysis of data are reported.

A general guideline is to test more than one specimens at a given stress amplitude, in order to have an estimation of the statistical dispersion under the same testing conditions. Depending on the purpose of the fatigue test the number of stress levels and of specimens varies. Generally it is suggested

to use 6-12 specimens for preliminary and exploratory tests and 12-24 specimens for design and reliability tests. A useful parameter to summarize the nature of a fatigue test is the *percent replication* (PR) parameter, defined as follows:

$$PR = 100 \left(1 - \frac{l}{n_s} \right) \quad (\text{A.1})$$

where l is the number of stress levels tested for the definition of the S-N curve and n_s is the total number of specimens used. PR is therefore a sort of measurement of how many specimens of a series are used to replicate a test at a given stress level. Using PR parameter, fatigue tests may be divided into [77]:

- preliminary and exploratory tests, $PR = 17 \div 33$
- research and development tests, $PR = 33 \div 50$
- design allowable data tests, $PR = 50 \div 75$
- reliability data tests, $PR = 75 \div 88$

In the following pages, some practical aspects to draw fatigue curves at desired reliability and confidence levels will be reported, considering both the finite life and the infinite life region of the S-N curve.

A.2 Finite life region

The finite life region of the fatigue curve must be first of all defined by fitting the experimental points obtained from the tests.

For stress based tests, there will be n_s couples of (S, N) points. The most common way to fit the data is to use a least square regression, which identifies a straight line that minimize the square of the distances between the points and the line itself. To make the application of the least square regression model possible, it is necessary that the data are linearly distributed. For this reason, the regression is generally applied to semi logarithmic or log-log charts, since the fatigue data appear linearized in such a case. It must be noted that for stress-based tests, the independent variable is the applied stress (S_a or $\log S_a$) chosen for the execution of the tests, while the number of cycles to failure ($\log N$) is the dependent variable.

Generally, given n_s couples of (X_i, Y_i) , where $i = 1, \dots, n_s$, the least square regression model is based on the following statement:

$$Y = A + BX + \varepsilon \quad (\text{A.2})$$

where ε is a random variable of error, i.e. that a dependent variable is approximated with a certain error by a straight line. The best approximation of the dependent variable is obtained using the regression line:

$$\hat{Y} = \hat{A} + \hat{B}X \quad (\text{A.3})$$

where \hat{A} and \hat{B} are the fitting parameters chosen in order to minimize the sum of the square of the deviations of the experimental Y from those predicted, which is:

$$\Delta^2 = \sum_{i=1}^{n_s} (Y_i - \hat{Y}_i)^2 = \sum_{i=1}^{n_s} (Y_i - \hat{A} - \hat{B}X_i)^2 \quad (\text{A.4})$$

The minimization of Δ^2 is made imposing:

$$\frac{\partial \Delta^2}{\partial \hat{A}} = - \sum_{i=1}^{n_s} 2(Y_i - \hat{A} - \hat{B}X_i) = 0 \quad (\text{A.5})$$

$$\frac{\partial \Delta^2}{\partial \hat{B}} = - \sum_{i=1}^{n_s} 2(Y_i - \hat{A} - \hat{B}X_i)(X_i) = 0 \quad (\text{A.6})$$

Solving the system of two equations A.5 and A.6 it can be obtained:

$$\hat{B} = \frac{\sum_{i=1}^{n_s} (X_i - \bar{X})(Y_i - \bar{Y})}{\sum_{i=1}^{n_s} (X_i - \bar{X})^2} \quad (\text{A.7})$$

$$\hat{A} = \bar{Y} - \hat{B}\bar{X} \quad (\text{A.8})$$

where \bar{X} and \bar{Y} are the average values of X and Y respectively, that is:

$$\bar{X} = \frac{1}{n_s} \sum_{i=1}^{n_s} X_i \quad (\text{A.9})$$

$$\bar{Y} = \frac{1}{n_s} \sum_{i=1}^{n_s} Y_i \quad (\text{A.10})$$

Assuming a normal distribution of the variable Y , the standard error σ_Y of \hat{Y}_i estimates on X_i is evaluated as follows:

$$\sigma_Y = \sqrt{\frac{1}{n_s - 2} \sum_{i=1}^{n_s} [Y_i - (\hat{A} + \hat{b}X_i)]^2} \quad (\text{A.11})$$

Using the Basquin equation ¹ for S-N fatigue curve in log-log chart:

$$S_a = S'_f(2N')^b \rightarrow \log 2N' = -\frac{1}{b} \log S'_f + \frac{1}{b} \log S_a \quad (\text{A.12})$$

and remembering that $Y = \log 2N'$ is the dependent variable while $X = \log S_a$ is the independent one, it is easy to see that $\hat{A} = -\frac{1}{b} \log S'_f$ and $\hat{B} = 1/b$. Therefore, once the regression is performed from the experimental points, the characteristic values of the Basquin equation can be estimated as follows:

$$b = 1/\hat{B} \quad (\text{A.13})$$

$$S'_f = 10^{(-\hat{A} \cdot b)} \quad (\text{A.14})$$

Least square regression is already implemented in most calculation software. Just to give a useful example, Microsoft Excel perform the estimation of \hat{A} using the function =INTERCEPT($Y_1, \dots, Y_{n_s}; X_1, \dots, X_{n_s}$) and of \hat{B} using the function =SLOPE($Y_1, \dots, Y_{n_s}; X_1, \dots, X_{n_s}$).

The regression line corresponds to the fatigue "curve" at 50% of survival probability, since it is the most probable estimation of the fatigue life of the specimens. However, the risk that 50% of the component will break at the predicted life is used only for exploitative purposes. For design, it is necessary to define the lower-bound curve, that is the curve that prevent the failure of a certain desired percentage of specimens. Generally, a design requires a certain reliability, that corresponds to the survival probability (p). Since the tested sample size is limited, also the confidence level (γ) on the statistical prediction must be considered. If a huge number of components to be tested is available, after the test one could say that the fatigue curve of the components is very similar to the entire population of components. If the sample size is limited, the inferred fatigue curves is affected by a certain degree of risk that the sample size could not represent correctly the entire population, that means that the confidence on the experimental results may be low. For these reasons, generally the fatigue curves are given at a certain survival probability and confidence level.

To define the lower-bound fatigue curve, historically the engineers shifted the curve at 50% of survival probability on the safe size of $2 \div 3$ standard deviations, depending on the desired probability of survival. This approach can be summarized as follows:

$$Y_L(X_i) = \hat{Y}(X_i) - q \cdot \sigma_Y \quad (\text{A.15})$$

¹ S_a is the applied stress amplitude, S'_f is the fatigue strength coefficient, b is the fatigue strength exponent and N' is the number of reversals to fracture

where $Y_L(X_i)$ is the lower limit value of $Y = \log N$, σ_Y is the standard error of Y on X_i and q is a multiplier equals to the number of standard deviations that are used to shift the regression curve. The expression A.15 can be rewritten as follows:

$$\log(N_L(S_a)) = \log(\hat{N}(S_a)) - q \cdot \sigma_Y \quad (\text{A.16})$$

Since this approach fails to account for the statistical distribution of fatigue life due to the sample size and the reliability level of interest, some other techniques were introduced.

A simple technique is that one proposed by Lieberman [14], which is based on shifting the median life of a factor q_{Lieb} dependent on the desired confidence level and the survival probability of the lower-bound. The values of q_{Lieb} are reported in Table 2.9. This method is valid when samples are tested at a fixed load level and the fatigue life is the unique log-normal distributed variable. Lieberman's method permits the estimation of the upper bound cure as well. In such a case the following expression must be used:

$$Y_U(X_i) = \hat{Y}(X_i) + q \cdot \sigma_Y \quad (\text{A.17})$$

It is interesting to note that in a Log-Log chart both the lower and the upper bound curves are straight lines, parallel to the regression line. A common statistical parameter used to characterize the statistical dispersion of data is the scatter index T_σ , which is defined as the ratio between the upper bound stress at a given number of cycles and the lower bound stress at the same N :

$$T_\sigma = \frac{S_{a,U}}{S_{a,L}} \quad (\text{A.18})$$

The scatter index T_σ is constant for every number of cycles considered (in the finite life region).

T_σ can be expressed also using standard error and the parameters of the regression line. The fatigue strength coefficients of Basquin's equations of upper and lower bound curves ($S'_{f,U}$ and $S'_{f,L}$ respectively) can be expressed as:

$$\begin{cases} S'_{f,U} = 10^{-\hat{A}_U/\hat{B}} = 10^{-(\hat{A}+q\sigma_Y)/\hat{B}} \\ S'_{f,L} = 10^{-\hat{A}_L/\hat{B}} = 10^{-(\hat{A}-q\sigma_Y)/\hat{B}} \end{cases} \quad (\text{A.19})$$

The Basquin's equations of the upper and lower bound curves are:

$$\begin{cases} S_{a,U} = S'_{f,U} N^{1/\hat{B}} = 10^{-\hat{A}_U/\hat{B}} = 10^{-(\hat{A}+q\sigma_Y)/\hat{B}} N^{1/\hat{B}} \\ S_{a,L} = S'_{f,L} N^{1/\hat{B}} = 10^{-\hat{A}_L/\hat{B}} = 10^{-(\hat{A}-q\sigma_Y)/\hat{B}} N^{1/\hat{B}} \end{cases} \quad (\text{A.20})$$

and therefore the scatter index can be obtained as following:

$$T_\sigma = \frac{S_{a,U}}{S_{a,L}} = 10^{-\frac{2q\sigma_Y}{B}} \quad (\text{A.21})$$

It can be proved also that:

$$S_{a,L} = \frac{\hat{S}_a}{\sqrt{T_\sigma}} \text{ and } S_{a,U} = \hat{S}_a \sqrt{T_\sigma} \quad (\text{A.22})$$

where \hat{S}_a is the stress (amplitude) of the regression line at a given number of cycles.

The Lieberman's method appears incorrect for a regression analysis in which both X and Y are variables, since only the variable Y is taken into account. To overcome this limitation, other more complex techniques were developed. For instance, ASTM method [75] evaluates the exact double-sided confidence interval of the whole finite-life region of the fatigue curve (for $\gamma=90\%$ and $\gamma=95\%$) but only for the median curve at 50% of survival probability. In such a case, the double-sided confidence band is estimated using in the equation A.15 a q_{ASTM} factor defined as follows:

$$q_{ASTM} = \mp \sqrt{2F_{\gamma,2,n_s-2}} \cdot \sqrt{\frac{1}{n_s} + \frac{(X_i - \bar{X})^2}{\sum_{i=1}^{n_s} (X_i - \bar{X})^2}} \quad (\text{A.23})$$

Where $F_{\gamma,2,n_s-2}$ is the F-distribution value evaluated for the confidence level γ and for $(2, n_s-2)$ degrees of freedom. Since a double-sided confidence band is defined, there are two values for q_{ASTM} : the negative one is for the upper-bound curve, the positive one for the lower-bound one.

To extend the possibility to estimates curves at different survival probabilities the techniques proposed by Shen [78] or ISO 12107 [7] may be used. Technique proposed by Shen is based on the Owen factor (q_{owen}), which can be evaluated using a set of equations. The explanation of this method is out of the scope of this section, but details can be found in [77] or [78].

ISO technique is instead based on the factor q_{ISO} , that can be evaluated using the following expression:

$$q_{ISO} = q_{Lieb,(p,\gamma,\nu)} \cdot \sqrt{1 + \frac{1}{n_s} + \frac{(X - \bar{X})^2}{\sum_{i=1}^{n_s} (X_i - \bar{X})^2}} \quad (\text{A.24})$$

where the $q_{Lieb,(p,\gamma,\nu)}$ factor is defined by the desired probability of survival p , confidence level γ , and the number of degrees of freedom used in the

calculation of the standard error on Y ($\nu = n_s - 2$, see Equation A.11). The term inside the root sign is a correction factor of the standard deviation σ_Y and tends to be negligible when the sample size is high. Using this technique, the lower-bound curve is not necessarily a straight line. The term under the root sign tends to extend the scatter band when the lower bound is estimated for stresses far away from the tested one. It is worth to remember that a log-normal distribution of the fatigue life is assumed.

It must be noted that the Table 2.9 is constructed for the cases where $\nu = n - 1$. In other words, the Lieberman's original table (where the sample size n is used to define q_{Lieb}) and the ISO 12107 table (where the number of degrees of freedom $\nu = n - 1$ is used to define q_{Lieb}) lead to the same results. When statistical dispersion has to be evaluated for the case where $\nu = n - 2$, q_{Lieb} must be evaluated from original Lieberman's table by reading the coefficient of the $(n - 1)$ -th line, being n the sample size.

A.3 Endurance limit

For design purposes, the fatigue strength is often the most important information. Historically, for steels, the fatigue curves admit a high-cycle knee which identifies an horizontal line for high number of cycles. The most effective way to estimate the endurance limit is the *stair case* method (also called "up-and-down" method). A target fatigue life must be defined before starting the test. The method can be used for the estimation of the fatigue strength for number of cycles both in the finite life region and in the horizontal part of the of the S-N curve. Firstly, the stress expected to be the fatigue strength for the target life is applied. If the specimen fails before reaching the target life, the next test is performed decreasing the applied stress by a fixed step d . Conversely, if the specimens does not fail, the next attempt is made increasing the applied stress by d . Following this rule a sequence of test is carried out. The higher the number of test, the higher the accuracy of the statistical estimation. The stress step d is generally chosen equal to the expected standard deviation on the fatigue strength σ_X , even if this value is sometimes hard to know at priori.

There are several methods to perform and analyze stair case sequences. The typically used one is the Dixon and Mood [79] method, which is also taken as reference from many standards, such as ISO 12107 [7] or UNI 3964 [80]. However, there are some more complex methods that take into account statistical distribution different from normal one and suspended tests (such as [81]), but they are not reported here.

Dixon method is based on the assumption of normal distribution of the fa-

tigue strength. The easiest formulation of the method assumes that the tested stress levels S_i are equally spaced with a chosen increment d . However, more complex formulations are available to account for non equal gaps among the stress levels [79]. The stress levels S_i are numbered in increasing order from $i = 0$ to $i = l$. S_0 is the minimum stress level of the less frequent event occurred during the stair case test: it can be either a failure or a run-out. Failures are denoted with "x" while run-out with "o" in the stair case sequence. Statistical computations are made only on the less frequent event: x or o . The number of times that the less frequent event take place at a S_i stress level is called n_i , while the total number of times the event occurs in the stair case sequence is $N = \sum n_i$. Some other auxiliary variables are defined as:

$$A_{DM} = \sum i \cdot n_i \quad (\text{A.25})$$

$$B_{DM} = \sum i^2 \cdot n_i \quad (\text{A.26})$$

$$C_{DM} = \frac{B_{DM} \cdot N - A_{DM}^2}{N^2} \quad (\text{A.27})$$

The estimate of the mean fatigue strength (μ_X) is defined as:

$$\mu_X = S_0 + d \left(\frac{A_{DM}}{N} \pm 0.5 \right) \quad (\text{A.28})$$

where the plus sign (+) is used if the less frequent event is survival and minus sign (-) is used if the less frequent event is a failure.

The standard deviation of the fatigue strength (σ_X) is estimated by:

$$\sigma_X = 1.62 \cdot d \left(\frac{NB - A^2}{N^2} + 0.029 \right) \quad (\text{A.29})$$

if $C_{DM} \geq 0.3$

Equation A.29 is an approximate one and rapidly breaks down when C_{DM} becomes less than 0.3. However, although complex formulations exist to consider the case when $C_{DM} < 0.3$ [79], in [77] the following expressions are reported:

$$\sigma_X = 0.53 \cdot d \quad (\text{A.30})$$

if $C_{DM} < 0.3$

It is important to note that the Dixon method is valid only if at least 15 specimens are tested in the stair case sequence. 15 is a relatively a low number of test for a sensitivity analysis, but the method works properly since the

up-and-down approach tends automatically to focus the results around the mean value. However, 15 specimens are sometimes too many to be tested in a fatigue test problem, due to time reasons (if the run-out number of cycles is high and the test frequency is low, several days may be necessary to complete only one run-out test). For this reason, other techniques were developed to permit the estimation of the fatigue strength with a limited number of specimens. This kind of methods are called *modified stair case methods*. There are at least two of these methods: one proposed by Dixon [82] and one proposed by Hodge-Rosenblatt [83].

The Dixon method permits the estimation of both the mean value and the standard error of the fatigue strength when samples shorter than 15 specimens are used to evaluate the stair case sequence. The value of the mean is evaluated with the following expression:

$$\mu_X = S_f + k_D \cdot d \quad (\text{A.31})$$

where S_f is the last value of stress applied in the stair case sequence and k_D is a coefficient depending on the sequence order of x 's and o 's, as reported in the table A.1. The standard error is evaluated on the basis of the number of the sample size, and resulted independent from x 's and o 's sequence. The method works if the stress step size d is nominally chosen equal to the standard deviation of the population σ_X . However, it was shown [82] that the method works properly even if a step size $d = (0.5 \div 2)\sigma$ is chosen.

The estimation of σ_X of Equation A.30 may be derived from the data reported in Table A.1. Considering that 15 specimens are tested (at least) and that the stair case tends to concentrate data around the mean stress value, the less frequent event may occur 7 times in a balanced stair case sequence. Since statistical analysis is based on a sequence of 7 data, extrapolating the standard error from a sample size of 7 specimens the value $\sigma_S = 0.53\sigma$ is obtained (as reported in Figure A.1). If we remember that nominally the method is valid for the condition $d = \sigma$, then we obtain the expression A.30.

The Hodge-Rosenblatt method permits the estimation of only the mean value of the fatigue strength μ_X . The problem of estimating the standard deviation σ_X is not considered from the authors, since (i) μ_X is usually the parameter of greater interest and (ii) because with small samples no estimate of σ_X can be accurate enough to have much value [83]. In a stair case sequence of n_s specimens, the first specimen does not contain any information about the μ_X , since it is usually chosen in advance by the experimenter. Conversely, even if the stair case sequence is terminated at the n_s -th, the experimenter knows the following stress levels of the sequence S_{n_s+1} stress level. Therefore the test $n_s + 1$, which is obviously not performed, contains useful information.

Table A.1: K_D coefficient for Dixon-Mood modified stair case method

N	Second part of Series	k_D for test series whose part is				Standard Error	
		o	oo	ooo	oooo		
2	x	-0.500	-0.388	-0.378	-0.377	o	0.88σ
3	xo	0.842	0.890	0.894	0.894	ox	0.76σ
	ox	-0.178	0.000	0.026	0.028	oo	
4	xoo	0.299	0.314	0.315	0.315	oxx	0.67σ
	xox	-0.500	-0.439	-0.432	-0.432	oxo	
	xxo	1.000	1.122	1.139	1.140	oox	
	xxx	0.194	0.449	0.500	0.506	ooo	
5	xooo	-0.157	-0.154	-0.154	-0.154	oxxx	0.61σ
	xoox	-0.878	-0.861	-0.860	-0.860	oxxo	
	xoxo	0.701	0.737	0.741	0.741	oxox	
	xoxx	0.084	0.169	0.181	0.182	oxoo	
	xxoo	0.305	0.372	0.380	0.381	ooux	
	xxox	-0.305	-0.169	-0.144	-0.142	ooxo	
	xxxo	1.288	1.500	1.544	1.549	ooox	
	xxxx	0.555	0.897	0.985	1.000	oooo	
6	xoooo	-0.547	-0.547	-0.547	-0.547	oxxxx	0.56σ
	xooox	-1.250	-1.247	-1.246	-1.246	oxxxo	
	xooxo	0.372	0.380	0.381	0.381	oxxox	
	xooxx	-0.169	-0.144	-0.142	-0.142	oxxoo	
	xoxoo	0.022	0.039	0.040	0.040	oxoxx	
	xoxox	-0.500	-0.458	-0.453	-0.453	oxoxo	
	xoxxo	1.169	1.237	1.247	1.248	oxoox	
	xoxxx	0.611	0.732	0.756	0.758	oxooo	
	xxooo	-0.296	-0.266	-0.263	-0.263	ooxxx	
	xxoox	-0.831	-0.763	-0.753	-0.752	ooxxo	
	xxoxo	0.831	0.935	0.952	0.954	ooxox	
	xxoxx	0.296	0.463	0.500	0.504	ooxoo	
	xxxoo	0.500	0.648	0.678	0.681	oooux	
	xxxox	-0.043	0.187	0.244	0.252	oooxo	
	xxxxo	1.603	1.917	2.000	2.014	oooox	
	xxxxx	0.893	1.329	1.465	1.496	ooooo	
		x	xx	xxx	xxxx	Second part of Series	
		$-k_D$ for test series whose part is					

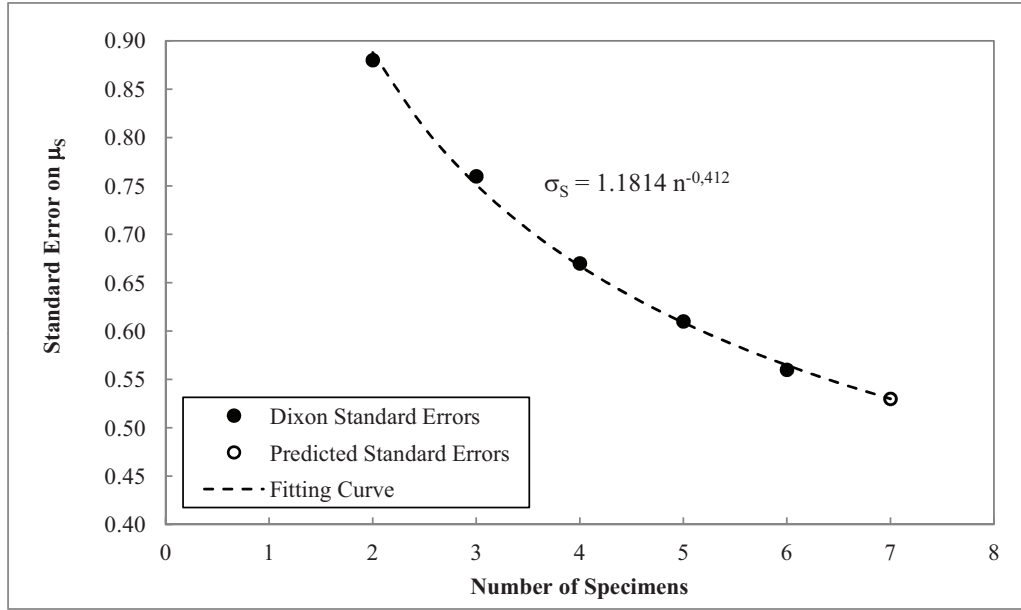


Figure A.1: Extrapolation of the standard error on μ_S

For these reasons, considering that the S_i is the stress used to test the i -th specimen in the stair case sequence, the fatigue strength is estimated as follows:

$$\mu_X = \frac{\sum_{i=2}^{n_s+1} S_i}{n_s} \quad (\text{A.32})$$

The Dixon's modified stair case method appears to be more powerful if compared to Hodge-Rosenblatt's one, but it is also more complex.

The ISO 12107 [7] suggests to use the Dixon method to perform stair case test (at least 15 specimens). However, the Standard does not allow estimation of the variance using Equation A.30. If only a small sample size is available for stair case testing (but at least 6 specimens), [7] allows the experimenter to use the modified stair case method of Hodge-Rosenblatt. The Standard requires that the variance of the population must be known in advance, and that the step size between the stress levels should be chosen close to it.

Once the mean value of the fatigue strength (at the desired fatigue life) and the standard error is known, the lower bound value for a given survival probability can be estimated. Two different approaches may be used for this purpose: (i) one based on the normal cumulative standard distribution and (ii) one based on Lieberman coefficients q_{Lieb} .

The first approach (i), used for instance by UNI3964 [80], is to consider a normal distribution of the stress (or Log-stress) with mean μ_X and variance σ_X . In this way the stress relevant to the desired probability of failure can

Table A.2: q_N values for Standard Normal Distribution [84]

Probability of survival	q_N
90 %	1.29
95 %	1.65
97.7 %	2.00
99 %	2.33

be estimated using the normal distribution percentiles. The one-sided lower bound limit for a survival probability p can be estimated as:

$$S_p = \mu_X - q_N \sigma_X \quad (\text{A.33})$$

where q_N is the value of the standardized variable S that leads to the p cumulative standard normal distribution. Tables of q_N can be found elsewhere, for instance in [84]. A short summary of q_N is reported in Table A.2. This approach cannot allow the experimenter to evaluate the confidence of the estimation, since the sample size is not considered and the distribution of the stress is considered perfectly normal (or log-normal). The second approach (ii) for the estimation of the lower bound value is based on Lieberman coefficients and is therefore more powerful since it takes into account the sample size. Only the data of the less frequent event (failure or survival) are used for the statistics. Therefore the lower bound value of the fatigue strength estimated for a survival probability p and a confidence level γ is evaluated using the expression:

$$S_{p,\gamma} = \mu_X - q_{Lieb,(p,\gamma,\nu)} \sigma_X \quad (\text{A.34})$$

where $q_{Lieb,(p,\gamma,\nu)}$ is evaluated from Table 2.9 using a number of degree of freedom $\nu = n' - 1$ (n' is the number of data of the less frequent event). In this case $\nu = n' - 1$ since in this case the variance of the population is estimated for a fixed level of stress (μ_X).

ISO 12107 Standard suggests to use approach (ii) for stair case tests.

A.4 Estimation of a full S-N curve

ISO 12107 suggests a procedure to evaluate the entire Wohler curve using at least 14 specimens. The approach is the same of that reported in JSME S 002 [76].

At least 8 specimens are used to evaluate the finite life region of the S-N

curve and at least 6 specimens are used for the fatigue limit. The number of specimens is determined in a way that the fatigue strength predicted in the finite life region of the curve and the fatigue strength predicted in the infinite life of the curve have the same statistical confidence. It is recommended that the following expression is satisfied:

$$\frac{n_2}{n_1} = \frac{l_1 + 1}{2l_1 - 1} \quad (\text{A.35})$$

where n_1 is the number of specimens for the inclined line of the curve and n_2 the specimens for the horizontal line, while l_1 is the number of stress levels tested for the inclined life. However, since different statistical techniques are used for evaluating the two parts of the curve, different scatter bands for the inclined and the horizontal lines may be obtained.

The finite life region of the curve is defined testing 8 specimens at 4 different stress levels. The data are then elaborated using the least square regression, which permits the estimation of a mean life for every applied stress. The standard error on the life is evaluated using Equation A.11 and then the standard error on the stress is evaluated as:

$$\sigma_X = \frac{\sigma_Y}{\hat{B}} \quad (\text{A.36})$$

The infinite life region of the curve is evaluated using the modified stair case approach of Hodge and Rosenblatt. The mean fatigue limit is therefore evaluated using a stair case sequence of 6 specimens where the step size d is equal to σ_X estimated with Equation A.36. The lower bound curve of the inclined line is evaluated using Equations A.16 and A.24, while for the endurance limit (horizontal line) the Equation A.34 is used. The choice of the Lieberman coefficients $q_{Lieb,(p,\gamma,\nu)}$ is made assuming $\nu = n_1 - 2$ for both the finite and the infinite life region of the SN curve, since statistics for standard errors is based only on the data of the inclined line (n_1 specimens).

A software was developed (using Visual Basic program language) to perform the statistical analyses of experimental sets of data. All the details on the software can be found in [54]. Starting from the set of experimental data, the software can draw the statistical curve at the desired survival probability for both the finite and infinite life region (implementing also the staircase calculation using the Dixon and the modified approach) and the confidence bands according to [75] and to [85].

Concerning the finite life region, the software was based on the Lieberman's approach, where statistics of two variables was considered ($\nu = n_s - 2$ degrees of freedom was used to calculate the standard deviation). The scatter along the stress levels was considered fixed, therefore the term under the root sign in Equation A.24 was considered equal to 1.

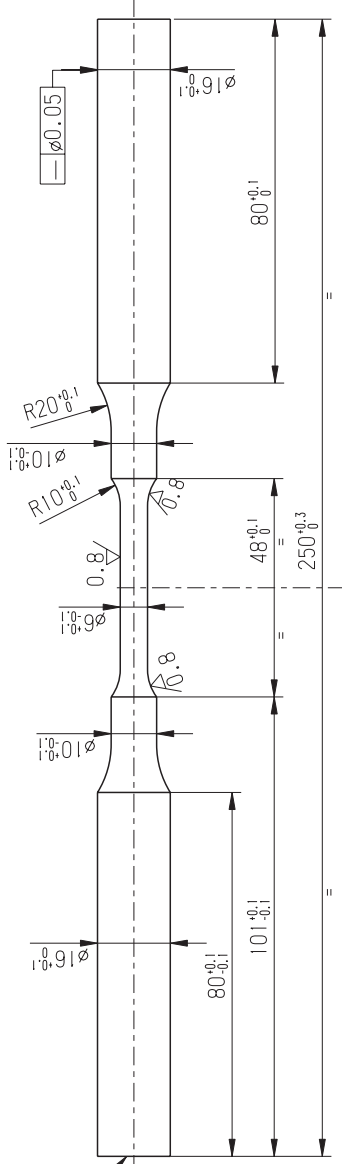
Appendix **B**

Technical Drawings

In the following pages the technical drawings of the specimens and of the four point plane bending equipment presented in Chapter 3 are reported.

DISEGNO N. SPECIMEN E
PART N.

MARCIARE LATO DI PARTENZA DELLA LAVOAZIONE
MARK STARTING SIDE OF MACHINING



1:1 (0.8)

TABELLA (A)
TABLE (A)

STEEL	STANDARD
20MnCr5	CARRARO 1-01-88
18NiCrMo5	CARRARO 1-12-88
EN353	(BS 970)
815M17	BS 970-1:1996
19CrNi5	CARRARO 1-00001/0
20CrMoH	GB/T 5216-2004

	PART WITH KEY C'S COMPONENTE CON CARATTERISTICHE CHIAVE	N. OF KEY C'S N. CARATTERISTICHE CHIAVE
	PART INCLUDES KEY CHARACTERISTICS WITH PROCESS CAPABILITY DEMONSTRATION SEE CARRARO STD N. 0-56-95	PART WITH SAFETY C'S COMPONENTE CON CARATTERISTICHE DI SICUREZZA
		PART INCLUDES SAFETY CHARACTERISTICS WITH DOCUMENTATION REQUIREMENTS AND PROCESS CAPABILITY DEMONSTRATION SEE CARRARO STD N. 0-56-95
		COMPONENTE CON CARATTERISTICHE DI SICUREZZA CON DOCUMENTAZIONE OBBLIGATORIA E DIMOSTRAZIONE CAPACITA' DI PROCESSO VEDERE CARRARO STD N. 0-56-95

DENOMINAZIONE / PROVA PER PROVE DI TRAZIONE STATICA / SPECIMEN FOR STATIC TENSILE TEST DESCRIPTION	
MODELLO N. / CASTING REF. A3	PESO / WEIGHT 0.294 daN
SOST. IL REMPLACE -	SCALA / SCALE 1:1
DISEGNO N. / DRAWING N. 37	TAV. / SHEET 1/1



CARRARO DRIVETECH S.p.A. - Via Olmo, 37
35011 CAMPODARSEGO (PD) - ITALY

3	DESCRIZIONE CHANGE
TUTTI I DIRITTI SONO RISERVATI E PROPRIETA' DI CARRARO S.P.A. SENZA IL CONSENSO SCRITTO DI CARRARO S.P.A. QUESTO DISEGNO NON PUO' ESSERE RIPRODOTTO, O IN ALCUN MODO ESSERE UTILIZZATO PER LA PRODUZIONE DEI COMPONENTI O ASSIEME ILLUSTRATO, NEE ESSERE TRASPRESO A ALTRE PARTI, CON INFRAZIONE VERBA, PERSECUZIONE LEGALE, O IN ALCUN MODO. ALL RIGHTS ARE RESERVED BY CARRARO S.P.A. ANY REPRODUCTION OR USE OF THIS DRAWING FOR THE MANUFACTURE OF THE COMPONENT OR ASSEMBLY ILLUSTRATED AND IN ANY MANNER WITHOUT WRITTEN CONSENT OF CARRARO S.P.A. WILL BE LEGALLY PROSECUTED.	
MATERIALE STD VEDI TABELLA A / SEE TABLE A DISEGNO / DRAWN DENCO CARLO	
MATERIALE OPT APPROVATO / APPROVED -	
TRATT. TERM. / HEAT TREAT.	DATA / DATE 18/01/2013
TRATT. SUPERF. / SURF. TREAT.	CL. FUNZ. / FUNC. CL. -
RIF. GENERALI / GENERAL REFS. 0-20-90	
PRODOTTO / ASSEMBLY -	

0	10	20	30	40	50	60	70	80	90	100
---	----	----	----	----	----	----	----	----	----	-----

DISEGNO N. SPECIMEN ECH
PART N.

MARCHIARE LATO DI PARTENZA DELLA LAVORAZIONE
MARK STARTING SIDE OF MACHINING

2-SPECIFICHE DI CEMENTAZIONE
2-CASE-HARDENING SPECS

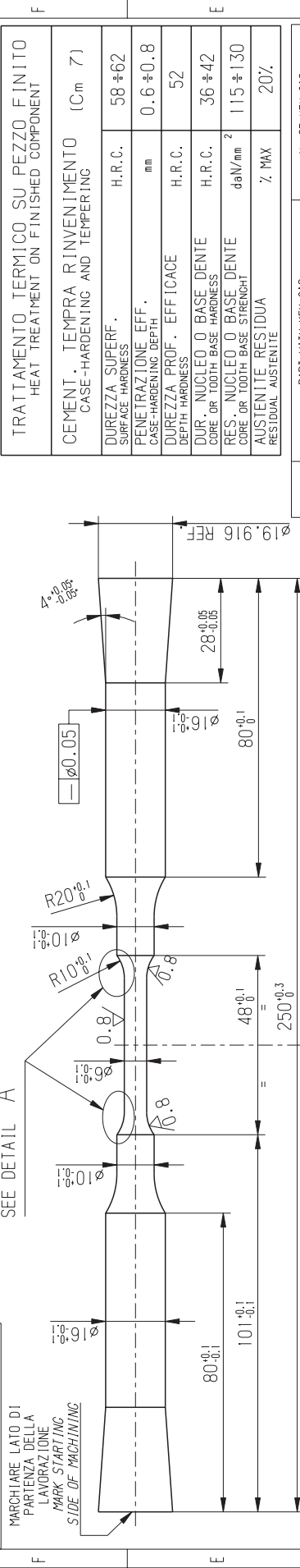


TABELLA (A)
TABLE (A)

STEEL	STANDARD
20MnCr5	CARRARO 1-01-88
18NiCrMo5	CARRARO 1-12-88
EN353	(BS 970)
815M17	BS 970-1:1996
19CrNi5	CARRARO 1-00001/0
20CrMoH	GB/T 5216-2004

PROCEDURA DI LAVORAZIONE:
1 - LASCIARE SOVRAMETALLO NELLE DUE ZONE DI RACCORDO E NEL TRATTO FRA ESSE COMPRESO COME INDICATO A DISEGNO
2 - ESEGUIRE TRATTAMENTO DI CEMENTAZIONE.
3 - LAVORARE LE SUPERFICIE AL PUNTO 1 FINO A DIMENSIONI DI FINITURA

MANUFACTURING PROCEDURE:
1 - LEAVE FINISHING ALLOWANCE IN THE TWO FILLET AREAS AND ON THE TRACT BETWEEN THEM AS REPORTED IN THE DRAWING
2 - PERFORM HEAT TREATMENT
3 - WORK SURFACES MENTIONED AT POINT 1 TO FINISHING DIMENSIONS



TRATTAMENTO TERMICO SU PEZZO FINITO
HEAT TREATMENT ON FINISHED COMPONENT

CEMENTAZIONE
CASE-HARDENING

DUREZZA SUPERF. H.R.C. 58 ± 62

PENETRAZIONE EFF. CASE-HARDENING DEPTH mm 0.6 ± 0.8

DUREZZA PROF. EFFICACE H.R.C. 52

DUR. NUCLEO O BASE DENTE H.R.C. 36 ± 42

RES. NUCLEO O BASE DENTE CORE OR TOOTH BASE STRENGTH daN/mm² 115 ± 130

AUSTENITE RESIDUA RESIDUAL AUSTENITE % MAX 20%

COMPONENTE CON CARATTERISTICHE CHIAVE
PART WITH KEY C'S CHARACTERISTICS WITH PROCESS CAPABILITY DEMONSTRATION

COMPONENTE CON CARATTERISTICHE DI SICUREZZA
PART WITH SAFETY C'S CHARACTERISTICS WITH DOCUMENTATION REQUIREMENTS

COMPONENTE CON CARATTERISTICHE DI SICUREZZA CON DOCUMENTAZIONE OBBLIGATORIA E DIMOSTRAZIONE CAPACITA' DI PROCESSO
VEEDERE CARRARO STD N. 0-56-95

DESCRIZIONE
CHANGE

DISGNAIO
DRAWN

APPROVATO
APPROVED

DATA
DATE

CL.FUNZ.
FUNC.CL.

RIF. GENERALI
GENERAL REFS.

PROVINO PER PROVE DI TRAZIONE STATICA / SPECIMEN FOR STATIC TENSILE TEST

MODELLO N. CASTING REF. A3

SOST. IL REMPLACES SCALA SCALE 1:1

DISEGNO N. PART N. IAV SHEET 1/1

PRODOTTO ASSEMBLY -

CARRARO DRIVETECH
CARRARO DRIVETECH S.p.A. - Via Olmo, 37
35011 CAMPODARSEGO (PD) - ITALY

DESCRIZIONE
DESCRIPTION

PROVINO PER PROVE DI TRAZIONE STATICA / SPECIMEN FOR STATIC TENSILE TEST

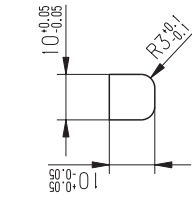
MODELLO N. CASTING REF. A3

SOST. IL REMPLACES SCALA SCALE 1:1

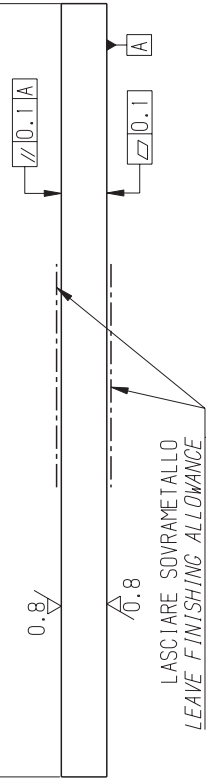
DISEGNO N. PART N. IAV SHEET 1/1

PRODOTTO ASSEMBLY -

DISEGNO N. SPECIMEN A
PART N.



170^{+0.1}



LASCiare SOVRAMETALLO
LEAVE FINISHING ALLOWANCE

PROCEDURA DI LAVORAZIONE:
 1 - LASCiare SOVRAMETALLO COME INDICATO A DISEGNO
 2 - ESEGUIRE TRATTAMENTO DI CEMENTAZIONE
 3 - LAVORARE LE SUPERFICI FINO A DIMENSIONI DI FINITURA

MANUFACTURING PROCEDURE:
 1 - LEAVE FINISHING ALLOWANCE AS REPORTED IN THE DRAWING
 2 - PERFORM HEAT TREATMENT
 3 - WORK THE SURFACES TO FINISHING DIMENSIONS

VISTA X
VIEW X
SCALE 5:1

1.6_A (0.8_V)

TRATTAMENTO TERMICO SU PEZZO FINITO HEAT TREATMENT ON FINISHED COMPONENT	
CEMENT. TEMPRA RINVENIMENTO CASE-HARDENING AND TEMPERING	(C _m 7)
DUREZZA SUPERF. SURFACE HARDNESS	H.R.C. 58 ±62
PENETRAZIONE EFF. CASE-HARDENING DEPTH	mm 0.6 ±0.8
DUREZZA PROF. EFFICACE DEPTH HARDNESS	H.R.C. 52
DUR. NUCLEO O BASE DENTE CORE OR TOOTH BASE HARDNESS	H.R.C. 36 ±42
RES. NUCLEO O BASE DENTE CORE OR TOOTH BASE STRENGTH	daN/mm ² 115 ±130
AUSTENITE RESIDUA RESIDUAL AUSTENITE	% MAX 20%

	PART WITH KEY C'S CHIAVE	N. OF KEY C'S 0
PART INCLUDES KEY CHARACTERISTICS WITH PROCESS CAPABILITY DEMONSTRATION SEE CARRARO STD N. 0-56-95		
COMPONENTE CON CARATTERISTICHE CHIAVE CON DIMOSTRAZIONE CAPACITA' DI PROCESSO VEDERE CARRARO STD N. 0-56-95		

	PART WITH SAFETY C'S SICUREZZA	N. OF SAFETY C'S 0
PART INCLUDES SAFETY CHARACTERISTICS WITH DOCUMENTATION REQUIREMENTS AND PROCESS CAPABILITY DEMONSTRATION SEE CARRARO STD N. 0-56-95		
COMPONENTE CON CARATTERISTICHE DI SICUREZZA CON DOCUMENTAZIONE OBBLIGATORIA VEDERE CARRARO STD N. 0-56-95		

4	REV.	DESCRIZIONE CHANGE
TUTTI I DIRITTI SONO RISERVATI E PROPRIETA' DI CARRARO S.P.A. SENZA IL CONSENSO SCRITTO DI CARRARO S.P.A. QUESTO DISEGNO NON POTRA' ESSERE RIPRODOTTO, O IN ALCUN MODO ESSERE UTILIZZATO PER LA PRODUZIONE DEI COMPONENTI O ASSIEME ILLUSTRATO, NESSUNO TRASPASO A ALTRE PARTI, CON INFRAZIONE VERBA, PERSECUZIONE LEGALE, O IN ALCUN MODO. ALL RIGHTS ARE RESERVED BY CARRARO S.P.A. ANY REPRODUCTION OR USE OF THIS DRAWING FOR THE MANUFACTURE OF THE COMPONENT OR ASSEMBLY HEREIN ILLUSTRATED AND MUST NOT BE RELEASED TO OTHER PARTIES WITHOUT WRITTEN CONSENT OF CARRARO S.P.A. ANY INFRINGEMENT WILL BE LEGALLY PUNISHED.		
MATERIALE STD OPT MATERIAL	VEDI TABELLA A / SEE TABLE A	DISEGNO DRAWN
MATERIALE OPT OPT MATERIAL	-	APPROVATO APPROVED
TRATT. TERM. HEAT TREAT.	CASE-HARDENED	DATA DATE
TRATT. SUPERF. SURF. TREAT.	-	CL.FUNZ. -- FUNC. CL.
PRODOTTO ASSEMBLY	-	RIF. GENERALI GENERAL REFS.

STEEL	STANDARD
20MnCr5	CARRARO 1-01-88
18NiCrMo5	CARRARO 1-12-88
EN353	BS 9701
815M17	BS 970-1:1996
19CrNi5	CARRARO 1-00001/0
20CrMoH	GB/T 5216-2004

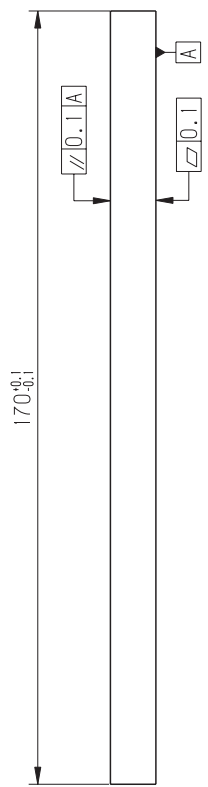
DENOMINAZIONE DESCRIPTION		PROVINO PER PROVE DI FATICHE/SPECIMEN FOR PLANE BENDING FATIGUE TESTS	
MODELLO N. CASTING REF.		A3	RESO WEIGHT
SOST. IL REPLACES			SCALA SCALE
DISEGNO N. PART N.		1/1	TAV. SHEET

CARRARO DRIVETECH S.p.A. - Via Olmo, 37
 35011 CAMPODARSEGO (PD) - ITALY

0 10 20 30 40 50 60 70 80 90 100

DISEGNO N. PART N. SPECIMEN X

TRATTAMENTO TERMICO SU PEZZO FINITO HEAT TREATMENT ON FINISHED COMPONENT	
CEMENT. TEMpra RINVENIMENTO (Cm 7) CASE-HARDENING AND TEMPERING	
DUREZZA SUPERF. SURFACE HARDNESS	H.R.C. 58 ±62
PENETRAZIONE EFF. CASE-HARDENING DEPTH	mm 0.6 ±0.8
DUREZZA PROF. EFFICACE DEPTH HARDNESS	H.R.C. 52
DUR. NUCLEO O BASE DENTE CORE OR TOOTH BASE HARDNESS	H.R.C. 36 ±42
RES. NUCLEO O BASE DENTE CORE OR TOOTH BASE STRENGTH	daN/mm ² 115 ±130
AUSTENITE RESIDUA RESIDUAL AUSTENITE	% MAX 20%



C	COMPONENTE CON CARATTERISTICHE CHIAVE PART INCLUDES KEY CHARACTERISTICS WITH PROCESS CAPABILITY DEMONSTRATION SEE CARRARO STD N. 0-56-95	N. OF KEY C'S N. CARATTERISTICHE CHIAVE
	COMPONENTE CON CARATTERISTICHE CHIAVE CON DIMOSTRAZIONE CAPACITA' DI PROCESSO VEDERE CARRARO STD N. 0-56-95	

S	COMPONENTE CON CARATTERISTICHE DI SICUREZZA PART INCLUDES SAFETY CHARACTERISTICS WITH DOCUMENTATION REQUIREMENTS SEE CARRARO STD N. 0-56-95	N. OF SAFETY C'S N. CARATTERISTICHE DI SICUREZZA
	COMPONENTE CON CARATTERISTICHE DI SICUREZZA CON DOCUMENTAZIONE OBBLIGATORIA E DIMOSTRAZIONE CAPACITA' DI PROCESSO VEDERE CARRARO STD N. 0-56-95	

2	DESCRIZIONE CHANGE
REV.	TUTTI I DIRITTI SONO RISERVATI E PROPRIETA' DI CARRARO S.P.A. SENZA IL CONSENSO SCRITTO DI CARRARO S.P.A. QUESTO DISEGNO NON POTRA' ESSERE RIPRODOTTO, O IN ALCUN MODO ESSERE UTILIZZATO PER LA PRODUZIONE DEI COMPONENTI O ASSIEME ILLUSTRATI NELL'ESSENZA DI UN ACCORDO PRELIMINARE CON CARRARO S.P.A. TUTTI I DIRITTI SONO RISERVATI. ALL'PROPRIETARY RIGHTS RESERVED BY CARRARO S.P.A. THIS DRAWING SHALL NOT BE REPRODUCED OR IN ANY WAY UTILIZED FOR THE MANUFACTURE OF THE COMPONENT OR ASSEMBLY HEREIN ILLUSTRATED AND MUST NOT BE RELEASED TO OTHER PARTIES WITHOUT WRITTEN CONSENT BY CARRARO S.P.A. ANY INFRINGEMENT WILL BE LEGALLY PURSUED.

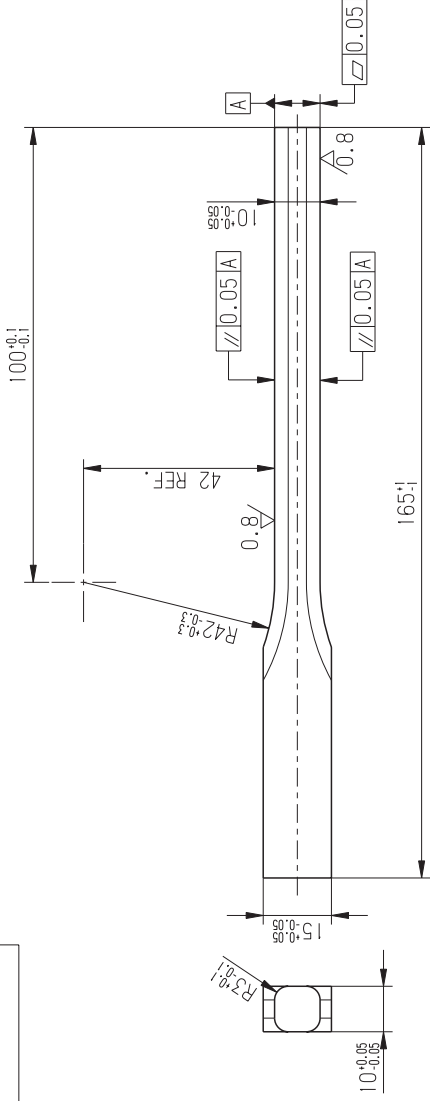
MATERIALE STD MATERIAL	20MnCr5 CARRARO STD 1-01-88	DISEGNATO DRAWN	DENGO CARLO
MATERIALE OPT OPT MATERIAL		APPROVATO APPROVED	-
TRATT. TERM. HEAT TREAT.	CASE-HARDENED	DATA DATE	19/02/2013
TRATT. SUPERF. SURF. TREAT.		CL.FUNZ. FUNC.CL.	--
PRODOTTO ASSEMBLY		RIF. GENERALI GENERAL REFS.	0-20-90

DENOMINAZIONE
DESCRIPTION

PROVINO PER PROVE DI FATICA A FLESSIONE/SPECIMEN FOR PLANE BENDING FATIGUE TESTS

A	MODELLO N. CASTING REF.	A3	PESO WEIGHT	0.128 daN
	SOST. IL REPLACES	-	SCALA SCALE	1:1
	DISEGNO N. PART N.		TAV SHEET	1/1
	<p>CARRARO DRIVETECH S.p.A. - Via Olmo, 37 35011 CAMPODARSEGO (PD) - ITALY</p>			

DISEGNO N. SPECIMEN B
PART N.



3.2 (0.8)

	PART WITH KEY C'S COMPONENTE CON CARATTERISTICHE CHIAVE	N. OF KEY C'S 0	N. CARATTERISTICHE CHIAVE
PART INCLUDES KEY CHARACTERISTICS WITH PROCESS CAPABILITY DEMONSTRATION AND PROCESS CAPABILITY DEMONSTRATION SEE CARRARO STD N. 0-56-95			
COMPONENTE CON CARATTERISTICHE CHIAVE CON DIMOSTRAZIONE CAPACITA' DI PROCESSO VEDERE CARRARO STD N. 0-56-95			
	PART WITH SAFETY C'S COMPONENTE CON CARATTERISTICHE DI SICUREZZA	N. OF SAFETY C'S 0	N. CARATTERISTICHE DI SICUREZZA
PART INCLUDES SAFETY CHARACTERISTICS WITH DOCUMENTATION REQUIREMENTS AND PROCESS CAPABILITY DEMONSTRATION SEE CARRARO STD N. 0-56-95			
COMPONENTE CON CARATTERISTICHE DI SICUREZZA CON DOCUMENTAZIONE OBBLIGATORIA VEDERE CARRARO STD N. 0-56-95			

5	REV.	DESCRIZIONE CHANGE
---	------	-----------------------

TUTTI I DIRITTI SONO RISERVATI E PROPRIETA' DI CARRARO S.P.A. SENZA IL CONSENSO SCRITTO DI CARRARO S.P.A. QUESTO DISEGNO NON PUO' ESSERE RIPRODOTTO, O IN ALCUN MODO ESSERE UTILIZZATO PER LA PRODUZIONE DEI COMPONENTI O ASSIEME ILLUSTRATO, NESSUNO TRASPASSO A ALTRE PARTI, CON INFRAZIONE VERBA, PERSECUZIONE LEGALE, O ALTRO MODO. THIS DRAWING AND ALL INFORMATION CONTAINED HEREIN IS THE PROPERTY OF CARRARO S.P.A. ANY REPRODUCTION OR USE OF THIS DRAWING OR ANY INFORMATION CONTAINED HEREIN WITHOUT WRITTEN CONSENT OF CARRARO S.P.A. ANY REPRODUCTION OR USE OF THIS DRAWING OR ANY INFORMATION CONTAINED HEREIN WILL BE LEGALLY PROSECUTED.

MATERIALE STD	20MnCr5 CARRARO STD 1-01-88	DISEGNO/DRAWN	DENGO CARLO
---------------	-----------------------------	---------------	-------------

MATERIALE OPT	APPROVATO APPROVED
---------------	--------------------

TRATT. TERM. HEAT TREAT.	DATA DATE	CL.FUNZ. --	FUNZ. CL. --
--------------------------	-----------	-------------	--------------

TRATT. SUPERF. SURF. TREAT.	CASE-HARDENED	RIF. GENERALI GENERAL REFS.	0-20-90
-----------------------------	---------------	-----------------------------	---------

PRODOTTO ASSEMBLY	-
-------------------	---

DENOMINAZIONE DESCRIPTION
PROVINO PER PROVE DI FATICA A FLESSIONE / SPECIMEN FOR PLANE BENDING TESTS

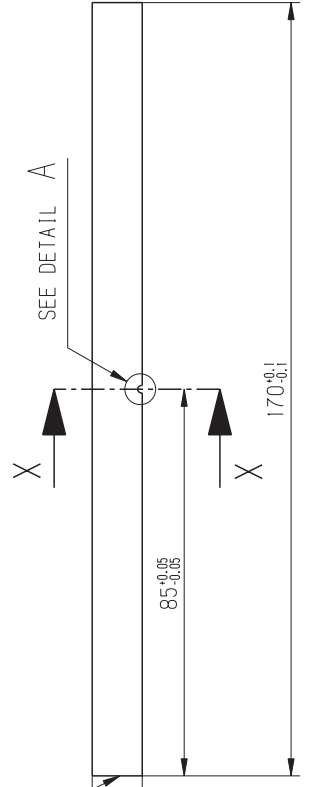
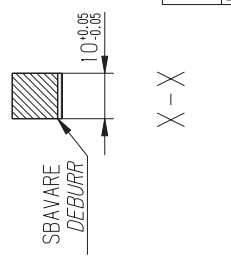
		MODELLO N. CASTING REF.	A3	RESO WEIGHT	0.147 daN
CARRARO DRIVETECH S.p.A. - Via Olmo, 37 35011 CAMPODARSEGO (PD) - ITALY		SOST. IL REPLACES	-	SCALA SCALE	1:1
		DISEGNO N. PART N.		TAV. SHEET	1/1

TRATTAMENTO TERMICO SU PEZZO FINITO HEAT TREATMENT ON FINISHED COMPONENT		H.R.C.	58 ± 62
CEMENT. TEMpra RINVENIMENTO CASE-HARDENING AND TEMPERING (Cm 7)		mm	0.6 ± 0.8
DUREZZA SUPERF. SURFACE HARDNESS		H.R.C.	52
DUREZZA PROF. EFFICACE DEPTH HARDNESS		H.R.C.	36 ± 42
DUR. NUCLEO O BASE DENTE CORE OR TOOTH BASE HARDNESS		daN/mm ²	115 ± 130
RES. NUCLEO O BASE DENTE AUSTENITE RES IDUA		% MAX	20%

100 90 80 70 60 50 40 30 20 10 0 3 4 5 6 7 8

DISEGNO N. SPECIMEN C
 2 - SPECIFICHE DI CEMENTAZIONE
 2 - CASE-HARDENING SPECS

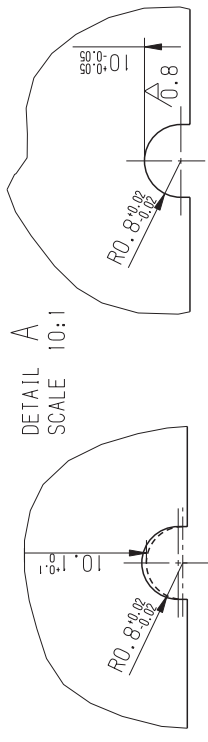
TRATTAMENTO TERMICO SU PEZZO FINITO HEAT TREATMENT ON FINISHED COMPONENT	
CEMENT. TEMpra RINVENIMENTO (Cm 7) CASE-HARDENING AND TEMPERING	
DUREZZA SUPERF. SURFACE HARDNESS	H.R.C. 58 ±62
PENETRAZIONE EFF. CASE-HARDENING DEPTH	mm 0.6 ±0.8
DUREZZA PROF. EFFICACE DEPTH HARDNESS	H.R.C. 52
DUR. NUCLEO O BASE DENTE CORE OR TOOTH BASE HARDNESS	H.R.C. 36 ±42
RES. NUCLEO O BASE DENTE CORE OR TOOTH BASE STRENGTH	daN/mm ² 115 ±130
AUSTENITE RESIDUA RESIDUAL AUSTENITE	% MAX 20%



$$1.6\sqrt{0.8}$$

- PROCEDURA DI LAVORAZIONE:
 1 - LASCIARE SOVRAMETALLO NELLA ZONA INTAGLIATA
 COME INDICATO A DISEGNO
 2 - ESEGUIRE TRATTAMENTO DI CEMENTAZIONE.
 3 - LAVORARE L'INTAGLIO FINO A DIMENSIONI DI FINITURA

- MANUFACTURING PROCEDURE:
 1 - LEAVE FINISHING ALLOWANCE IN THE NOTCHED AREA
 AS REPORTED IN THE DRAWING
 2 - PERFORM HEAT TREATMENT
 3 - WORK THE NOTCHED AREA TO FINISHING DIMENSIONS



1-DIMENSIONI CON SOVRAMETALLO
 1-DIMENSIONS WITH ALLOWANCE

3-DIMENSIONI DI FINITURA DEL PEZZO
 3-FINISHING DIMENSIONS OF SPECIMEN

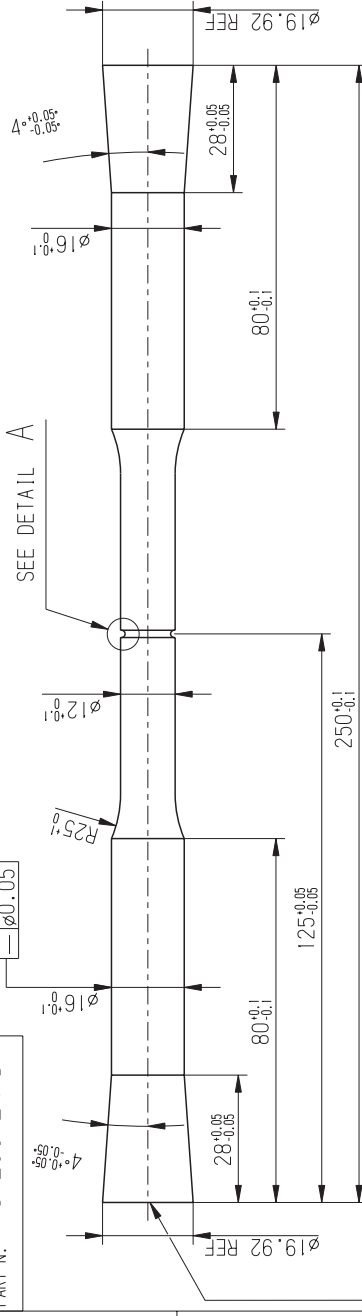
	PART WITH KEY C'S COMPONENTE CON CARATTERISTICHE CHIAVE	N. OF KEY C'S N. CARATTERISTICHE CHIAVE
PART INCLUDES KEY CHARACTERISTICS WITH PROCESS CAPABILITY DEMONSTRATION SEE CARRARO STD N. 0-56-95 COMPONENTE CON CARATTERISTICHE CHIAVE CON DIMOSTRAZIONE CAPACITA' DI PROCESSO VEDERE CARRARO STD N. 0-56-95		
	PART WITH SAFETY C'S COMPONENTE CON CARATTERISTICHE DI SICUREZZA	N. OF SAFETY C'S N. CARATTERISTICHE DI SICUREZZA
PART INCLUDES SAFETY CHARACTERISTICS WITH DOCUMENTATION REQUIREMENTS AND PROCESS CAPABILITY DEMONSTRATION SEE CARRARO STD N. 0-56-95 COMPONENTE CON CARATTERISTICHE DI SICUREZZA CON DOCUMENTAZIONE OBBLIGATORIA E DIMOSTRAZIONE CAPACITA' DI PROCESSO VEDERE CARRARO STD N. 0-56-95		

3	REV. REV.	DESCRIZIONE CHANGE
TUTTI I DIRITTI SONO RISERVATI E PROPRIETA' DI CARRARO S.P.A. SENZA IL CONSENSO SCRITTO DI CARRARO S.P.A. QUESTO DISEGNO NON POTRA' ESSERE RIPRODOTTO, O IN ALCUN MODO ESSERE UTILIZZATO PER LA PRODUZIONE DI COMPONENTI O ASSIEME ILLUSTRATO NELL'ESSEMPLO A LATO. OGNI INFRAZIONE VERRA' PERSECUITA' LEGALMENTE. ALL PROPRIETARY RIGHTS RESERVED BY CARRARO S.P.A. THIS DRAWING SHALL NOT BE REPRODUCED OR IN ANY MANNER UTILIZED FOR THE MANUFACTURE OF THE COMPONENT OR ASSEMBLY HEREIN ILLUSTRATED AND MUST NOT BE RELEASED TO OTHER PARTIES WITHOUT WRITTEN CONSENT OF CARRARO S.P.A. ANY INFRINGEMENT WILL BE LEGALLY PURSUED.		
MATERIALE STD	20MnCr5 CARRARO STD 1-01-88	DISEGNATO DENG0 CARLO
MATERIALE OPT		APPROVATO -
TRATT. TERM. HEAT TREAT.	CASE-HARDENED	CL.FUNZ. 14/12/2012
TRATT.SUPERF. SURF. TREAT.		FUNC.CL. --
PRODOTTO ASSEMBLY		RIF. GENERALI 0-20-90
DENOMINAZIONE DESCRIPTION PROVINO PER PROVE DI FATICA A FLESSIONE /SPECIMEN FOR PLANE BENDING FATIGUE TEST		

	MODELLO N. CASTING REF.	A3	PESO WEIGHT	0.146 daN
	SOST. IL REPLACES	-	SCALA SCALE	1:1
	DISEGNO N. PART N.		TAV SHEET	1/1

CARRARO DRIVETECH S.p.A. - Via Olmo, 37
 35011 CAMPODARSEGO (PD) - ITALY

DISEGNO N. SPECIMEN D
PART N.



MARCHIARE LATO
DI PARTENZA DELLA
LAVORAZIONE
MARK STARTING SIDE
OF MACHINING

3.2 (0.8)

2-SPECIFICHE DI CEMENTAZIONE
2-CASE-HARDENING SPECS

TRATTAMENTO TERMICO SU PEZZO FINITO HEAT TREATMENT ON FINISHED COMPONENT	
CEMENT. TEMPRA RINVENIMENTO (Cm 7) CASE-HARDENING AND TEMPERING	
DUREZZA SUPERF. SURFACE HARDNESS	H.R.C. 58 ±62
PENETRAZIONE EFF. CASE-HARDENING DEPTH	mm 0.6 ±0.8
DUREZZA PROF. DEPTH HARDNESS	H.R.C. 52
DUR. NUCLEO O BASE DENTE CORE OR TOOTH-BASE HARDNESS	H.R.C. 36 ±42
RES. NUCLEO O BASE DENTE CORE OR TOOTH-BASE STRENGTH	daN/mm ² 115 ±130
AUSTENITE RESIDUA RESIDUAL AUSTENITE	% MAX 20%

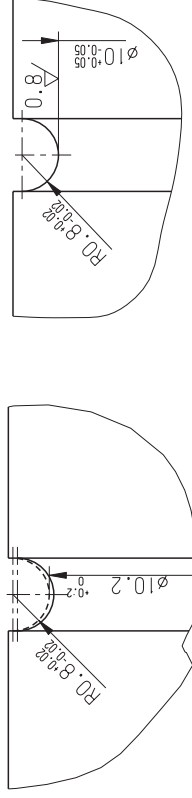
	PART WITH KEY C'S CHIAVE	N. OF KEY C'S
	COMPONENTE CON CARATTERISTICHE CHIAVE	N. CARATTERISTICHE CHIAVE
PART INCLUDES KEY CHARACTERISTICS WITH PROCESS CAPABILITY DEMONSTRATION SEE CARRARO STD N. 0-56-95		
COMPONENTE CON CARATTERISTICHE CHIAVE CON DIMOSTRAZIONE CAPACITA' DI PROCESSO VEDERE CARRARO STD N. 0-56-95		

	PART WITH SAFETY C'S SICUREZZA	N. OF SAFETY C'S
	COMPONENTE CON CARATTERISTICHE DI SICUREZZA	N. CARATTERISTICHE DI SICUREZZA
PART INCLUDES SAFETY CHARACTERISTICS WITH DOCUMENTATION REQUIREMENTS AND PROCESS CAPABILITY DEMONSTRATION SEE CARRARO STD N. 0-56-95		
COMPONENTE CON CARATTERISTICHE DI SICUREZZA CON DOCUMENTAZIONE OBBLIGATORIA E DIMOSTRAZIONE CAPACITA' DI PROCESSO VEDERE CARRARO STD N. 0-56-95		

- PROCEDURA DI LAVORAZIONE:
1 - LASCIARE SOVRAMETALLO NELLA ZONA INTAGLIATA
COME INDICATO A DISEGNO
2 - ESEGUIRE TRATTAMENTO DI CEMENTAZIONE.
3 - LAVORARE L'INTAGLIO FINO A DIMENSIONI DI FINITURA

- MANUFACTURING PROCEDURE:
1 - LEAVE FINISHING ALLOWANCE IN THE NOTCHED AREA
AS REPORTED IN THE DRAWING
2 - PERFORM HEAT TREATMENT
3 - WORK THE NOTCHED AREA TO FINISHING DIMENSIONS

DETAIL A
SCALE 10:1

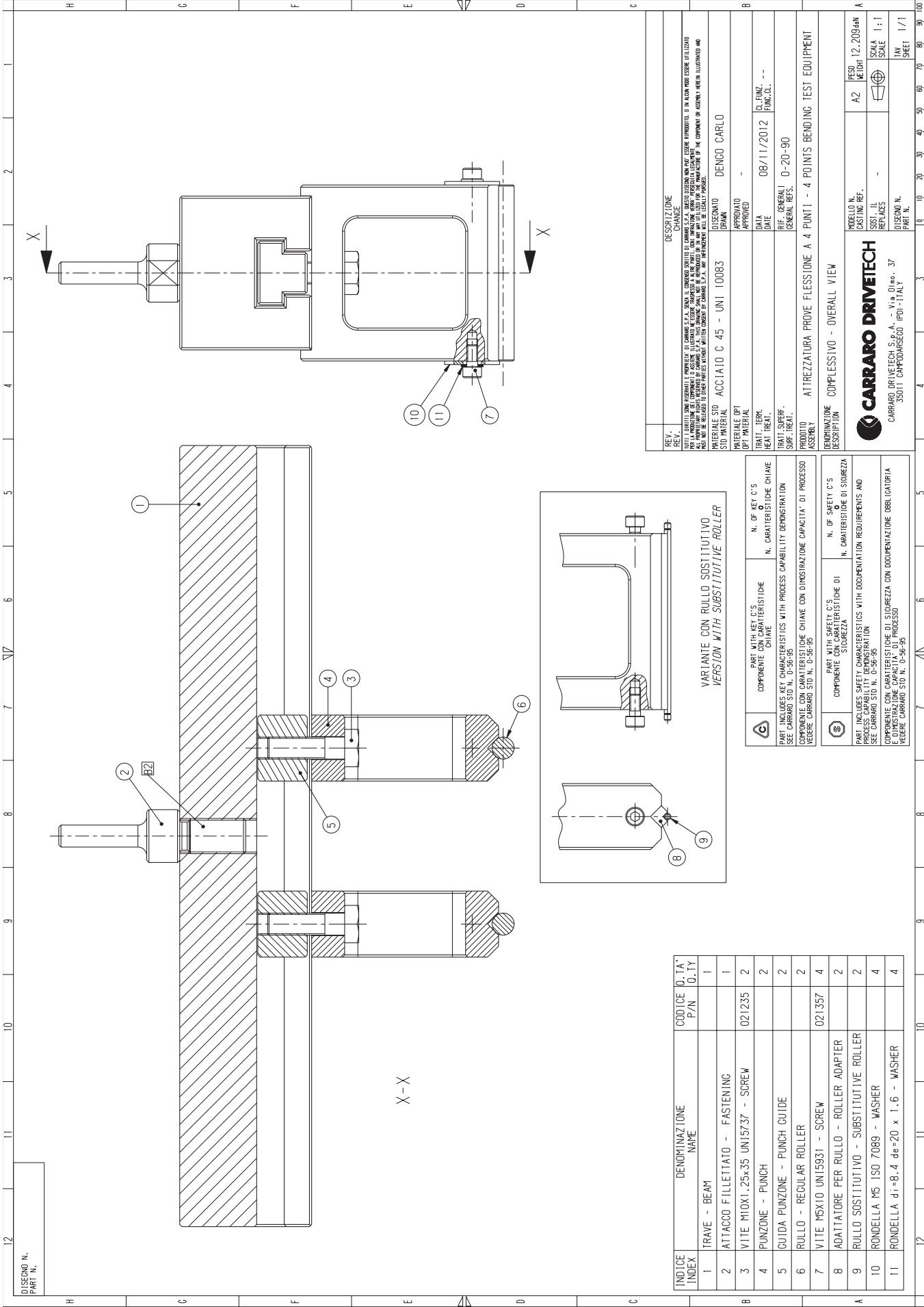


1-DIMENSIONI CON SOVRAMETALLO
1-DIMENSIONS WITH ALLOWANCE

3-DIMENSIONI DI FINITURA DEL PEZZO
3-FINISHING DIMENSIONS OF SPECIMEN

7	REV. REV.	DESCRIZIONE CHANGE			
TUTTI I DIRITTI SONO RISERVATI E PROPRIETA' DI CARRARO S.P.A. SENZA IL CONSENSO SCRITTO DI CARRARO S.P.A. QUESTO DISEGNO NON PUO' ESSERE RIPRODOTTO, O IN ALCUN MODO ESSERE UTILIZZATO PER LA PRODUZIONE DEI COMPONENTI O ASSIEME ILLUSTRATO, NESSUNO TRASPASO A ALTRE PARTI, CON INFRAZIONE VERBA, PERSECUZIONE LEGALE. ALL RIGHTS ARE RESERVED AND PROPERTY OF CARRARO S.P.A. WITHOUT WRITTEN CONSENT OF CARRARO S.P.A. ANY REPRODUCTION OR USE OF THIS DRAWING FOR THE MANUFACTURE OF THE COMPONENT OR ASSEMBLY HEREIN ILLUSTRATED AND FOR THE PRODUCTION OF THE COMPONENTS OR ASSEMBLY ILLUSTRATED, WITHOUT THE WRITTEN CONSENT OF CARRARO S.P.A. ANY INFRINGEMENT WILL BE LEGALLY PURSUED.					
	MATERIALE STD OPT MATERIAL	20MnCr5 CARRARO STD 1-01-88	DISEGNO DRAWN	DENGO CARLO	
	MATERIALE OPT OPT MATERIAL		APPROVATO APPROVED	-	
	TRATT. TERM. HEAT TREAT.	CASE-HARDENED	DATA DATE	14/12/2012	CL.FUNZ. -- FUNC. CL. --
	TRATT. SUPERF. SURF. TREAT.		REF. GENERALI GENERAL REFS.	0-20-90	
	PRODOTTO ASSEMBLY				
DENOMINAZIONE DESCRIPTION					
PROVINO PER PROVE DI FATICA ASSIALI / SPECIMEN FOR AXIAL FATIGUE TEST					

		MODELLO N. CASTING REF.	A3	RESO WEIGHT	0.357 daN
		SOST. IL REPLACES	-	SCALA SCALE	1:1
		DISEGNO N. PART N.		TAV. SHEET	1/1
CARRARO DRIVETECH S.p.A. - Via Olmo, 37 35011 CAMPOPARSEGO (PD) - ITALY					



DISEGNO N.
PART N.

INDICE INDEX	DENOMINAZIONE NAME	CODICE P/N	Q. T. A. D. T. Y
1	TRAVE - BEAM		1
2	ATTACCO FILLETTATO - FASTENING		1
3	VITE M10x1,25x35 UNI5737 - SCREW	021235	2
4	PUNZONE - PUNCH		2
5	CUIDA PUNZONE - PUNCH GUIDE		2
6	RULLO - REGULAR ROLLER		2
7	VITE M5x10 UNI5931 - SCREW	021357	4
8	ADATTATORE PER RULLO - ROLLER ADAPTER		2
9	RULLO SOSTITUTIVO - SUBSTITUTE ROLLER		2
10	RONDELLA M5 ISO 7089 - WASHER		4
11	RONDELLA d1=8,4 de=20 x 1,6 - WASHER		4

REV.	DESCRIZIONE CHANGE
	<p>QUESTA VERSIONE È SOSTITUITA DA VERSIONI 01, 02, 03, 04, 05, 06, 07, 08, 09, 10, 11, 12, 13, 14, 15, 16, 17, 18, 19, 20, 21, 22, 23, 24, 25, 26, 27, 28, 29, 30, 31, 32, 33, 34, 35, 36, 37, 38, 39, 40, 41, 42, 43, 44, 45, 46, 47, 48, 49, 50, 51, 52, 53, 54, 55, 56, 57, 58, 59, 60, 61, 62, 63, 64, 65, 66, 67, 68, 69, 70, 71, 72, 73, 74, 75, 76, 77, 78, 79, 80, 81, 82, 83, 84, 85, 86, 87, 88, 89, 90, 91, 92, 93, 94, 95, 96, 97, 98, 99, 100.</p>

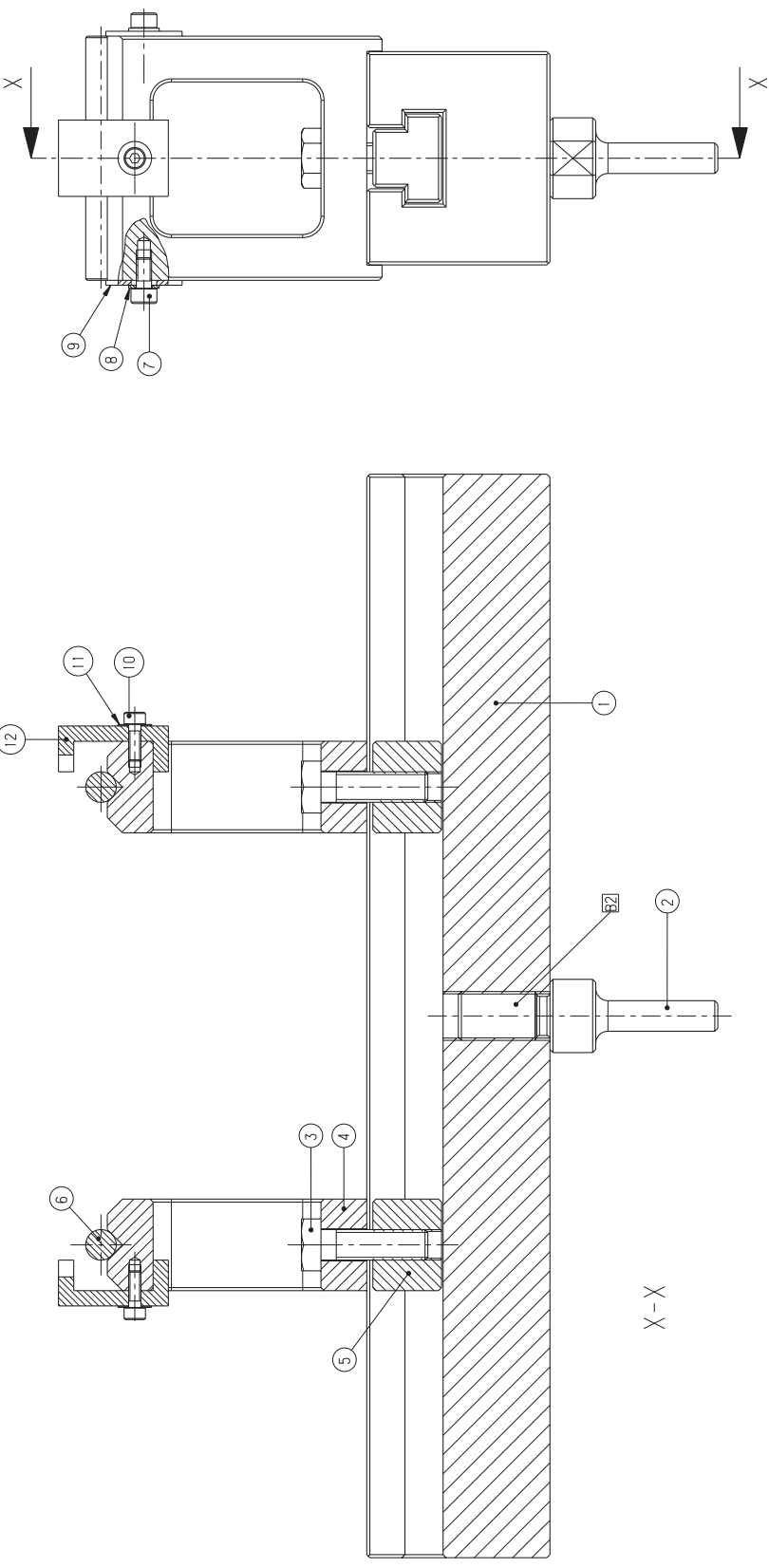
MATERIALE STD	ACCIAIO C 45 - UNI 10083
MATERIALE OPT	APPROVATO
TRATT. TERM.	08/11/2012
TRATT. SUPERF.	0-20-90
PRODOTTO ASSEMBLATO	AT TREZZATURA PROVE FLESSIONE A 4 PUNTI - 4 POINTS BENDING TEST EQUIPMENT
DESCRIZIONE	COMPLESSIVO - OVERALL VIEW

MODELLO N.	PESO
CARRARO DRIVETECH	A2
CARRARO DRIVETECH S.p.A. - V.le D'Adda, 37	
35011 CARPI (MO) - ITALY	

SCALE	SCALE
1:1	1:1
1/1	1/1

MODELLO N.	SCALE
CARRARO DRIVETECH S.p.A. - V.le D'Adda, 37	1:1
35011 CARPI (MO) - ITALY	1/1

DISEGNO N.
PART N.



INDICE INDEX	DENOMINAZIONE NAME	CODICE P/N	Q. TA Q. TY
1	TRAVE - BEAM		1
2	ATTACCO FILLETTATO - FASTENING		1
3	VITE M10x1.25x35 UNI5737 - SCREW	021235	2
4	PUNZONE - PUNCH		2
5	GUIDA PUNZONE - PUNCH GUIDE		2
6	RULLO - REGULAR ROLLER		2
7	VITE M5x10 UNI5931 - SCREW	021357	4
8	RONDELLA M5 ISO 7089 - WASHER		4
9	RONDELLA de=16 di=8.4 x 1.6 - WASHER		4
10	VITE M4x12 UNI 5931 - SCREW		2
11	RONDELLA M4 ISO 7089 - WASHER		2
12	FERMO PROVINO - SPECIMEN CLAMP		2

	PART WITH KEY C'S COMPONENTE CON CARATTERISTICHE CHIAVE	N. OF KEY C'S 0
	PART INCLUDES KEY CHARACTERISTICS WITH PROCESS CAPABILITY DEMONSTRATION VEDERE CARRARO STD N. 0-56-95	N. CARATTERISTICHE CHIAVE 0
	COMPONENTE CON CARATTERISTICHE CHIAVE CON DIMOSTRAZIONE CAPACITA' DI PROCESSO VEDERE CARRARO STD N. 0-56-95	N. OF SAFETY C'S 0
	PART INCLUDES SAFETY CHARACTERISTICS WITH DOCUMENTATION REQUIREMENTS AND PROCESS CAPABILITY DEMONSTRATION VEDERE CARRARO STD N. 0-56-95	N. CARATTERISTICHE DI SICUREZZA 0
	COMPONENTE CON CARATTERISTICHE DI SICUREZZA CON DOCUMENTAZIONE OBLIGATORIA VEDERE CARRARO STD N. 0-56-95	N. OF SAFETY C'S 0
	PART INCLUDES SAFETY CHARACTERISTICS WITH DOCUMENTATION REQUIREMENTS AND PROCESS CAPABILITY DEMONSTRATION VEDERE CARRARO STD N. 0-56-95	N. CARATTERISTICHE DI SICUREZZA 0

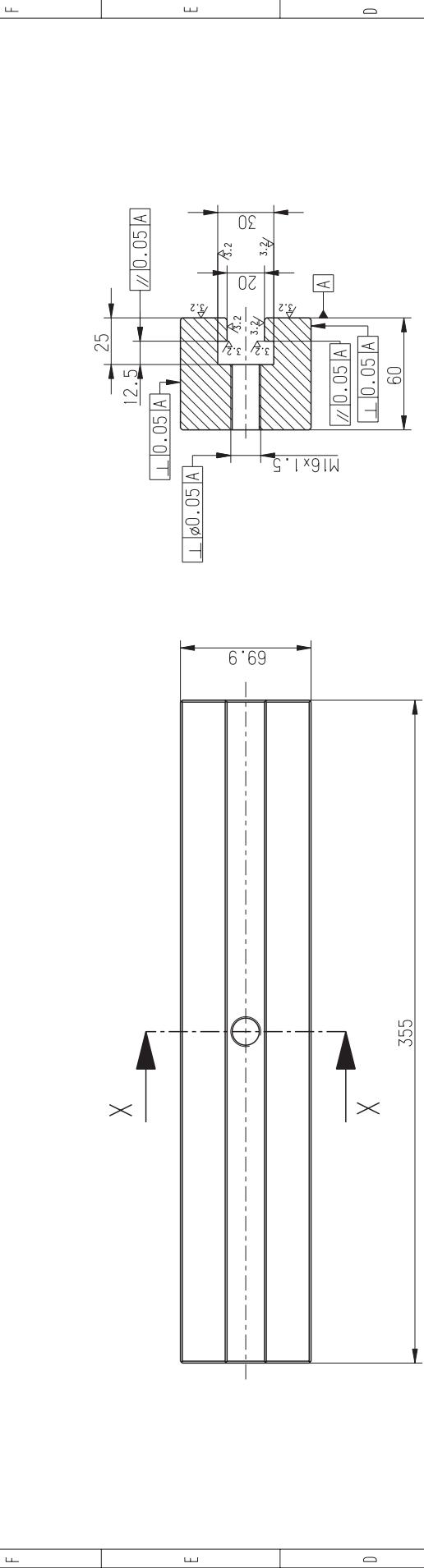
REV.	DESCRIZIONE				
CHG.	CHANGE				
TUTTI I DIRITTI SONO RISERVATI. PROPRIETA' DI CARRARO S.P.A. SENZA IL CONSENSO SCRITTO DI CARRARO S.P.A. NUNCA I DISegni NON VUOL ESSERE RIPRODOTTO, O IN ALTRA MODO ESSERE UTILIZZATO SENZA IL CONSENSO SCRITTO DI CARRARO S.P.A. CARRARO S.P.A. NON E' RESPONSABILE PER IL DANNO CAUSATO DA UN'USUA PRATICA DI PRODUZIONE O DI ASSEMBLAGGIO CHE NON HA IN MENTE NE' PER IL DANNO CAUSATO DA UN'USUA PRATICA DI PRODUZIONE O DI ASSEMBLAGGIO CHE NON HA IN MENTE NE' PER IL DANNO CAUSATO DA UN'USUA PRATICA DI PRODUZIONE O DI ASSEMBLAGGIO CHE NON HA IN MENTE.					
MATERIALE STD	ACCIAIO C45 - UNI 10083	DISCOMANDO			
OPT MATERIAL		DRUM			
APPROVAZIONE	APPROVED				
DATA	20/05/07	CL. FINZ.	--		
TRATT. TERM.		TRATT.			
TRATT. SUPERF.		TRATT. SUPERF.			
PRODOTTO	0-20-90	REF. GENERALI			
ASSEMBLY	ATTREZZATURA PER FLESSIONE A 4 PUNTI - 4 POINTS BENDING EQUIPMENT	GENERAL REFS.			
DENOMINAZIONE	COMPRESSIVO - OVERALL VIEW				
DESCRIPTION					
MODELLO N. CASTING REF.	A2	IPSD	13.0384		
SIST. II REPLACES		SCALE	1 : 1		
DISEGNO N. PART N.	35011 CAMPIODARSEGO (PD) - ITALY	SCALE	1 : 1		



CARRARO DRIVETECH S.p.A. - V.le D. no. 37
35011 CAMPIODARSEGO (PD) - ITALY

12 11 10 9 8 7 6 5 4 3 2 1 0 90 80 70 60 50 40 30 20 10 0

DISEGNO N. PART N.	2	3	4	5	6	7	8	9	10	11	12	13	14	15	16	17	18	19	20	21	22	23	24	25	26	27	28	29	30	31	32	33	34	35	36	37	38	39	40	41	42	43	44	45	46	47	48	49	50	51	52	53	54	55	56	57	58	59	60	61	62	63	64	65	66	67	68	69	70	71	72	73	74	75	76	77	78	79	80	81	82	83	84	85	86	87	88	89	90	91	92	93	94	95	96	97	98	99	100
-----------------------	---	---	---	---	---	---	---	---	----	----	----	----	----	----	----	----	----	----	----	----	----	----	----	----	----	----	----	----	----	----	----	----	----	----	----	----	----	----	----	----	----	----	----	----	----	----	----	----	----	----	----	----	----	----	----	----	----	----	----	----	----	----	----	----	----	----	----	----	----	----	----	----	----	----	----	----	----	----	----	----	----	----	----	----	----	----	----	----	----	----	----	----	----	----	----	----	----	----	-----



SMUSSI NON QUOTATI: 1x45°
UNQUOTED CHAMFERS: 1x45°

REV.	DESCRIZIONE
REV.	CHANGE
TUTTI I DIRITTI SONO RISERVATI E PROPRIETÀ DI CARRARO S.P.A. SENZA IL CONSENSO SCRITTO DI CARRARO S.P.A. QUESTO DISEGNO NON POTRÀ ESSERE RIPRODOTTO, O IN ALCUN MODO ESSERE UTILIZZATO PER LA PRODUZIONE DEI COMPONENTI O ASSIEME ILLUSTRATO NÈ ESSERE TRASPRESO A ALTRE PARTI, OGNI INFRAZIONE VERrà PERSICUATA LEGALMENTE. ALL PROPRIETARY RIGHTS RESERVED BY CARRARO S.P.A. THIS DRAWING SHALL NOT BE REPRODUCED OR IN ANY WAY UTILIZED FOR THE MANUFACTURE OF THE COMPONENT OR ASSEMBLY HEREIN ILLUSTRATED AND MUST NOT BE RELEASED TO OTHER PARTIES WITHOUT WRITTEN CONSENT BY CARRARO S.P.A. ANY INFRINGEMENT WILL BE LEGALLY PURSUED.	
MATERIALE STD	ACCIAIO C45 - UNI 10083-1
DISEGNATO	DENGO CARLO
APPROVATO	-
DATA	24/10/2012
CL.FUNZ.	---
FUNC.CL.	---
RIF. GENERALI	0-20-90
GENERAL REFS.	
PRODOTTO ASSEMBLY	ATTREZZATURA PROVE FLESSIONE A 4 PUNTI - 4 POINTS BENDING TEST EQUIPMENT
DENOMINAZIONE DESCRIPTION	TRAVE - BEAM

MODELLO N. CASTING REF.	A3	PESO WEIGHT	9.846 daN
SOST. IL REPLACES	-	SCALA SCALE	1:2
DISEGNO N. PART N.		TAV SHEET	1/1

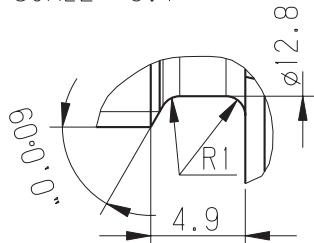


CARRARO DRIVETECH S.p.A. - Via Olmo, 37
35011 CAMPODARSEGO (PD) - ITALY

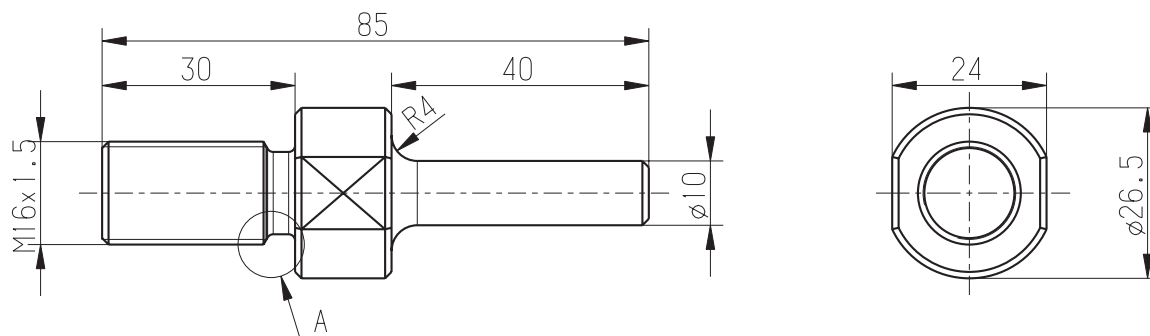
	PART WITH KEY C'S COMPONENTE CON CARATTERISTICHE CHIAVE	N. OF KEY C'S N. CARATTERISTICHE CHIAVE
	PART INCLUDES KEY CHARACTERISTICS WITH PROCESS CAPABILITY DEMONSTRATION SEE CARRARO STD N. 0-56-95 COMPONENTE CON CARATTERISTICHE CHIAVE CON DIMOSTRAZIONE CAPACITA' DI PROCESSO VEDERE CARRARO STD N. 0-56-95	
	PART WITH SAFETY C'S COMPONENTE CON CARATTERISTICHE DI SICUREZZA	N. OF SAFETY C'S N. CARATTERISTICHE DI SICUREZZA
	PART INCLUDES SAFETY CHARACTERISTICS WITH DOCUMENTATION REQUIREMENTS AND PROCESS CAPABILITY DEMONSTRATION SEE CARRARO STD N. 0-56-95 COMPONENTE CON CARATTERISTICHE DI SICUREZZA CON DOCUMENTAZIONE OBBLIGATORIA E DIMOSTRAZIONE CAPACITA' DI PROCESSO VEDERE CARRARO STD N. 0-56-95	

DISEGNO N.
PART N.

DETAIL A
SCALE 3:1



COLA DI SCARICO - UNI 5709
RUN OUT - UNI 5709



SMUSSI NON QUOTATI: 1x45°
UNQUOTED CHAMFERS: 1x45°

C	PART WITH KEY C'S COMPONENTE CON CARATTERISTICHE CHIAVE	N. OF KEY C'S 0 N. CARATTERISTICHE CHIAVE
	PART INCLUDES KEY CHARACTERISTICS WITH PROCESS CAPABILITY DEMONSTRATION SEE CARRARO STD N. 0-56-95 COMPONENTE CON CARATTERISTICHE CHIAVE CON DIMOSTRAZIONE CAPACITA' DI PROCESSO VEDERE CARRARO STD N. 0-56-95	
S	PART WITH SAFETY C'S COMPONENTE CON CARATTERISTICHE DI SICUREZZA	N. OF SAFETY C'S 0 N. CARATTERISTICHE DI SICUREZZA
	PART INCLUDES SAFETY CHARACTERISTICS WITH DOCUMENTATION REQUIREMENTS AND PROCESS CAPABILITY DEMONSTRATION SEE CARRARO STD N. 0-56-95 COMPONENTE CON CARATTERISTICHE DI SICUREZZA CON DOCUMENTAZIONE OBBLIGATORIA E DIMOSTRAZIONE CAPACITA' DI PROCESSO VEDERE CARRARO STD N. 0-56-95	

REV.	DESCRIZIONE
REV.	CHANGE

TUTTI I DIRITTI SONO RISERVATI E PROPRIETA' DI CARRARO S.P.A. SENZA IL CONSENSO SCRITTO DI CARRARO S.P.A. QUESTO DISEGNO NON PUO' ESSERE RIPRODOTTO, O IN ALCUN MODO ESSERE UTILIZZATO PER LA PRODUZIONE DEI COMPONENTI O ASSIEME ILLUSTRATO NE' ESSERE TRASMESSO A ALTRE PARTI. OGNI INFRAZIONE VERRA' PERSECUITA LEGALMENTE
 ALL PROPRIETARY RIGHTS RESERVED BY CARRARO S.P.A. THIS DRAWING SHALL NOT BE REPRODUCED OR IN ANY WAY UTILIZED FOR THE MANUFACTURE OF THE COMPONENT OR ASSEMBLY HEREIN ILLUSTRATED AND MUST NOT BE RELEASED TO OTHER PARTIES WITHOUT WRITTEN CONSENT BY CARRARO S.P.A. ANY INFRINGEMENT WILL BE LEGALLY PURSUED.

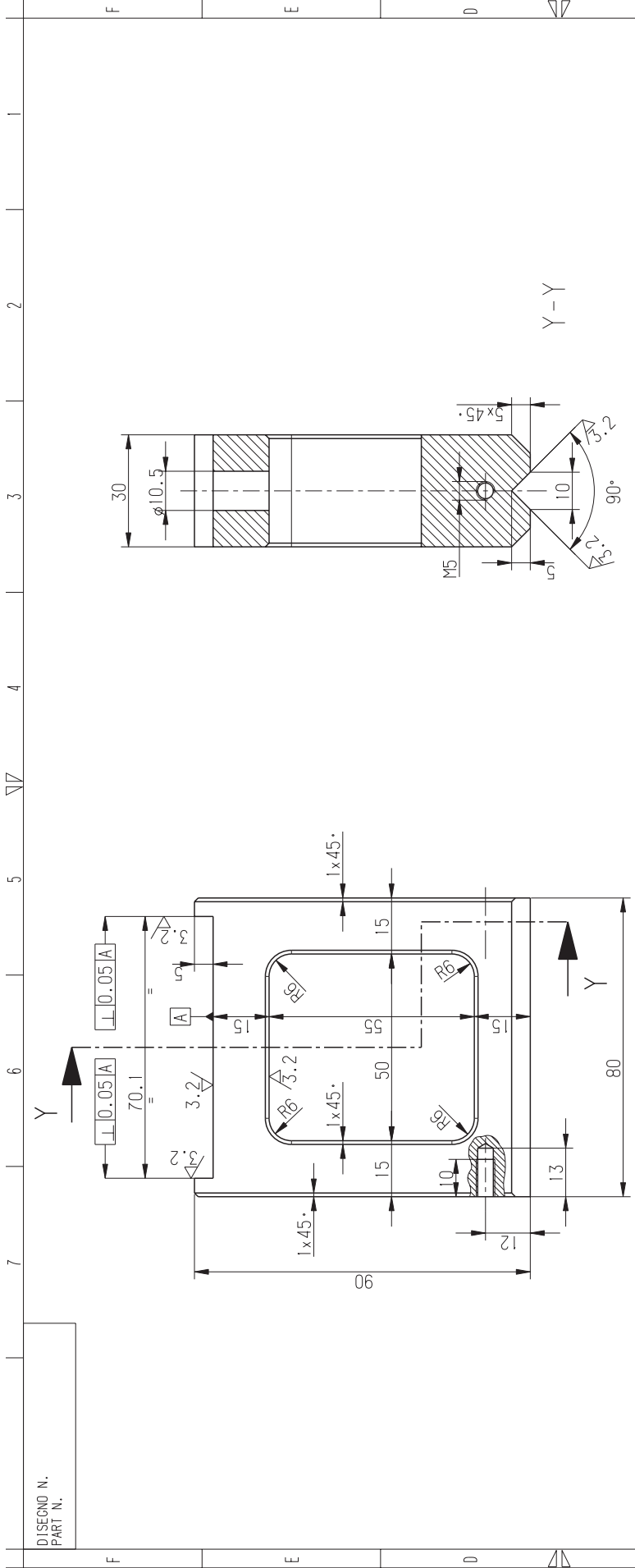
MATERIALE STD STD MATERIAL	ACCIAIO C45 - UNI10083	DISEGNATO DRAWN	DENGO CARLO
MATERIALE OPT OPT MATERIAL		APPROVATO APPROVED	-
TRATT. TERM. HEAT TREAT.		DATA DATE	12/11/12
TRATT. SUPERF. SURF. TREAT.		RIF. GENERALI GENERAL REFS.	0-20-90
PRODOTTO ASSEMBLY	ATTREZZATURA PROVA FLESSIONE A 4 PUNTI - 4 POINTS BENDING TEST EQUIPMENT		
DENOMINAZIONE DESCRIPTION	ATTACCO - FASTENING		



CARRARO DRIVETECH S.p.A. - Via Olmo, 37
35011 CAMPODARSEGO (PD) - ITALY

MODELLO N. CASTING REF.	A4	PESO WEIGHT	0.132 daN
SOST. IL REPLACES	-	SCALA SCALE	1:1
DISEGNO N. PART N.		TAV SHEET	1/1

4 3 0 10 20 30 40 50 60 70 80 90 100



-	REV. / REV.	DESCRIZIONE / CHANGE	-
-	-	-	-
-	-	-	-
-	-	-	-
-	-	-	-
-	-	-	-
-	-	-	-
-	-	-	-
-	-	-	-
-	-	-	-
-	-	-	-
-	-	-	-
-	-	-	-
-	-	-	-
-	-	-	-
-	-	-	-
-	-	-	-
-	-	-	-
-	-	-	-

6.3 (3.2)

DISEGNO N. / PART N.



CARRARO DRIVETECH S.p.A. - Via Olmo, 37
35011 CAMPODARSEGO (PD) - ITALY

PRODOTTO / ASSEMBLY: ATTREZZATURA PROVE FLESSIONE A 4 PUNTI - 4 POINTS BENDING TEST EQUIPMENT

TRATT. TERM. / HEAT TREAT.: -
TRATT. SUPERF. / SURF. TREAT.: 0-20-90

DATA / DATE: 30/10/2012
CL. FUNZ. / FUNC. CL.: --

APPROVATO / APPROVED: -
MATERIALE OPT / OPT MATERIAL: -

DISEGNATO / DRAWN: DENGO CARLO
MATERIALE STD / STD MATERIAL: ACCIAIO C45 - UNI 10083

DESCRIZIONE / CHANGE: -

REV. / REV.: -

REV. / REV.: -

REV. / REV.: -

REV. / REV.: -

REV. / REV.: -

REV. / REV.: -

REV. / REV.: -

A3

PESO / WEIGHT: 0.919 daN

SCALA / SCALE: 1:1

TAV. / SHEET: 1/1

MODELLO N. / CASTING REF.: -

SOST. IL REMPLACES: -

DISEGNO N. / PART N.: -

35011 CAMPODARSEGO (PD) - ITALY

3

4

5

6

7

8

90

100

110

120

130

140

150

160

170

180

190

200

210

220

230

240

250

260

270

280

290

300

310

320

330

340

350

360

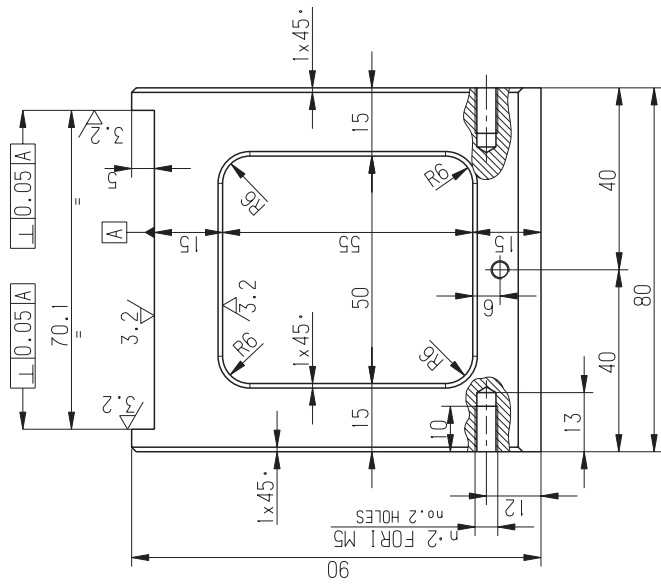
370

380

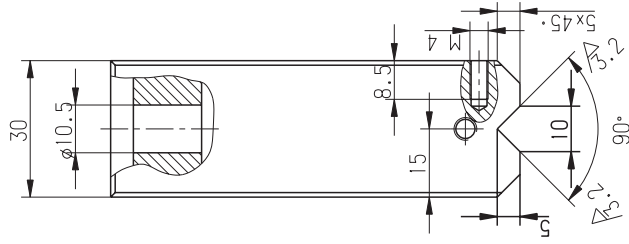
390

400

DISEGNO N.
PART N.



SECTION C-C


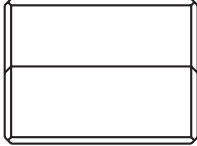

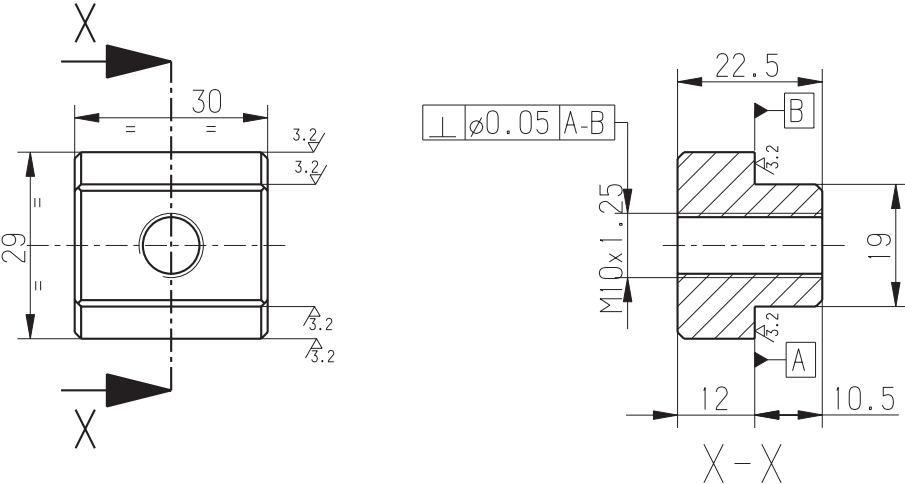




6.3 (3.2)

REV.	DESCRIZIONE CHANGE
TUTTI I DIRITTI SONO RISERVATI E PROPRIETA' DI CARRARO S.P.A. SENZA IL CONSENSO SCRITTO DI CARRARO S.P.A. QUESTO DISEGNO NON PUO' ESSERE RIPRODOTTO, O IN ALCUN MODO ESSERE UTILIZZATO PER LA PRODUZIONE DEI COMPONENTI O ASSIEME ILLUSTRATO, NESSUNO TRASPASSO A ALTRE PARTI, CON INFRAZIONE VERBA, PERSECUZIONE LEGALEMENTE PERSECUZIONE PENALE. ALL RIGHTS RESERVED BY CARRARO S.P.A. ANY INSTRUMENT WILL BE LEGALLY PERSECUED.	
MATERIALE STD	ACCIAIO C45 - UNI 10083
MATERIALE OPT	DISEGNO DISEGNO CARLO
TRATT. TERM.	APPROVATO APPROVATO
TRATT. SUPERF.	DATA DATA 30/10/2012
TRATT. IRCAT.	CL.FUNZ. --
PRODOTTO ASSEMBLY	RIF. GENERALI GENERAL REFS. 0-20-90
DENOMINAZIONE DESCRIPTION	ATTREZZATURA PROVA FLESSIONE 4 PUNTI - 4 POINTS BENDING TEST EQUIPMENT
MODELLO N. CASTING REF.	PUNZONE INFERIORE - LOWER PUNCH
SOST. IL REPLACES	RESO WEIGHT 0.918 daN
DISEGNO N. PART N.	SCALA SCALE 1:1
CARRARO DRIVE TECH S.p.A. - Via Olmo, 37 35011 CAMPOARSEGO (PD) - ITALY	TAV SHEET 1/1



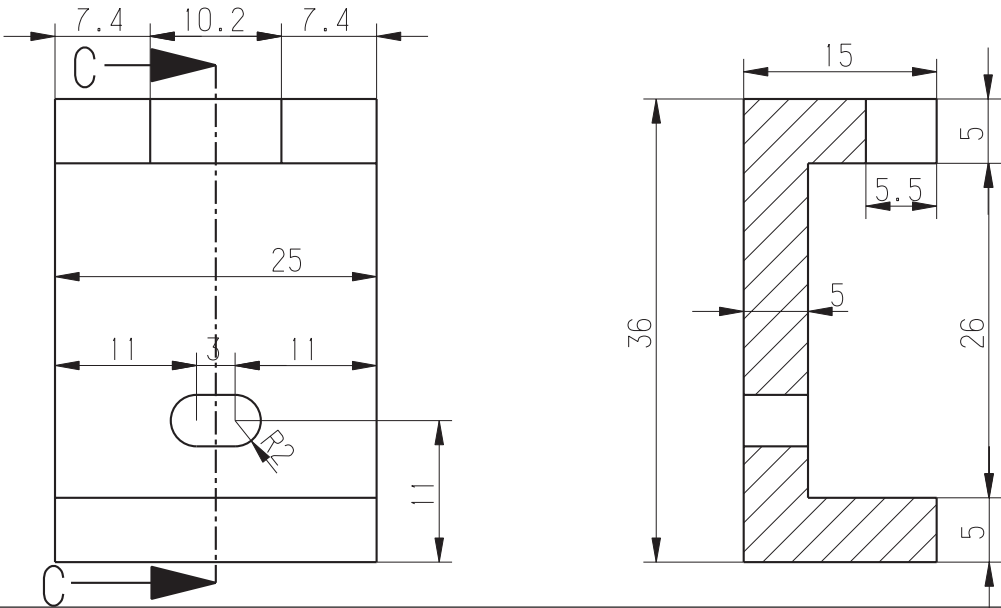

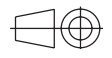
PART WITH KEY C'S COMPONENTE CON CARATTERISTICHE CHIAVE	N. OF KEY C'S N. CARATTERISTICHE CHIAVE
PART INCLUDES KEY CHARACTERISTICS WITH PROCESS CAPABILITY DEMONSTRATION SEE CARRARO STD N. 0-56-95	VEDERE CARRARO STD N. 0-56-95
PART WITH SAFETY C'S COMPONENTE CON CARATTERISTICHE DI SICUREZZA	N. OF SAFETY C'S N. CARATTERISTICHE DI SICUREZZA
PART INCLUDES SAFETY CHARACTERISTICS WITH DOCUMENTATION REQUIREMENTS AND PROCESS CAPABILITY DEMONSTRATION SEE CARRARO STD N. 0-56-95	VEDERE CARRARO STD N. 0-56-95



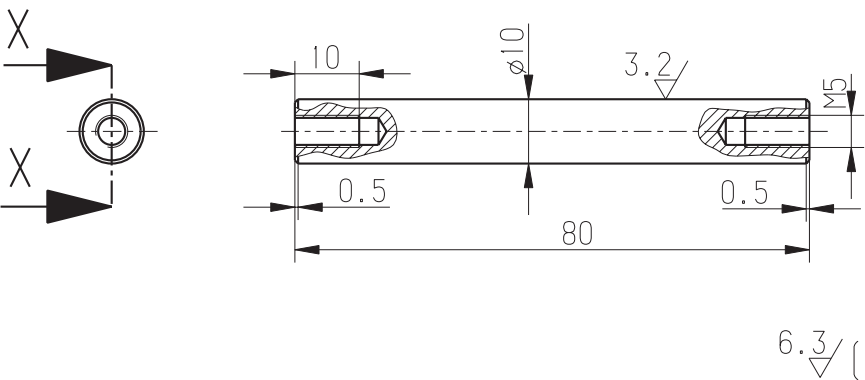


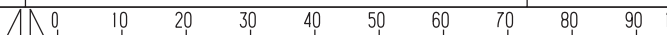
7 6 5 4 3 2 1

F	DISEGNO N. PART N.		PART WITH KEY C'S COMPONENTE CON CARATTERISTICHE CHIAVE	N. OF KEY C'S 0 N. CARATTERISTICHE CHIAVE								
		PART INCLUDES KEY CHARACTERISTICS WITH PROCESS CAPABILITY DEMONSTRATION SEE CARRARO STD N. 0-56-95	COMPONENTE CON CARATTERISTICHE CHIAVE CON DIMOSTRAZIONE CAPACITA' DI PROCESSO VEDERE CARRARO STD N. 0-56-95									
			PART WITH SAFETY C'S COMPONENTE CON CARATTERISTICHE DI SICUREZZA		N. OF SAFETY C'S 0 N. CARATTERISTICHE DI SICUREZZA							
		PART INCLUDES SAFETY CHARACTERISTICS WITH DOCUMENTATION REQUIREMENTS AND PROCESS CAPABILITY DEMONSTRATION SEE CARRARO STD N. 0-56-95	COMPONENTE CON CARATTERISTICHE DI SICUREZZA CON DOCUMENTAZIONE OBBLIGATORIA E DIMOSTRAZIONE CAPACITA' DI PROCESSO VEDERE CARRARO STD N. 0-56-95									
		PART INCLUDES SAFETY CHARACTERISTICS WITH DOCUMENTATION REQUIREMENTS AND PROCESS CAPABILITY DEMONSTRATION SEE CARRARO STD N. 0-56-95	COMPONENTE CON CARATTERISTICHE DI SICUREZZA CON DOCUMENTAZIONE OBBLIGATORIA E DIMOSTRAZIONE CAPACITA' DI PROCESSO VEDERE CARRARO STD N. 0-56-95									
	-	-										
	REV. REV.	DESCRIZIONE CHANGE										
TUTTI I DIRITTI SONO RISERVATI E PROPRIETA' DI CARRARO S.P.A. SENZA IL CONSENSO SCRITTO DI CARRARO S.P.A. QUESTO DISEGNO NON PUO' ESSERE RIPRODOTTO, O IN ALCUN MODO ESSERE UTILIZZATO PER LA PRODUZIONE DEI COMPONENTI O ASSIEME ILLUSTRATO NE' ESSERE TRASMESSO A ALTRE PARTI. OGNI INFRAZIONE VERRA' PERSECUITA LEGALMENTE. ALL PROPRIETARY RIGHTS RESERVED BY CARRARO S.P.A. THIS DRAWING SHALL NOT BE REPRODUCED OR IN ANY WAY UTILIZED FOR THE MANUFACTURE OF THE COMPONENT OR ASSEMBLY HEREIN ILLUSTRATED AND MUST NOT BE RELEASED TO OTHER PARTIES WITHOUT WRITTEN CONSENT BY CARRARO S.P.A. ANY INFRINGEMENT WILL BE LEGALLY PURSUED.												
MATERIALE STD STD MATERIAL	ACCIAIO C45 - UNI 10083	DISEGNATO DRAWN	DENGO CARLO									
MATERIALE OPT OPT MATERIAL		APPROVATO APPROVED	-									
TRATT. TERM. HEAT TREAT.		DATA DATE	12/11/12	CL.FUNZ. _ _ FUNC.CL. _ _								
TRATT. SUPERF. SURF. TREAT.		RIF. GENERALI GENERAL REFS.	0-20-90									
PRODOTTO ASSEMBLY	ATTREZZATURA PROVA FLESSIONE 4 PUNTI - 4 POINTS BENDING TEST EQUIPMENT											
DENOMINAZIONE DESCRIPTION	GUIDA PER PUNZONE - PUNCH GUIDE											
 CARRARO DRIVETECH CARRARO DRIVETECH S.p.A. - Via Olmo, 37 35011 CAMPODARSEGO (PD) - ITALY	MODELLO N. CASTING REF.	A4	PESO WEIGHT	0.118 daN								
	SOST. IL REPLACES	-		SCALA SCALE	1:1							
	DISEGNO N. PART N.		TAV SHEET	1/1								
4	3	0	10	20	30	40	50	60	70	80	90	100

SMUSSI NON QUOTATI: 1x45°
UNQUOTED CHAMFERS: 1x45°

6.3 / (3.2)

4		3		2		1	
DISEGNO N. PART N.		 PART WITH KEY C'S COMPONENTE CON CARATTERISTICHE CHIAVE		N. OF KEY C'S 0 N. CARATTERISTICHE CHIAVE			
F		PART INCLUDES KEY CHARACTERISTICS WITH PROCESS CAPABILITY DEMONSTRATION SEE CARRARO STD N. 0-56-95 COMPONENTE CON CARATTERISTICHE CHIAVE CON DIMOSTRAZIONE CAPACITA' DI PROCESSO VEDERE CARRARO STD N. 0-56-95					
E		 PART WITH SAFETY C'S COMPONENTE CON CARATTERISTICHE DI SICUREZZA		N. OF SAFETY C'S 0 N. CARATTERISTICHE DI SICUREZZA			
D		PART INCLUDES SAFETY CHARACTERISTICS WITH DOCUMENTATION REQUIREMENTS AND PROCESS CAPABILITY DEMONSTRATION SEE CARRARO STD N. 0-56-95 COMPONENTE CON CARATTERISTICHE DI SICUREZZA CON DOCUMENTAZIONE OBBLIGATORIA E DIMOSTRAZIONE CAPACITA' DI PROCESSO VEDERE CARRARO STD N. 0-56-95					
C							
-		-					
REV. REV.		DESCRIZIONE CHANGE					
<small>TUTTI I DIRITTI SONO RISERVATI E PROPRIETA' DI CARRARO S.P.A. SENZA IL CONSENSO SCRITTO DI CARRARO S.P.A. QUESTO DISEGNO NON PUO' ESSERE RIPRODOTTO, O IN ALCUN MODO ESSERE UTILIZZATO PER LA PRODUZIONE DEI COMPONENTI O ASSIEME ILLUSTRATO NE' ESSERE TRASMESSO A ALTRE PARTI. OGNI INFRAZIONE VERRA' PERSECUITA LEGALMENTE ALL PROPRIETARY RIGHTS RESERVED BY CARRARO S.P.A. THIS DRAWING SHALL NOT BE REPRODUCED OR IN ANY WAY UTILIZED FOR THE MANUFACTURE OF THE COMPONENT OR ASSEMBLY HEREIN ILLUSTRATED AND MUST NOT BE RELEASED TO OTHER PARTIES WITHOUT WRITTEN CONSENT BY CARRARO S.P.A. ANY INFRINGEMENT WILL BE LEGALLY PURSUED.</small>							
MATERIALE STD STD MATERIAL		ACCIAIO C45 - UNI 10083		DISEGNATO DRAWN		DENGO CARLO	
MATERIALE OPT OPT MATERIAL				APPROVATO APPROVED		-	
TRATT. TERM. HEAT TREAT.				DATA DATE		30/10/2012	
TRATT. SUPERF. SURF. TREAT.				RIF. GENERALI GENERAL REFS.		0-20-90	
PRODOTTO ASSEMBLY		ATTREZZATURA PROVA FLESSIONE 4 PUNTI - 4 POINTS BENDING TEST EQUIPMENT					
DENOMINAZIONE DESCRIPTION		FERMO PROVINO - SPECIMEN CLAMP					
A		 CARRARO DRIVETECH S.p.A. - Via Olmo, 37 35011 CAMPODARSEGO (PD) - ITALY		MODELLO N. CASTING REF.		A4	
		SOST. IL REPLACES		-		 PESO WEIGHT 0.918 daN SCALA SCALE 2:1	
		DISEGNO N. PART N.				TAV SHEET 1/1	
4		3		0		100	

F	DISEGNO N. PART N.		PART WITH KEY C'S COMPONENTE CON CARATTERISTICHE CHIAVE	N. OF KEY C'S 0 N. CARATTERISTICHE CHIAVE	
	PART INCLUDES KEY CHARACTERISTICS WITH PROCESS CAPABILITY DEMONSTRATION SEE CARRARO STD N. 0-56-95				
	COMPONENTE CON CARATTERISTICHE CHIAVE CON DIMOSTRAZIONE CAPACITA' DI PROCESSO VEDERE CARRARO STD N. 0-56-95				
	E		PART WITH SAFETY C'S COMPONENTE CON CARATTERISTICHE DI SICUREZZA	N. OF SAFETY C'S 0 N. CARATTERISTICHE DI SICUREZZA	
PART INCLUDES SAFETY CHARACTERISTICS WITH DOCUMENTATION REQUIREMENTS AND PROCESS CAPABILITY DEMONSTRATION SEE CARRARO STD N. 0-56-95					
COMPONENTE CON CARATTERISTICHE DI SICUREZZA CON DOCUMENTAZIONE OBBLIGATORIA E DIMOSTRAZIONE CAPACITA' DI PROCESSO VEDERE CARRARO STD N. 0-56-95					
D					
	C	-	-		
		REV. REV.	DESCRIZIONE CHANGE		
		TUTTI I DIRITTI SONO RISERVATI E PROPRIETA' DI CARRARO S.P.A. SENZA IL CONSENSO SCRITTO DI CARRARO S.P.A. QUESTO DISEGNO NON PUO' ESSERE RIPRODOTTO, O IN ALCUN MODO ESSERE UTILIZZATO PER LA PRODUZIONE DEI COMPONENTI O ASSIEME ILLUSTRATO NE' ESSERE TRASMESSO A ALTRE PARTI. OGNI INFRAZIONE VERRA' PERSECUITA LEGALMENTE. ALL PROPRIETARY RIGHTS RESERVED BY CARRARO S.P.A. THIS DRAWING SHALL NOT BE REPRODUCED OR IN ANY WAY UTILIZED FOR THE MANUFACTURE OF THE COMPONENT OR ASSEMBLY HEREIN ILLUSTRATED AND MUST NOT BE RELEASED TO OTHER PARTIES WITHOUT WRITTEN CONSENT BY CARRARO S.P.A. ANY INFRINGEMENT WILL BE LEGALLY PURSUED.			
B		MATERIALE STD STD MATERIAL	HSS STEEL	DISEGNATO DRAWN	DENGO CARLO
	MATERIALE OPT OPT MATERIAL	APPROVATO APPROVED			
	TRATT. TERM. HEAT TREAT.	DATA DATE	12/11/12	CL.FUNZ. _ _ FUNC.CL. _ _	
	TRATT. SUPERF. SURF. TREAT.	RIF. GENERAL I GENERAL REFS.	0-20-90		
A	PRODOTTO ASSEMBLY	ATTREZZATURA PROVE FLESSIONE A 4 PUNTI - 4 POINTS BENDING TEST EQUIPMENT			
	DENOMINAZIONE DESCRIPTION	RULLO DI CARICO / LOADING ROLLER			
	 CARRARO DRIVETECH CARRARO DRIVETECH S.p.A. - Via Olmo, 37 35011 CAMPODARSEGO (PD) - ITALY	MODELLO N. CASTING REF.	A4	PESO WEIGHT	0.046 daN
		SOST. IL REPLACES	-		SCALA SCALE
DISEGNO N. PART N.		TAV SHEET			1/1
	4	3			

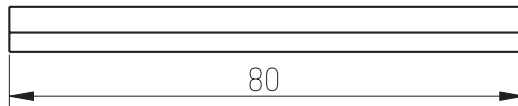
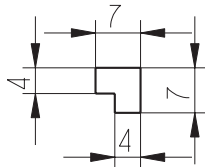
4

3



2

1

DISEGNO N.
PART N.PART WITH KEY C'S
COMPONENTE CON CARATTERISTICHE
CHIAVEN. OF KEY C'S
0
N. CARATTERISTICHE CHIAVEPART INCLUDES KEY CHARACTERISTICS WITH PROCESS CAPABILITY DEMONSTRATION
SEE CARRARO STD N. 0-56-95COMPONENTE CON CARATTERISTICHE CHIAVE CON DIMOSTRAZIONE CAPACITA' DI PROCESSO
VEDERE CARRARO STD N. 0-56-95PART WITH SAFETY C'S
COMPONENTE CON CARATTERISTICHE DI
SICUREZZAN. OF SAFETY C'S
0
N. CARATTERISTICHE DI SICUREZZAPART INCLUDES SAFETY CHARACTERISTICS WITH DOCUMENTATION REQUIREMENTS
AND PROCESS CAPABILITY DEMONSTRATION
SEE CARRARO STD N. 0-56-95COMPONENTE CON CARATTERISTICHE DI SICUREZZA CON DOCUMENTAZIONE OBBLIGATORIA
E DIMOSTRAZIONE CAPACITA' DI PROCESSO
VEDERE CARRARO STD N. 0-56-95

3.2

REV.
REV.DESCRIZIONE
CHANGETUTTI I DIRITTI SONO RISERVATI E PROPRIETA' DI CARRARO S.P.A. SENZA IL CONSENSO SCRITTO DI CARRARO S.P.A. QUESTO DISEGNO NON PUO' ESSERE RIPRODOTTO, O IN ALCUN MODO ESSERE UTILIZZATO
PER LA PRODUZIONE DEI COMPONENTI O ASSIEME ILLUSTRATO NE' ESSERE TRASMESSO A ALTRE PARTI. OGNI INFRAZIONE VERRA' PERSECUITA LEGALMENTE
ALL PROPRIETARY RIGHTS RESERVED BY CARRARO S.P.A. THIS DRAWING SHALL NOT BE REPRODUCED OR IN ANY WAY UTILIZED FOR THE MANUFACTURE OF THE COMPONENT OR ASSEMBLY HEREIN ILLUSTRATED AND
MUST NOT BE RELEASED TO OTHER PARTIES WITHOUT WRITTEN CONSENT BY CARRARO S.P.A. ANY INFRINGEMENT WILL BE LEGALLY PURSUED.MATERIALE STD
STD MATERIAL ACCIAIO C45 - UNI 10083DISEGNATO
DRAWN DENGO CARLOMATERIALE OPT
OPT MATERIALAPPROVATO
APPROVED -TRATT. TERM.
HEAT TREAT.DATA
DATE 12/11/12CL.FUNZ. _ _
FUNC.CL.TRATT.SUPERF.
SURF.TREAT.RIF. GENERALI
GENERAL REFS. 0-20-90PRODOTTO
ASSEMBLY ATTREZZATURA PROVE FLESSIONE A 4 PUNTI - 4 POINTS BENDING TEST EQUIPMENTDENOMINAZIONE
DESCRIPTION ADATTATORE PER RULLO / ROLLER ADAPTERCARRARO DRIVETECH S.p.A. - Via Olmo, 37
35011 CAMPODARSEGO (PD) - ITALYMODELLO N.
CASTING REF.

A4

PESO
WEIGHT 0.025 daNSOST. IL
REPLACES -SCALA
SCALE 1:1DISEGNO N.
PART N.TAV
SHEET 1/1

4

3



0

10

20

30

40

50



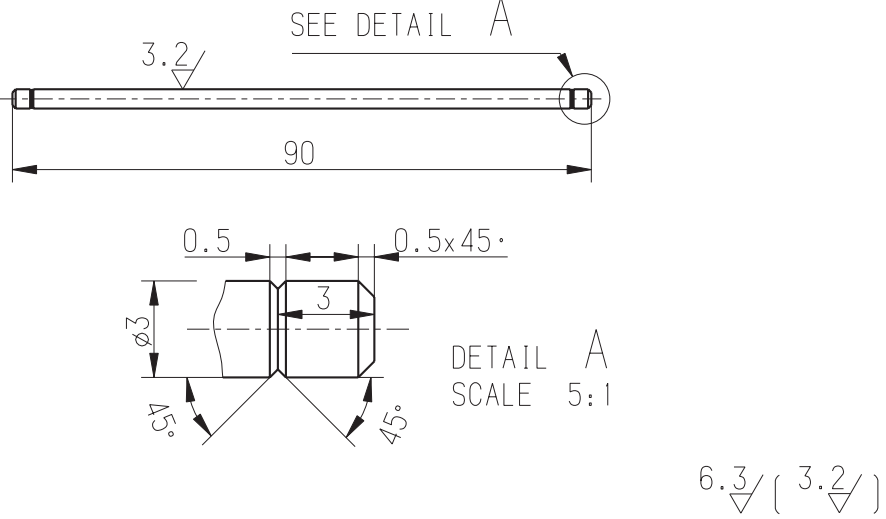

60

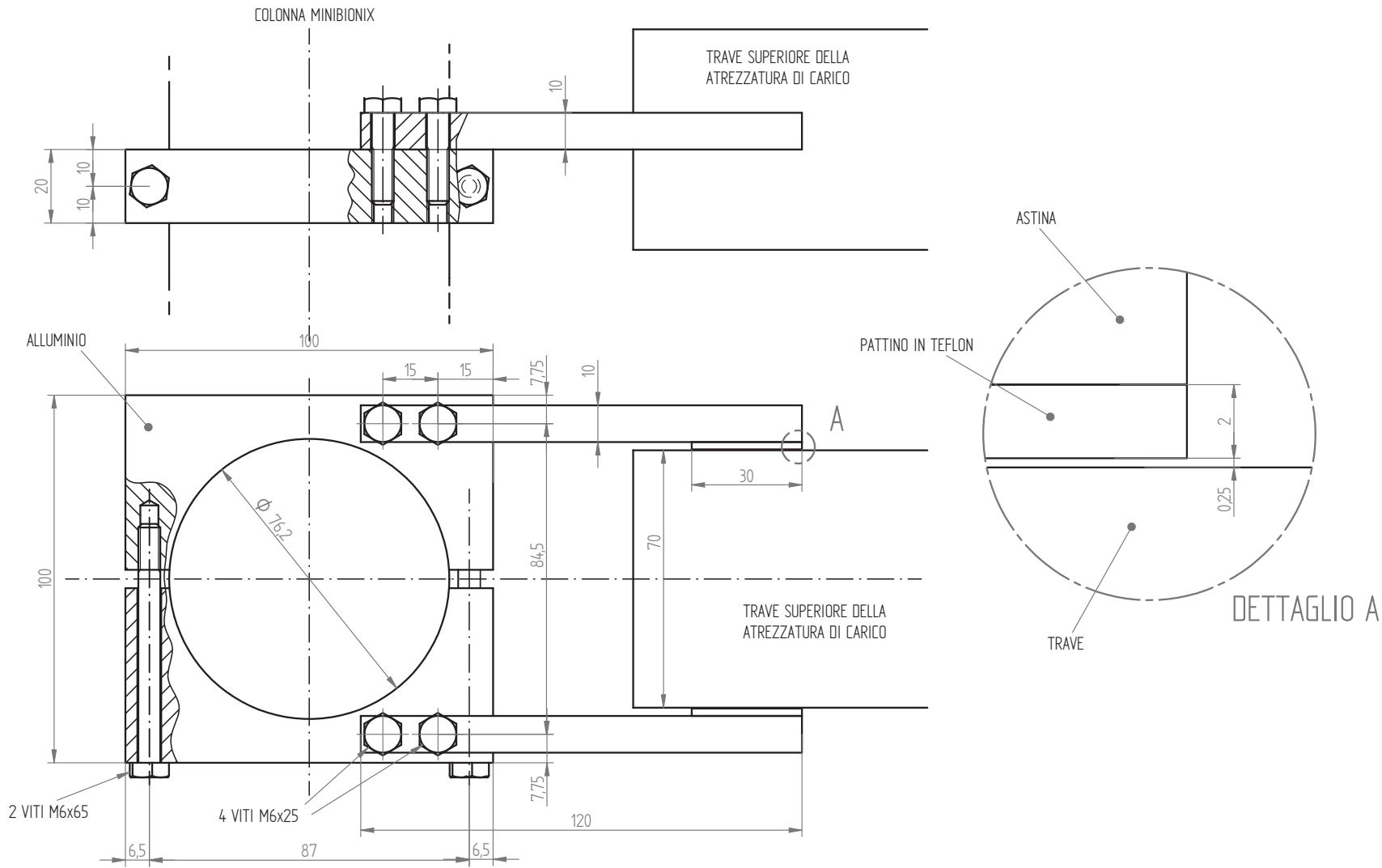
70

80

90

100

DISEGNO N. PART N.	 PART WITH KEY C'S COMPONENTE CON CARATTERISTICHE CHIAVE	N. OF KEY C'S 0 N. CARATTERISTICHE CHIAVE
F	PART INCLUDES KEY CHARACTERISTICS WITH PROCESS CAPABILITY DEMONSTRATION SEE CARRARO STD N. 0-56-95 COMPONENTE CON CARATTERISTICHE CHIAVE CON DIMOSTRAZIONE CAPACITA' DI PROCESSO VEDERE CARRARO STD N. 0-56-95	
E	 PART WITH SAFETY C'S COMPONENTE CON CARATTERISTICHE DI SICUREZZA	N. OF SAFETY C'S 0 N. CARATTERISTICHE DI SICUREZZA
D	PART INCLUDES SAFETY CHARACTERISTICS WITH DOCUMENTATION REQUIREMENTS AND PROCESS CAPABILITY DEMONSTRATION SEE CARRARO STD N. 0-56-95 COMPONENTE CON CARATTERISTICHE DI SICUREZZA CON DOCUMENTAZIONE OBBLIGATORIA E DIMOSTRAZIONE CAPACITA' DI PROCESSO VEDERE CARRARO STD N. 0-56-95	
C		
B	-	-
A	REV. DESCRIZIONE REV. CHANGE	
A	TUTTI I DIRITTI SONO RISERVATI E PROPRIETA' DI CARRARO S.P.A. SENZA IL CONSENSO SCRITTO DI CARRARO S.P.A. QUESTO DISEGNO NON PUO' ESSERE RIPRODOTTO, O IN ALCUN MODO ESSERE UTILIZZATO PER LA PRODUZIONE DEI COMPONENTI O ASSIEME ILLUSTRATO NE' ESSERE TRASMESSO A ALTRE PARTI. OGNI INFRAZIONE VERRA' PERSECUITA LEGALMENTE. ALL PROPRIETARY RIGHTS RESERVED BY CARRARO S.P.A. THIS DRAWING SHALL NOT BE REPRODUCED OR IN ANY WAY UTILIZED FOR THE MANUFACTURE OF THE COMPONENT OR ASSEMBLY HEREIN ILLUSTRATED AND MUST NOT BE RELEASED TO OTHER PARTIES WITHOUT WRITTEN CONSENT BY CARRARO S.P.A. ANY INFRINGEMENT WILL BE LEGALLY PURSUED.	
A	MATERIALE STD HSS STEEL STD MATERIAL	DISEGNATO DENGO CARLO DRAWN
A	MATERIALE OPT OPT MATERIAL	APPROVATO - APPROVED
A	TRATT. TERM. HEAT TREAT.	DATA 12/11/12 DATE
A	TRATT. SUPERF. SURF. TREAT.	RIF. GENERALI 0-20-90 GENERAL REFS.
A	PRODOTTO ATTREZZATURA PROVE FLESSIONE A 4 PUNTI - 4 POINTS BENDING TEST EQUIPMENT ASSEMBLY	
A	DENOMINAZIONE RULLO SOSTITUIVO / SUBSTITUTIVE ROLLER DESCRIPTION	
A	 CARRARO DRIVETECH S.p.A. - Via Olmo, 37 35011 CAMPODARSEGO (PD) - ITALY	MODELLO N. A4 PESO 0.006 daN CASTING REF. WEIGHT SOST. IL - REPLACES DISEGNO N. - PART N. TAV 1/1 SHEET
A	4	100



POS	DENOMINAZIONE	Q.TA'	MATERIALE	NOTE
	ATTREZZATURA ANTI ROTAZIONE TRAVE	17/01/2014		
	UNIVERSITA' DI PADOVA	Dengo Carlo	SCALA:	

References

- [1] CARRARO Internal Standard. Std 0-30-92/2 FOUR SQUARE TEST, 1996.
- [2] CARRARO Internal Standard. Std 0-45-94/3 AXLE PRODUCT FEATURES, 2013.
- [3] ISO 6336-2. Calculation of surface durability (pitting), 2006.
- [4] KISSsoft: Calculation programs for machine design, Release 03/2013 F. <http://www.kisssoft.ch/>.
- [5] UNI 5394. Pallinatura per miglioramento della resistenza a fatica su organi meccanici di acciaio (*in Italian*), 1972.
- [6] ISO 6336-1. Basic principles, introduction and general influence factors, 2006.
- [7] ISO 12107. Metallic materials - Fatigue testing - Statistical planning and analysis of data, 2003.
- [8] R. I. Stephens, A. Fatemi, R. R. Stephens, and H. O. Fuchs. *Metal Fatigue in Engineering*. John Wiley & Sons, Inc, second edition, 2000.
- [9] R. W. Hertzberg. *Deformation and Fracture Mechanics of Engineering Materials*. John Wiley & Sons, Inc, second edition, 1989.
- [10] ISO 6336-5. Strength and quality of materials, 2003.
- [11] B.R. Hohn and K. Michaelis. Influence of oil temperature on gear failures. *Tribology International*, 37:103 – 109, 2004.

- [12] B.R. Hohn, K. Michaelis, and A. Doleschel. Limitations of Bench Testing for Gear Lubricants. *Bench Testing of Industrial Fluid Lubrication and Wear Properties Used in Machinery Applications*, ASTM STP 1404, 2001.
- [13] AGMA 2101-D04. Fundamental Rating Factors and Calculation Methods for Involute Spur and Helical Gear Teeth [Metric Edition], 2004.
- [14] G. J. Lieberman. Tables for one-sided statistical tolerance limits. *Industrial Quality Control*, Vol. XIV, No. 10:7–9, 1958.
- [15] AGMA 2003-B97. Rating the Pitting Resistance and Bending Strength of Generated Straight Bevel, Zerol Bevel and Spiral Bevel Gear Teeth, 2003.
- [16] ISO 10300. Calculation of load capacity of bevel gears, 2001.
- [17] Gleason. <http://www.gleason.com/cms/en/181/company-profile>.
- [18] Gleason Works. *Bending Stresses in Bevel Gear Teeth*. Gleason Works, 1965.
- [19] CARRARO Internal Standard. Std 1-01-88 / MANGANESE-CHROMIUM CASE HARDENING STEEL 20MnCr5, 1988.
- [20] CARRARO Internal Standard. Std 1-12-88 / NICKEL-CHROMIUM-MOLYBDENUM CASE HARDENING STEEL 18NiCrMo5, 1988.
- [21] CARRARO Internal Standard. Std 1-00001-0 / CASE HARDENING STEELS - CHROME-NICKEL STEEL 19CrNi5, 2010.
- [22] GBT 5216-2004. Structural steels subject to end-quench hardenability requirements, 2004.
- [23] BS 970-1. Specification for wrought steels for mechanical and allied engineering purposes. General inspection and testing procedures and specific requirements for carbon, carbon manganese, alloy and stainless steels, 1996.
- [24] J.L. Pacheco and G. Krauss. Microstructure and High Bending Fatigue Strength in Carburized Steel. *Journal of Heat Treatment*, 7:77–86, 1989.
- [25] H. Lin, G.A. Fett, R.R. Binoniemi, J.A. Sanders, D.K. Matlock, and G. Krauss. Investigation of S-N Test Data Scatter of Carburized 4320 Steel. *SAE Technical Paper 2007-01-1006*, 2007.

- [26] K.O. Findley, G. Krauss, R.J. Johnson, and D.K. Matlock. Deterministic Analysis of Crack Growth Rates in Carburized Steels. *Procedia Engineering*, 10(0):370 – 375, 2011. 11th International Conference on the Mechanical Behavior of Materials (ICM11).
- [27] K.A. Erven, D.K. Matlock, and G. Krauss. Effect of Sulfur on Bending Fatigue of Carburized Steel. *Journal of Heat Treatment*, 9:27–35, 1991.
- [28] D. Medlin, G. Krauss, D.K. Matlock, K. Burriss, and M. Slane. Comparison of Single Gear Tooth and Cantilever beam Bending Fatigue Testing of Carburized Steel. *International Congress and Exposition, Detroit, Michigan, February 27-March 2, 1995*, 1995.
- [29] J. John, K. Li, and H. Li. Fatigue Performance and Residual Stress of Carburized Gear Steels Part I: Residual Stress. *SAE International Journal of Materials & Manufacturing*, 1(1):718–724, 2009.
- [30] J. John, K. Li, and H. Li. Fatigue Performance and Residual Stress of Carburized Gear Steels Part II: Fatigue Performance. *SAE International Journal of Materials & Manufacturing*, 1(1):709–717, 2009.
- [31] K. Ogawa, H. Yamada, K. Saruki, M. Yokoi, and M. Inuzuka. Influence of residual stress on fatigue strength of carburized and shot peened notched specimens. Toyota Central R&D and Toyota Motor Corp.
- [32] S. Farfán, C. Rubio-González, T. Cervantes-Hernández, and G. Mesmacque. High cycle fatigue, low cycle fatigue and failure modes of a carburized steel. *International Journal of Fatigue*, 26(6):673 – 678, 2004.
- [33] O. Asi, A. Ç. Can, J. Pineault, and M. Belassel. The relationship between case depth and bending fatigue strength of gas carburized {SAE} 8620 steel. *Surface and Coatings Technology*, 201(12):5979 – 5987, 2007.
- [34] Y. Liu, M. Wang, J. Shi, W. Hui, G. Fan, and H. Dong. Fatigue properties of two case hardening steels after carburization. *International Journal of Fatigue*, 31(2):292 – 299, 2009.
- [35] O. Asi, A. Ç. Can, J. Pineault, and M. Belassel. The effect of high temperature gas carburizing on bending fatigue strength of {SAE} 8620 steel. *Materials & Design*, 30(5):1792 – 1797, 2009.
- [36] L. Ma, M.Q. Wang, J. Shi, W.J. Hui, and H. Dong. Influence of niobium microalloying on rotating bending fatigue properties of case carburized steels. *Materials Science and Engineering: A*, 498(1–2):258 – 265, 2008.

- [37] H.J. Kim and Y.G. Kweon. High Cycle Fatigue Behavior of Gas Carburized Medium Carbon Cr-Mo Steel. *Metallurgical and Materials Transactions A*, 27:2557–2564, 1996.
- [38] K. Burkart, H. Bomas, and H.-W. Zoch. Fatigue of notched case-hardened specimens of steel SAE 5120 in the VHCF regime and application of the weakest-link concept. *International Journal of Fatigue*, 33(1):59 – 68, 2011.
- [39] R.E. Cohen, P.J. Haagensen, D.K. Matlock, and G. Krauss. Assessment of Bending Fatigue Limits for Carburized Steel. *International Congress and Exposition, Detroit, Michigan, February 25-March 1, 1991*, 1991.
- [40] H. Brugger and G. Krauss. Influence of Ductility on the Behavior of Carburizing Steel During Static and Dynamic Bend Testing. *Archiv Eisenhüttenwesen*, 32:529–539, 1961.
- [41] ISO 6336-3. Calculation of tooth bending strength, 2006.
- [42] ASTM E8/E8M-11. Standard Test Method for Tension Testing of Metallic Materials, 2012.
- [43] ANSYS Mechanical APDL. <http://www.ansys.com/>, Release 11.
- [44] R.E. Cohen, D.K. Matlock, and G. Krauss. Specimen Edge Effects on Bending Fatigue of Carburized Steel. *Journal of Materials Engineering and Performance*, 1(5):695–704, 1992.
- [45] ISO 6336. Calculation of load capacity of spur and helical gears, 2006.
- [46] W. D. Pilkey and D.F. Pilkey. *Peterson's Stress Concentration Factors*. John Wiley & Sons, Inc., 2008.
- [47] EN 10083-1. Steel for quenching and tempering - Part 1: General technical delivery conditions, 2006.
- [48] UNI 3244. Esame microscopico dei materiali ferrosi. Valutazione delle inclusioni non metalliche negli acciai mediante immagini tipo. (*in Italian*), 1980.
- [49] UNI 3245. Esame microscopico dei materiali ferrosi. Determinazione della grossezza del grano austenitico o ferritico degli acciai. (*in Italian*), 1987.

- [50] ASTM E45-97. Standard Test Method for Determining the Inclusion Content of Steel, 2002.
- [51] ASTM E112-96. Standard Test Methods for Determining Average Grain Size, 1996.
- [52] ISO 2639. Determination and verification of the depth of carburized and hardened cases, 2002.
- [53] V. Pellizzato. Analisi della resistenza a fatica a flessione di acciai cementati e applicazione a ruote dentate. Master's thesis, Università di Padova, Italy (*in Italian*), 2014.
- [54] F. Baldisserotto. Progettazione a fatica di ruote dentate e analisi statistica di risultati sperimentali. Master's thesis, Università di Padova, Italy (*in Italian*), 2015.
- [55] Y. Murakami. *Metal Fatigue: Effects of Small Defects and Nonmetallic Inclusions*. Elsevier Science Ltd, first edition, 2002.
- [56] G. Krauss. Bending Fatigue of Carburized Steels. *ASM Handbook, Fatigue and Fracture*, 19, 1996.
- [57] J. Komotori, M. Shimizu, Y. Misaka, and K. Kawasaki. Fatigue strength and fracture mechanism of steel modified by super-rapid induction heating and quenching. *International Journal of Fatigue*, 23, Supplement 1(0):225 – 230, 2001.
- [58] G. Chai. The formation of subsurface non-defect fatigue crack origins. *International Journal of Fatigue*, 28(11):1533 – 1539, 2006.
- [59] E. Bayraktar, I. M. Garcias, and C. Bathias. Failure mechanisms of automotive metallic alloys in very high cycle fatigue range. *International Journal of Fatigue*, 28(11):1590 – 1602, 2006.
- [60] H. Bomas, K. Burkart, and H.W. Zoch. Evaluation of S–N curves with more than one failure mode. *International Journal of Fatigue*, 33(1):19 – 22, 2011.
- [61] T. Krug, K.H. Lang, T. Fett, and D. Löhe. Influence of residual stresses and mean load on the fatigue strength of case-hardened notched specimens. *Materials Science and Engineering: A*, 468–470(0):158 – 163, 2007.

- [62] D. Jeddi and H.P. Lieurade. Effect of retained austenite on high cycle fatigue behavior of carburized 14NiCr11 steel. *Procedia Engineering*, 2(1):1927 – 1936, 2010.
- [63] N.E. Dowling. *Mechanical Behavior of Materials*. Prentice Hall, fourth edition, 2012.
- [64] B. Hanel, E. Haibach, T. Seeger, G. Wirthgen, and H. Zenner. *Analytical strength assessment of components in mechanical engineering*. Forschungskuratorium Maschinenbau (FKM), 5th edition, 2003.
- [65] E. Siebel and M. Stieler. Ungleichförmige spannungsverteilung bei schwingender beanspruchung. *VDI-Z*, 97:121–126, 1955.
- [66] G. Niemann and H. Winter. *Elementi di macchina*, volume I. EST - SPRINGER, 1986.
- [67] M. Stieler. *Untersuchungen über die Dauerschwingfestigkeit metallischer Bauteile bei Raumtemperatur*. Dissertation, TU Stuttgart, 1954.
- [68] R. F. Handschuh, T. L. Krants, B. A. Lerch, and C. S. Burke. Investigation of Low-Cycle Bending Fatigue of AISI 9310 Steel Spur Gears. *10th International Power Transmission and Gearing Conference, Las Vegas, Nevada*, 2007.
- [69] B. Tufts and T. Krantz. Pitting and Bending Fatigue Evaluations of a New Case-Carburized Gear Steel. *International Design Engineering Technical Conferences and Computers and Information in Engineering Conference, Las Vegas, Nevada*, 2007.
- [70] Romax Technology Ltd, Romax Designer R14, Nottingham, United Kingdom. <http://www.romaxtech.com/>.
- [71] B.S. Saini and V.K. Gupta. Effect of WC/C PVD coating on fatigue behaviour of case carburized SAE8620 steel. *Surface and Coatings Technology*, 205(2):511 – 518, 2010.
- [72] T. Hayama and H. Yoshitade. Effect of mean stress on fatigue strength of carburized steel. *Bulletin of JSME*, 1970.
- [73] UNI7670. Meccanismi per apparecchi di sollevamento. istruzioni per il calcolo (*in Italian*), 1988.

- [74] S. Meneghello. Previsione della resistenza a fatica di ruote dentate mediante prove su provini e normativa ISO 6336. B.S. Thesis, Università di Padova, Italy (*in Italian*), 2015.
- [75] ASTM 739-91. Standard Practice for Statistical Analysis of Linear or Linearized Stress-Life (S-N) and Strain-Life (ϵ -N) Fatigue Data, 2004.
- [76] JSME S 002-1981. Standard method of statistical fatigue testing, 1981.
- [77] Y. L. Lee, J. Pan, R. Hathaway, and M. Barkey. *Fatigue Testing and Analysis*. Elsevier, first edition, 2004.
- [78] C. L. Shen, P. H. Wirshing, and G. T. Cashman. Design curve to characterize fatigue strength. *Journal of Engineering Material and Technology*, Vol. 118:535–541, 1996.
- [79] A. M. Mood W. J. Dixon. A Method for Obtaining and Analyzing Sensitivity Data. *Journal of the American Statistical Association*, Vol. 43, No. 241:109–126, 1948.
- [80] UNI 3964. Prove meccaniche dei materiali metallici - prove di fatica a temperatura ambiente, principi generali (*in Italian*), 1985.
- [81] J. Zhag and D. B. Kececioglu. New approaches to determine the endurance strength distribution. *Proceedings of the 4th ISSAT International Conference on Reliability & Quality in Design*, pages 243–245, 1998.
- [82] W. J. Dixon. The Up-and-Down Method for Small Samples. *Journal of the American Statistical Association*, Vol. 60, No. 312:967–978, 1965.
- [83] K.A. Brownlee, J. L. Hodges, and M. Rosenblatt. The Up-and-Down Method with Small Samples. *Journal of the American Statistical Association*, Vol. 48, No. 262:262–267, 1953.
- [84] D. C. Montgomery. *Design and Analysis of Experiments*. John Wiley & Sons, Inc, 8th edition, 2012.
- [85] W. Nelson. *Accelerated Testing*. Wiley, fourth edition, 1990.